

Forschungszentrum Karlsruhe
Technik und Umwelt

Wissenschaftliche Berichte
FZKA 6550
EUR 19707 EN

Nuclear Fusion Programme
Annual Report of the
Association Forschungszentrum
Karlsruhe/EURATOM
October 1999 – September 2000

Programm Kernfusion

Dezember 2000

Forschungszentrum Karlsruhe

Technik und Umwelt

Wissenschaftliche Berichte

FZKA 6550
EUR 19707 EN

Nuclear Fusion Programme
Annual Report of the
Association Forschungszentrum Karlsruhe/
EURATOM
October 1999 - September 2000

compiled by G. Kast
Programm Kernfusion

Forschungszentrum Karlsruhe GmbH, Karlsruhe
2000

Als Manuskript vervielfältigt
Für diesen Bericht behalten wir uns alle Rechte vor

Forschungszentrum Karlsruhe GmbH
Postfach 3640, 76021 Karlsruhe

ISSN 0947-8620

Preface

The need for fusion energy

Nuclear Fusion is one of the options to replace fossil fuels in energy production. The worldwide demand of energy with an estimated increase of electricity production by at least a factor of two in the second half of this century, fading resources of raw materials and a growing concern about global warming require innovative solutions.

While energy converted from radiation of the sun may become attractive for wide spread settlements, the growing number of megacities will require large units of power. This is the market where nuclear fusion energy may, once developed, play an important role. Practically inexhaustible fuel resources, attractive safety features and no emissions of gases that cause global warming are the advantageous features of fusion energy.

Fusion research in the European Union

Considering the importance of a secure, environmentally acceptable and affordable supply of energy for the welfare and prosperity of their citizens the European Union supports the development of new energy sources. The fusion research programme, integrating the total research work of the member states and Switzerland, represents the worlds largest effort in this field and has gained a leading position worldwide.

Fusion research with its integration and coherence represents already a research network of the kind proposed to be implemented within the next 5 years European Research Programme.

The role of Forschungszentrum Karlsruhe

The growing complexity and technical orientation of future large fusion experiments and perspective power reactors gave origin to the European Fusion Technology Programme in 1982. Design and r+d tasks were first guided by the Next European Torus (NET) project, which later on, gave input to the world wide project of the International Tokamak Experimental Reactor ITER.

While the German research laboratories Forschungszentrum Jülich and Max-Planck-Institute for Plasma Physics Garching/Greifswald concentrate on plasma physics and plasma wall interaction, Forschungszentrum Karlsruhe is engaged in different key issues of design and technologies that are required for ITER or future fusion reactors.

The main work areas

For the ITER project, Forschungszentrum Karlsruhe developed **superconducting magnets** to confine the plasma, gyrotron type **microwave generators** to start the nuclear burn, and **exhaust gas pumping** and fuel **clean-up systems**. ITER will demonstrate the physics of a reactor grade plasma implementing already these essential reactor technologies.

One of the highlights of the Associations research programme will be the test of the ITER toroidal field model coil. The TOSKA **superconducting magnet test facility** is being prepared for accepting the test coil by end of the current year.

Tritium, one of the fuel components that catalyses the fusion reaction, will be produced in a nuclear fusion reactor by reactions of fusion neutrons within a lithium containing **breeding blanket**. Development of an energy convertor that delivers high grade heat and supplies enough tritium to maintain the operation is one of the most challenging engineering tasks undertaken by the Association in the frame of the European Blanket Project.

One of the main experimental facilities, the **Tritium Laboratory** TLK, serves as a focus for the experimental work related to fuel cycle issues of ITER, and, more recently, of the Joint European Torus (JET).

Cost and environmental characteristics of future fusion reactors will crucially depend on solutions to the **structural materials** issue. Radiation damage from fusion neutrons and high loads of heat and mechanical stresses are expected to limit the lifetime of plasma near components and to determine the amount and radioactivity of waste. The development of low activation radiation resistant steels requires a long term programme proceeding stepwise to final qualification in a large **dedicated fusion neutron source**. The Association devotes a major activity in this field of work.

Reactor studies will gain importance in the programme. Contributions of the Associations relate to technical issues and studies of safety/environmental impact.

The work for fusion technology, as briefly outlined above, is carried out in the frame of the European Fusion Development Activity (EFDA). EFDA was founded to foster cooperative efforts of the laboratories associated to the EU Fusion Programme, in particular in view of construction

and exploitation of larger experimental facilities such as JET and ITER.

Support to the Physics Programme

The tokamak represents the main development line of the common programme. In parallel, the stellarator concept is under development to potentially improve the confinement for reactor operation. The Association, assisted by the University of Stuttgart, contributes the complete **10 megawatt microwave heating** installation to the Wendelstein-7X stellarator, being built by the IPP-EURATOM Association in Greifswald, Germany.

Organisation of the work

Forschungszentrum Karlsruhe is engaged at present in 12 research programmes of different scopes and sizes. Programmes are organized in a matrix form where small management groups coordinate the work that is executed in a variety of scientific and technical departments. Competition of the programmes lead to frequent fluctuations of contributions from the departments depending on the attractiveness of the task and the provision of resources. A continuous support from the European Commission together with the longer term perspective of the programme are important, therefore, to maintain the competence available for the fusion programme.

About 150 professionals and technicians are involved in the fusion programme of the Association FZK-EURATOM with additional support of the central technical departments.

This report

Progress from October 1999 to September 2000 is reported. For more information please contact the programme management or the responsible scientists.

Our website www.fzk.de/pkf may help to give further access to our work.

J.E. Vetter

Contents

Page

Preface

EFDA Technology Programme	1
Heating and Current Drive	3
G 52 TT 07 (TWO-IRR/CER) Irradiation Effects in Ceramics for Heating and Current Drive, and Diagnostics Systems.....	5
G 55 TT 19 EU ITER ECRF Window Development.....	7
G 52 TT 22 EU ITER ECRF Advanced Source Development	9
Plasma Facing Components	11
DV 7a Tritium Permeation, Retention, Wall Conditioning and Clean-up (Dust Removal, Baking)	13
T 438/04 Investigation of D/T Retention in n-irradiated PFC Materials	14
T 438/06 Chemical Reactivity of Dust and Flakes and D Mobilisation Experiments from Co-deposited Layers.....	18
T 438/08 Effect of Plasma Interaction	20
Vessel/Mechanical Structures	29
T 204-9 Plasma Arc Cutting of ITER Containment Vessel.....	31
Coil System	33
M 44 TFMC Installation and Test	35
M 31 Development of 60 kA Current Leads Using High Temperature Superconductors	38
M 45 ITER Coil Casing and Intercoil Structures	40
T 400-1/01 TF Model Coil	44
T 400-1/01 Stress Analysis for the TFMC Tests in TOSKA	45
T 400/1-01a Test of the ITER Model Coils, Contribution to the Test of the ITER Central Solenoid Model Coil	47
T 405-2/01 Conductor Layout and Optimisation	48
Materials Development	51
T 228.1 Influence of Higher Hydrocarbons on Vacuum Pumping	53
Fuel Cycle	55
VP 1 Cryopump Development and Testing	57
TR 1 Tokamak Exhaust Processing.....	62
TR 2 Development of Tritium Instrumentation.....	64
TEP 3A Tritium Storage in ZrCo.....	65
TR 4 Tritium Extraction from Plasma-exposed Graphite and Carbon Fibre Composite Tiles.....	66
TR 5 Tritium Recovery from Liquid and Solid Wastes.....	69
TR 6 Tritium Extraction and Helium Purification.....	70
T 456/02 Development of a Tritium Compatible Roots Pump Pumping Test of a Roots Pump under ITER Relevant Conditions.....	71

TTBA-006	Magneto Hydrodynamics (MHD)	
	TTBA-006/1, 2, 3 Test and Modelling of Forces Convection MHD.....	117
Structural Materials		121
TTMS-001	Irradiation Performance	
	HFR Irradiation Programs.....	123
	Work on OPTIFER- and F82H.-mod Alloy	124
	Correlation between Microstructure and mechanical Properties.....	126
TTMS-002	Metallurgical and Mechanical Characterisation of RAFM Steels	
	Transformation Behaviour and Tensile, Creep and Impact Toughness Properties.....	128
	Thermal and Isothermal Fatigue Properties of Base Metal	130
TTMS-003	Compatibility with Hydrogen and Liquid	
	Thermal Fatigue Scoping Tests under Hydrogen Atmosphere.....	131
	Corrosion of Reduced Activation Ferritic Martensitic (RAFM) Steels in Pb-Li.....	132
TTMS-004	Qualification of Fabrication Processes	
	Mechanical Properties of Diffusion Weldments.....	133
TTMS-005	Rules for Design, Fabrication and Inspection	
	Local Fracture Criteria for EUROFER in the Ductile-of-Brittle Transition Regime	134
	Life Time Prediction Rules for RAFM Steels.....	136
	Development of Miniaturised Push-pull (Creep-) Fatigue Specimen	137
	Qualify Control and Distribution of EUROFER 97	138
TTMS-006	Qualification of High Performance Steels	
	Specification and Characterisation of a Reduced Activation (RA) Heat.....	140
	Irradiation in a Temperature Controlled Test Rig of BOR 60.....	141
Neutron Source		143
ERB 5005 CT 990061	(NET/99-507) IFMIF Test Cell and Accelerator Optimisation and Cost Reduction	
	Test Cell Design.....	145
	Accelerator Design.....	150
Nuclear Data Base		159
TTMN-001	EFF/EAF Date File Update, Processing and Benchmark Analysis	
	TTMN-001/5, 6, 8	161
TTMN-002	Benchmark Experiments to Validate EFF/EAF Data	
	TTMN-002/4 Activation Experiments in Fusion Peak Spectrum.....	163
TTMN-002/5	Activation Experiments in White Neutron Spectrum.....	165
T 426	Experimental Validation of Shut-down Dose Rates	167

Page

Socio-economic Research on Fusion	169
International Power Supply Policy Globalisation of Research: The Example of Fusion Research	171
Preparatory Work for a Power Plant Conceptual Study	173
TRP 2 Economic and Operation Requirements	
TRP2-D 1 Critical Review of Economic-related Objectives Used in Earlier European, USA, and Japanese Power Plant Studies	175
Underlying Technology	177
Physics Integration	183
Microwave Heatings for Wendelstein 7-X	185
Appendix I FZK Departments Contributing to the Fusion Programme.....	187
Appendix II Fusion Programme Management Staff.....	189
Appendix III Glossary	191

EFDA Technology Programme

Heating and Current Drive

**G 52 TT 07 (TWO-IRR/CER)
Irradiation Effects in Ceramics for Heating and
Current Drive, and Diagnostics Systems**

In electron cyclotron wave systems for heating and current drive (ECH-CD) and for plasma diagnostics, special window structures have to fulfill vacuum operation and tritium retention requirements with ideally broadband transmission and low power absorption. Neutron irradiation effects are a substantial safety concern at the primary window position before the bioshield, as structural damage potentially degrades the material properties. In previous studies, radiation-induced increases in the dielectric properties have been identified to set in at a fast fluence level of 10^{22} n/m^2 ($E > 0.1 \text{ MeV}$) for reference window materials such as sapphire, high resistivity silicon and CVD diamond. Accordingly, a recommended maximum fast fluence level of 10^{21} n/m^2 was chosen as a characteristic testing condition which is compatible with ITER design where the radiation levels are reduced by deflecting mirrors in a 'dog-leg' arrangement. This fluence level was the guideline for the present materials studies which were focused on three areas: commercial large area CVD diamond discs (RF grade from DeBeers, UK) for ECH-CD systems, alternative CVD diamond grades for general EC window uses and selected silica grades for windows in EC emission diagnostics.

The special requirements of a neutron irradiation for large area discs could be accomplished at the HFR reactor (Petten, NL) by the end of the last reporting period. With a structural damage introduced at $0.9 \cdot 10^{21} \text{ n/m}^2$ ($E > 0.1 \text{ MeV}$), the irradiated CVD diamond discs serves as the essential part of a torus window demonstrator fabricated for high power tests in cooperation with the JA Home Team. The different stages of window processing were accompanied by dielectric property measurements. Pre- and post-irradiation measurements showed comparable values of the median loss value of the loss distribution ($3 \cdot 10^{-5}$ at 145 GHz). After brazing of waveguide cuffs, the median value was found to be increased ($4 \cdot 10^{-5}$ at 145 GHz). This is most probably related with annealing effects for indications of surface losses as typical extrinsic terms were absent. Thermal conductivity in the irradiated disc in the pre-brazed condition was found to be strongly reduced (840 W/m-K as compared to 1800-2000 W/m-K for unirradiated CVD diamond). These findings are in agreement with the physical model proposed before which identifies single point defects as the predominant factor affecting the thermal conductivity. Radiation-induced increases in the dielectric loss are potentially related with the formation of small defect clusters.

Mechanical strength, which governs also the general over-pressure capability of general EC windows during off-normal events, was determined for model discs of 0.9 and 1.5 mm thickness prepared from alternative CVD diamond grades ('ellipsoidal reactor' grade from FhG-IAF, Freiburg, D). For both neutron irradiated (10^{21} n/m^2) and unirradiated control specimens mean values of 400 MPa were measured. Model discs for millimeter wave measurements (30 mm dia.) showed loss levels comparable to RF grade discs before and after irradiation.

Dielectric measurements of the (unirradiated) brazed window component for the 170 GHz / 1 MW gyrotron (collaboration with the RF Home Team) identified a significant contribution of surface losses at selected stages of the window integration. Surface losses were apparently initiated by the brazing process, high power operation (including window failure) was not effective in changing surface losses. However chemical treatments turned out to be very critical in this respect, thus the removal of the CVD diamond discs from the brazed structure by caustic solutions enhanced strongly the loss levels whereas chemical processes involving atomic oxygen formation

completely removed surface losses. In this disc, termination of chemical bonds by hydrogen are suspected to play a major role.

The mm-wave characterisation of large area CVD diamond discs ('RF grade') goes in-line with the results obtained for a set of some 10 discs delivered for ECH-CD systems operating at 140 GHz. There it was also found that loss distributions can be kept within close margins with respect to lateral homogeneity; at 145 GHz, typical median values in the set fall below $2 \cdot 10^{-5}$ and the terminal values stay below $4 \cdot 10^{-5}$. The influence of subsequent brazing on the dielectric properties being an issue of unsettled origin and importance, still requires continued investigations.

Irradiation studies on silica materials for EC emission windows were performed on a typical commercial grade (Infrasil from Heraeus, Hanau, D) and a special radiation-hardened grade for the optical range (KU1, Iruvisil, St.Petersburg, RF). It was found already in the pre-irradiation studies performed with the Infrasil grade that (in contrast to CVD diamond) the ultimate bending strength is strongly dependent on the surface finish. The effect could be perfectly worked out by the 'ball-on-ring' method where crack initiation starts at the centre faces of the disc thus being fully separated from the (untypical) finish at edges for standard bar-shaped testing geometries. As a consequence, the optical polish (Ra better $0.2 \mu\text{m}$) available for Infrasil was modified to standard polish (Ra about $1 \mu\text{m}$) for one disc face. The ongoing post-irradiation characterisation of the discs from the most recent irradiation project clearly prove that structural damage introduced into Infrasil at a fluence of 10^{21} n/m^2 is hardly effective in degrading the strength (cf. Fig.1). In the case of the optical surface finish the distribution is broadened, but median values remain still far above the level of 100 MPa typically specified in data sheets. Mechanical testing of KU1 discs is actually being performed on material with a standard polish. The dielectric loss of both unirradiated grades increases linearly with frequency. In KU1, it is higher by a factor of 4 than in Infrasil and amounts to $1 \cdot 10^{-3}$ at 90 GHz. The same loss values were found in KU1 also after the neutron irradiation.

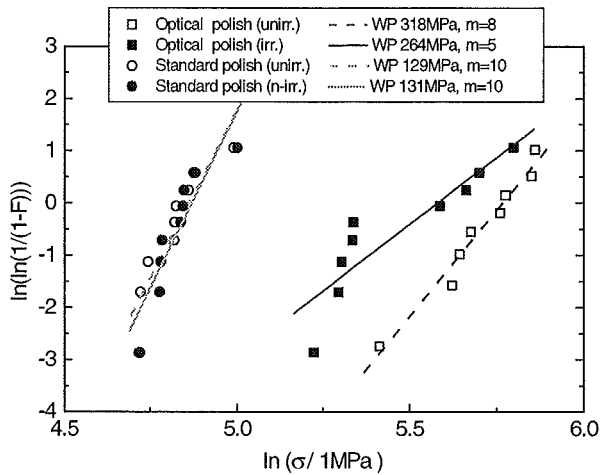


Fig. 1: Results of mechanical strength tests performed by the 'ball-on-ring' method on 'Infrasil' grade silica discs: Weibull plot of failure probability F over stress σ , and Weibull para-meters (WP) indicating median strength and modulus m.

Literature:

- [1] R. Heidinger, A. Meier, M. Rohde, R. Spörl, M. Thumm, A. Arnold, Millimeter wave characterisation of large area MPACVD diamond windows, Digest 25th Int. Conf. on IR+MM Waves, Beijing (China), 2000, IEEE Press, ISBN 0-7803-6513-5, pp. 389-390.
- [2] R. Heidinger, A. Meier, M. Rohde, R. Spörl, M. Thumm, A. Arnold, Millimeter wave characterisation of large area MPACVD diamond windows, Proc. 12th Joint Russian-German Meeting on ECRH and gyrotrons, 21-28/06/2000, Nizhny Novgorod – Moscow (RF).
- [3] R. Heidinger, M. Rohde, R. Spörl, Neutron irradiation studies on window materials for EC wave systems, Proc. 21st Symposium on Fusion Technology, 11-15/09/2000, Madrid (E).

Staff:

M. Blumhofer
R. Heidinger
A. Meier
M. Rohde
P. Severloh
R. Spörl

G 55 TT 19 EU ITER ECRF Window Development

1. Introduction

Gyrotrons with high unit output power (in excess of 1 MW) and high-efficiency significantly lower the cost of Electron Cyclotron Heating (ECH) systems by reducing the amount of the auxiliary support equipment (power supplies, cooling system, number of SC-magnets, ...). Continuous wave operation is required for some of the anticipated ITER-FEAT applications: 3 s for start-up, 100 s for heating to ignition and 100-400 s for current drive. In order to perform these functions for ECH systems a window has to be developed to serve as both the tritium containment barrier on the torus and as the output window of the gyrotron. The former application is technically more demanding as the torus window, must also serve as a high pressure barrier during off-normal events (0.2 MPa overpressure capability). It should not use FC-cooling liquids, must not degrade unacceptably under modest neutron and γ (including x-rays) irradiation, and, in the case of cryo-cooling, must be prevented by a cold trap from cryo-pumping.

A very promising material is chemical vapor deposited (CVD)-diamond which nowadays can be manufactured in window disks of up to 120 mm diameter and 2.3 mm thickness [1, 2]. A water-cooled diamond window would provide two very important advantages, namely employing a cheap and simple as well as effective coolant.

2. 1 MW, 170 GHz, CW CVD-Diamond Gyrotron Window

The 1 MW, 170 GHz, CW, CVD-diamond window unit (disk diameter 119 mm, thickness 2.22 mm, aperture 100 mm) of Forschungszentrum Karlsruhe was welded to the new GYCOM-M 170 GHz ITER gyrotron with single-stage depressed collector (Fig. 1).

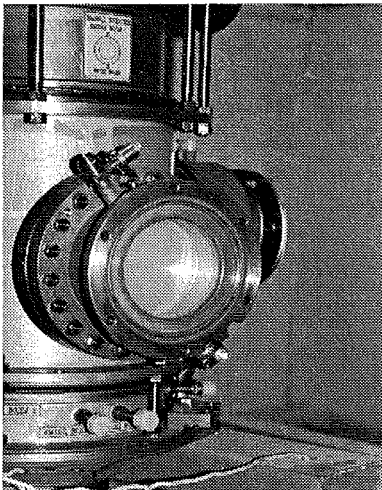


Fig. 1: Picture of the 1 MW, 170 GHz, CW, CVD-diamond window mounted to the GYCOM-M ITER Gyrotron

Up to now the experimental parameters are 0.7 MW, 1 s, 46 % efficiency. On 9.11.1999 a failure took place after 20 routine pulses at this day (at this time a total amount of pulses through the window was approximately 250). Two radial cracks from the window rim to the center are visible. The crack's lengths are 1 and 2 cm. The reasons for the window failure are still under discussion. These are: arcing, external mechanical stress (mounting of calorimeter), increased losses due to hydrogen loading of outer surface (growth side), heating of the Inconel waveguide cuffs by stray radiation in the tube [3], or corrosion of the Al-braze.

A new CVD-diamond disk has been purchased by the Forschungszentrum Karlsruhe and a new window unit (disk diameter 106 mm, thickness 1.85 mm, aperture 88 mm) has been manufactured in collaboration with the ITER Home Team of the Russian Federation and is currently being characterized at low power levels. The high power tests are scheduled for late fall of this year.

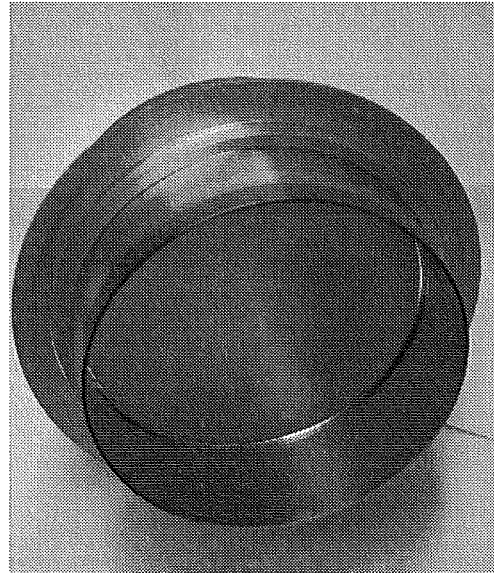


Fig. 2: ITER torus window structure mounted with neutron-irradiated CVD-diamond disk

3. 1 MW, 170 GHz, CW CVD-Diamond Torus Window

The design and fabrication of a 1 MW, 170 GHz, CW, CVD-diamond torus window unit employing an irradiated disk (10^{21} n/m² neutron fluence, 106 mm diameter, 1.85 thickness, 80 mm window aperture) with encased water cooling rim (0.4 mm electroplated copper) is being performed in collaboration with the Japanese ITER Home Team. It will be tested in an evacuated corrugated HE₁₁ waveguide with 63.5 mm inner diameter.

The disk was irradiated at the High Flux Reactor (HFR) Petten. The structural damage ($\sim 10^{-4}$ dpa) created by a neutron fluence of $0.9 \cdot 10^{21}$ n/m² ($E > 0.1$ MeV) in the disk did not lead to significant radiation induced degradation in mm-wave losses. This is in contrast to the thermal conductivity which in this disk is degraded to the level of 840 W/mK. This has to be compared to values of typically 1800-2000 W/mK for unirradiated CVD-diamond [4,5]. After the low power characterization measurements the two Inconel waveguide cuffs were brazed to the CVD-diamond disk and the disk cooling rim was metallized (Au/Ti). The torus window unit is shown in Fig. 2. Due to annealing during the brazing process, the mean loss tangent of the disk increased from $3 \cdot 10^{-5}$ to $4 \cdot 10^{-5}$. Currently, the metallized water cooling rim is being encased by a 0.4 mm thick electroplated copper cover saving as a tritium and water barrier in case of a window failure. The high power tests of the torus window unit at JAERI are scheduled for late fall of this year.

Literature:

- [1] M. Thumm, A. Arnold, R. Heidinger, M. Rohde, R. Schwab, R. Spoerl: Proc. 11th Joint Workshop on Electron Cyclotron Emission and Electron Cyclotron Resonance Heating (EC11), Oh-arai, Japan, 1999, pp. 593-602.

- [2] Brendon, J.R., S.E. Coe, R.S. Sussmann, K. Sakamoto, R. Spoerl, R. Heidinger, S. Hanks, Proc. 11th Joint Workshop on Electron Cyclotron Emission and Electron Cyclotron Resonance Heating (EC11), Oh-arai, Japan, 1999, pp. 593-602.
- [3] Thumm, M.: MPACVD-diamond windows for high-power and long-pulse millimeter wave transmission, Proc. 7th Int. Conf. on New Diamond Science & Technology (ICNDST-7), Hong Kong, China, July 24-28, 2000, Invited Paper 5.4.
- [4] Thumm, M., A. Arnold, R. Heidinger, A. Meier, M. Rhode, R. Spoerl, R. Schwab, P. Severloh, ITER ECH R&D Task Meeting, ITER Joint Work Site, Garching, 23-24, March 2000.
- [5] Heidinger, R., A. Meier, M. Rohde, R. Spoerl, M. Thumm, A. Arnold: Millimeter wave characterisation of large area MPACVD diamond windows, Conf. Digest 25th Int. Conf. on Infrared and Millimeter Waves, Beijing, P.R. China, 2000, pp. 389-390.

Staff:

A. Arnold (Uni Karlsruhe)
R. Heidinger
A. Meier
M. Rohde
P. Severloh
R. Spoerl
M. Thumm

**G 52 TT 22 EU
ITER ECRF Advanced Source Development**

Introduction

The physics advantage of ECRH is the possibility of well-localized power absorption, where the deposition region is defined by the crossing of the ECR layer with the RF-beam. The technology advantages of ECRH are as follows. Antennas can be located far from the plasma, thus avoiding impurity release and providing decoupling of heating from particle refuelling. Compact optical antennas allow very high injected power densities (in excess of 100 MW m^{-2}), implying the use of fewer ports. Millimeter-wave vacuum windows provide a tritium barrier in the waveguide separating the vessel from the source so that the sources can be placed in a "hands-on" location far away from the plasma.

The main application of powerful gyrotrons is plasma start-up and electron cyclotron resonance heating (ECRH) in tokamaks and stellarators as well as non-inductive current drive (ECCD) and stability control in tokamak plasmas [1]. For example, for its ECRH system with power up to 40 MW the International Thermonuclear Experimental reactor (ITER) will need about 20-40 continuous wave (CW) gyrotrons at a frequency of 170 GHz with 1 to 2 MW of output power per tube [2]. For the new German stellarator Wendelstein 7-X which is under construction at IPP Greifswald ten 140 GHz, 1 MW, CW gyrotrons will be needed to achieve a total output power of about 10 MW [3].

The limiting factors of conventional gyrotron cavities can be considerably reduced with the use of coaxial cavities, which offer the possibility of operation in high order volume modes with reduced mode competition problems. Furthermore, the presence of the inner conductor practically eliminates the restrictions of voltage depression and limiting current. Therefore gyrotrons with coaxial cavities have the potential to generate, in CW operation, rf-output powers in excess of 1 MW at frequencies above 140 GHz.

1. Advanced coaxial cavity gyrotron

The coaxial gyrotron under development at the Forschungszentrum Karlsruhe has been equipped with a new 4.5 MW electron gun to be operated at 90 kV and 50 A. It is a diode-type gun with dispenser cathode which was designed by the Forschungszentrum [4,5]. Different from the LaB_6 IMIG currently used, the emission of the electrons is not directed towards the coaxial insert but towards the anode similar to conventional MIG gyrotron electron guns. The inner conductor is supported from the bottom of the gun and can be aligned in a reproducible way in the fully assembled tube. The gun has been fabricated by Thomson Tubes Electroniques (TTE), Vélizy. The advanced quasi-optical mode converter for transforming the $\text{TE}_{31,17}$ cavity mode at 165 GHz into a single rf-output beam consists of a simple launcher and two mirrors. The first mirror is quasi-elliptical and the second mirror has a non-quadratic phase-correcting surface.

A fused quartz window with a diameter of 100 mm and a thickness of 13 half wave lengths at 165 GHz was used. The measurements have been performed in pulsed operation. Most data have been taken with an rf pulse length of 1 ms and a repetition rate of 1Hz.

A maximum output power of 2.2 MW with an efficiency of 28% at a beam current of 84 A has been achieved. The maximum output efficiency of 30 % (48% with depressed collector) has been measured at an output power of 1.5 MW at 56 A (Fig. 1).

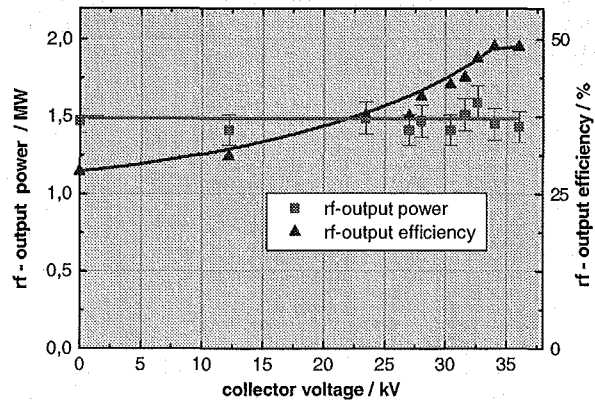


Fig. 1: rf output power as a function of collector voltage

Fig. 2 gives the rf output power and efficiency as a function of the beam current. The cathode voltage has been adjusted between 84 kV and 94.6 kV for maximum rf output. The magnetic field was 6.65 T. The numerical calculations have been performed with a self-consistent, time dependent multi-mode code using the operating parameters as input. The rf losses inside the tube are estimated to be 10%. The results of the numerical calculations (solid line) are in good agreement with the experiment.

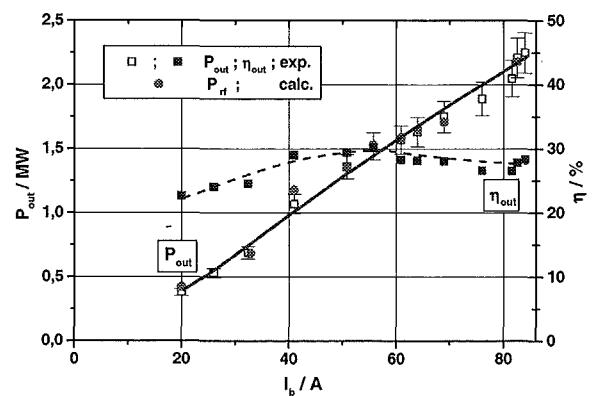


Fig. 2: rf output power and efficiency as a function of beam current. $B = 6.65 \text{ T}$, $U_c = 84 - 94,6 \text{ kV}$

To operate with longer pulse lengths ($\sim 100 \text{ ms}$) the window had to be exchanged by a brazed Si_3N_4 window. Unfortunately, due to arcing this window was destroyed.

2. Fast frequency tuning

Fast frequency-tunable gyrotrons are of interest for controlling instabilities in magnetically confined plasmas via ECCD at fixed toroidal or poloidal antenna launching angle.

The 140 GHz $\text{TE}_{22,6}$ gyrotron with conventional hollow cylindrical resonator [6] has been used to demonstrate fast stepwise frequency-tunability with 1 s time steps at a power level of 1 MW. Small auxiliary normal conducting magnets placed between the superconducting solenoid and the gyrotron are used. The frequency range is limited by the maximum achievable variation of the magnetic field. A fast change of the magnetic field by $\pm 326 \text{ mT}$ results in a fast frequency change of $\pm 7,5 \text{ GHz}$ [7,8].

The measurements were carried out at a beam current of about 40 A and a cathode voltage of 80-85 kV optimized for maximum

output power of each mode. The gyrotron was tuned within 1s time steps between the TE_{20,6} mode at 132.8 GHz via the TE_{21,6}, TE_{22,6}, TE_{23,6} modes to the TE_{24,6} mode at 147.5 GHz.

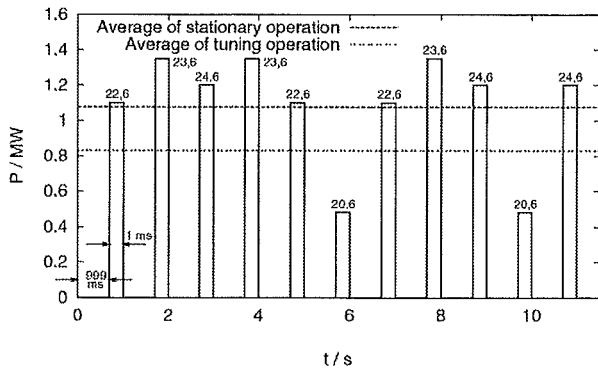


Fig. 3: Fast magnet frequency-step tuning (pulse length 1 ms, duty cycle 1:1000)

The best operating point for every mode was used as input for the new computer aided gyrotron control system, which controls not only the current in the normal conducting magnets, including the complete current regulation but also the output voltage of the gyrotron power supply and the starting trigger for every pulse. Making use of this system different mode series were excited; one of them is shown in Fig. 4. The pulse length was 1 ms and the time between two pulses 1 s. This means that a frequency step of nearly 15 GHz (TE_{20,6} ↔ TE_{24,6}) was achieved within 1 s. We conclude that the demands for ITER (several GHz within a few seconds) are achievable.

The possibility of going to longer pulses at powers greater than 1 MW has been investigated theoretically [9].

Literature:

- [1] M. Thumm, A. Arnold, E. Borie, O. Braz, G. Dammertz, O. Dumbrajs, K. Koppenburg, M. Kuntze, G. Michel, B. Piosczyk, JAERI-memo 12-041 (2000), 466-479.
- [2] N. Kobayashi, G. Bosia, B. Petzold, JAERI-memo 12-041 (2000), 540-549.
- [3] V. Erckmann, G. Dammertz, D. Dorst, L. Empacher, W. Förster, G. Gantenbein, T. Geist, W. Kasperek, H.P. Laqua, G.A. Müller, M. Thumm, M. Weissgerber, H.Wobig, IEEE Trans. on Plasma Science, PS-27, (1999), 538.
- [4] B. Piosczyk, O. Braz, G. Dammertz, M. Kuntze, G. Michel, O.S. Lamba, M. Thumm, 24th Int. Conf. Infrared Millimeter Waves, Monterey (1999) TU-A9.
- [5] B. Piosczyk, O. Braz, G. Dammertz, C.T. Iatrou, S. Illy, M. Kuntze, G. Michel, M. Thumm, IEEE Trans. on Plasma Science 27 (1999) 484-489.
- [6] G. Dammertz, E. Borie, C.T. Iatrou, M. Kuntze, B. Piosczyk, M. Thumm, IEEE Trans. on Plasma Science 28 (2000), to be published.
- [7] K. Koppenburg, B. Piosczyk, M. Thumm, 24th Int. Conf. Infrared Millimeter Waves, Monterey (1999) W-D5.
- [8] K. Koppenburg, G. Dammertz, M. Kuntze, B. Piosczyk, M. Thumm, IEEE Trans. Electron Devices 20 (2000), to be published.
- [9] M.V. Kartikeyan, E. Borie, M. Thumm, IEEE Trans on Plasma Science 28 (2000), to be published.

Staff:

- J. Anderer (Uni Karlsruhe)
- A. Arnold (Uni Karlsruhe)
- H. Baumgärtner
- E. Borie
- H. Budig
- G. Dammertz
- O. Drumm (Uni Karlsruhe)
- S. Illy
- K. Koppenburg (Uni Karlsruhe)
- H. Kunkel
- M. Kuntze
- B. Piosczyk
- J. Szczesny
- M. Thumm
- R. Vincon

Plasma Facing Components

DV 7a Tritium Permeation, Retention, Wall Conditioning and Clean-up (Dust Removal, Baking)

About 1 gram of flakes from the first tritium campaign of the JET reactor has been delivered to the Forschungszentrum Karlsruhe in 1999.

The flakes were specified by JET to consist of carbon saturated with deuterium and tritium and with a tritium activity of about 1 TBq/g [1]. This activity is about 5 orders of magnitude higher than that measured in case of flakes collected at JET before the tritium campaign.

The flakes are stored in a special container filled with argon. They are loose within the cyclone pot, with argon at atmospheric pressure covering them. As yet the flakes have not been removed from their container, because of the very high tritium activity which requires specific safety procedures. However, sample preparation techniques and characterization methods (i.e. optical and scanning electron microscopy, microprobe, thermal desorption, liquid scintillation counting etc.) have been successfully tested with flakes recovered before the tritium campaign.

Literature:

[1] J.P. Coad, JET, Private Communication

Staff:

E. Damm
R.D. Penzhorn
R. Rolli
C. Sand
F. Scaffidi-Argentina
H. Ziegler

T 438/04 Investigation of D/T Retention in n-irradiated PFC Materials

The knowledge of the tritium and helium release kinetics as a function of neutron fluence, temperature and damage dose represents an important issue for any plasma facing material (PFM) to be used in a next step fusion reactor. However, the tritium and helium behavior in neutron-irradiated PFMs like beryllium and carbon-based materials is usually a complex function of both the irradiation history (e.g. flux, irradiation temperature, time at temperature, etc.) and of the material grade.

In general, there are three main processes leading to tritium retention in carbon-based materials exposed to a tritium plasma [1], namely: a) the formation of a surface layer, saturated with the implanted tritium; b) the co-implantation of tritium with eroded carbon; c) the atomic diffusion of the implanted/co-implanted tritium to trapping sites usually located well beyond the implantation/co-implantation zone.

On the other hand, tritium produced and/or implanted in beryllium diffuses at a significant rate to sites of lower free energy (i.e. He bubbles) and/or chemically reacts with impurities for which it has a particular affinity (e.g. beryllium oxide). If tritium is trapped in a helium-filled bubble, it follows the destiny of the bubble and will be released only if the bubble is vented into an open porosity network, through which the gas can escape with effectively no activation energy. On the other hand, tritium chemically bound in form of beryllium hydroxide ($\text{Be}(\text{OH})_2$) at oxide inclusions is energetically stable with respect to single tritium atoms and therefore, requires a sufficiently high thermal energy to be released. Due to the two different tritium trapping mechanisms in beryllium, the release kinetics is therefore, expected to be dependent on the particular trapping mechanisms and, in particular, to be hindered both by structural sinks and by beryllium oxide impurities.

1. Samples and irradiation conditions

1.1 Graphite and carbon fiber composites

Both graphite and carbon-based material specimens analyzed consist of cylindrical bars with a diameter of 5 mm and a length of 15 mm. They include three graphite grades (i.e. A05, RGTi(91) and CL 5890), two Dunlop CFC grades (i.e. Concept 1, Concept 2) and four SepCarb CFC grades (i.e. N312C, NS11, N112, N312B). A description of the specimens and their properties can be found in Ref. 2

The samples were irradiated between December 1995 and February 1996 at the High Flux Reactor Petten (Netherlands) as a part of the PARIDE D 302 experiment [3]. A first set of samples was irradiated at a nominal temperature of 335 °C up to a neutron dose of 0.31 displacements per atom (dpa) during two reactor cycles (i.e. 49.64 effective full power irradiation days) with a fast ($E_n > 0.1$ MeV) neutron fluence up to $3.34 \cdot 10^{24} \text{ m}^{-2}$, while a second set of samples was irradiated at a nominal temperature of 775 °C up to a neutron dose of 0.35 dpa during one reactor cycle (i.e. 23.75 effective full power irradiation days) with a fast ($E_n > 0.1$ MeV) neutron fluence up to $4.0 \cdot 10^{24} \text{ m}^{-2}$.

After irradiation the bars were axially cut in four parts the length of which was about 3.75 mm, and used for the post-irradiation examination (PIE) tests. A cutting method which did not severely heat the samples was used to prevent release of contained gases.

Because in a fusion reactor tritium is loaded in the first wall materials during irradiation, several graphite and CFC samples were out-of-pile loaded with tritium after neutron irradiation. The loading was performed in an alumina tube at 0.2 MPa (absolute) and 850 °C for 6 hours in a atmosphere of $\text{H}_2 + 50 \text{ appm T}_2$. Details on the loading procedure can be found in [4].

1.2 Beryllium

The analyzed beryllium specimens consist of segments of a cylindrical bar with a diameter of 15 mm and a length of 100 mm produced by the Kawecki Beryllco Industries by vacuum hot pressing (VHP) of impact attritioned powder of 100 mesh at least (S-200E grade) [5]. The average grain size is 10-13 μm , the total beryllium oxide (BeO) content is lower than 2% and the bulk density corresponds to 99.5% of the theoretical one.

The bar was irradiated at 40-50 °C in the BR2 reactor in Mol (Belgium) for 2440 effective irradiation days with a fast ($E_n > 1$ MeV) neutron fluence of $3.925 \cdot 10^{26} \text{ m}^{-2}$. The calculated helium content after irradiation amounted to 20670 atomic parts per million (appm) while the tritium content amounted to 110 appm [5].

After irradiation the bar was ultrasonically treated to remove the outer oxide layer which is always present on the external beryllium surface. Then it was rinsed with water and dried, and appropriate samples were cut from the bar. A cutting method which did not severely heat the samples was used to prevent release of contained gases. During the cutting it was experienced that the irradiated material was rather brittle.

2. Gas release measurements

Annealing and gas-release measurements for both irradiated/loaded CFC and beryllium specimens were carried out with a flow-through tritium release facility installed at the Forschungszentrum Karlsruhe. The system essentially consists of an inlet gas manifold, a sample furnace chamber connected by a short, heated line ($T \sim 300$ °C) to a zinc-reducer ($T \sim 390$ °C) which transforms any tritium water to tritium gas, and an ionization chamber or a proportional counter downstream from the furnace for analysis of the purge gas tritium activity. The use of the zinc-reducer avoids problems with tritium water absorption on the inner wall of the release facility pipes, thus allowing quantitative tritium measurements. The total released tritium is determined by integrating the measured release rate over the time.

The release kinetics and total amount of released tritium are determined by annealing the specimens with temperature ramps up to 1100 °C. For these annealing experiments the thermal ramp from room temperature to annealing temperature consisted, in the case of beryllium, of two ramp segments (i.e. 7 °C/min from room temperature up to 500 °C and 15 °C/min from 500 °C up to 1100 °C). On the other hand, in the case of graphite and CFC a single ramp of 15 °C/min from room temperature up to 1100 °C was applied. In both cases, the final annealing temperature of 1100 °C was kept constant for about 3 hours. A 50 cm^3/min high-purity argon with 1vol% H_2 was used as a purge gas for the annealing experiments with beryllium, while a high-purity helium with 0.1vol% H_2 was used for the annealing experiments with graphite and CFC.

Tritium release rate was measured with an in-line ionization chamber or a proportional counter. In order to determine the total retained tritium (i.e. inventory) in both graphite and CFC samples after the annealing, the specimens were afterwards totally burned in a pure oxygen atmosphere at 1500 °C for 5-6 minutes. The released tritium is trapped in a bubbler and then measured by means of liquid scintillation counting.

In the case of beryllium the gas composition in the process line as well as the helium release rate were measured with a quadrupole mass spectrometer (QMS) connected downstream from the specimen furnace. QMS signature were mass-2 for H₂, mass-4 for ⁴He and mass-40 for ⁴⁰Ar. Based on previous studies [6] the contribution of HT to the QMS mass-4 peak can be considered as negligible.

The QMS was calibrated with gas standard mixtures flowing in the process line, while the ionization chamber and the proportional counter were calibrated with a standardized tritiated gas mixture. A dummy release measurement is performed before a tritium release experiments is started, in order to determine the background of the system.

3. Results

3.1 Graphite and carbon fiber composite

In order increase the confidence in the obtained experimental data, the measurements were repeated at least two times. The tests showed a reproducibility ranging from 36% to 76% for the unloaded samples and from 1.9% to 51% for the tritium-loaded samples.

The first surprising result is that, contrary to any theoretical expectation, both graphite and CFC samples contain after irradiation a relatively high amount of tritium. A possible explanation is that during the irradiation some tritium coming from the reactor core was implanted in the samples and there trapped until they were out-of-pile annealed.

The kinetics of tritium release in both graphite and CFC in general depends on the irradiation temperature and damage dose. In agreement with previous studies [4] and independent from the irradiation temperature, both graphite and CFC tritium-loaded specimens do not show any tritium release at temperature of 700-750 °C and below. In all cases the tritium release rate starts to increase above about 700-750 °C, reaches a maximum when the specimens first reach 1100 °C and than starts to decrease monotonically with the time when the annealing temperature is kept constant at 1100 °C. On the contrary, the not-loaded specimens irradiated at 335 °C show a release rate which starts already at about 400-450 °C, reaches a maximum at about 750 °C and then monotonically decreases with the time. Furthermore, the not-loaded specimens irradiated at 775 °C do not show any release at all temperatures, thus indicating that the tritium was probably already released during the in-pile irradiation. This fact seems to confirm the hypothesis that tritium in not-loaded samples is probably coming from the reactor core and therefore, weakly bound at the specimens surface. Figures 1 and 2 show the tritium release before and after the tritium loading from the SepCarb NS11 CFC samples irradiated at 335 °C and 775 °C, respectively.

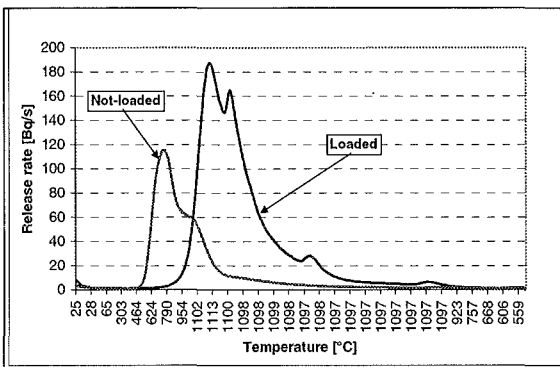


Fig. 1: Tritium release before and after the tritium loading from the SepCarb NS11 CFC samples irradiated at 335 °C and out-of-pile heated on to an anneal temperature of 1100 °C

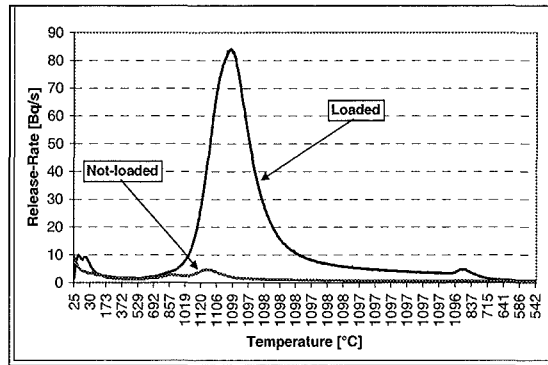


Fig. 2: Tritium release before and after the tritium loading from the SepCarb NS11 CFC samples irradiated at 775 °C and out-of-pile heated on to an anneal temperature of 1100 °C

The not-loaded specimens release almost all the tritium during the annealing at 1100 °C, except the SepCarb NS11 and SepCarb N112 CFC samples, and RGTi(91) graphite irradiated at 775 °C, which show a tritium inventory of 32.6%, 62.7% and 20.1%, respectively. On the contrary, independent of the irradiation temperature all the tritium-loaded specimens release only about 50% of the tritium during the annealing at 1100 °C, as shown in Figures 3 and 4. The remaining tritium inventory is then released only after burning of the samples at 1500 °C in a pure oxygen atmosphere.

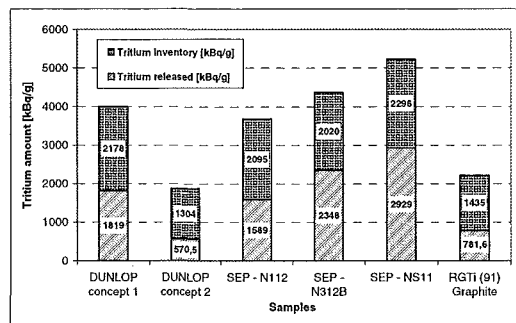


Fig. 3: Tritium inventory and release from tritium-loaded graphite and CFC samples irradiated at 335 °C

Contrary to the SepCarb N312B which is a pure three-dimensional CFC material, the SepCarb NS11 has undergone during the production process a final infiltration of liquid silicon leading partially to the formation of silicon carbide (10-12 at% of silicon) [2]. In order to investigate the effects that a silicon doping has on the tritium performance of the CFC samples, the behavior of tritium-loaded SepCarb N312B and SepCarb NS11 irradiated specimens has been compared. The result of the measurements showed that tritium is mainly released in form of HTO and therefore, the silicon doping does not have any significant effect on the tritium release kinetics either at 335 °C or at 775 °C irradiation temperature. In all cases, the largest peak of release rate is observed at 1100 °C and the only minor effect that the silicon doping seems to produce on the specimens irradiated at 775 °C is an earlier (about 30 minutes) release than in the case of a pure CFC, as shown in Figure 5.

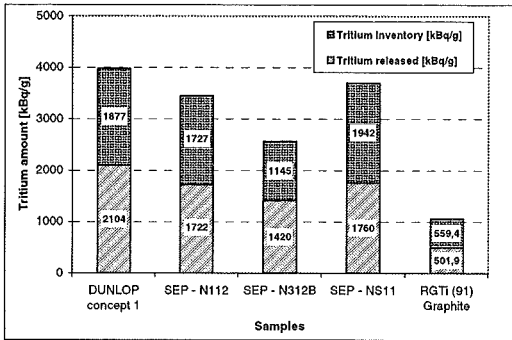


Fig. 4: Tritium inventory and release from tritium-loaded graphite and CFC samples irradiated at 775 °C

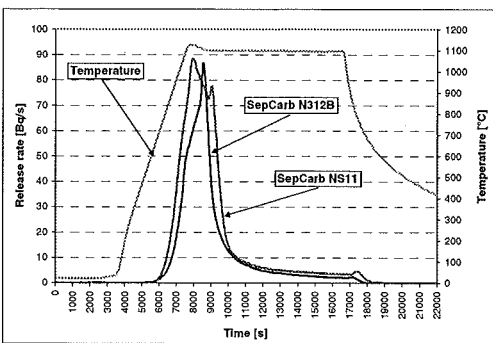


Fig. 5: Tritium release after tritium loading from the SepCarb NS11 and the SepCarb N312B CFC samples irradiated at 775 °C and out-of-pile heated on to an anneal temperature of 1100 °C

3.2 Beryllium

According to previous studies [7, 8, 9], the results of the measurements indicated that helium and tritium release behavior is a complex function of both irradiation temperature and time at temperature. Anyhow, in agreement with the studies reported in Refs. 7 and 8, the beryllium specimens do not show any tritium and helium release at temperature of 600 °C and below. Although tritium is released between 600 °C and 900 °C, no helium release is observed in that temperature range.

The tritium release rate has a rapid increase during the temperature ramp and a sharp peak is observed when the specimens first reach 1100 °C. In agreement with a previous study [8] this sharp peak is probably related with the formation of micro-cracks at the specimen surface. Due to the very high neutron fluence (i.e. $3.925 \cdot 10^{26} \text{ m}^{-2}$), in fact, the beryllium specimens has become very brittle and consequently they easily crack under thermal stresses during the heating-up phase of the annealing test. After reaching a maximum when the specimens first reach 1100 °C, the release rate starts to decrease monotonically fast with the time when the annealing temperature is kept constant at 1100 °C. At the time when the largest peak occurs, about 33% of the total tritium is released. Correspondingly, a strong and narrow peak of helium release is observed.

Figure 6 shows quite clearly that tritium and helium are unambiguously released concurrently, thus leading to the conclusion that tritium and helium reside in common bubbles in the irradiated material. In fact, the burst release is due to the migration of the helium bubbles to form interconnected grain-edge tunnels to the specimen-free surfaces. Therefore, the tritium trapped in the helium-filled bubbles follows the destiny of the bubbles and will be released concurrently to the helium only after their migration and venting from an open-porosity network.

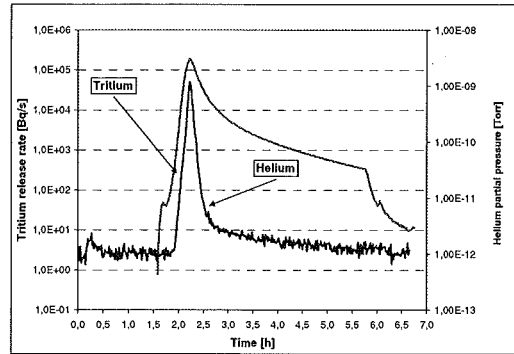


Fig. 6: Tritium and helium release from a beryllium sample (S-200E grade) heated on a segmented ramp to an anneal temperature of 1100 °C

Literature:

- [1] P. Franzen et al., Nucl. Fusion, Vol. 37, No. 10 (1997) 1374-1393.
- [2] J.P. Bonal and D. Moulinier, "Thermal Properties of Advanced Carbon Fiber Composites for Fusion Application", Report DMT/95-495, SEM/LEMA/95-073, Commissariat à l'Energie Atomique, Direction des Réacteurs Nucléaires, Saclay, October 1995.
- [3] R. Conrad, "PARIDE: Irradiation of Plasma Facing Materials for DEMO at the High Flux Reactor Petten. Projects D 302.1 and D 302.2", Technical Memorandum HFR/4439, Joint Research Center, Institute of Advanced Materials, Petten, October, 1997.
- [4] H. Kwast et al., Phis. Scripta, Vol T64, 41-47, 1996.
- [5] L. Sannen, "Final Report Characterisation of Irradiated Beryllium", SCK-CEN Report FT/Mol/92-01, Mol, July, 1992.
- [6] R.A. Anderl et al., Fus. Techn. 28 (1995) 1114.
- [7] R.A. Anderl et al., "Tritium and Helium Retention and Release from Irradiated Beryllium", in: Proc. 3rd IEA International Workshop on Beryllium Technology for Fusion, Mito City, Japan, October 22-24, 1997.
- [8] F. Scaffidi-Argentina and H. Werle, "Tritium Release from Neutron Irradiated Beryllium: Kinetics, Long-Time Annealing and Effect of Crack Formation", in: Proc. 2nd IEA International Workshop on Beryllium Technology for Fusion, Jackson Lake Lodge, Wyoming, September 6-8, 1995.
- [9] F. Scaffidi-Argentina et al., "Beryllium R&D for Fusion Applications", in: Proc. 5th International Symposium on

Fusion Nuclear Technology, Rome, September 19-24, 1999.
To be published.

Staff:

E.Damm

C. Sand

F. Scaffidi-Argentina

C.H. Wu

H. Ziegler

**T 438/06
Chemical Reactivity of Dust and Flakes and
D Mobilisation Experiments from Co-deposited
Layers**

Results of materials characterization analyses and chemical reactivity experiments for Be pebbles and Be powder that are exposed to steam at elevated temperatures have been obtained. Be pebbles are proposed as the neutron multiplier material for the European Helium Cooled Pebble Bed (HCPB) Blanket and the reference breeding blanket for the International Thermonuclear Experimental Reactor (ITER). Reactivity of Be powder is of interest to evaluate the consequences of steam interaction with Be powder debris generated in plasma devices by mechanisms such as disruption-induced vaporization or sputtering of Be surfaces. A detailed description of this work can be found in [1, 2, 3]

The results of steam-reactivity measurements for Be pebble and powder material have been compared with those for fully-dense, CPM-Be cylinder and disc samples. The results indicate, as shown in Figures 1 and 2, that H₂ generation rates for the powder material, based on BET surface area, are quite consistent with the CPM-Be data. In contrast, the rates for 2 mm and 0.1-0.2 mm diameter Be pebbles, based on BET surface area, are systematically lower than corresponding CPM Be H₂ generation rates.

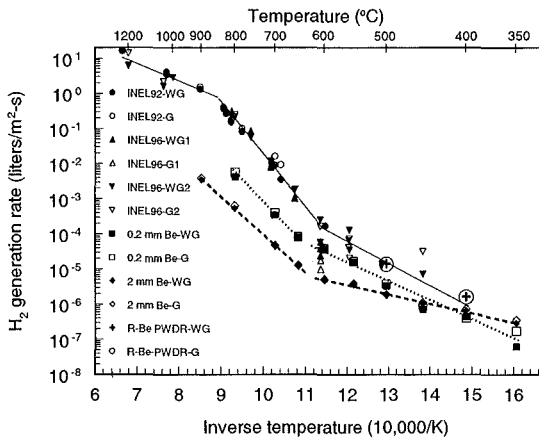


Fig. 1: Comparison of average H₂ generation rates (liters/m²-s) for Be pebble and powder material with those for fully-dense CPM Be

The observed H₂ generation rate differences for the pebble data can be attributed primarily to differences in the surface and microstructural features for the pebble material, as compared to the CPM-Be machined samples.

In fact, both the 2 mm and 0.1-0.2 mm pebble material have microstructural and surface topographical features that are substantially different for the pebbles. In addition, the bulk and surface impurity composition for the pebble material was substantially different from the CPM-Be material, especially for the 2 mm pebble material that had an ~2µm thick impurity surface layer of SiO₂ and/or BeF₂. The impact of such surface features and impurities could contribute to the BET surface area, as measured by gas adsorption techniques, but also affect the oxidation process at the material surface, resulting in some ambiguity between the BET surface area and the reactive

surface area. If the reactive surface area is less than the BET surface area, the derived H₂ generation rates for the pebble material, based on BET surface area, could be smaller than they should be.

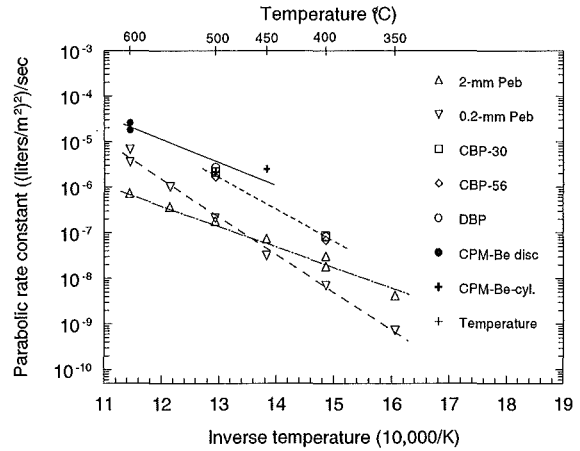


Fig. 2: Comparison of H₂ generation, parabolic rate constants for Be pebble, Be powder and fully-dense CPM Be

The reaction rate results, presented in Figure 3 as weight-gain/(initial mass-min), demonstrate that specific surface area has a significant influence on the chemical reactivity of the various materials. Reactivity is directly proportional to the specific surface area of the material, the larger the specific surface area, the larger the reaction rate. As shown in Figure 3, the slopes of the reaction-rate data for the 0.1-0.2 mm pebbles, the powders and the porous CPM Be are comparable, indicating that the mechanism controlling the reaction is similar for these materials and the magnitude of the reaction rate is governed by each materials' reactive surface area. In contrast, for temperatures below 650°C, the reaction-rate slope for the 2 mm pebbles is much less than that for the 0.1-0.2 mm ones, the powder and the porous Be, indicating that the reaction mechanism could be different. For temperatures above 650°C, the reaction-rate slope for the 2 mm pebbles is comparable to that for fully-dense CPM Be, indicating that the controlling mechanisms may be similar in this temperature range. These differences in reactivity mechanism for the 2 mm pebbles are probably due to the presence of the ~2µm thick impurity layer of SiO₂ and/or BeF₂, that can affect the oxidation process at the surface.

The performed analysis has contributed new experimental results of the reactivity of Be pebbles and powder exposed to steam at elevated temperatures. However, the work suggests the need for additional experiments, materials characterization and modeling analyses to better understand reactivity behavior for different forms of Be exposed to steam over a wide temperature range. In particular, experiments are required to elucidate the influence of bulk and surface impurities and other surface and microstructural features on both the BET surface area determinations and on oxidation behavior for materials exposed to steam.

Literature:

[1] R. A. Anderl et al., "Steam Chemical Reactivity of Be Pebbles," INEEL/EXT-98-01149, Idaho National Engineering and Environmental Laboratory (December 9, 1998).

[2] R. A. Anderl et al., "Steam Chemical Reactivity of Be Powder," *INEL/EXT-99-00338*, Idaho National Engineering and Environmental Laboratory, (April 30, 1999).

[3] R. A. Anderl et al., "Steam chemical reactivity of Be pebbles and Be powder". To appear in *Fusion Technology*.

Staff:

R.A. Anderl

D. Davydov

R.J. Pawelko

F. Scaffidi-Argentina

G.R. Smolik

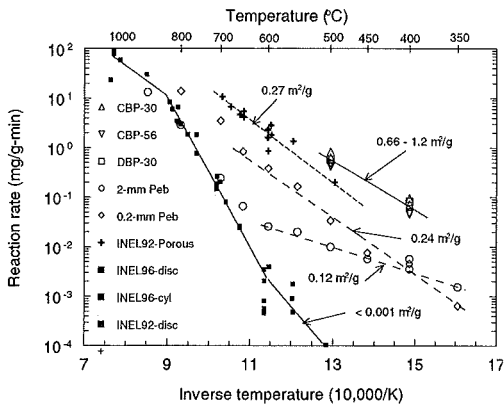


Fig. 3: Comparison of average Be reaction rates (weight gain per unit time, per initial mass of sample) for different Be types. Specific surface areas are identified in the figure for each data set

T438/08 Effect of Plasma Interaction

1. Introduction

Whether graphite or tungsten will be used as divertor material is still an open issue. The low Z material graphite doesn't melt, shows rather low erosion by evaporation and has a low impurity radiation level. However chemical erosion and Tritium co-deposition might be unacceptably high [1,2]. Thermal stress produces cracks in graphite. Crack propagation into the depth of the sample indicates predamaging. Enhancement of brittle destruction under cyclic heat loads then can't be excluded [3]. This might increase total erosion of graphite considerably and could reduce the lifetime and by dust formation could cause a safety problem [3,4]. The high Z material tungsten has low sputtering yields and the contamination of the central plasma with tungsten remains low [5]. But there is melt layer erosion resulting in rather large total erosion, in formation of a large surface roughness and in droplet splashing as indicated in simulation experiments with electron beams [6]. The influence of melt motion on melt layer erosion was discussed recently for tokamak off normal events [7]. The influence of eddy currents on melt layer dynamics was recently emphasized [8]. However the numerical results given in [8] are not consistent and thus this problem still remains to be solved for tokamak off normal conditions. A combination of both materials such as graphite as vertical target and tungsten as dome material could result in still more complex surface layers being a mixture of graphite dust, of metal droplets of redeposited carbon and of flakes. Such layers show a drastically reduced heat conductivity and they might enhance impurity production at hot spots and thus could limit the tolerable ELM energy [7].

Before any recommendations for any material to be used as divertor material can be given the total erosion of these materials has to be quantified among others. Damage mechanisms to be considered are evaporation and brittle destruction of graphite and evaporation and melt layer erosion of metals. Vapor shielding and target screening by dust particles was taken into account in the numerical simulations [4].

A numerical simulation model for brittle destruction of carbon based materials (CBMs) based on crack generation by thermal shocks is under development. Crack generation in heated graphite samples depends among others on the grain anisotropy, the grain size, the failure stress value of the bonds connecting adjacent grains and on the temperature and the temperature gradient in the sample. The value to be used for the characteristic failure stress was obtained from a numerical simulation of destructive compression tests and from a comparison of calculated and measured onset of brittle destruction for volumetric heating. Crack propagation into the depth of the sample indicates that predamaging might occur resulting in an enhancement of brittle destruction under cyclic heat loads for typical ITER-FEAT off-normal events [3].

Erosion in metals is mainly due to melt layer motion. For description of melt motion, mountain formation at the crater edge and melt layer erosion a 1-D fluid dynamics model is being developed and first numerical results on melt layer erosion and formation of mountains were obtained [9].

For calculation of target erosion by evaporation, the plasma shield formation and its shielding efficiency in front of the target have to be known. For this purpose the 2-D multifluid radiation magnetohydrodynamics (R-MHD) code FOREV-2 was developed. FOREV-2 validation is completed with numerical simulation of plasma shield dynamics and erosion of vertical graphite targets and comparison with experimental results obtained at

the MK-200 UG plasma gun facility. The plasma shield stability for such targets is essential for a high shielding efficiency and needs to be modelled for calculation of realistic erosion values of vertical targets. FOREV-2 was used for calculation of erosion of vertical targets by hot plasma impact typical for off normal events in ITER-FEAT.

2. Vertical graphite target in simulation experiments

Recently disruption simulation experiments have been performed at the plasma gun facility MK-200 UG at Troitsk with vertical graphite targets, inclined at 20° to the direction of the incident hot hydrogen plasma [10]. The experimental arrangement schematically is shown in Fig. 1.

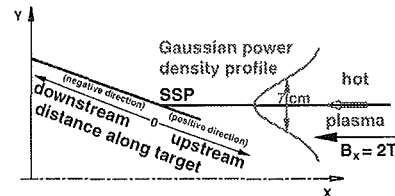


Fig. 1: Experimental arrangement in the simulation experiments at the MK-200 UG plasma gun facility with vertical targets showing up- and downstream direction

The hot plasma in these experiments has a Gaussian power density profile with half width of about 7 cm. The peak target heat load was 100 GW/m². The distance along the target is counted in upstream direction with the separatrix strike point (SSP) at $y = 0$ cm. In the experiments the SSP was located close to the target edge. Thus the target covered only the downstream half of the power density profile. Experimentally determined have been the erosion profiles and the time integrated visible and soft X ray radiation. Moreover time dependent photographs of visible radiation were taken by a high speed framing camera. From the plasma pictures which showed that the radiating region at the target widens it was concluded that the plasma expands along the target downstream and thus across the magnetic field lines. From the additionally measured time integrated soft X ray spectras CV and CVI lines have been found near the target, indicating plasma temperatures higher than 20 eV (only at these temperatures CV and CVI ions are existing in noticeable quantities). Thus it was concluded that a high temperature plasma moves across the magnetic field lines. This can only be understood by assuming that turbulence is existing in the plasma shield [10].

From the results of the numerical analysis of this experiment with FOREV-2 using the classical Spitzer diffusion coefficient different conclusions were drawn. First of all, from the widening of the radiative spot close to the target it can't be concluded that there is a plasma movement across magnetic field lines. From Fig. 2 it is seen that the widening of the radiative spot is due to an increase of the width of the vaporization region with time reflecting the width of the Gaussian profile of the incoming power density. Fig. 3 shows calculated plasma electron temperature distributions at the SSP, perpendicular to the target and at different times. A high temperature plasma shield exists at distances less than 1 cm only during the first about 9 μ s. At later times due to ongoing evaporation and consequently increasing carbon density a cold plasma layer is formed near the target. Calculated plasma flow patterns are shown in Fig. 4 at two different times. The arrows indicate the plasma flow $\Gamma = n_e v$ with n_e the carbon density and v the velocity, the lines show carbon density contours. The densities n_e are indicated. At early times the plasma flow is strictly along the magnetic field lines. After formation of the cold plasma layer there is a plasma flow along the target surface in downstream direction. Therefore, the observed drift of the plasma shield along the target surface can

be explained without any assumption on turbulence near the target, simply by motion of cold dense plasma across magnetic field lines due to classical diffusion. There is another interesting fact.

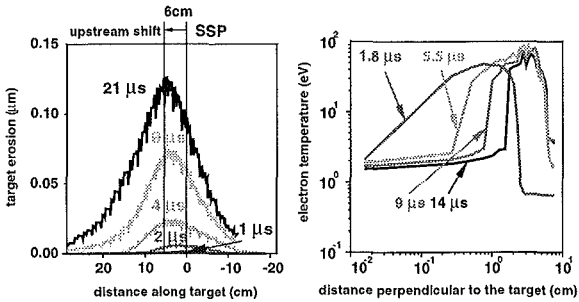


Fig. 2: Calculated erosion profiles for a vertical graphite target at the MK-200 UG facility at different times showing widening of the evaporation region and upstream shift of the profiles

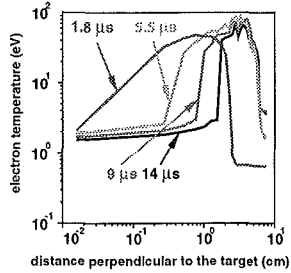


Fig. 3: Carbon density profiles at 0.5 cm distance to the vertical target at the MK-200 UG facility at the same time moments as in Fig. 2 showing widening of the plasma shield preferentially upstream with ongoing time

As seen from Fig. 2 the erosion profile is gradually shifted upstream. As a consequence the position of the maximum erosion is upstream of the SSP. This is not a consequence of the downstream plasma drift but follows from the fact that the radiative target heat load has its maximum upstream of the separatrix because the radiation coming from a region symmetrical to the separatrix has shorter distances to the upstream part of the target and moreover hits it under angles closer to 90°. The increase of the upstream shift with time is caused by the expansion of the radiation region away from the target.

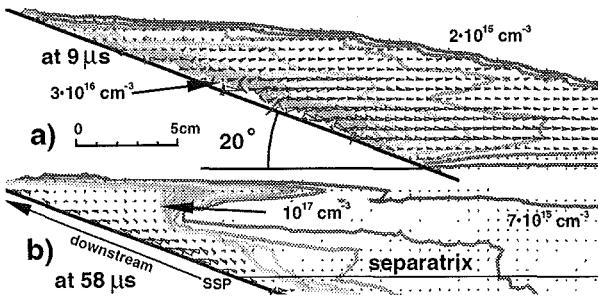


Fig. 4: Calculated plasma flow pattern (arrows show $n_e v$) and distributions of carbon density in a carbon plasma shield at the MK-200 UG facility at two time moments for a vertical target and classical Spitzer diffusion coefficient

The theoretically predicted upstream shift of the erosion profile is confirmed by the experimental results. Fig. 5 shows measured erosion profiles for the vertical target in downstream direction and for a target with surface perpendicular to the impacting hot plasma. The profile width is rather similar for both targets. However the vertical target should show a profile widening of a factor of 3. There is only one possible explanation: namely upstream shift of the profile by 70 mm. As can be seen from Fig. 2 the experimentally determined profile shift is in agreement with the theoretically predicted value. The plasma shields in the simula-

tion experiments are tokamak typical. Therefore turbulent processes are also not expected to occur in the plasma shields of vertical targets produced in ITER-FEAT off normal events. The long term plasma shield stability and the target erosion thus can be adequately described by FOREV-2 [11].

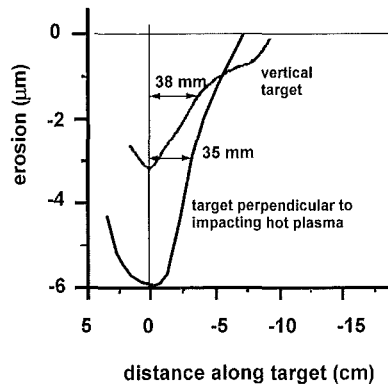


Fig. 5: Comparison of erosion profiles measured at the MK-200 UG facility for a vertical target and a target with surface perpendicular to the impacting hot plasma after 15 shots

3. Erosion of ITER-FEAT vertical targets

The divertor arrangement and the realistic unsymmetrical power density profile of the impacting hot plasma used in the 2-D FOREV-2 calculations are the same as described in [11]. Target materials are graphite and tungsten. The two peak target heat loads 3 and 30 GW/m² with 10 ms and 1 ms time duration (total energy density of the hot plasma of 30 MJ/m² in each case) were used. The inclination of the magnetic field lines in toroidal direction is 2°, the target inclination in the poloidal plane is 20°. Fig. 1 also describes the tokamak situation but only in the poloidal plane. The power density profile across the scrape off layer (SOL) is unsymmetrical and not Gaussian [11]. Fig. 6 shows the obtained results on erosion profiles and time evolution of target heat loads for tungsten vertical targets.

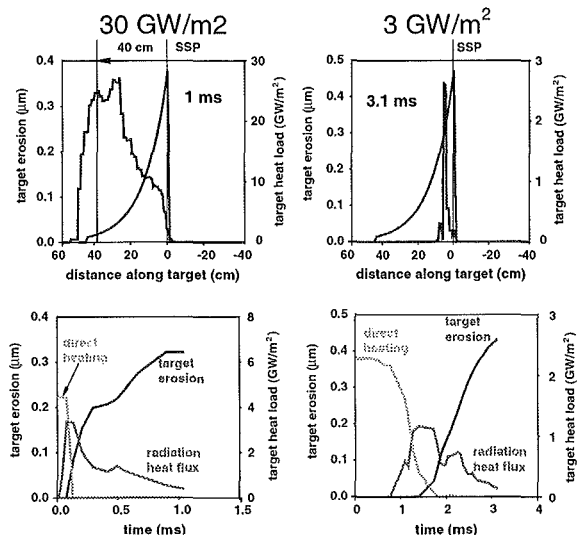


Fig. 6: Erosion and time evolution of target heat loads for a vertical tungsten target at two different target heat loads for ITER-FEAT for downstream SSP for the 2 different target heat loads 3 and 30 GW/m²

The SSP is at position zero and the positive direction is along the target upstream. The target heat loads belong to the position of maximum erosion. Similar to the results from the simulation experiment (compare Fig. 6 with Fig. 2) the erosion profiles for the 30 GW/m² case always are shifted upstream with respect to the SSP. The upstream shift at 1 ms is up to 40 cm for tungsten. There is erosion where the power density of the impacting hot plasma is below 3 W/m² and negligible erosion at the SSP with peak power density of 30 GW/m². With only direct heating negligible evaporation would occur at the 3 GW/m² position within 1 ms. The shift rate in the tokamak case is much less than for the UG facility. For the tokamak case because of the toroidal inclination angle of the magnetic field lines of 2° the plasma shield expansion velocity along the separatrix in the poloidal plane is smaller than for the UG facility where there is no such toroidal inclination. The smaller expansion velocity keeps the radiating region closer at the SSP and thus causes the smaller shift rate in comparison with the UG situation. The time dependence of the upstream shift of the radiative target heat load is shown in Fig. 7 for the tungsten vertical target. The reduced radiative target heat load at the SSP and the more pronounced plasma drift along the target surface downwards favored by the unsymmetrical power density profile of the impacting hot plasma and by the larger density of the cold plasma close to the target provide the strong shielding at the SSP which effectively results in zero erosion there.

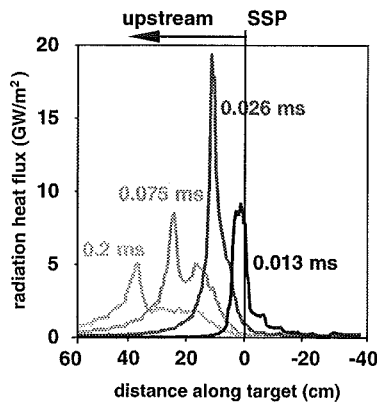


Fig. 7: Radiative target heat load profiles and time dependent upstream shift of the radiation profiles for vertical tungsten target for downstream SSP and ITER-FEAT conditions with peak target heat load of 30 GW/m²

The situation is quite different for the low power density (3 GW/m²) case having larger heat deposition times. For the case with downstream SSP there is only a small upstream shift of the peak erosion in relation to the SSP. As can be seen from the time evolution of the target heat loads direct heating dominates up to 1,0 ms, evaporation starts after 1 ms when radiation contributes to the target heat load. 0,5 ms later the radiative target heat load decreases again. The radiation is confined to a narrow region around the SSP and therefore the upstream shift of the

erosion profile remains rather small. Again zero erosion at the SSP is due to downstream drift of the plasma.

Despite a factor of 10 lower power density of the impacting hot plasma the erosion for tungsten because of longer deposition times and reduced plasma shielding efficiency becomes comparable to the high power density case. Vertical targets are effectively dissipating the energy in high power density off normal events. For low power densities however vertical targets offer no advantage in comparison with horizontal targets.

4. Brittle destruction and target screening by dust particles

A comparison of measured and calculated total mass losses (evaporation and brittle destruction) for fine grain graphite and for CFC for the JEBIS facility [12] for a 70 keV electron beam with peak power density of 1,8 GW/m² Gaussian power density profile of half width of 5 mm and pulse duration of 2 ms is given in [4]. Fig. 8 shows the calculated time dependencies of brittle destruction and of evaporation for fine grain graphite of initial temperature of 1200 K. Brittle destruction occurs several times within the heat load deposition time of 2 ms.

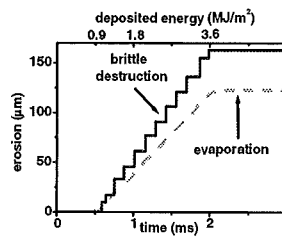


Fig. 8: Calculated erosion rates for JEBIS conditions for pyrolytic graphite. Initial temperature of the sample is 1200 K.

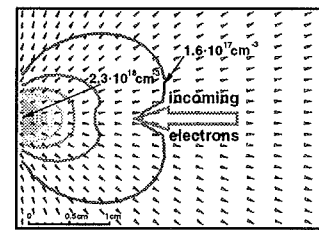


Fig. 9: Expansion of the ablated material into vacuum. The arrows indicate the particle flow Γ with $\Gamma = n_c v$, the lines show carbon density contours for indicated densities

Target screening by the carbon vapor is of no concern in these JEBIS experiments because the vapor density within the region of the impacting electron beam as obtained from a 2-D hydrodynamic calculation of the expansion of the ablated material into vacuum with FOREV-2 remains rather small. Fig. 9 shows the vapor flow and the vapor densities in the cloud. The arrows indicate the particle flow Γ given as $\Gamma = n_c v$ with n_c the carbon density and v its velocity. The lines describe density contours with given densities. The vapor density drops within a distance of 1 cm from the target by more than a factor of 10 to values below $2 \cdot 10^{17} \text{ cm}^{-3}$. Therefore the energy deposition into the vapor cloud is negligible. The vapor temperature is around 0,7 eV and thus consists of neutrals.

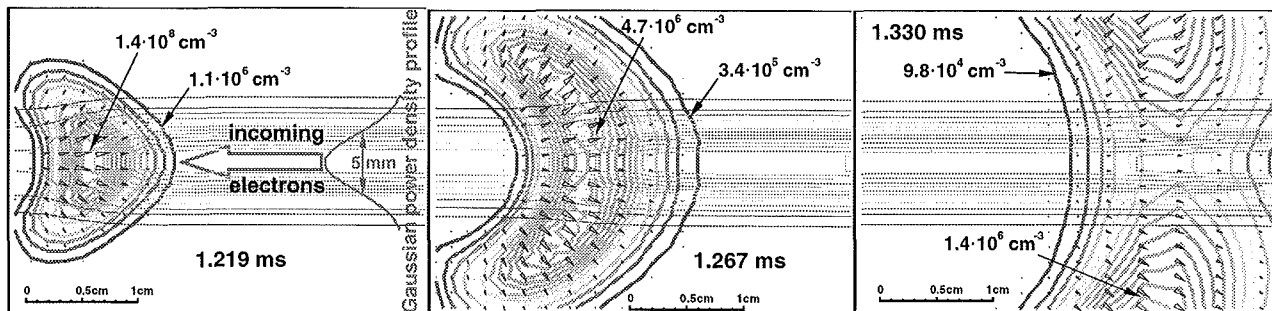


Fig. 10: Expansion of the cloud of dust particles at 3 different times after a brittle destruction event which occurs at 1,2 ms. Evaporation of the particles decreases their density and the energy deposition into the cloud decreases

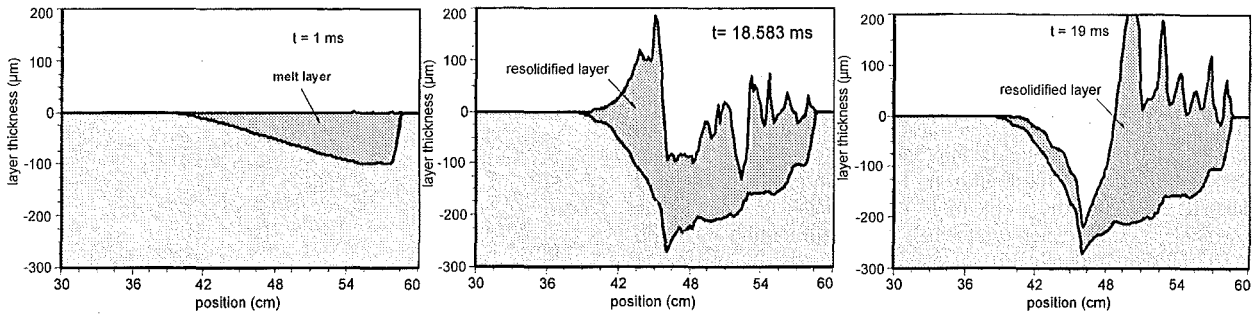


Fig. 13 a: Calculated melt layer erosion profile for a tungsten vertical target for ITER-FEAT conditions for hot plasma impact with peak heat load of 30 GW/m² and 1 ms time duration without target current and Lorentz force at end of heating
 Fig. 13 b: Calculated melt layer erosion profile and thickness of resolidified layer after complete resolidification. The same conditions as in Fig. 13a without target current.
 Fig. 13 c: The same conditions as in Fig. 13b but with a target current of density of 50 A/cm². The influence of the Lorentz force is demonstrated

Target screening due to the dust particles from brittle destruction in these JEBIS experiments was investigated with FOREV-2. Results on dust particle motion are shown in Fig. 10 at three different times after onset of a brittle destruction event at 1,2 ms. The dust cloud due to pressure gradients initially expands isotropically later the isotropy is destroyed in the region where the electron beam heats and evaporates the particles. After about 130 μs the dust vapor cloud becomes transparent again for the electron beam as can be seen from Fig. 11 showing the energy deposition into the target which with onset of brittle destruction drops to half the initial value but recovers within 130 μs. Moreover it is seen that the time during which the target is shielded decreases with ongoing time. This is due to the increased density of the background vapor which drives the dust particles by drag forces [4].

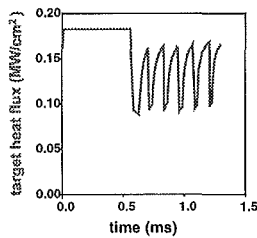


Fig. 11: Energy deposition into the target showing target screening by the dust particles after onset of brittle destruction and time duration of target shielding by the dust cloud

5. Melt layer erosion of metals

5.1 JEBIS electron beam simulation experiments

Experimental results from the JEBIS e-beam facility on melt layer erosion of tungsten targets demonstrate a rather pronounced motion in the melt layer. As a result the erosion depth on average was about 150 microns and mountains of ejected melt material are formed at the crater edge [6]. Due to the melt motion the melt layer erosion was a factor of 2 larger than the melt layer thickness. For a quantification of melt layer erosion therefore cause and consequences of melt motion has to be investigated.

The 1-D shallow water model is used for calculation of melt layer motion under the external forces surface tension, recoil force of the evaporated metallic atoms and vapor pressure and Lorentz force. Radiation cooling of the melt is taken into account. The equations to be solved together with numerical details are described elsewhere [9]. In order to validate the developed model the JEBIS results for tungsten were simulated. Gaussian profiles for the spatial and time distribution of the heat load were used. The calculated erosion profile is shown in Fig. 12 after complete resolidification. The crater depth is 30 microns, the thickness of the resolidified layer is 60 μm. A mountain is formed at the crater edge. However the numerical results differ significantly from the experimental ones. Variations of such parameters as viscosity and pressure of saturated vapor only weakly are influencing the depth of the erosion crater. For example decreasing the viscosity by a factor of 2 resulted in an increase of the depth of not more than 30%. For the e-beam facility typical electric currents of densities up to 3 A/cm² contribute negligible to Joule heating. Lorentz forces because of no external magnetic field are absent. Droplet splashing from the melt produces momentum which results in additional pressure acting on the melt. This effect was estimated too by assuming that 10% of the melt is splashed by droplets. Negligible influence on melt motion was obtained.

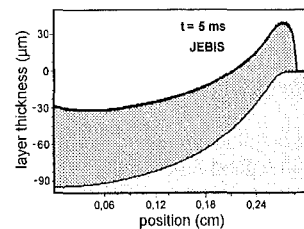


Fig. 12: Calculated melt layer erosion profile and thickness of resolidified layer for a tungsten target at JEBIS

5.2 Tokamak conditions

A first application of numerical simulation to hot plasma impact onto a vertical tungsten target typical for ITER-FEAT with peak power density of 30 GW/m² and time duration of 1 ms is given. Time dependent target heat loads and plasma shield pressures

were obtained from FOREV-2 calculations. During irradiation the temperature of the molten material reaches boiling temperature and thus a significant amount of energy is accumulated in the melt layer. For resolidification 19 ms are needed. During the load time the melt motion is still not developed and the depth of the melt layer is about 100 microns as is to be seen from Fig. 13a. After stop of heating the melt front propagates further into the bulk till resolidification starts from the bottom of the melt. In Fig. 13b the calculated erosion profile after resolidification being completed after 19 ms is shown. The depth of the resolidified layer is 250 μm , the weak melt motion which is going on till complete resolidification produces a significant roughness at the melted region and causes melt layer erosion with 100 microns.

The influence of electric currents crossing the melt layer perpendicularly to the target surface was estimated. A typical target current of 1 kA/cm^2 in a magnetic field of 5 T parallel to the target surface was assumed. The depth of the melt layer is not influenced, but the Lorentz force reverses the flow direction, increases the melt motion, shifts the mountains to the right and increases the melt layer erosion up to 250 microns as is seen from Fig. 13c. Melt front propagation during resolidification, and melt motion might result in melt layer erosion being up to a factor of 3 larger than the melt layer thicknesses calculated without melt motion.

6. Numerical simulation of brittle destruction

For volumetric heating brittle destruction dominates erosion and produces considerable amounts of dust [4]. There are experimental indications that under hot plasma impact brittle destruction might also occur [14]. Brittle destruction of CBMs when occurring could become a limiting factor for the lifetime of graphite divertor targets because predamage of the sample under volumetric heating and under cyclic surface heat loads finally might result in a drastic increase of divertor plate erosion. For understanding of brittle destruction and its quantification for ITER-FEAT off normal conditions a numerical simulation model was developed [15]. It was shown previously that thermal stress in a heated graphite sample results in breaking of lattice bonds due to the anisotropy of the thermal expansion and due to thermal conductivity [16]. As a consequence of intense cracking macroscopic layers are destroyed and graphite dust is produced. Important for brittle destruction to occur are the anisotropy of the graphite grains, the failure stress distribution of the bonds connecting adjacent grains, the value of the pulsed heat load and, consequently the temperature and its gradient in the bulk target. Cracks preferentially are propagating into the depth of the sample. Such a crack propagation indicates occurrence of predamage under repetitive heat loading and finally might result in drastically enhanced erosion of graphite. This could reduce the lifetime and by dust formation could cause a safety problem.

6.1 Lattice model of graphite

For numerical simulation of brittle destruction a lattice model was developed simulating real graphite which consists of grains of different size and different anisotropy directions [15]. The numerical lattice model uses a special procedure which generates grains of random size and shape in a rectangular coordinate system. A typical numerical lattice is shown in Fig. 14. It consists of cubic cells of identical size a . Grains consist of an integer number of cells. The grain sizes are Gaussian distributed around a mean number of cells per grain - mean grain size (MGS). Neighbouring cells of the same grain are connected via internal bonds, neighbouring grains via surface bonds. In Fig. 14 for better illustration of the grains the cell sizes are drastically increased. Additionally there are small grains filling the gaps between the larger ones.

The anisotropy of the physical properties of the grains determined by the atomic structure of graphite is taken into account. The Young's moduli E_1 and E_2 , the thermal conductivities λ_1 and λ_2 and the thermal expansion coefficients α_1 and α_2 are assumed to be different parallel and perpendicular to the anisotropy axis which denotes the direction perpendicular to the atomic carbon layers.

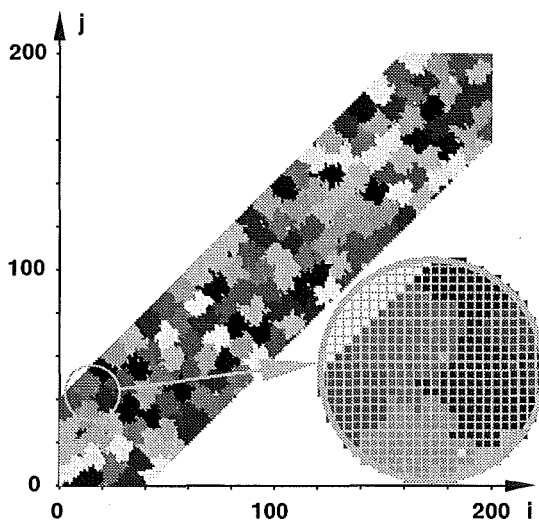


Fig. 14: Rectangular lattice as used in the numerical simulation of graphite with a Gaussian distribution of the grain sizes. The mean grain consists of 55 cells of identical size a . Detailed description of the model is given in the Appendix

The failure stress value of the internal bonds is assumed to be a factor of 10 larger than the value for the surface bonds. Therefore breaking of bonds preferentially will occur along the surface of the grains. In case of broken bonds the expansion of the cells during heating can result in stretching (increasing distance between broken bonds) or in compression (closure of gap with disappearance of the crack). Heating of a graphite sample results in local temperature changes thus producing forces acting on the grains due to thermal expansion. Nevertheless, the sample is at rest during heating. In the 2-D numerical lattice model, heating results in 8 different forces acting on each individual cell as described in the appendix. Using these forces the evolution of the lattice is calculated with ongoing temperature changes. It is assumed that the relaxation of the stress occurs much faster than the propagation of the heat wave. Therefore after each change of temperature the mechanical equilibrium of the lattice system is established instantaneously using embedding in an auxiliary mechanics. The fundamental equations used in the model are described in [15].

A broken bond represents an elementary crack. The mechanical properties of the sample with cracks depend on the crack density and are, thus, time-dependent. The merging of the neighbouring cracks simulates the process of the crack propagation. Furthermore, due to merging of cracks at various places of the sample, different clusters of grains can arise within the target. Isolated graphite clusters arising near the surface of the target are removed from the sample as dust particles. This process simulates the motion of the fracture boundary inside the sample.

6.2 Estimation of the characteristic failure stress

For a numerical simulation of brittle destruction, failure stresses have to be known. However these parameters can't be measured. Assuming that the failure stress for the surface bonds with the characteristic value σ_{bs} is uniformly distributed in the interval $\sigma_{bs} (1/p, 1)$ with $2 \leq p \leq 5$ then the failure stress distribution function of the surface bonds is determined by the two parameters p and σ_{bs} being estimated from a comparison with experimental results on destruction by mechanical compression and by volumetric heating. For obtaining a fracture deformation in the range of about 1% the characteristic failure stress for surface bonds was obtained to be in the range $\sigma_{bs} = (0.5-1) 10^{-2}$. Experimental results on brittle destruction by volumetric heating were used for a determination of the characteristic failure stress value σ_{bs} . Onset of brittle destruction was obtained at about 10 MJ/m^2 at the GOL-3 electron beam facility [17]. The numerical simulation with a failure stress value of $\sigma_{bs} = 0.005$ is in rather close agreement with this value.

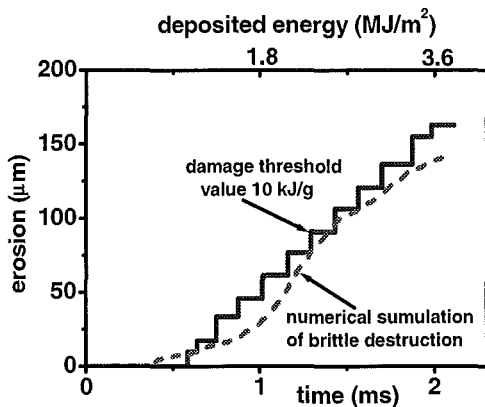


Fig. 15: Comparison of calculated erosion rates by brittle destruction for pyrolytic graphite for JEBIS conditions. Initial sample temperature is 1200 K

6.3 Brittle destruction and crack propagation

The numerical simulation model was applied to the calculation of brittle destruction at the electron beam facility JEBIS [12]. It is assumed that initially the graphite sample is at a uniform temperature of 1200 K. Heating of the surface near target layer occurs due to a constant heat flux of 1.8 GW/m^2 for 2 ms. The energy deposition into graphite shows a maximum at a depth of 20 microns. A comparison of calculated erosion rates by brittle destruction using numerical simulation and results from another analysis in which a damage threshold value of 10 kJ/g was used for start of brittle destruction [17] is shown in Fig. 15.

Impact of hot plasma during the thermal quench phase of a disruption results in surface heating and erosion of the vertical

divertor target. A typical case with peak power density of 30 GW/m^2 and heat load duration of 1 ms was used for quantification of total erosion and target screening in a FOREV-2 calculation and was used for numerical simulation of erosion by brittle destruction. The time evolution of the target heat load was taken from [11]. Calculated crack formation and brittle destruction are shown in Fig. 16 for one and for two heat pulses with cooling down of the sample till initial temperature during 1ms between both pulses. After one pulse the numerical simulation clearly shows crack formation inside of the bulk target as is typical for predamage of the sample. According to these first numerical results erosion during the second pulse increases by a factor of 1.5 thus indicating enhancement of brittle destruction after predamage.

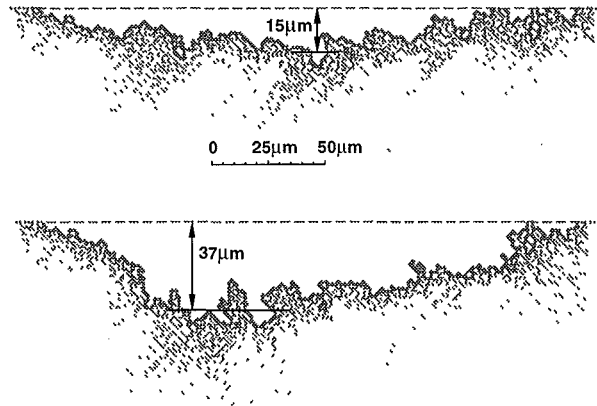


Fig. 16. Erosion by brittle destruction and crack pattern for a vertical divertor target for an ITER-FEAT typical off normal event with initial peak target surface heat load of 30 GW/m^2 and heat load duration of 1 ms shown on Fig. 11 after one and after two heat pulses

6.4 Predamage and enhancement of brittle destruction

Influence of run away electrons of several MeV energy on the graphite divertor target results in volumetric heating of rather thick graphite layer and erosion of several hundreds of microns if the energy deposition exceeds the threshold value of approximately 10 kJ/g [17]. But even much lower energy deposition from run away electrons can produce cracks deep inside of the graphite target. For example the deposition of 2 kJ/g results in a rather low erosion value of $3-5 \text{ µm}$ for the divertor target, as shown in Fig. 17a, but this energy deposition causes predamage of graphite up to a depth of several hundreds of microns. This predamaged layer is not eroded, but has reduced mechanical properties due to the increased crack density. Exposing such a predamaged graphite to the same cyclic surface heat load as described above results in a drastic increase of erosion as seen from Fig. 17b. The time dependence of the mean erosion of undamaged graphite and graphite predamaged by run away electrons is shown in Fig. 18. Both samples are heated with cyclic

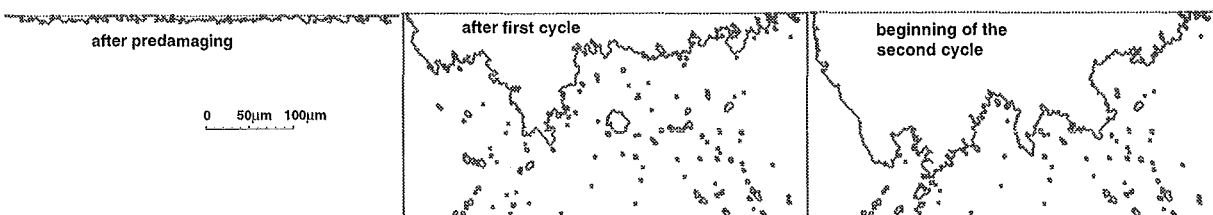


Fig. 17: Erosion pattern for predamaged graphite under cyclic surface heat load shown in Fig.11. Predamage is from deposition of 2 kJ/g from run away electrons. Dashed lines show initial surface of graphite sample

surface heat loads with 1 ms time duration and 1 ms cooling down time. For the predamaged sample brittle destruction starts during cooling of the sample after deposition of 2 kJ/g from run away electrons. For the undamaged sample brittle destruction occurs from the heating phase. Time dependence of erosion of predamaged and undamaged graphite under surface heat load shown in Fig.11. Left panel shows erosion of graphite, predamaged with deposition of 2 kJ/g from run away electrons, right panel corresponds to unscathed graphite.

7. Conclusions

The experimentally observed downstream drift of the plasma shield along the surface of a vertical target can be explained by use of the classical Spitzer diffusion coefficient in the solution of the multidimensional magnetic field equations. Therefore plasma turbulence is not occurring in the experimental plasma shields. The plasma shields in the simulation experiments are tokamak typical. Therefore turbulent processes are also not expected to occur in the plasma shields of vertical targets produced in ITER-FEAT tokamak plasma disruptions. The long term plasma shield stability and the divertor erosion thus can be adequately described by FOREV-2. The observed upstream shift of the erosion profiles of vertical targets in the simulation experiments can be explained by the distribution of the radiative heat load along the target surface with a maximum always upstream of the SSP. The downstream drift of the plasma shield only weakly influences this situation. For the tokamak upstream shift of erosion occurs too. Additionally the enhanced plasma drift downstream together with the reduced radiative heat load at the SSP results in negligible erosion at the SSP.

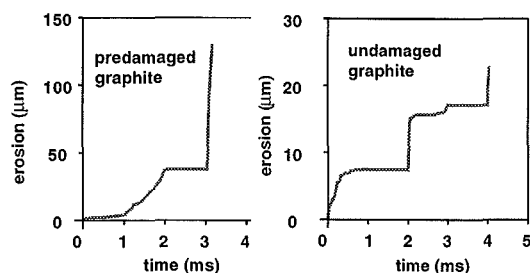


Fig. 18: Time dependence of erosion of predamaged and undamaged graphite under surface heat load shown in Fig.11. Left panel shows erosion of graphite, predamaged with deposition of 2 kJ/g from run away electrons, right panel corresponds to unscathed graphite

Brittle destruction of graphite under volumetric heating produces rather large amounts of dust. Graphite as FW material thus causes safety problems. Vapor shielding and target screening by dust particles for the first time are taken into account in the numerical simulations. Melt layer erosion of metals is dominated by melt flow. The driving force behind the melt flow is still unclear. Taking heat transport during resolidification and Joule heating by currents flowing in the target during the heat load period into account might result in an increase of the melt depth by up to a factor of 3. Lorentz forces might trigger a pronounced melt motion which might sweep away a considerable part of the melt layer. The melt layer erosion thus can be considerably larger than the melt thickness formed during the heat load period. Due to the considerable implications of melt motion on melt layer more experimental and theoretical investigations on this topic are urgently required both for surface and volumetric heating.

It has to be clarified why the calculation underestimates melt layer erosion for e-beam experiments and why it predicts in opposition to the experimental results zero melt layer erosion for plasma gun experiments. Finally during the resolidification

phase the decay of the poloidal magnetic field induces remarkable eddy currents producing a Lorentz force which exists for a longer time period thus increasing melt motion and melt layer erosion further.

For simulation of brittle destruction in carbon based materials a numerical model was developed. By comparing the numerical results on brittle destruction with experimental results for volumetric heating and with results from mechanical destruction tests of graphite samples a typical failure stress value for surface bonds of $\alpha_s=0.005$ was derived. Volumetric heating produces cracks inside of the sample, surface heating results in crack propagation into the depth of the sample. In both cases some predamaging of the sample occurs. It has been found, that volumetric predamaging by run away electrons has a considerably stronger influence on erosion than predamaging by surface heat loads only. Before any conclusions on enhancement of brittle destruction can be drawn cyclic heat loading has to be simulated numerically.

Literature:

- [1] G. Federici et al., In vessel tritium retention and removal in ITER, J.Nucl. Mater 266-269, 1999, 14
- [2] J. Roth, Chemical erosion of carbon based materials in fusion devices, J. Nucl. Mater 266-269, 1999, 51
- [3] S. Pestchanyi, H. Würz, Brittle destruction of carbon based materials under off-normal ITER-FEAT conditions, submitted to Physica Scripta
- [4] H. Würz et al., Dust production in ITER-FEAT off normal events and target screening by dust particles, Proceedings EPS-27, June 2000, Budapest
- [5] K. Krieger et al., Conclusions about the use of tungsten in the divertor of ASDEX Upgrade, J. Nucl. Mater 266-269, 1999, 207
- [6] K. Nakamura et al., Disruption erosion of various kinds of tungsten, Fus. Eng. and Design 39-40, 1998, 295-310
- [7] H. Würz et al., Vertical target and FW erosion during off normal events and impurity production and transport during ELMs typical for ITER-FEAT, presented at PSI-14, May 2000, Rosenheim; submitted to J. Nucl. Mater.
- [8] G. Tsotridis, Modeling of surface deformations during plasma disruptions. Fus. Technology 37 (2000) 185
- [9] Landman, H. Würz, 1-D fluiddynamic simulation of melt motion, FZKA report 6517, 2000
- [10] N. Arkiphov et al., Turbulent diffusion of divertor vapor cloud across inclined magnetic field during a tokamak disruption, Proceedings of EPS Conference 1999, Maastricht
- [11] H. Würz et al., Hot plasma target interaction and quantification of erosion of the ITER slot divertor during disruptions and ELMs, FZKA report 6198, 1999
- [12] K. Nakamura et al., Erosion of CFCs and W at high temperature under high heat loads, J. Nucl. Mater 212-215, 1994, 1201-1205
- [13] V.V. Semak et al., Temporal evolution of the temperature field in the beam interaction zone during laser material processing, J. Phys. D: Appl. Phys. 32 (1999) 1819

- [14] M. Guseva et al., Tech. Phys. 41, 578, 1996
- [15] S. Pestchanyi, H. Würz, N.Usov, Numerical simulation of brittle destruction of graphite due to severe thermal shocks, FZKA report 6466, 2000
- [16] S. Pestchanyi et al., Fusion Technology 1998, Vol. 1, 275, 1998
- [17] V.T. Astrelin et al., Nucl. Fusion 37, 1541, 1997

Staff:

B. Bazylev
F. Kappler
I. Landmann
S. Pestchanyi
V. Safronov
N. Usov
H. Würz

Vessel/Mechanical Structures

T 204-9 Plasma Arc Cutting of ITER Containment Vessel

The objective of this technology programme was the development of cutting techniques for the field disassembly of segments from the ITER containment vessel, required for remote replacement in the event of failure of toroidal field coils. Further on a backplate protection system had to be developed to avoid heat affection to the outer backplate and to capture the emissions, i.e. gases, fumes, dust and dross generated by the thermal cutting process. A mock-up has been constructed for the near-reality tests to prove the functionality of the protection system. For application of the protection system different devices and methods for positioning and fixing of the required components have been developed.

In contrast to current state of the art tests and modifications enabled the use of a 300 A-cutting torch instead of the hitherto used 600 A-torch for cutting 60 mm stainless steel. As shown in cutting trials the use of the smaller torch offers some advantages including less tool weight, narrower cutting kerfs (and thus less emissions) and less thermal stress (Fig. 1).

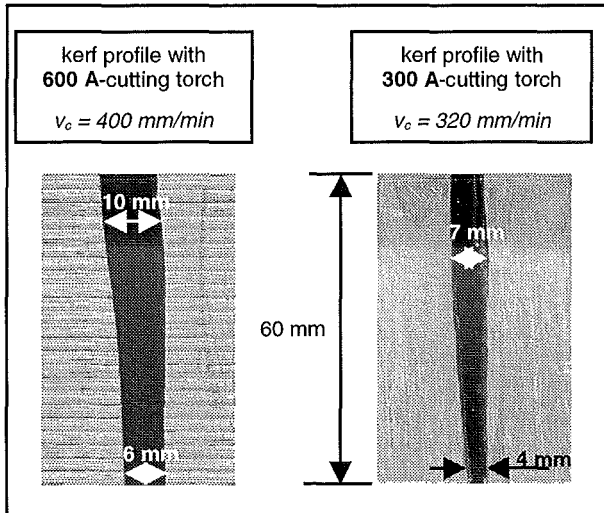


Fig. 1: View of cutting kerf profiles with different cutting torches

For cutting under near-reality conditions an arched mock-up has been constructed. Its main geometric characteristics are similar to those of the ITER backplate with a radius of curvature of 1,70 m and wall thickness of 60 mm. For improved visibility of the fixation process of the protection system the back wall is made of plexiglas (Fig. 2).

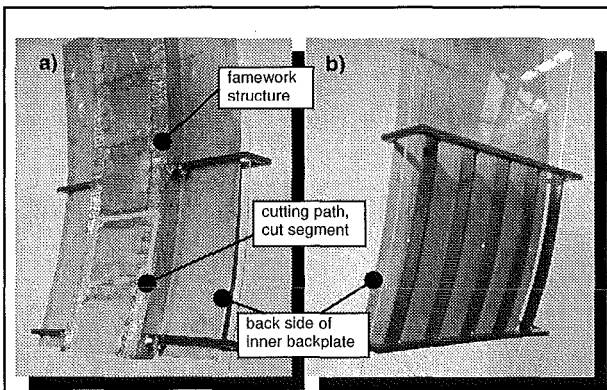


Fig. 2: Two views of mock-up; a) front view with cutting path and cut segments, b) rear view with stiffeners frame of plexiglas screen

The concept of the backside protection system with a reciprocating thermal shield from earlier stages of the technology programme was changed towards a system with a static shield. This design works more reliable and offers a comparable performance as the reciprocating wall. Besides the new protection system has got a bent shape to fit to the greatest just as well as the smallest curvature of the backplate.

The fixing of the protection system in between the backplate gap is performed with an inflatable hose (Fig. 3).

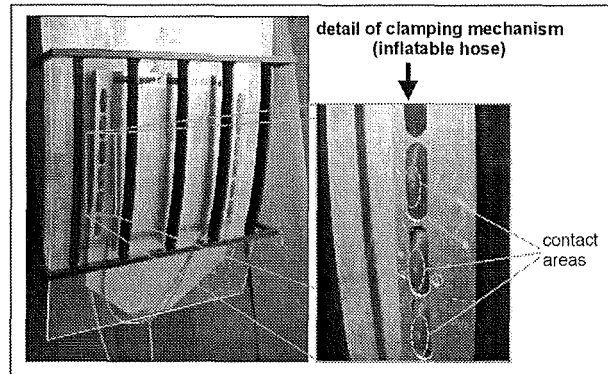


Fig. 3: View of protection system installed the mock-up

The confinement of dust, particles and generated fumes is realised by a double sealing lip. The inner lip consists of brush wires and keeps off spattered particles. Around that, a flexible sealing lip prevents fumes and dust from escaping the backside protection system. The flexible lip is capable to compensate gaps up to 3 mm which may occur when the bent protection system is attached to an flat part of the backplate. These sealing lips are protected against thermal effects by carbon shoulders mounted along the rim of the inner thermal shield (Fig. 4).

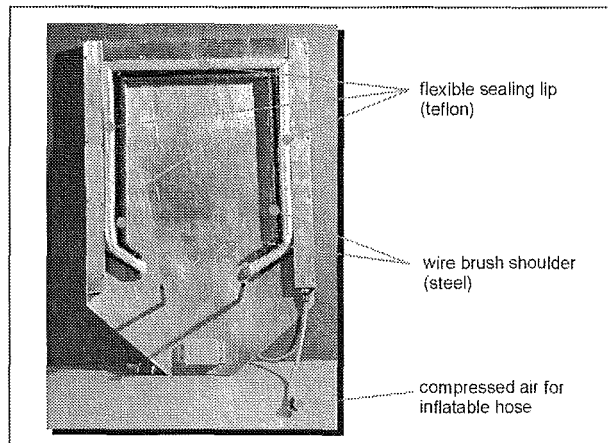


Fig. 4: Shield plate with sealing system

According to earlier tests CFC-tiles proved to be the most endurable thermal protection. Moreover, the endurance of the thermal shield has been significantly improved by application of a gas flushing system to create an inert gas atmosphere protecting the carbon from oxidising.

The emitted dross and spattered particles are collected by an exchangeable on-way dross reservoir mounted at the bottom of the protection system. The generated fumes and aerosols are captured by a suction hood mounted to the front of the protection system and connected with a suction pump (Fig. 5).

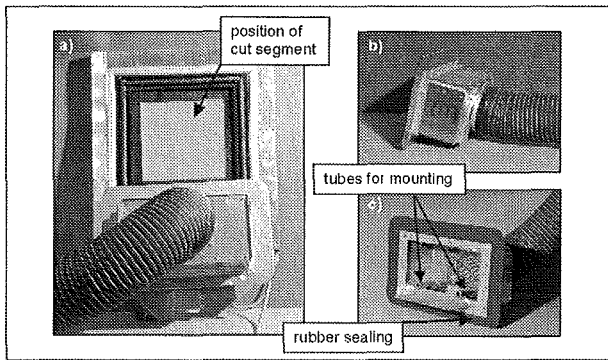


Fig. 5: Views and attachment of suction hood

With the set-up described the cutting of splice plates of 200 x 200 x 60 mm was repeatedly and successfully performed at the mock-up. The amount of escaping emissions was inevitable but very low.

Staff:

T. Grimm
G. Schreck
H. Haferkamp
Unterwassertechnikum Hannover
des Instituts für Werkstoffkunde
Universität Hannover

Coil System

M 44 TFMC Installation and Test

The TOSKA facility at Forschungszentrum Karlsruhe is being upgraded for testing the ITER TF model coil. The facility has been taken into operation in the following steps:

- Test of the LCT coil at 1.8 K (1996/1997)
- Test of the stellarator prototype coil W 7-X (1999)
- Start of the test of the TFMC (June 2001).

The first step qualified the LCT coil for the use as background coil for the TFMC test configuration. The basic facility with its electrical and cryogenic supply system as well as data acquisition and control was taken into operation. The specific facility configuration needed for the TFMC test is nearly complete. The commissioning of the 80 kA dump circuit and the 20 kA power supply is being in the final stage of completion. The fabrication of two 80 kA current leads was finished. Some brazing faults are being repaired. Two extensions of the TOSKA vacuum vessel for the vertical installation of the current leads were delivered.

For the performance of the TFMC test, an organization scheme was approved for decision making and handling the daily work of testing. The management of the test is handled by the Coordination Group which is supported by the Operation and the Test Group. Members of the groups are delegates from the ITER JCT and the Home Teams.

The fabrication of the TFMC in the European industry is in the final stage. The winding is enclosed in the coil case and the mounting of the instrumentation has been started. The intercoil structure (ICS) was delivered in May 2000 to the TOSKA facility. The acceptance tests and the preparation of the test program of the TFMC are accompanied by the special skills of the European superconducting laboratories. The areas of EURATOM Association Forschungszentrum Karlsruhe are:

- Instrumentation (included in M 44)
- Conductor measurements (NET Contract No.: NET/97-458 concluded)
- Mechanical material and component testing (EU Task No: M 45 concluded)
- High voltage component delivery and testing (NET Contract No.:NET/96-438 concluded)
- Finite element analysis (EU Task M 12)
- Electromagnetic and thermohydraulic analysis (included in M 44 and 3 D quench analysis with code system MAGS, IRS, EU Task SEA 5)
- Transient voltage behaviour of the TFMC (included in M 44)
- Leak testing acceptance tests during fabrication (included in M 44)

It was recommended by the TFMC Coordination Group in March and concluded by the EURATOM Association Forschungszentrum Karlsruhe Steering Committee in July 2000 that the TFMC will be tested in two phases:

1. Phase: The TFMC will be tested as single coil. The LCT coil will be replaced by an auxiliary structure.

2. Phase: The TFMC will be tested in the background field of the LCT coil.

The intention is to achieve results of the TFMC as soon as possible in less sophisticated configuration with a lower risk of occurring faults.

The installation of the TFMC is scheduled for 1st quarter of 2001 and the test end at the 2nd quarter 2002.

1. The TOSKA facility

The activity in the reporting period has been as follows:

- Assembly and alignment of delivered structural components
- Change of the header position of the LCT coil
- Repair of the brazing faults of the 80 kA current leads
- Final commissioning of the 80 kA dump circuit and the 20 kA power supply
- Commissioning and delivery of the 125 t lifting beam.
- Modification of cryogenic supply and control system as well as data acquisition for testing the TFMC

Assembly and alignment of delivered structural components: In the first half year all assembly tools for the TFMC mounting were delivered to the TOSKA facility. The assembly frame were water leveled in the TOSKA area at the foreseen position. The gravitational support and the delivered auxiliary structure were assembled and aligned on the assembling frame. The ICS was delivered in May. A overall leak test and check-out of the instrumentation were performed by FZK staff. A trial assembly is performed for achieving the correct alignment in the TOSKA vacuum vessel which avoid repetitive lifting procedures with the much heavier configuration with the TFMC (Fig. 1).

The 125 t cross head for lifting the TFMC configuration in the TOSKA vacuum vessel approved by the authority, TÜV, and delivered in August at TOSKA site.

Change of the header position of the LCT coil: The header position at the LCT coil side adjacent to the TFMC was changed for having a sufficient large support area for the horizontal plates of the ICS. All reinforcements belts of the LCT coil had to be removed. The header was moved in the upper part. The header and the pipes specially those covered later by the reassembled reinforcement belts were carefully leak tested. The belts are preloaded and the work is completed except the routing of the capillaries of the venturies

The 80 kA current leads: The fabrication of two 80 kA current leads were completed. During vacuum brazing procedure of cooling fins and Nb₃Sn inserts a leak between the electrolytic copper part (cold end) and the phosphorous deoxidized copper part (heat exchanger) led to a running out of brazing material. This resulted in no brazed Nb₃Sn inserts in the electrolytic copper section and blockage of the heat exchangers cooling fins by accumulation of running out brazing material in some sections. The blocked areas of the cooling fins were successfully milled free. Accompanying pressure drop measurements confirmed that 5 g/s mass flow can be achieved by a pressure drop of about 0.2 MPa with an inlet pressure of 0.35 MPa. The half bores of the Nb₃Sn inserts adjacent to the joint surface are being opened by a milling procedure controlled by ultrasonic measurements of the thickness of the remaining material which was finally successfully removed by manual peeling. It is planned to cover the Nb₃Sn inserts by several soft soldered copper profiles to form a new cold end joint surface for

the joint with the superconducting bus bar. The soldering procedure is being qualified by a 400 mm dummy piece.

For the vertical installation of the current leads two cryostat extensions are needed containing the bus bar type II which connects the TFMC bus bars with the current lead terminals for each polarity [1]. The cryostat extensions were delivered in July 2000. They were installed at the flanges of the TOSKA vacuum vessel for measuring the position of the contact surfaces of bar type II (Fig. 2).

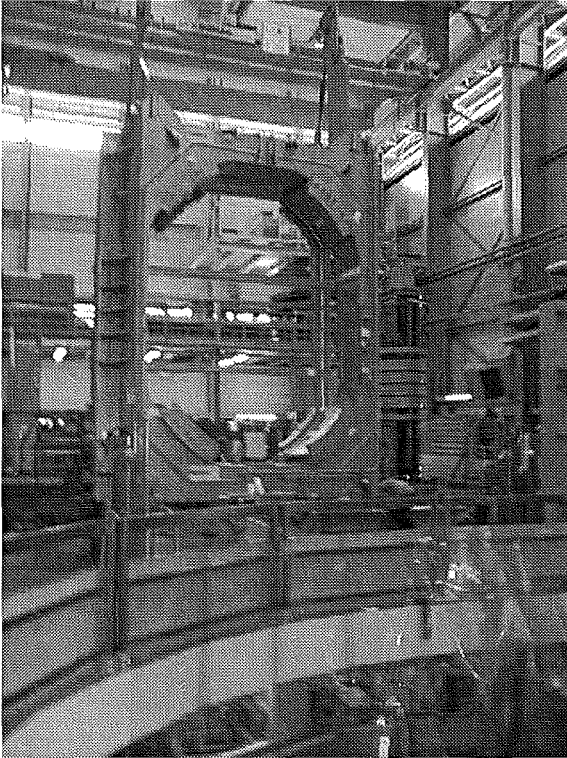


Fig. 1: The ICS (intercoil structure) after up-righting, in background direct behind the vertical beams of the auxiliary structure and on the left hand side the LCT coil with reduced reinforcement belt

80 kA dump circuit and the 20 kA power supply. Both components are in the final commissioning phase. They were tested with a copper coil up to the maximum possible current of 10 kA. The switching sequence of the 80 kA dump circuit worked well. Some improvements considering the achievement of a lower resistance of the short circuit path and the synchronization between 80 kA power supply and dump circuit are necessary.

The reference current measurements for control of the 50 kA and 30 kA power supply will be changed in October 2000 from zero flux transducers to shunt resistors in order to eliminate the impact of magnetic fringing fields on the power supply control as experienced in the test of the W 7-X prototype coil.

The 20 kA power supply were connected to the LCT coil dump circuit. The safety discharge was successfully tested by the copper coil.

Accompanying calculation for the power supply control and safety discharge circuits were performed by suitable developed codes [2]

Modification of cryogenic supply and control system as well as data acquisition for testing the TFMC: The piping in the TOSKA vacuum vessel, installation of cryogenic facility instrumentation and control valves have been completed as far as it was possible without the TFMC configuration. All pipes were closed and an overall vacuum leak test will be performed to reduce the risk of leaks after TFMC test configuration installation which would generate further delays.

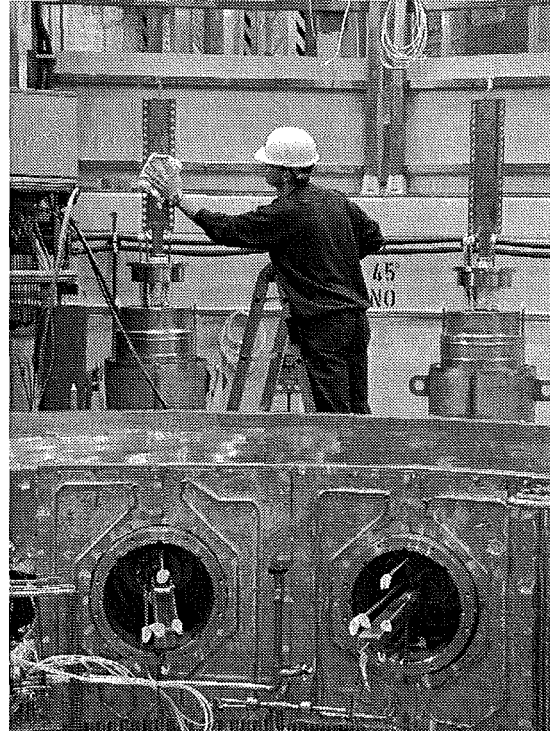


Fig. 2: The two cryostat extensions mounted at the flanges of the TOSKA vacuum vessel for determination of exact position of the contact surfaces to bus bar type II

A flow scheme together with an interlock scheme for the cryogenic system with links to the electrical high current supply has been elaborated and is being implemented on the process control system and data acquisition.

For the access of TFMC test data by the Internet, a clear structure of menus has been elaborated guiding the external user for the selection of sensors and the retrieval of test data.

The preparation for the installation work was coordinated in meetings of the Operation Group.

2. Preparations for the test program of the TFMC

In collaboration with the European superconducting laboratories the preparing work for the test program and related analysis for the TFMC result has been continued [3].

The work has been coordinated in meetings of the Testing Group.

The following progress was achieved in the different areas:

Electromagnetics : The elaboration of the operation diagram of the critical current of the TFMC in the test configuration without and with LCT coil was performed. Magnetic fields in the high field regions and in the joint regions for the two test configurations were calculated. In the joint region the performance of current sharing measurements are planned.

Thermohydraulics: The elaboration of a thermohydraulic data set for the TFMC conductor was concluded. The quench analysis for design of the venting system of the facility was concluded for specified quench scenarios [4]. A quench analysis for the complete coil was performed by the MAGS code (IRS) [5].

Mechanics: The TFMC alone was analyzed without and with friction between coil case and winding to see the effect of the stresses in the joint region. The TFMC stresses without background field are about 50 % lower than with it (see also Task M 12) [6].

Dielectrics: A low voltage pulse generator was constructed and tested with pulse rise times in the range of μs for investigating the TFMC transient behaviour.

Instrumentation: The instrumentation of TFMC and the ICS was fixed. The implementation in the fabrication drawings is concluded.

Test procedure: The draft frame was distributed for comments.

3. TFMC fabrication

The fabrication of the TFMC and ISC was supported by acceptance leak testing and sensor testing [7].

Literature:

- [1] P. Libeyre, P. Decool, J. L. Duchateau, H. Cloez, A. Kienzler, A. Lingor, H. Fillunger, R. Maix, A. Bourquard, F. Beaudet, NbTi superconducting bus bars for the ITER TFMC, Proc. 21st SOFT, Madrid, 11 – 15 September, Spain
- [2] V. Marchese, S. M. Darweschad, G. Nöther, A. Ulbricht, F. Wüchner, Circuit analysis and control of the power supply system for testing of the ITER TF model coil, Proc. 21st SOFT, Madrid, 11 – 15 September, Spain
- [3] J. L. Duchateau, H. Fillunger, S. Fink, R. Heller, P. Hertout, P. Libeyre, R. Maix, C. Marinucci, A. Martinez, R. Meyder, S. Nicollet, S. Raff, M. Ricci, L. Savoldi, A. Ulbricht, F. Wüchner, G. Zahn, R. Zanino, Test program preparations of the ITER toroidal field model coil (TFMC), Proc. 21st SOFT, Madrid, 11 – 15 September, Spain
- [4] R. Heller, Quench analysis for safety purposes, 11th Test & Analysis Meeting, Forschungszentrum Karlsruhe, March 20, 2000
- [5] R. Meyder; R. Heller, Behavior of a superconducting magnet, with the conductor built into plates, during quench and subsequent fast discharge, Proc. 21st SOFT, Madrid, 11 – 15 September, Spain
- [6] S. Raff, P. Schanz, H. Fillunger, B. Glaß, Structural analysis and verification of the ITER TF model coil test conditions, Proc. 21st SOFT, Madrid, 11 – 15 September, Spain
- [7] H. Fillunger, F.H. Hurd, G. Zahn, A. Ulbricht, P. Libeyre, E. Theisen, F. Beaudet, ITER TF model coil assembly, commissioning and instrumentation, Proc. 21st SOFT, Madrid, 11 – 15 September, Spain

Staff:

A. Augenstein
H. Bai (till Nov. 26, 1999)
S. Darweschad
G. Dittrich
P. Duelli
W. Eppler
S. Fink
G. Friesinger
A. Götz (till 31. 12. 1999)
A. Grünhagen
R. Heller
W. Herz
P. Hutapea (till June 30, 2000)
R. Kaufmann
A. Kienzler
O. Langhans
W. Lehmann
V. Leibbrand
V. Marchese
W. Maurer
I. Meyer
J. Müller (since May 1, 2000)
G. Nöther
U. Padligur
P. Rohr
G. Schleinkofer
V. Schulmeister (since July 1, 2000)
K. Schweikert (till August 31, 2000)
E. Specht
H.-J. Spiegel
M. Süßer
A. Ulbricht (for 2)
D. Weigert
F. Wüchner
G. Zahn (for 1, 3)
H.P. Zinecker
V. Zwecker

M 31 Development of 60 kA Current Leads Using High Temperature Superconductors

Introduction

According to the European Fusion Technology Programme, the Forschungszentrum Karlsruhe and the Fusion Technology Division of the Centre de Recherches en Physique des Plasmas, Ecole Polytechnique Federale de Lausanne (CRPP-EPFL) are responsible for the design and construction of a 60 kA current lead for the ITER Toroidal Field Coil system using high temperature superconductors (HTS) in the temperature range between 4 K and 77 K to reduce the steady state heat load at the 4 K level.

Results of stage B (test of the 20 kA HTS current lead)

The 20kA HTS current lead consists of an HTS part in the temperature range from 4.5 K to 70 K and a conventional copper part in the range from 70 K to room temperature. The HTS part is conduction cooled at 4.5 K and the copper part is actively cooled with 60 K helium. The 20 kA HTS module is constructed such to connect the two tested 10 kA modules (stage A-2 of the task) in parallel whereas for the copper part, a conventional heat exchanger of the Forschungszentrum Karlsruhe type is used. Figure 1 shows the completed HTS module including the copper adapters and the clamp contact.

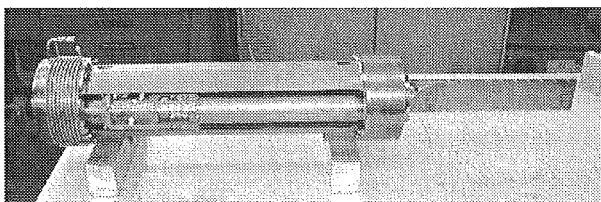


Fig. 1: The 20 kA HTS module including the Cu adapters and clamp contact

The test has been performed within a new collaboration at the National Institute for Fusion Science, NIFS (within the LIME project). There, a test cryostat constructed for testing model coils for the PF coils of the Large Helical Device, LHD, was used. One of the existing 30 kA vapour cooled current leads was replaced by the 20 kA HTS current lead, and both leads were connected by a superconducting bus bar consisting of a W 7-X prototype conductor. The first cooling and excitation tests were done for two weeks from the end of May 2000.

This HTS current lead is world's largest HTS current lead which succeeded in the excitation up to 40 kA. The operation up to steady-state currents of 20 kA was quite successful. No problems occurred during various tests and the results were reproducible. Short time tests up to 40 kA were performed without any problems for both the HTS module and the heat exchanger.

The steady state operation up to 20 kA, using different inlet temperatures and mass flow rates for the helium cooling of the conventional heat exchanger, shows that there were no problems for the HTS part as well as for the conventional heat exchanger.

The electrical resistance of the clamp contact was measured to be 6.6 nΩ, the resistance of the cold contact region is about 5.9 nΩ. Both numbers agree well with the measured losses. The resistance of the intersection region between the HTS modules and the heat exchanger including the screw contact was about

63 nΩ at 70 K, but more than 50 nΩ were due to the copper used in the heat exchanger. The total contact resistance inside the HTS module (averaged by power law) is about 3 nΩ, the corresponding ones between both modules and the copper adapters are 17.2 nΩ and 2.4 nΩ. Comparing these numbers to the ones extrapolated from the measured ones at CRPP for the individual 10 kA modules, one gets now larger values but in the same range.

The steady state losses at zero current were measured to be 6 W, i.e., much higher than expected from the two 10 kA HTS modules tested at CRPP (3.3 W). Measurements of the heat load for various He inlet temperatures results in background losses of the cryostat of about 2.6 W. Using a 2nd order polynomial fit to the data results in a nominal heat load of 3.5 W which is close to the expectations.

For the evaluation of the quench current of the HTS part, the temperature at the upper end of the module had to be increased to about 83 K. The quench test was done for different quench detection levels (up to 100 mV) and integration times (up to 1 s) for the quench detector. The measured quench current at 85 K is about 30 kA, twice as high as expected from single tape which is mainly due to the different (and much weaker) voltage level criterion used in this experiment.

Helium mass flow stop tests (LOFA tests) were done at 20 kA and 70 K and for different quench detection levels (up to 100 mV) for the quench detector to evaluate the safety margin of the current lead. The critical temperature measured in this test is about 90 K and agrees well with the results obtained in the quench current test. It took about 15 minutes to quench the HTS after the He mass flow rate was stopped. The time delay between a resistive voltage signal of 50 mV and 100 mV is about 8 s, between 10 mV and 100 mV even 12 s. Comparing this to the ITER scenarios, the measured time delay is well above these requirements.

Figure 2 shows the measured quench currents during quench test and LOFA test and the expected critical current of the HTS module as a function of temperature.

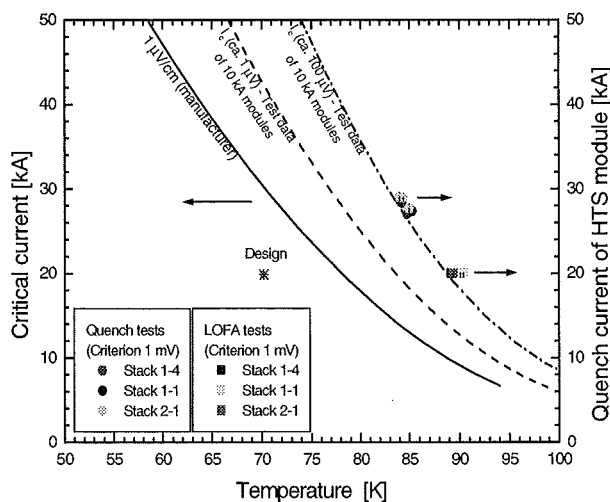


Fig. 2: Quench current of the HTS module as measured during quench test and loss of mass flow test and expected critical current of the HTS module as a function of temperature. The dashed lines represent the critical current for different criteria (from data of the single 10 kA modules).

Special tests were done at the end of the experiment, i.e., ramp rate tests up to 20 kA, 30 kA and 40 kA with 10 s flat top. It could be demonstrated that at about 60 K, the HTS current lead could be excited to 40 kA for 10 s without any problem neither in the HTS part nor in the conventional heat exchanger.

For the determination of the current flowing in each of the fourteen stacks, Hall sensors were positioned on the outer surface of each HTS module. It turned out that the current distribution is less homogeneous than measured at CRPP on the single modules as shown in Figure 3. This indicates that the current transfer from the heat exchanger to the two HTS modules is responsible for this imbalance and not the contact resistances between the individual stacks and the copper endcaps. The connection between the copper conductor of the heat exchanger and the the copper adapter in which the two HTS modules are soldered is done via a screw contact. The measured current distribution results in a current imbalance between the two modules of about 11800 A (module 1) and about 8200 A (module 2) at a total current of 20 kA. This ratio is rather independent on the transport current.

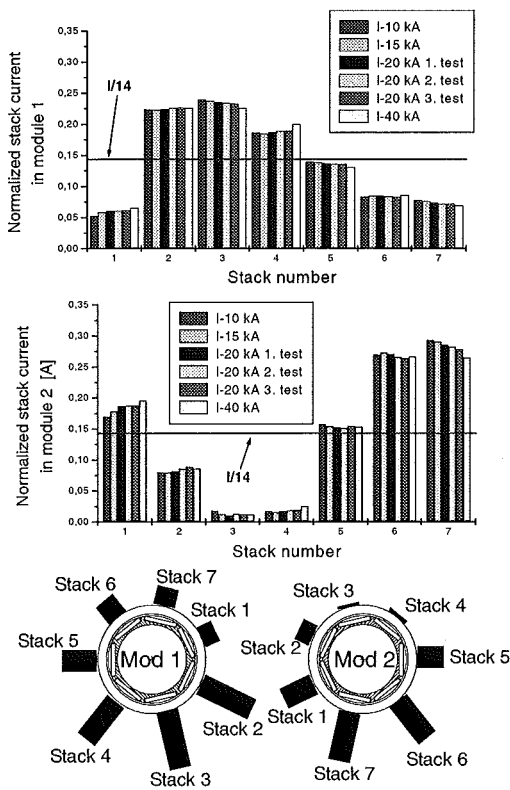


Fig. 3: Normalized stack currents of modules 1 and 2 of the 20 kA HTS module for different currents and location of the stacks within the HTS modules

If reaching the critical current of the HTS modules, there is a current redistribution. It is interesting that the redistribution takes place mainly between the two modules and not within the modules although the current imbalance in the modules is much larger than between them.

Summing up, the robustness of the HTS current lead was demonstrated. Of course some modifications of the design have to be done if going to 60 kA.

Design of a 60 kA HTS current lead

Because the tests of both individual 10 kA HTS modules as well as of the 20 kA current lead were very successful, it was

decided to use their basic layout and design parameters as a reference for the 60 kA HTS module, as critical current density, contact resistances, modular arrangement of the HTS tapes in stacks and use of stainless steel as support structure. Three different arrangements of the stacks have been considered.

The first layout is an extrapolation of the 20 kA HTS module: Five HTS modules of the same layout as for the 10 kA ones are arranged cylindrically resulting in 35 HTS stacks. This solution could be advantageous from the manufacturer's point of view because it minimizes the risk of failure of the whole HTS module during fabrication.

The second solution consists of two concentric rings of cylindrically arranged HTS stacks which form a very compact module. Due to the different stack numbers and maximum B_{\perp} in the inner and outer rings, the current distribution could be a problem even in steady state. This has to be considered during the design of the connectors between the HTS module and the conventional parts of the current lead.

In the third solution, 26 stacks are cylindrically arranged. The advantage of this design is manifold: The relatively simple manufacturing, the small angle between two adjacent stacks allowing a smaller B_{\perp} than in the other designs, the particular geometrical symmetry.

It is planned to continue in more detail as soon as the programme has been approved.

Design of a 10 kA HTS module using Bi-2212 tubes

As an extension to the development programme, an alternative design of a 10 kA current lead using Bi-2212 tubes clad with AgAu sheath is being investigated. This option was not available yet at the beginning of the task but has the advantage of being much cheaper than the tape option. Presently, two 5 kA tubes are being connected in parallel to form a 10 kA HTS module and will be tested at CRPP in October this year. During the test, two questions have to be answered, i.e., what is the safety margin in case of a quench (this was the main reason to use the tape option in the stages A-2 and B of the development programme), and what is the current balance between the two tubes in both steady state and transient operation.

Literature:

[1] M. Tasca et al., "Design of a 60 kA HTS current lead for the ITER toroidal field coils", presented at 6th Advanced Studies on Superconducting Engineering (ASSE 2000), Eger, H, July 1-9, 2000

[2] R. Heller et al., "Development Program of a 60 kA High Temperature Superconductor Current Lead for the ITER Toroidal Field Coils", presented at 21st Symposium on Fusion Technology, Madrid, Spain, Sept. 11 – 14, 2000

[3] R. Heller et al., "Test Results of a 20 kA Current Lead using Ag/Au stabilized Bi-2223 Tapes", presented at Applied Superconductivity Conference, Virginia Beach, VA, Sept. 17-22, 2000

Staff:

- G. Friesinger
- Dr. R. Heller
- M. Tasca
- S. Zimmer

M 45 (N 11 TT 15)
ITER Coil Casing and Intercoil Structures

Background of these investigation series are the 25 t casting of the ITER model 2 full size mock-up produced by Creusot Loire Industries (CLI), France and a thick section (80 mm) Type 316LN commercial plate steel product foreseen for the design of ITER Toroidal Field Model Coil (TFMC) intercoil structures. Within this context the materials cryogenic mechanical properties have been determined at 7 and 4.2 K with respect to tensile, fracture toughness (6 mm diameter EDM notched bar), and fatigue crack growth rate. For a delivered heavy weld metal consisting of 316LN plate material the cryogenic fatigue life properties were established. Besides, the low temperature friction coefficients necessary for the design of wedges between intercoil structures are determined. To investigate the possible cracking reason of the heat treated TFMC pancake consisting of Incoloy 908 jacketed conductor, heat treatment experiments were performed by recording the very low oxygen concentration levels at vacuum. In addition, the ongoing activities with the installation of a new cryogenic mechanical test facility comprising a 630 kN tensile unit are described.

Materials

The supplied materials for the cryogenic mechanical investigations and heat treatment experiments are given in following:

- A heavy block consisting of 316LN plate 80 mm thick material (produced by CLI) provided by Noell company. Material heat number is 60679 and the designation is C 516 (see. Figure 1).
- Several blocks were provided by EFDA from different spatial positions of the full size 25 t casting (produced by CLI).
- An 80 mm thick welded block (Type 316LN) with the MAG (metal arc gas) process was provided by Noell company under the designation of Fravit (see. Figure 2).
- Original superconducting cables (about 100 mm long) from the manufacturing route of the Incoloy 908 jacketed TFMC pancake.

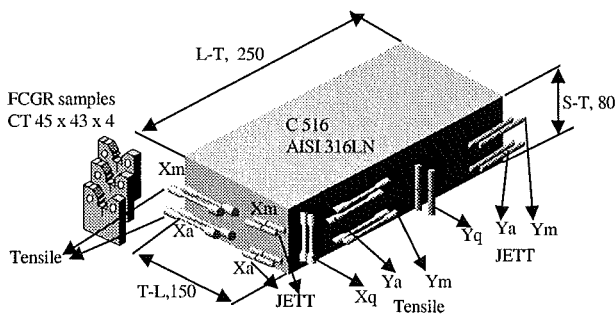


Fig. 1: 80 mm thick Type 316LN metal sample and the position of the machined specimens

The chemical compositions of the investigated intercoil base metal C516 are given in Table 1.

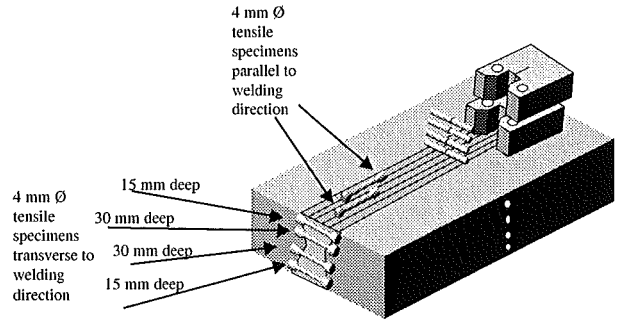


Fig. 2: 80 mm thick Type 316LN metal sample with a MAG weld metal and the position of the machined specimens inside the weld zone.

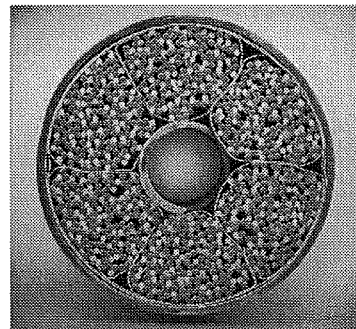


Fig. 3: Incoloy 908 jacketed superconducting cable in as received state

Table 1: Chemical composition of the investigated Type 316LN plate steel in weight %.

Mat. / Codes	C	Si	Mn	P / S	Cr	Mo	Ni	N
316LN C516	.020	.49	1.58	.027/ .008	17.18	2.53	11.89	.160

Results with 316LN base metal

Table 2 gives the results with the carried out tensile tests at 7 K. with respect to the 316LN plate material designated as C 516. The scatter of the results are so far small with a statistical average and standard deviation of 204 +/-7 GPa for Young's modulus and 1007 +/- 20 MPa for yield strength, respectively. The material shows also a homogeneous elongation in all three spatial orientations.

For the fracture toughness measurements of the 80 mm thick Type 316LN plate material the JETT (EDM notched round bar) method has been applied. In Table 2 all data obtained from the three spatial orientations are collected together and the measured J-Integral test results are converted to K_{Ic} corresponding to the crack plane orientation. The achieved values of K_{Ic} show homogeneous fracture toughness behavior of this investigated plate material. In addition, the obtained fracture toughness data fulfills the specified level of the common commercial Type 316LN plate materials.

Table 2: Tensile test results of Type 316LN 80 mm thick plate sample designated as C 516 at 7 K

Spec. orientation	E GPa	Yield MPa	UTS MPa	Un EL. %	Tot. EL. %
T-I	209	1051	1662	40	47
T-L, surface	193	1002	1631	43	50
T-L, mid plane	204	1000	1619	42	42
T-L, mid plane	206	1015	1641	40	40
S-T	210	1009	1551	38	38
S-T	211	1003	1616	43	49
L - T surface	210	991	1620	43	49
L - T surface	192	1026	1565	42	45
L - T mid plane	204	977	1614	44	52
L - T mid plane	198	994	1639	42	48

E = Young's modulus, yield = yield strength, UTS = ultimate tensile strength, EL= Elongation (Un = uniform, Tot = total)

Table 3: Fracture toughness test results of Type 316LN 80 mm thick plate sample designated as C 516 at 7 K with respect to different orientations

Specimen orientation	Critical J N/mm	K _{IC} MPa√m
T-L, surface	251	226
T-L, surface	306	250
T-L, mid plane	280	239
T-L, mid plane	255	228
S-T	232	218
S-T	246	224
L-T, surface	220	212
L-T, surface	296	246
L-T, mid plane	290	243
L-T, mid plane	259	230

The fatigue crack growth rate (FCGR) tests of the material was conducted using small compact tension specimens of the size 45 mm x 43 mm x 4 mm. Altogether three specimens were tested at 7 K. The results of these test are given in Figure 4. The drawn line gives the worse case of the investigated results and hence the Paris line coefficients are calculated using this trend line as $C = 2.1 \cdot 10^{-9}$ mm/cycle and $m = 3.15$.

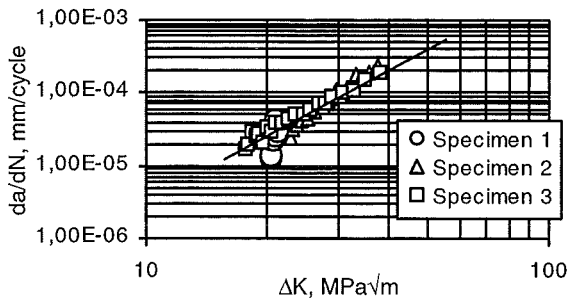


Fig. 4: Fatigue crack growth rate test results of the material C516 (Type 316LN) at 7 K and at R = 0.1.

Results with 25 t cast steel

Following the experiences of the trial casting with one ton weight produced by company CLI the casting for the model 2 as a final piece for the ITER mock-up were investigated in a similar way with respect to cryogenic mechanical tests given in the paper [1]. Table 4 gives the obtained cryogenic tensile results determined in different spatial orientations of this heavy sample.

Table 4: Results on tensile properties of 25 t cast steel mock-up between 4.2 K and 7 K

Size, mm & Temp. & Orientation	Young's modulus GPa	Yield strength MPa	UTS MPa	Uniform elongation %
4 Ø, 7 K, Y	159	944	1086	25
4 Ø, 7 K, Y	124	852	1055	40
12 Ø, 4.5 K He gas, Y	179	800	1231	26
12 Ø, 4.2 K, Y	173	870	1183	17
4 Ø, 7 K, Y	162	911	1216	33
4 Ø, 7 K, Y	176	847	1048	27
4 Ø, 7 K, Y	214	877	1060	20
4 Ø, 7 K, Y	168	869	984	20

As given, the Table 4 shows the results obtained with different size of specimens. In fact, the measurements are carried out also between 7 K and 4.2 K resulting no significant differences of the major engineering tensile behavior. For a final judgement, the average of all results with respect to trial casting (1 t) and the 25 t casting were compared considering the spatial orientation. The results shows so far that the yield strength variation regarding the orientation is less significant for the final casting. Also the Young's modulus values are more homogenous and higher in case of the 25 t mock-up. The fracture toughness properties at 7 K are also improved in case of the final casting.

In addition, the cast stainless steel showed no anisotropic behavior of the FCGR data. The measurements carried out at 7 K show for the casting material a superior FCGR behavior compared with other alloys even compared to the aged Incoloy 908. The fatigued surface appearance of the tested cast steels differ also considerable from the 316LN type structural steels. The high resistance against the cyclic loading with respect to crack growth can be attributed to the completely different microstructure owing to the big grain sizes, a common feature of cast steels.

Results with 80 mm thick MAG weld metal

The welded 80 mm thick weld metal sample (Fravit) showed after specimen machining (see Fig. 2) several weld process related defects. The X-ray diagnostics of the compact tension specimens showed in both long and transverse weld orientations statistical distributed defects in the entire weld metal (pores and flaws). To check the weld metal performance in as received condition it was decided to perform fatigue life measurements at 7 K with the already machined common standard 4 mm Ø tensile specimens. All fatigue life tests were carried out in a temperature variable helium flow cryostat equipped with a MTS servo hydraulic unit of +/- 25 kN load capacity. The tests were performed at a load ratio R (P_{min} / P_{max}) of 0.1 and at 7 K. Prior to the test of specimen No 2 the stress - strain behavior of the weld metal was measured with loading and unloading of the specimen twice up to 1 % strain. This tensile measurement resulted a yield strength value of 1119 MPa. The yield strength of the weld metal with 1119 MPa shows that the weld metal has a considerable higher strength compared to the base metal of Type 316LN. Therefore the thread section (with a cross section of 15.9 mm²) of specimens

machined from transverse weld orientation and consisting of base metal is assumed to be the weak link of the system which could be confirmed by the tests. All specimens were directly cyclic loaded to the envisaged stress level and the cyclic load was held constant throughout the experiment. The plotted data with respect to stress versus cycle number in semi logarithmic scale confirm the following findings: Between the transverse and long orientation specimens there is an obvious tendency indicating that the transverse specimens cyclic life are inferior to the longitudinal specimens life. This can be attributed to the following circumstances; the longitudinal specimens consist of pure weld metal having higher yield strength values compared to the base metal and therefore this implies to a higher fatigue life. Contrary to that, the thread region of the transverse specimens consist of base metal and therefore these specimens are weaker compared to the specimens with pure weld metal. These tests are also not comparable with smooth section standard fatigue life specimens because of the failure of specimens at early stages due to the severe thread region. However, even with the existing high concentration stress at the thread region the material could resist stresses of circa 600 MPa for > 100 000 cycles at 7 K.

Results with heat treatment investigations on Incoloy 908

During the heat treatment of the TFMC pancake consisting of Incoloy 908 jacketed conductor large SAGBO (Stress-Accelerated-Grain-Boundary-Oxidation) related cracks [2, 3] were observed after the process. Despite the precautionary measures including shot peening of the outer jacket surface and keeping the oxygen content during the aging at 650°C below the 0.1 ppm level several longitudinal cracks were formed thus resulting to a rejection of the fabricated pancake. To investigate the oxidation conditions of the cable a measurements program has been started at Forschungszentrum Karlsruhe comprising heat treatment tests carried out in a resistance furnace specially installed for the aging process. The conductor or jacket samples were placed in the temperature constant zone (+/-0.2 K) of an one side closed 150 mm diameter quartz tube. A turbomolecular pumping device maintained a vacuum of $3 \cdot 10^{-4}$ hPa at the process temperature of 923 K inside the quartz tube. The pressure was measured at the outlet, near the pumping unit and could be maintained constant throughout the process. The oxygen concentrations and the temperature was measured in situ directly at the vicinity (circa 10 mm apart) of the specimens using a high precision commercial gauge (Zirox Company, Greifswald, Germany) based on zirconia emf cell capable of measuring oxygen concentrations lower than 10^{-20} ppm between 873 K and 1273 K. The aging process started after a temperature ramp up to 923 K and holding this temperature constant for the rest of the time. However, the oxygen could be recorded starting from 873 K. Oxygen content in ppm versus time data were acquired for several sample combinations, such as original as received non heat treated TFMC sample (Fig. 5) or Incoloy 908 jacket removed from the superconductor strands and calibration tests with empty furnace.

The measured initial oxygen concentration of $\sim 1 \cdot 10^{-13}$ ppm (Fig. 5) refers to an oxygen partial pressure of $\sim 1 \cdot 10^{-21}$ hPa (or $\sim 1 \cdot 10^{-25}$ MPa or $\sim 1 \cdot 10^{-24}$ bar) accounting to the pressure of $3 \cdot 10^{-4}$ hPa at the furnace outlet (with respect to air as reference of 210000 Vol ppm oxygen). The initially extremely low oxygen partial pressure is related to the rapid reaction of the oxygen with alloy constituents forming the reaction products (oxidation). This can be confirmed by the equilibrium oxygen partial pressures at 923 K of chromium and nickel according to the thermodynamics yielding for pure substances (chemical activity equal to unity) $\sim 10^{-33}$ MPa and $\sim 10^{-17}$ MPa, respectively. The nickel equilibrium oxygen partial pressure are thereafter much higher than the measured oxygen content by the emf cell. Therefore, in this initial stage of the aging the majority of the oxygen gas in the furnace atmosphere are involved with the

oxide formation of the nickel surface and the emf cell region was oxygen depleted (low oxygen ppm) as the measurement shows. The oxidation phenomenon at the surface of the Incoloy 908 forces the diffusion of the oxygen along the grain boundaries of the material. The drastic increase of the measured oxygen concentration to ~ 2 ppm (or $\sim 3 \cdot 10^{-13}$ MPa) after a certain time at 923 K shows that the oxidation process is almost stopped and the equilibrium between the alloy constituents and oxygen partial pressure is maintained during the remaining aging time. The higher content of the oxygen is most probable given by the furnace system (leaks, pumping unit or else). These in situ measurements could verify these phenomena owing to the capability of the oxygen content determination at the very site of the aged alloy.

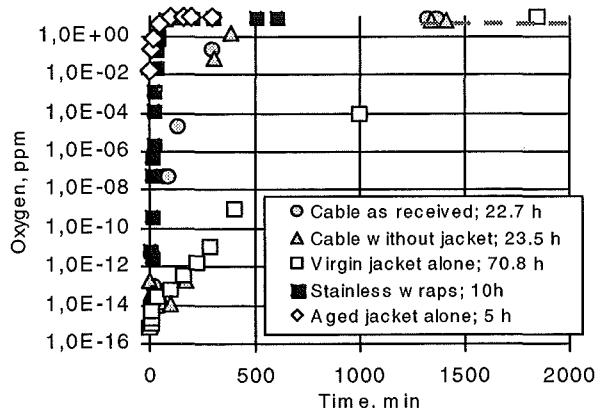


Fig. 5: Oxygen content versus time diagram obtained for different samples during the 650° C aging process in a vacuum emf cell monitored furnace system up to 2000 minutes. The dotted line at the far right gives the oxygen content of the empty furnace at 650° C as reference.

As shown in Fig. 5 the oxygen take up kinetics of the Incoloy 908 material in form of a jacket (tube) is very slow and takes several thousands of minutes up to thermodynamic equilibrium. Here the Incoloy 908 material determines the kinetics of the take up. Stainless steel structures (wraps) or an already aged Incoloy 908 tube (saturated with oxygen) reach in a very short time their thermodynamic equilibrium. The stainless steel reaches at around ~40 minutes whereas the once aged jacket structure reaches within some minutes the equilibrium. Cable without the jacket which consist of chromium plated superconducting strands or as received cable (complete cable including the jacket) show almost the similar kinetic behavior because the oxygen partial pressure conditions are determined by the chromium. However, this means that the oxygen gas still will diffuse through the jacket material (~ 2 ppm after ~ 500 minutes) because of the high partial pressure. This concludes that the origin of the cracks observed in the Incoloy 908 pancake are a combination of an initial welding residual stresses and oxidation during the aging. Investigation of the oxidation indicates a fully penetration of the oxygen inside the jacket metal. A safe manufacturing of thin Incoloy 908 jacket would need first an understanding of grain boundary diffusion mechanism and setting up conservative actions to avoid it.

Determination of friction coefficient at 7 K

For the design of the ITER intercoil structures the necessary friction coefficient between plasma nitrided surfaces and machined 316LN material pairs were determined using a developed novel device capable to measure the axial and transverse forces during pressing of different material combinations. The obtained results show a decrease of the

friction coefficient from an average value of 0.3 at 300 K to 0.25 at 7 K for the above given material combination.

Installation of a new cryogenic test facility

The need of axial fatigue life tests with ITER central solenoid superconductor jackets half size cross section necessitate the use of servohydraulic machines with high load capacity. The target conductor jackets cross section of about 1000 mm² require a cyclic peak load of 1000 kN considering the upper point of S-N curve to be around 1000 MPa. This high load restricts the to date worldwide existing machines considerably, because most machines have limiting load capacities approximately around 200 - 100 kN. The problem is in the reality not so much the tensile testing machines but the 4 K rig's. So e. g., the existing 1200 kN machine at Breda Scientifico, Milan has the load capacity but the 4 K rig is placed into an open dewar, which will lead to high liquid helium losses due to the non existing helium recovery system. Therefore at Forschungszentrum Karlsruhe, it was decided to use the existing 630 kN servo hydraulic machine for such a task. The present 630 kN four column testing machine was in recent years part of the FBI test facility. To keep the FBI facility with the 100 kN capacity rig in its original state the mechanical screw driven test machine (200 kN) of the materials testing laboratory was moved to the FBI site. At present state the 630 kN machine is positioned at the former site of the mechanical testing facility after structural reinforcement of the platform. The machine's control unit is foreseen for modernization with a new electronic control system. All necessary orders are placed and according to the present time schedule the new facility will be able to work at the end of 2000.

Literature:

- [1] Nyilas, D. R. Harries, and G. Bevilacqua, "Status of European Testing Program for ITER Model Coils and Full Size Mockups", Adv. in Cryo. Eng. (Materials) 1999, Volume 46A, p. 443- 450
- [2] M. Morra et al., "Incoloy 908." A low coefficient of expansion alloy for high strength cryogenic applications", Part 1 – Physical Metallurgy, Met. Trans. A., December 1992, pp. 3177-3192.
- [3] P. Libeyre et al., "Risks and benefits of Incoloy 908", To be published at Proc. 21th SOFT, Madrid, Spain, Sept 11 – 15, 2000.

Staff:

A. Nyilas
H. Kiesel

T 400-1/01
TF Model Coil (TFMC)

Subtask : 3d Quench Analyses with the Code System MAGS

To investigate the effect of 3d heat conduction during quench at a delayed shut down a set of 3+1 pancakes of the Toroidal Field Model Coil (TFMC) was analyzed [1]. The pancakes were selected such that heat conduction between pancakes in the same radial plate and heat conduction between pancakes in different radial plates could be investigated. The fourth pancake is to provide undisturbed boundary conditions for the Helium flow analysis outside of coil. The shut down delay time was varied between 1 (s) and 10 (s) after quench initiation.

The analysis has shown that 3d effects within one pancake, i.e. between the turns of the same pancake, are negligible here. This is because eddy currents and radial plate heating is considered, providing larger heat fluxes to the downstream turns than the fluxes due to turn to turn conduction. Also heat conduction between the pancakes in the same radial plate is not important. One reason is that for the adjacent pancake quench propagation takes place via the inlet joint, causing such disturbances that effects due to transversal heat conduction are not to be seen. Another reason is the high current. This leads to a sharp temperature ramp and gives not sufficient time for heat conduction to become effective. Heat conduction to the pancake in the other radial plate is even less effective because of the insulation layer between the plates.

In terms of quench propagation the analysis has shown that propagation via the inlet joints within a radial plate is a reliable effect. Quench propagation via the manifold is also possible and will occur in TFMC if dump is considerably delayed.

Literature:

[1] R. Meyder: Report on four pancake analysis, TF Model coil
October 1999

Staff:

R. Meyder

**T400-1/01
Stress Analysis for the TFMC Tests in TOSKA**

Under this task finite element electromagnetic and mechanical stress analysis is performed to prepare, support and evaluate the Toroidal Field Model Coil (TFMC) tests in TOSKA (Task M44).

The work to perform test predictions starting in the last period [1] was continued. The mechanical model used during the test design [4] was modified to meet the final design and extended concerning the supporting structure of the test assembly. First the predictions for the TFMC tested alone (single coil test) being the first test step were calculated [2,3] for the maximum current of 80 kA. As expected, the stress level in this test is lower than in the two coil test and reaches a level of about 40%. The deformations of a coil slice are shown in Fig. 1.

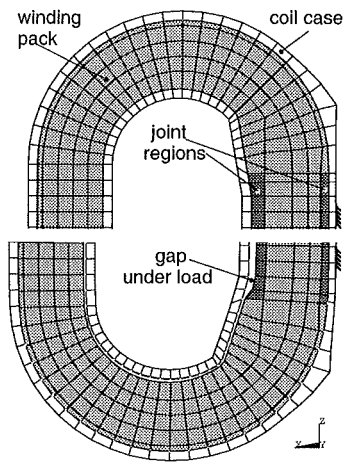


Fig. 1: Single coil test (80 kA): undeformed (top) and deformed (bottom) coil slice

A special aspect of the analysis was the effect of friction between winding pack and casing on the coil behaviour. So far in all predictions perfect sliding was assumed which should be pessimistic concerning the winding pack. But during the test the real friction behaviour may have some influence on the stressing of the different coil parts, especially on the joints which were recognized to be critical during the design phase. Since the actual friction parameter is unknown a parameter study with limiting friction values was done to get its importance. E.g. the uttermost influence on the coil part with the joints could be an elongation reduction of about 30%.

Before the tests the predictions for the quantities going to be measured have to be assembled in the 'Test and Analysis Summary Report' [5] being in preparation. Our contribution is to give predictions for the mechanical sensors mounted on the outer coil case surface shown in Fig. 2. By post processing the results this has been done for the single coil test. But it could only be done using the above mentioned friction as parameter and the question arises, whether the measured values will allow for a determination of the actual friction behaviour. This was discussed in some detail in [3].

In preparation of the two coil tests further analyses concerning the highly loaded side wedge is being done. Although, as reported in [4], local plastic deformations occur on that side wedge the load bearing capacity of the wedge was judged to be not exceeded since it was shown by a submodel investigation that the plastic deformations will not accumulate during cyclic loading. But the used FEM model has some deficiencies

concerning the applied coil loading and possible load redistributions caused by plastic deformations. Therefore an extended submodel shown in Fig. 3 is under investigation. Compared to the previous model a quarter of the coil was added allowing for a better simulation of the load transfer between coil and wedge for varying load and plastic deformations.

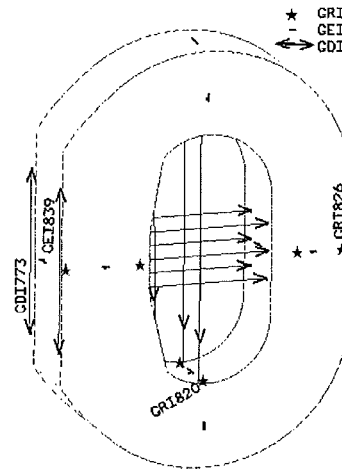


Fig. 2: Mechanical sensors on the coil case: uniaxial strain gauges (GEI), rosettes (GRI) and displacement devices (GDI)

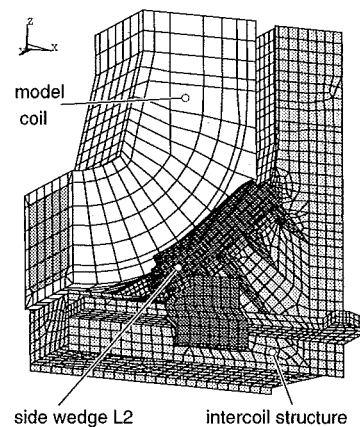


Fig. 3: Submodel with the highly loaded side wedge for plastic analysis

Literature:

- [1] 'Nuclear Fusion Annual Report of the Association FZK/EURATOM, October 1998 – September 1999.
- [2] S. Raff, 'Stress Analysis for the TFMC Tests in TOSKA – Global Model Analysis for the Single Coil Test, Internal Report IRS / PKF , Dec.1999.
- [3] S. Raff, P. Schanz, H. Fillunger, B. Glaßl, 'Structural Analysis and Verification of the ITER TF Model Coil Test Conditions', Proc.21th SOFT, Madrid, Spain, 11-15 September, 2000.
- [4] B. Glaßl, 'Structural Analysis of the Inter Coil Structure ICS by a 3D FE Programme (Load 70/16 kA), Final Report, AGAN Technical Report TR-NO-004, Consortium AGAN, February 1998.

[5] Ulbricht ed. 'Test and analysis summary report (Testing Handbook), report in preparation.

Staff:

G. Hallfinger

S. Raff

P. Schanz

T 400/1-01a Test of the ITER Model Coils, Contribution to the Test of the ITER Central Solenoid Model Coil (CSMC)

The goal of the Task is the participation of members of the European Home Team (EUHT) in the installation and test of the CSMC as well as application of existing and new developed codes for the evaluation of the test results. The Task shall assure the transfer of experience of the CSMC test to the EUHT.

The Forschungszentrum Karlsruhe is involved in the following fields:

- Assessment of the cryogenic system and the operation during testing of the CSMC
- Behaviour of the CSMC against transient voltages

1. Behaviour of the cryogenic system and the operation during beginning of testing of the CSMC

The participation in the test from Forschungszentrum Karlsruhe covered the period after an interrupted cool down and the start of the current tests after second cool down.

The first cool down had to be interrupted because a leak opened at the 20 K temperature level. One staff member supported JAERI staff over a time of 3 weeks in the localization of the helium leak.

After the second cool down one staff member participated in the start-up of the current test. The CSMC was energized in steps to 50, 80 and 100 % (46 kA) at a magnetic field up to 13 T. After each step the coil was ramped down and in a second step a safety discharge with a time constant of $\tau = 20$ s was performed. Most of the stored energy (99.8 %) was transferred into the dump resistor during the safety discharge. The cooling system was not disturbed.

After 100 % current was reached and the coil stable operated at nominal current, current sharing measurements were performed by the injection of heated gaseous helium slugs. Due to the powerful refrigeration system with a cooling capacity of 5 kW there was no restriction of the heater power used to generate He at current sharing temperature T_{csh} .

For the T_{csh} measurements, the He inlet temperature of layer 1 and 2 of the inner module was increased slowly at constant conductor current of 46 kA until current shearing voltage could be observed at a temperature of 7.2 K. At a voltage level of 600 mV the coil was manually dumped without a quench. The impact on the cryogenic system was negligible.

This test was repeated with a conductor current of 40 kA and a temperature up to 9 K. Shortly after the manually dump the coil quenched with a large influence of the refrigerator system because of the heat input caused by the quenched conductor.

The experiences gained during this test period will be used for planning and testing of the TFMC in TOSKA. The developed code (Multi conductor MITHRANDIR) for the TFMC test was already validated during the CSMC test.

The lower refrigeration power of 2 kW of the TOSKA facility has to be taken into account by the selection of the current sharing measurement parameters.

2. Behaviour of the CSMC against transient voltages

Counteracting switches are applied in the dump circuits of superconducting coils if the discharge voltage comes in the range of 5 kV. Fast capacitor discharges generate fast voltage transients across magnet winding which can lead to non-linearities of the voltage distribution in the winding. This effects were studied by an electrical network model for the ITER TF full size coil and the TFMC.

A network model for the CSMC is under development in collaboration with Institut für Energiesysteme und Hochspannungstechnik (IEH) of the University of Karlsruhe.

Assuming a linear behaviour of the coil a low voltage pulse generator with pulse rise times down to 1 μ s was constructed and tested for experimental investigation of the ITER model coils and validation of the network model codes.

Staff:

S. Fink
W. Herz
A. Ulbricht
G. Zahn

T 405-2/01 Conductor Layout and Optimization

The task has the objective to improve the performance and to find means to reduce the costs of the ITER conductors which means to use more effectively the current carrying capacity of Nb₃Sn and NbTi. This requires a better quantification of the actual current behaviour inside large cable-in-conduit conductors as well as qualification tests of new layouts. The related work program is divided into two parts: (i) investigations on the impact of end and self field effects and (ii) conductor optimization tests considering the tolerance of broken strands, the impact of transverse resistivity, the potential of separating copper from the superconducting strands.

In the stability experiment SeCRETs in SULTAN, CRPP, two cable-in-conduit conductors (CICC) are investigated considering the effect of additional copper strands besides the Nb₃Sn strands.

For having a data base about this conductors to evaluate and assess the experimental results of the SeCRETs experiment, four conductor samples, two of each type were investigated in the high field test facility FBI at Forschungszentrum Karlsruhe.

The specified test program of the samples was as follows:

- I_c versus B curve at 0 applied load, starting from 14 T, decreasing the field in steps of 0.5 T as long as the range of the power supply allows it
- I_c versus ϵ curve at 14 T applied load, in loading steps < 0.05%
- Load versus strain curve (taken during the I_c versus ϵ)

The measurements were performed. The Final Report was submitted to EFDA July 2000. The Task was concluded.

1. Conductors tested

Two conductors, A and B, are manufactured by VNIINM (Moscow) with different layouts. Conductor A is a typical ITER last but one cable stage, with all stabilizing material copper included in the superconducting strand cross section. Conductor B has the identical non-Cu cross section and almost identical Cu cross section by adding pure copper strands. The Cu:non-Cu is reduced in the superconducting strands and the number of cable stages is three instead of four [1].

From each type of conductor two samples (SeCA1/2) and (SeCB1/2) have been prepared and heat treated for 150 h at 575 °C and 200 h at 650 °C at CRPP. After the reaction heat treatment the samples were completed with terminal grips for force and current transmission.

2. Results

2.1 Critical current versus magnetic field

The I_c versus B results of all samples tested without strain are summarized in Fig. 1. The big scattering of the data of the two identical A- and B- type samples may reflect the different care during sample preparation and / or reaction heat treatment. According to the basic strand test at the University of Twente the A- and B- type samples should have the same I_c data.

2.2 Strain dependence of critical current

The typical I_c versus ϵ characteristic shows Fig. 2. The numbers attached to the curve represent the sequence of testing under loaded and unloaded conditions. First I_c was measured at $\epsilon = 0$

(10) ($I_{c0} = 6.47$ kA), then under load up to (29) and without load at (30) where plastic deformation amounts to 0.61 %. The sample was then loaded again up to (32) and

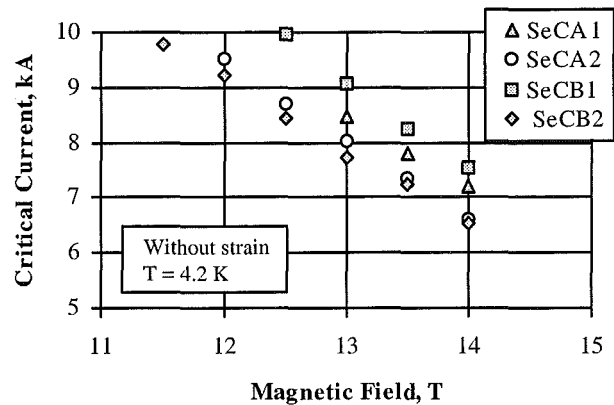


Fig. 1: Field dependence of critical current without applied strain of all samples

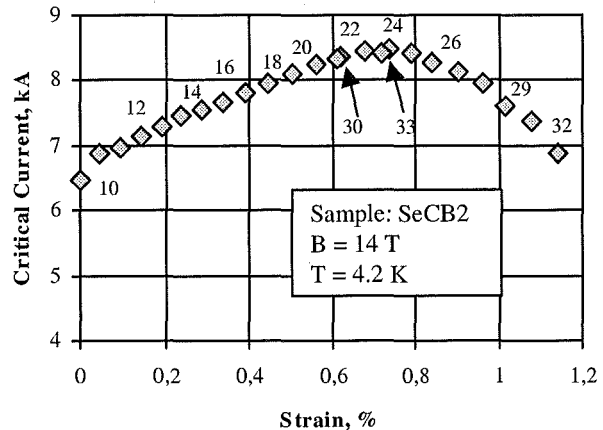


Fig. 2: Critical current as function of applied axial strain of conductor SeCB2

unloaded at (33). The peak, $I_{cm} = 8.49$ kA, occurs at a prestrain of $\epsilon_m = 0.74$ %, where the stress on the Nb₃Sn filaments is expected to be zero or a minimum. The pre-strain results mainly from the difference in thermal stress between 316L conduit (and copper) and the filaments during cool down from reaction to liquid helium temperature. The ratio I_{c0} / I_{cm} is a measure of critical current degradation due to pre-strain. It amounts to $0.70 - 0.81$ at $B = 14$ T for these conductors. Former investigations reveal $I_{c0} / I_{cm} \approx 0.5$ at 13 T [2] and should be even lower at 14 T, since I_{c0} / I_{cm} decreases with increasing magnetic field based on the strand results [3], the I_{c0} data obtained in this work seemed to be reasonable, which means that I_{cm} values are too low. The reason for this behaviour is not clear. One possible explanation could be that the axial loading of the conductor release the internal stress (axial and / or radial) on the Nb₃Sn filaments of this complex cable 144 / 122 strands is less effective than at more simple composed cables (3 x3 x4 strands in [2]).

2.3 Stress – strain curve

The stress - strain characteristic at 14 T and 4.2 K of the sample SeCB2 is shown in Fig. 3 and is representative for all samples. The stress is related to the total conductor cross section including voids. The run numbers attached to the curve correspond to those of I_c versus ϵ plot Fig. 2. Under these conditions the Young's modulus (E) and the yield stress (σ_y) amount to about 70 GPa and 220 MPa, respectively.

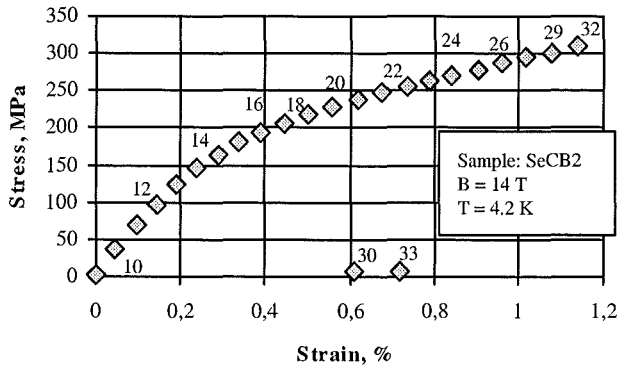


Fig. 3: Stress – strain curve at 14 T and 4.2 K of conductor SeCB2

2.4 Conclusions

The big scattering of the of the I_c versus B data reflects the difficulty of preparing identical samples. The results with respect to pre-strain (ϵ_m) confirm former experiences, however the max. critical current (I_{cm}) is too low in this work. Investigations at conductors with similar parameters but smaller number of strands and more simple cable configuration may clarify this problem.

Literature:

- [1] P. Bruzzone et. al., Characterization tests of the Nb₃Sn cable-in-conduit conductors for Se.C.R.E.T.S, Proc. MT-16 Sept. 26 –Oct. 1, 1999, Jacksonville, FL, USA
- [2] W. Specking, H. Kiesel, Acceptance test of strands and sub-stage CICC's with respect to heat treatment of TFMC pancakes, Final Report, ERB 5004CT9700B2, June 1999
- [3] P. Bruzzone, CRPP, private communication

Staff:

W. Specking
H. Kiesel

Materials Development

T 228.1 Influence of Higher Hydrocarbons on Vacuum Pumping

Higher hydrocarbons have systematically been found in the fusion exhaust gas of tokamaks with graphite first wall materials. The formation of these substances may be explained by radiochemical reactions, induced by β -radiation emitted by the tritium. The presence of higher hydrocarbons in the ITER-FEAT exhaust would necessitate highly demanding regeneration techniques of the cryosorption panels and it should therefore be kept at a minimum level. Moreover, as the pumping speed performance of the cryopump provides a considerable contingency with respect to what is required for ITER-FEAT, a certain poisoning effect can be tolerated, thus requiring less frequent high temperature full regeneration, which is the ultimate regeneration stage within the three-stage concept developed for ITER-FEAT [1].

To assess the regeneration conditions in detail, experiments were performed using an ITER-FEAT cryopanel mock-up in the component test facility TITAN, which was upgraded so as to be able to inject defined quantities of liquid substances into the vacuum vessel. As the production mechanisms of potential higher hydrocarbons are still not yet well understood, a broad range of gas loads was investigated. The panel was preloaded in the range of up to $0.1 \text{ Pa}\cdot\text{m}^3/\text{cm}^2$. Due to the complicated transport path between the first wall region and the cryopump, the arrival of hydrocarbon species from the torus on the cryopanel becomes less probable with increasing molecular weight. On the other side, the regeneration problems are more drastic for high-boiling substances. Thus, to detect the operation limits of the pump, two untypically heavy hydrocarbons were used for the poisoning tests, namely n-hexane and i-octane. Pumping speed tests were performed with two different ITER exhaust model gas mixtures, so as to simulate DT-shot and H_2 -shot conditions. The measured pumping speed decreases due to the accumulated gas load are illustrated in Fig. 1. It is revealed that the poisoning influence of water and n-hexane is quite moderate, but i-octane causes drastic pumping speed losses. However, it should be noted that such large molecules are contained in the exhaust gas only to a very little percentage, if at all. The test results obtained in the TITAN facility will be cross-checked at the level of the model pump within the upcoming TIMO test programme (Task VP 1).

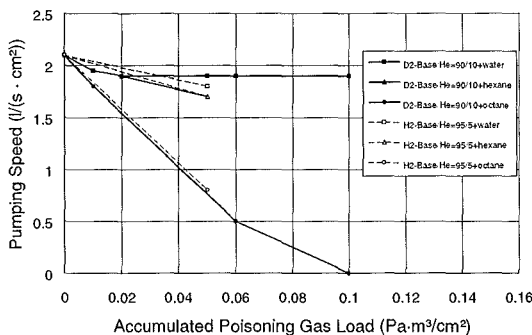


Fig. 1: Poisoning effects of higher hydrocarbons on pumping of two different model gas mixtures, comprising hydrogens and helium as indicated. The water results are given for comparison [2]

To assess the impact of the pumping speed curves plotted in Fig. 1, they have to be related to the actual gas compositions (impurity contents) and flow rates encountered in ITER-FEAT. For a typical scenario [3], 17 allowable pumping cycles with only 85 K regeneration in between are obtained. The 50% decrease

in pumping speed (which is just the contingency compared to what is required for ITER) accompanied with that is caused by poisoning due to air-likes with 30% and owing to the hydrocarbons with 20%, whereas the water influence is negligible. After the 17 cycles a complete regeneration may be initiated. An only 300 K regeneration step performed at that point of time would release the air-likes and still allow for 7 more cycles to follow. The longest pulse of 3000 s presently foreseen for ITER-FEAT operation corresponds to only 4 consecutive pump cycles. This illustrates the large margins and flexibilities available in the cryopump system, thus offering enough time to regenerate earlier than necessary from the poisoning point of view to allow for reducing the tritium inventory [1].

Literature:

- [1] D.K. Murdoch et al.; Tritium Inventory Issues for Future Reactors; Choices, Parameters, Limits, Fusion Engineering and Design 46 (1999) 2-4, 255-271.
- [2] Chr. Day et al.; The influence of water on the performance of ITER cryosorption vacuum pumps, Proc. ISFNT-5, Roma, Sept. 1999.
- [3] Chr. Day et al.; New operational aspects of the ITER-FEAT primary vacuum pumping system, 21st SOFT, Madrid, Sept. 2000.

Staff:

Chr. Day
A. Edinger
B. Kammerer
A. Mack
R.-D. Penzhorn

Fuel Cycle

VP 1 Cryopump Development and Testing

1. Introduction

The final acceptance tests with the ITER-FEAT-model pump have been performed in the test facility TIMO. Travelling time, positioning accuracy and leak rate of the main valve were checked. The cryogenic consumptions of the 5 K and the 80 K circuits were determined. Pumping cycles with pure gases have demonstrated the pumping behaviour under different throughputs, valve positions and loading capacities.

Parametric tests with ITER-FEAT-relevant gas mixtures using the 700 l cryostat have also been started.

On the basis of the pumping and regeneration tests performed in TITAN pumping scenarios for the future ITER-machine were developed.

The COOLSORP facility for qualification of charcoal materials at cryogenic temperatures (5 – 15 K) has started its operation.

The components for upgrading the TIMO-facility have been prepared.

2. Final acceptance tests

The objective of the final acceptance tests was the verification of the contractual design values during certain specified operating conditions [1].

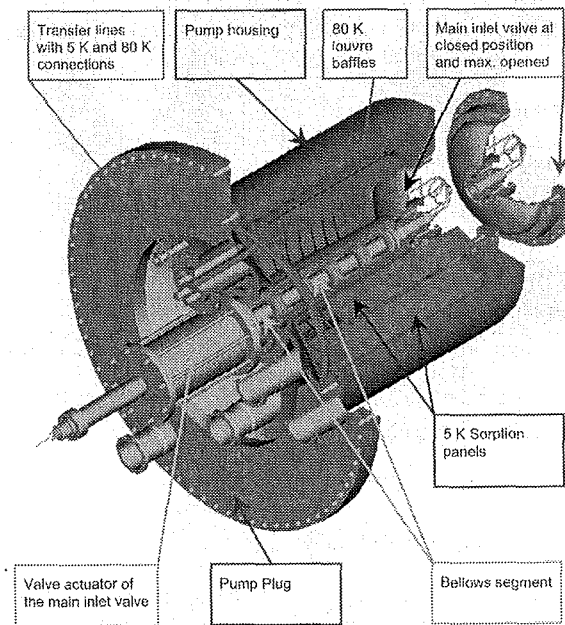


Fig. 1: 3D view of ITER model pump

2.1 Main valve

The combined regeneration and throttling valve at the pump inlet is an integral part of the pump assembly (see Fig. 1). A travel time of less than 10 s is specified in order to adapt pump performance to fluctuations in divertor pressure and exhaust gas flow rate.

The specified pressure range of 0.1 – 10 Pa over which pump throughput is to be held constant by throttling, requires a positioning accuracy of ± 1 mm over the total stroke of 400 mm.

The valve disc is cooled with 300 K water to avoid heating up by the 450 K hot walls of the test vessel which simulates the divertor duct of the ITER-FEAT. During closed position a metallic HELICOFLEX HND 229 sealing with a diameter of 700 mm is used to achieve the specified leak rate of 10^{-3} Pam³/s. With 10 KN force of the pneumatic actuator a leak rate of 10^{-5} Pam³/s at a pressure difference of 2×10^3 Pa was measured which is well below the design value.

2.2 Cryogenic supply rates

The requirements of the maximum allowable heat loads to the 80 K circuit and the 4.5 K circuit are a criterion for the quality of the insulation and consequently for the consumption of the cryogenic fluids [2].

The heat loads were determined by the enthalpy difference of the 4.5 K supercritical Helium flow and the 80 K gaseous He flow. To include the heat losses in the cryotransfer line with a total length of 6000 mm and the heat losses in the pump structures the inlet and outlet temperatures have been recorded in the cold box. The pressure of the model pump and the insulation vacuum in the cryotransfer line were kept below 10^{-3} Pa for all measurements.

With a mass flow rate of 10 g/s supercritical Helium a heat load of 18.7 W to the 4.5 K He circuit was measured which is approximately a factor 2 better than the designed value of 30 W.

The measurement for the 80 K GHe circuit was performed with a mass flow rate of 50 g/s and yielded a value of 258 W which is also a factor 2 better than the specified target value.

Table 1: Heat loads to the 4.5 K and the 80 K circuit

Circuit	Component included	Specified heat load	Measured heat load	Pressure in cryotransfer line and model pump [Pa]
		[W]	[W]	
80 K	Cryotransfer line 80 K-shielding, 80 K-baffle	500	258	$< 10^{-3}$
4.5 K	Cryotransfer line 4.5 K panels	30	18.7	$< 10^{-3}$

2.3 Contractual pumping requirements

For verifying the designed pumping speeds the single gases Ne, He, H₂ and D₂ were used.

For the tests the opening position of the main valve has been kept constant while the throughput of the process gas has been

adjusted to 100, 300, 500, 800, 1000, 3000, 5000 sccm; the latter corresponds to about 50 % of the ITER-FEAT maximum throughput. In a series of test runs the valve has been progressively opened to 5, 10, 25, 35, 50, 100 %. For each step the given parameters of throughput were checked. The pumping time for each throughput was 3 min. Between each interval there was a stop of 5 min to reestablish the equilibrium pressure. After the last dosage step the gas load on the pumping panel was 3250 Pam³ which is close to the ITER-FEAT value. The pump was regenerated by heating up the pumping panel with an 80 K gaseous Helium flow of 100 g/s maintaining the baffle and shields at 80 K. The achieved heating up times with this flow were approximately 150 s. After pumping down the released process gas the pumping panels were recooled to 4.5 K and the next test run with increased valve opening was started. The cooling down times are in the range of 150 s with a supercritical He mass flow of 30 g/s.

The max. pumping speed values for single gases at a 100 % opened inlet valve are shown in Table 2. As expected the H₂ gas with the lowest molecular weight has the highest pumping speed. But there is not a strict proportionality to the square root of the reciprocal value of the molecular weight, because He will be fixed by adsorption to the charcoal particles while the other three gases will be pumped by a combination of condensation and adsorption. That causes different sticking coefficients for each gas, which explains the above mentioned difference.

Table 2: Pumping speeds for single gases with throughputs of 100 – 5000 sccm.

Gas	Valve opening [%]	Max. pumping speed [m ³ /s]	Max. gas load on panels [Pam ³]	SCHe mass flow rate [g/s]	80 K GHe mass flow rate [g/s]	Panel temperature distribution during pumping [K]
Ne	100	34	3250	30	50	5.0 – 6.5
He	100	54	3250	30	50	5.0 – 6.5
D ₂	100	58	3250	30	100	4.5 – 6.5
H ₂	100	72	3250	30	100	5.0 – 6.5

The design value of 40 m³/s pumping speed for D₂ was well achieved.

3. Parametric tests

3.1 Pumping behaviour of pure gases

The influence of the valve opening and the throughput of the process gas is shown in the 3D-diagramm, Fig. 2. It shows the specific pumping speed of Ne, related to the pumping panel area of 4 m², versus the valve opening and the throughputs. There is a strong throttling efficiency until an opening ratio of 35 %. Then the inlet gap of the main valve increases and throttling efficiency diminishes. However, there is no constant level of pumping speed at 100 % opening, but an increase at higher throughput. That means the conductance of the valve is a limit for the pumping speed and the valve can still be used to control the throughput even when nearly fully opened.

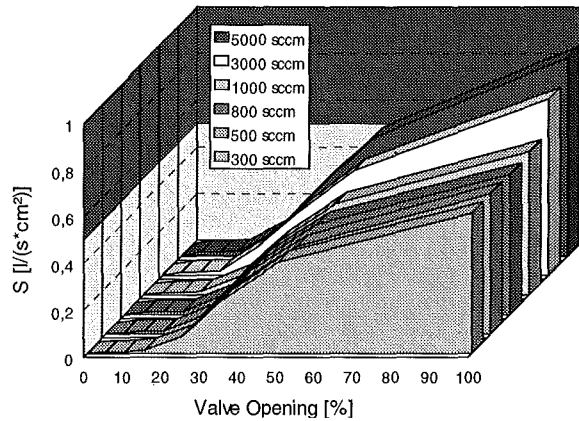


Fig. 2: Pumping speeds for Ne at different valve openings and throughputs

ITER-FEAT relevant throughputs (10 000 sccm = 4.6 Pam³/s·m²) which have been doubled compared to the ITER-FDR values, were checked with helium and a valve opening of 35 %. Table 3 lists measurement results obtained at approximately 10 %, 40 % and 100 % of that typical flow rate. It becomes obvious that the pumping speed is not very much influenced by the resulting increase in panel temperatures at higher flow rates. The increase in flow rate by a factor of 10 (at constant valve position) is accompanied with a simultaneous increase in the inlet pressure, but an even stronger increase of the pressure inside the pump.

Table 3: Dependence of pump performance on He throughput conditions at 35 % valve opening

Surface-related flow rate [Pam ³ /s·m ²]	Surface-related pumping speed [l/s·cm ²]	Pressure inside pump [Pa]	Pressure outside pump [Pa]	Panel temperatures [Pa]
0.435	0.42	10 ⁻²	10 ⁻¹	5.5 – 5.7
1.832	0.50	6·10 ⁻²	5·10 ⁻¹	5.9 – 6.3
4.600	0.50	3·10 ⁻¹	9·10 ⁻¹	7.6 – 7.9

3.2 Pumping behaviour of mixtures

Fig. 3 gives a more detailed insight into the interrelation of pumping speed, valve position, throughput and the pressure conditions upstream and downstream of the main valve for a fusion exhaust model gas mixture, containing 86.6 % D₂, 10 % He, 1.3 % CO, 1.1 % CH₄, 0.6 % CO₂, and 0.4 % O₂. The pumping speed values obtained at 4 different valve positions (100 %, 35 %, 25 % and 10 % open) and varied throughputs (between 100 and 5000 sccm) are plotted twice, firstly, vs. the pressure inside the pump, and secondly, vs. the pressure at the pump inlet. It is revealed that the pumping situation inside the pump depends only on the throughput, but is completely decoupled from the valve position, whereas the pressure at the pump inlet can be adjusted by appropriate choice of the valve position. This demonstrates that the inlet valve has excellent control properties and is suited to establish the specified inlet pressure range between 0.1 Pa and 10 Pa [3].

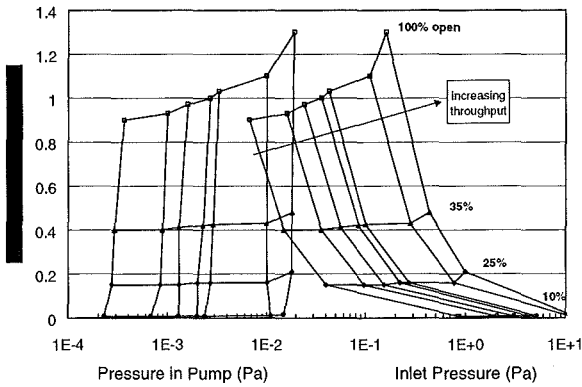


Fig. 3: Pumping speed characteristics for a fusion exhaust model gas, illustrating the control influences of variable throughput and valve position

Due to optimised pump design by Monte-Carlo simulation, the dependence of pumping speed on gas composition could be reduced to an absolute minimum. This is illustrated in Fig. 4, where 4 gas compositions are compared, viz. pure helium, pure deuterium, D₂-base (deuterium containing 3.6 % impurities), and D₂-base mixed with 10 % helium. All these gases have approximately the same molecular mass, which means that any difference in pumping speed is not caused by mass discrimination effects but by the physics of pumping. He and deuterium, which have different sticking coefficients by a factor of 5 show almost the same pumping speed behaviour. These characteristics allow for a simple and uniform pump control by the main valve, independent from the actual gas composition.

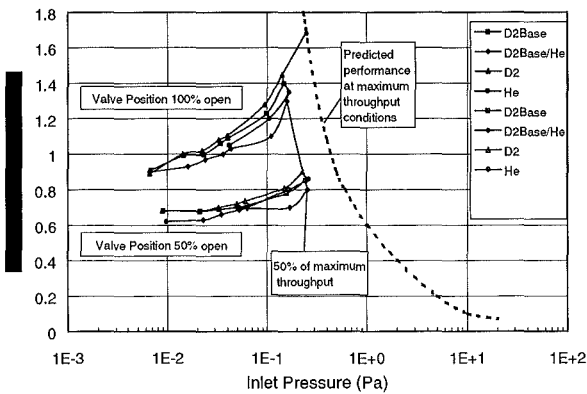


Fig. 4: Dependence of pumping speed on composition of the gas mixture to be pumped at two different valve positions and varied throughput

Within cross-check tests, it could be demonstrated that the pumping speed values can be exactly and reliably reproduced. The parametric tests made so far confirm a robust and well-determined pump design. Presently, additional pump tests covering H₂-containing systems are performed and more detailed tests are scheduled to follow after the upgrade of the TIMO facility.

4. The leak detection operation scenario

The leak tightness within the primary vacuum boundary and the torus is a crucial point, as the impurity influx due to leaks must be reduced to an absolute minimum. Thus, for ITER-FEAT a

10^{-10} Pam³/s He leak rate shall be detectable in a background hydrogen isotope flow of $5 \cdot 10^{-3}$ Pam³/s [4], which corresponds to a required sensitivity of the leak detection system of $5 \cdot 10^7$. The idea for ITER-FEAT is to combine a selective pumping system, which suppresses the hydrogen relative to the helium, with the sensitivity of a high-resolution mass spectrometer. To achieve this, the cryopumps shall be operated partly (half of the pumps) at elevated temperature. This threshold temperature has to be chosen in such a way that hydrogen isotopes are still pumped with He pumping being suppressed. Thus, a certain selective amplification of the He flow signal relative to the lowered hydrogen background is achieved.

As the relevant He flow rates are extremely small, no direct pumping speed measurements could be made to assess the needed temperature range. But own experiments were considered to be mandatory as the values for zero He pumping given in literature are very diverse, covering the whole range from 20 K up to 60 K. Therefore, pumping speed data were derived from rate of pressure change measurements when the facility was filled up with helium or a helium containing gas and the cryopanel was cooled to 5 K and warmed up again. Such measurements were performed in the component test facility TITAN and validated for the model pump in TIMO, see Fig. 5.

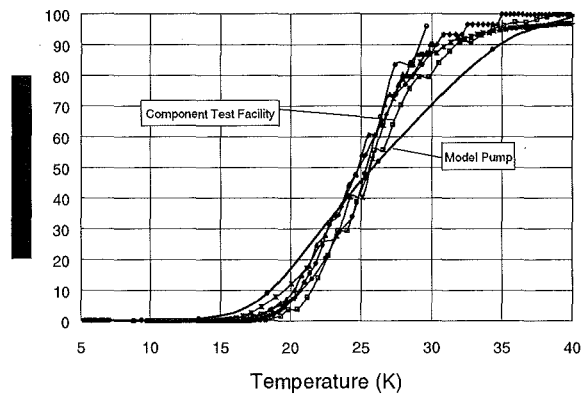


Fig. 5: Helium ad- and desorption behaviour as a function of panel temperature during natural warm-up of the cryopanel in the two facilities TITAN and TIMO

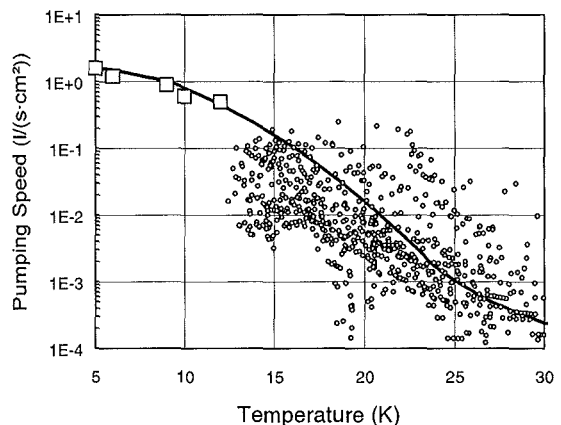


Fig. 6: Pumping speed values for helium vs. panel temperature. The bold curve indicates a common fit of static (small symbols) and dynamic (big squares) measurements

The final pumping speed measurements which were derived from Fig. 5 are plotted in Fig. 6. This figure also contains some results from dynamic measurements at high throughput condi-

tions, which fit the overall impression very well. A decrease in He pumping speed by four orders of magnitude is achieved at a panel temperature of about 30 K. Thus, in combination with the best high resolution mass specs offering a maximum resolution of 5000 to 10000 (at mass 4), a dynamic range of 8 orders of magnitude in total is possible. This demonstrates that the very high requirements for the ITER-FEAT leak detection system are technically feasible, when the cryopumps are involved. As hydrogen desorption starts at temperatures not below 50 K, the optimum temperature window for this operation of the cryopump system is between 40 and 50 K.

5. Upgrading of TIMO

The main objective of the TIMO upgrade is to achieve ITER relevant cooling times of the panels of the model pump and a significant increase of the number of experiments. Therefore, it is necessary to install a new 2600 l cryostat and a new 200 l water bath in the TIMO facility. The new cryostat with a maximum super critical helium mass flow-rate of 250 g/s has been manufactured by Air Liquide, whereas the new water bath is produced by an industrial company. In the period of this report the new cryostat has been delivered and installed in a new steel scaffold. Afterwards the new cryostat was connected to power and compressed air supply. Furthermore the cryostat devices and sensors were wired to its switch board. In the meanwhile the old cryostat and water bath were removed from the facility and preparations were made to install the new water bath which will take place in October 2000. The cryostat is going to be connected to the valve box and the liquid helium supply line by cryo transfer lines which are supplied by the company CryoVac. The cryo transfer lines are already manufactured, pre-checked and delivered. They will be assembled also in October 2000.

Another essential objective is to verify the quality of the regeneration of the cryo-panels. For this reason it is important to have an appropriate equipment to store the desorped and exhausted gases of one pump cycle in a gas collecting tank. In this gas collecting tank a uniform gas temperature distribution is achieved and the sampling and analysing of the collected gases with a quadrupole mass spectrometer can be carried out. An exact analysis of quality and quantity of the released gases of one pump cycle will be possible. The gas collecting tank has a volume of 100 litres and is designed to store hydrogen by a maximum absolute pressure of 1.5 bar. The calculated maximum hydrogen explosion pressure of 14.5 bar and the design of the vessel were proofed and accepted by the TÜV. The manufacturing of the vessel is presently running and it is anticipated to be installed until the end of the year 2000.

6. COOLSORP Facility

The COOLSORP facility for characterisation and optimisation of cryosorbent materials has successfully been built and been set into operation, see Figs. 7 and 8.

The lowest temperature measured at the cold head was 2.6 K (at zero refrigeration power). The long-time temperature constancy was excellent, e.g. 4.20 K \pm 0.05 K over 24 h to simulate LHe conditions. Typical cool-down times from ambient to about 4 K with filled sample holder are about 6 h. Due to the 100 W heating device installed at the cooler's second stage, the whole temperature range up to 100 K is achievable. Fig. 9 illustrates two first measurement results for the microporous granular charcoal material SC-II which is the reference material for the ITER-FEAT cryosorption panels. The intended test programme will include several charcoal materials of different porosity and activation.

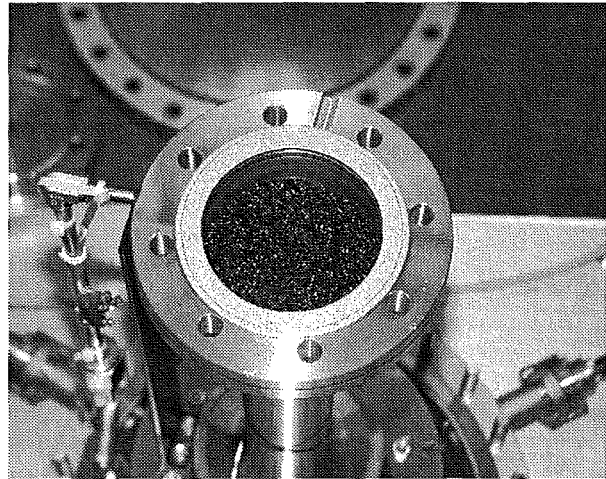


Fig. 7: View of the COOLSORP sample holder, filled with granular activated charcoal material

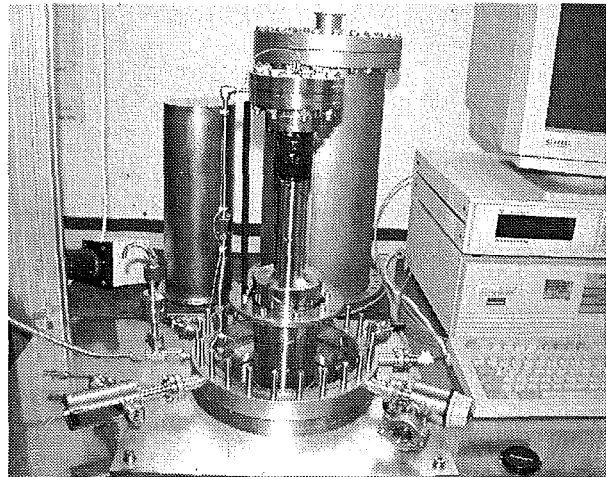


Fig. 8: Photograph of the cryocooler part of the COOLSORP facility, providing 1 W cooling power at 4 K

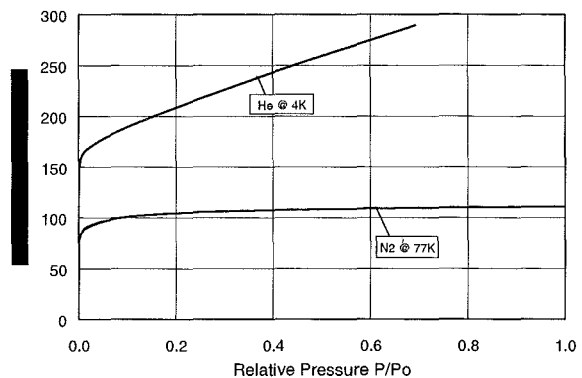


Fig. 9: Measured sorption isotherms in the COOLSORP facility. The pressure is related to the saturation vapour pressure, which is about 1 atm in both cases.

Literature:

- [1] P. Ladd, C. Ibbott, G. Janeschitz, E. Martin; Design of the RTO/RC-ITER primary pumping system, Proceedings ISFNT-5, Roma, Sept. 1999.
- [2] A. Mack, Chr. Day, H. Haas, D.K. Murdoch, J.C. Boissin, P. Schummer; First operation experiences with ITER-FEAT model pump, 21st SOFT, Madrid, Sept. 2000.
- [3] Chr. Day, H. Haas, A. Mack; New operational aspects of the ITER-FEAT primary vacuum pumping system, 21st SOFT, Madrid, Sept. 2000.
- [4] P. Ladd, A. Antipenko, G. Janeschitz, R. Marrs; ITER vacuum pumping and leak detection system, 21st SOFT, Madrid, Sept. 2000.

Staff:

Chr. Day
A. Edinger
J. Grimm
H. Haas
V. Hauer
T. Höhn
H. Jensen
A. Mack
R. Simon
Th. Waldenmaier
J. Weinhold
St. Zebescek
D. Zimmerlin

TR 1 Tokamak Exhaust Processing

Demonstration of CAPER with Tritium

The requirements of the tritium plant for ITER have been persistently detailed in the last decade and have led to increasing demands, especially for the Tokamak Exhaust Processing (TEP). Efficient multistage processes have been designed and commissioned to demonstrate the very high detritiation factors required. The CAPER facility of the Tritium Laboratory Karlsruhe (TLK) is operated under different conditions expected during the various operational phases of ITER to validate by integrated experiments the three step process proposed by TLK and to test main components on a long term basis.

For plasma burn pulses of up to 450 seconds two front-end permeators are foreseen for the separation of molecular hydrogen from impurities in the present TEP design of ITER-FEAT, each with an active Pd/Ag area of 1 m². They are operated at 400°C and feed pressures of up to 0.25 MPa supplied by feed and transfer pumps used to evacuate the torus cryo-pumps. At TLK the performance of the CAPER permeator PP001 (first process step) was tested under the operational conditions expected for the ITER front-end permeators. Hydrogen isotope mixtures (approx. 12% H, 83% D and 5% T) from a reservoir and impurities (He with 2% D₂ and 1% O₂ passed over a catalyst to generate water) were fed into the permeator while keeping the feed and permeate pressures constant by control valves at the bleed and permeate outlets. The flow of impurities was automatically controlled to achieve the selected impurity concentration. The break-through behaviour of the permeator PP001 (active Pd/Ag area 0.21 m²) is plotted in Figs. 1 and 2.

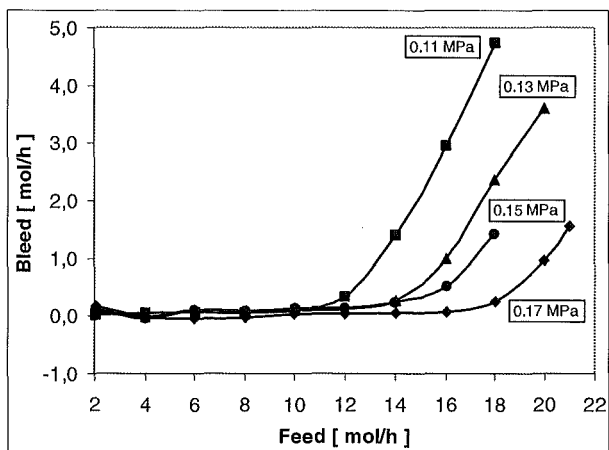


Fig. 1: Break-through behaviour of PP001 for mixtures of 6% helium and 0.12% water vapour in hydrogen at different feed pressures. The permeate pressure is kept constant at 0.025 MPa.

Fig. 1 clearly shows that an increase of the bleed pressure from 0.11 to 0.17 MPa moves the occurrence of any break-through of hydrogen from 12 to 18 mol/h. Fig. 2 presents various break-through curves for different permeate pressures demonstrating low Q₂ bleed at high feeds and low permeate pressures. In summary, high pressure operation of the front-end permeators is possible and advantageous with respect to their permeation behaviour, maximum acceptable impurity concentrations, number and size of pumps on the permeate side and finally cost of the auxiliary equipment needed. The experimental results will

be employed to further refine the mathematical model developed to predict the performance of permeators operated under ITER conditions.

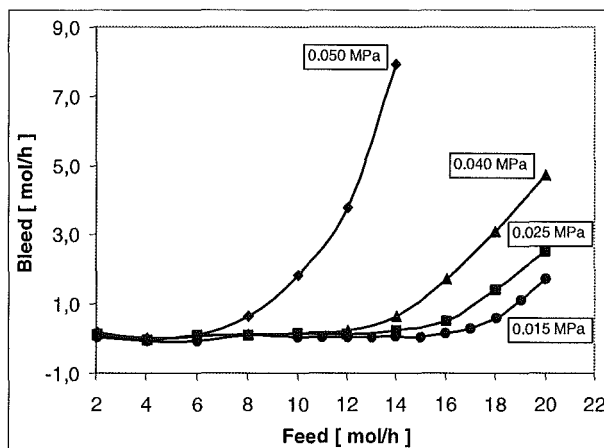


Fig. 2: Break-through behaviour of PP001 for mixtures of 6% helium and 0.12% water vapour in hydrogen at different permeate pressures. The feed pressure is kept constant at 0.15 MPa.

The main components of the CAPER facility, that is the methane cracker (KT001), the water gas shift reactor (KT002) and the permeators (PP001 and PP002) have been operated almost continuously since their commissioning in 1994 at 500°C, 200°C and 400°C, respectively. The catalyst reactors and the Pd/Ag membranes are heated by one and two thermocoax cables, respectively, and each inlet tube of these components by one pre-heater. Next to each heater a spare one is installed. The heaters are controlled in burst firing mode with zero voltage switching. Four of the main heaters of KT001, KT002 and PP002 no longer function. In the case of KT002 and PP002 the spare heaters are currently in use. Both main heaters of KT001 are defective and the reactor can only be heated by means of the inlet tube heaters - a solution now used until a new methane cracker is installed. Each of the main heaters of KT001 failed after approximately three years of operation, whereas those in KT002 and PP002 functioned for more than six years. The thermocoax heaters of these first generation components are simply wound around the primary containment, are kept in position by stainless steel foils spot-welded to the primary wall and are installed in well evacuated secondary containments. The heat transport from the thermocoax cables to the reactors occurs mainly via radiation and not by heat conductance. Furthermore, the shielded thermocouples used for the control loops are not in direct contact with the heaters which can lead to higher local temperatures of the thermocoax heaters than actually indicated. These factors probably caused the limited lifetime of the heaters. In recently built components, e.g. the PERMCAT or the new methane cracker to replace KT001, the thermocoax heaters are installed in grooves machined in the outer surface of the wall to permit good heat transfer, which is the recommended construction technique for ITER-FEAT.

Before the replacement of the defective methane cracker from the impurity processing loop (second process step) of CAPER the tritium inventory in the catalyst bed was determined and tritium removed as far as possible. The Q₂ inventory in KT001 was measured to be 0.055 moles from exchange reactions of pure deuterium with the catalyst material assuming that the Q₂ inventory is constant and that the hydrogen isotopic ratio in any hydrogen containing species is the same as in the catalyst. 6.2% of the hydrogen inventory was tritiated, yielding a tritium inventory of 7.32 TBq (200 Ci). Five detritiation runs removed

6.3 TBq (170 Ci) from the catalyst. During the first two cycles large amounts of methane were generated, but afterwards a rapid decrease in CQ_4 product was observed as the catalyst became depleted in carbon.

The PERMCAT (third process step) is a TLK development of a permeator with the main feature that the feed/bleed volume is filled with a catalyst and that the permeate side is operated in counter flow mode with H_2 . The impurity stream leaving the PERMCAT is thereby detritiated and the protium purge gas tritiated. The catalyst supporting the exchange between protium and chemically bound tritium plays an important role in achieving the very high detritiation factors. A flow through apparatus equipped with an FT-IR spectrometer was therefore built for the analysis of various gas mixtures (e.g. $\text{CH}_4/\text{D}_2/\text{He}$, $\text{H}_2/\text{CO}/\text{He}$) before and after their passage over a variety of catalysts at 400°C . The optimum catalyst supports the isotope exchange reaction in any hydrogen containing species, but does not promote side reactions such as the conversion of carbon monoxide to hydrocarbons (methanization) and is not poisoned by other gas species present in TEP. From quite a number of different catalysts prepared at TLK a Pd catalyst supported on silica showed high isotope exchange rates with the $\text{CH}_4/\text{D}_2/\text{He}$ mixture, but almost no methanization at the operation temperature of 400°C with the $\text{H}_2/\text{CO}/\text{He}$ mixture. Very recent results however indicate that in the presence of CO the isotope exchange rate on the Pd catalyst is reduced due to (reversible) poisoning. The preferred catalyst for the PERMCAT is therefore a Ni based catalyst supported on kieselguhr.

Staff:

M. Glugla

K. Günther

R. Lässer

T.L.Le

R.-D. Penzhorn

K.H. Simon

Fa. D. Niyongabo

TR 2 Development of Tritium Instrumentation

Analysis of Tritiated Species by Laser Raman Spectroscopy

The unprecedented levels of Raman signal and sensitivity enhancements that have been achieved at the Tritium Laboratory Karlsruhe (TLK) with the new Laser-Raman analysis system LARA have been submitted for publication in a manuscript "Enhanced Raman Sensitivity using an Actively Stabilized External Resonator". Earlier observations of 200-fold enhancements inferred from measurements of circulating power within the Actively Stabilized External Resonator (ASER) have been affirmed by comparable enlargements in Raman signals. Also significant improvements in Raman detectability have been achieved using LARA. Hence Laser Raman spectroscopy is well suited to provide real-time quantitative analyses in tritiated gas mixtures of all tritiated chemical species as well as analyses of impurities and other species simultaneously, including excellent differentiation among hydrogen isotopes as seen in Figure 1 showing the rotational Raman spectrum of a sample from a deuterium cylinder containing traces of HD.

demonstrated using mixtures of protium and deuterium, the subsequent sealing of the glove box will bring to LARA the capability of quantitative analyses of tritiated gas mixtures with sensitivity unprecedented by Raman spectroscopy.

Staff:

M. Glugla
C. Caldwell Nichols
Fa. D. Taylor

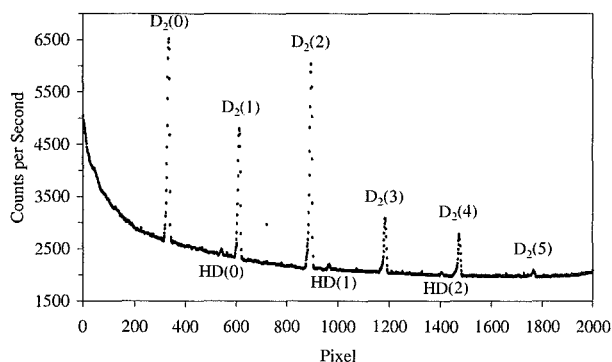


Fig. 1: Rotational Raman Spectrum of D₂ with HD impurities

LARA is operated within a movable glove box currently located inside a small room especially constructed in the TLK main experimental hall for Laser protection purposes. After alignment and calibration the LARA glove box can be repositioned and directly connected to experiments such as CAPER or to infrastructure units such as the Isotope Separation System for on-line and in-line analyses. In these cases Laser protection is provided by shutters installed at all window sides of the LARA glove box.

Quantitative analyses of tritiated gas mixtures with completely unknown compositions require the precise calibration of LARA for both spectral locations and intensities of Raman lines. As the first step of an absolute calibration of LARA, initial rotational Raman spectra such as shown in Figure 1 have been recorded of both deuterium and hydrogen, and a software program LARAROT.C has been written to analyze the relative hydrogen isotope concentrations. As these spectra were recorded right after aligning LARA for optimal vibrational Raman signals from hydrogen, an inconsistency in the basic wavelength drive of the Triax-320 spectrometer from the company ISA was observed from the displacements of the rotational Raman lines by as much as 60 pixels from their expected locations. This problem is currently being solved in collaboration with ISA. In parallel efforts continue to improve the software for LARA. Another peculiarity in the TRIAX-320 spectrometer/CCD that had not been notable in previous Raman systems is an apparent tilt in the spectral focal-plane at the CCD, which also requires appropriate adaptations in calibrations. After satisfactory completion of all calibrations and alignments have been

TEP 3A Tritium Storage in ZrCo

Zirconium-cobalt (ZrCo) is the currently accepted reference material for the Storage and Delivery System (SDS) of the ITER-FEAT Tritium Plant to store and handle pure deuterium and deuterium/tritium mixtures. This has triggered intensified and increasingly practice oriented ZrCo-related research at the TLK. To permit good comparison between uranium and ZrCo, the Tritium Storage System of the TLK, previously equipped with only five uranium storage beds, was recently upgraded by four additional uranium beds and one containing ZrCo (max. storage capacity 8.9 g tritium). All ten beds of the Storage System are of identical construction.

Loading/unloading experiments were carried out using the combined Tritium Storage and Tritium Transfer Systems of the TLK. In practice, the accountancy vessel of the Transfer System was first filled with deuterium and then the gas was loaded on to the cold getter bed containing either zirconium cobalt or uranium. The gas absorbed by the getters was determined by pvt-procedures. After completion of the getter loading, the getter was heated and the released gas pumped into the accountancy vessel employing a pump combination. To simulate conditions at the SDS of ITER-FEAT two different heating procedures were applied:

- heating the getter bed up to 300°C followed by pumping into the accountancy vessel maintaining the temperature constant
- heating the getter bed up to 300°C followed by pumping into the accountancy vessel while progressively increasing the temperature

The results indicate that under the employed conditions the sorption rate by zirconium-cobalt is slightly faster than that of uranium. The experimental evidence also shows that deuterium is released faster from ZrCo than from U.

To investigate the isotope effect of the hydrogen release from the ZrCo/Q₂ (Q = H, D, T) system, the getter was first loaded with tritium and subsequently with deuterium. The absorbed hydrogen isotope mixture was then released into the accountancy vessel of the Tritium Transfer System and analysed by radio gas chromatography employing a grab sampling procedure. Then the released hydrogen isotopes were again loaded on the now cold ZrCo getter and the treatment, i.e. heating of the getter up to 320 °C, repeated. Sampling and partial de-loading of the getter bed was repeated several times. Typically, when deuterium/tritium mixtures were released from ZrCo, the tritium concentration of the initially liberated gas was found to be higher than that initially loaded onto the getter. In agreement with this, when similar experiments were performed with H/D-mixtures, deuterium was predominantly released. Summarising, it can be concluded that at 320°C the heavier hydrogen isotopes are released more readily from ZrCo than the lighter ones. In ongoing experiments this kinetic effect is being further investigated at other temperatures and at various getter loading. When the ZrCo bed was loaded with a T₂ 90% - D₂ 10% mixture, tritium was found to be enriched in the initially released gas. However, the effect was found to be comparatively small.

During several consecutive experiments the ZrCo getter of the Tritium Storage System was fully disproportionated and thereafter completely regenerated. In general, after the maximum release pressure (570 mbar) was attained a progressive pressure decrease was observed until the disproportionation of ZrCoQ_x (Q = H, D, T) was completed. When equilibrium conditions were established the gas pressure

remained constant. Experiments with D₂ and T₂ indicate that faster disproportionation rates occur with the lighter hydrogen isotopes. The getter was regenerated by heating up to 470°C while fully evacuating with the available pumping system. After an integral pumping time of 15 h the loading/deloading properties of the ZrCo were completely restored, which demonstrates that this getter fulfills important requirements for the storage and handling of tritium.

The residual amount of tritium remaining trapped in a uranium getter bed after baking depends on the prolongation of the heating and on the temperature. Results of earlier investigations indicate that the hydrogen tenaciously trapped in uranium after baking at 527 °C is about 1.8×10^{-5} mole/g uranium. Analogous experiments were performed with tritium using ZrCo. To this effect a transportable storage vessel identical to those containing uranium presently used at the TLK for the transport of tritium was designed and build. The bed was filled with 160 g of ZrCo turnings and hydrided. After four loading/de-loading cycles the storage capacity reached a Q/ZrCo ratio of 2.69. The getter bed was then loaded with 1.21×10^{15} Bq tritium. In two tests the bed was heated up to 470°C and then evacuated while the desorbed gas was collected in the accountancy vessel. The residual tritium in the bed was determined with a calorimeter. The measurements show that under the employed conditions the amount of tenaciously trapped tritium is higher in ZrCo than in uranium. According to the literature the tritium remaining trapped in uranium was estimated to be 9×10^{12} Bq/mole, which is about ten times higher than the value found for ZrCo.

Staff:

U. Besserer
R.-D. Penzhorn
R. Brandt (Uni. Marburg)

TR 4 Tritium Extraction from Plasma-Exposed Graphite and Carbon Fibre Composite Tiles

For the development of technology for the removal of tritium from first wall materials previously exposed to D-T plasmas it is first necessary to determine accurately the total content in and - even more important - the distribution of tritium within the tiles. For this reason i) a TFTR graphite tile exposed to D-D plasmas only, ii) a JET graphite tile exposed to low tritium level D-T plasma, and iii) several JET carbon fibre composite (CFC) divertor tiles as well as a graphite poloidal limiter tile, all previously exposed to high tritium level D-T plasmas, have been examined with respect to their plasma-facing surface and depth tritium content employing a full combustion technique and a pin diode method.

Basically, cylindrical specimens were drilled from the tiles using a hollow drill and from the cylinders disks were cut employing a diamond-grinding disk. For a tritium depth determination by the "coring"/pin diode method the rear side of each disk was marked with a small scratch to allow the unequivocal identification of the obverse and reverse sides. Each disk was then examined from both sides employing a portable, windowless pin photodiode detector. Measurements were performed while flushing the chamber with approx. 50 [ml/min] of helium. The depth resolution of this technique is less than one micrometer and the detection limit under helium is of the order of 10^9 [T/cm²].

Results from pin diode measurements performed on disks obtained from JET divertor tile IN3_{S1} have been compiled in Table 1. The minimum and maximum depths correspond to the obverse and reverse side, respectively. From the results it is evident that with progressing distance from the plasma-exposed surface a decrease in tritium concentration is clearly detectable.

The full combustion technique was chosen because of its simplicity, sensitivity, and high accuracy. To obtain accurate tritium depth profiles in graphite and CFC tiles cylinders were drilled at pre-determined positions of selected tiles and disks were cut as above. The tritium content in each disk was determined following a technique which basically consists in full combustion followed by liquid scintillation counting (LSC) of the liberated tritium trapped in a bubbler placed downstream of the combustion chamber.

The tritium depth profile determined by full combustion/LSC expressed as total tritium in the disks was compared with that obtained with the pin diode procedure for the surface tritium on each side of each disk. With the exception of a few pin diode values at a depth of about 15 mm, the correlation between both measurements is surprisingly good. Even the increase in tritium concentration usually observed at the rear side of the tiles is registered by both techniques. The good correlation is possible because the surface concentration on each disk is mostly determined by that in the bulk of the disk and not by spurious surface concentrations originating from such plasma/wall interactions as co-deposition, implantation, erosion, etc. which as a rule limit the usefulness of a surface tritium detection.

The surface concentrations of tritium on the analysed CFC tiles showed usually variations within a factor of 4 - 25. Occasionally, however, much larger variations, i.e. by a factor of 126, were observed, which is caused by an

exceedingly high contribution from a co-deposited layer at the plasma occulted side of the tile. In view that very high levels of co-deposits were found on the lateral side of tile DTE1/IN3_{S1} it was of interest to compare the depth profile from the plasma-facing side of the tile having fibre planes parallel to the plasma with one from an immediately neighbouring site but taken from the edge of the tile through the fibre planes.

Table 1: Tritium depth profile from the JET inner wall divertor tile IN3_{S1} determined with the pin diode method

Depth min/max [mm]	Upper side of disk [Bq/cm ²]	Lower side of disk [Bq/cm ²]
1.45/2.45	2260	663
2.90/3.90	640	605
4.35/5.35	601	603
5.80/6.80	552	381
7.25/8.25	375	318
8.70/9.70	345	311
10.15/11.15	291	225
11.60/12.60	229	192
13.05/14.05	155	154
14.50/15.50	173	151
15.95/16.95	222	106
17.40/18.40	427	133
18.85/19.85	126	113
20.30/21.30	82	85
21.75/22.75	70	58
23.20/24.20	65	45
24.65/25.65	60	68
26.10/27.10	72	68
27.55/28.55	65	51
29.00/30.00	61	73
30.45/31.45	116	221

The results show that in spite of the very high tritium concentration in the thin surface layer the concentration of tritium drops rapidly with depth and then changes only little in the direction through the fibre planes. The tritium profile between the planes from the plasma-exposed side on the other hand drops initially less sharply but then continues to decrease exponentially with increasing depth. The two lines cross at the depth/concentration point at which both tritium profiles have the same values, i.e. about 7 mm, an indication that diffusion between the carbon fibre planes is much more efficient than through the planes.

Tritium was found to be present in the bulk of all examined JET and TFTR tiles (see Table 2). In general, the lowest tritium bulk concentrations were found in the graphite tiles, i.e. TFTR, JET FTE/004/2-20 and DTE1/PL4B Mod 7B TOP. While the presence of tritium in the bulk of the first two tiles was identified with certainty, it was not possible to obtain reliable values due to the very low concentrations, i.e. barely above the background of about 10 Bq. In the PL4B poloidal tile, on the other hand, removed from the torus after completion of the DTE1 campaign, the lowest activities were of the order of 20 kBq, which are easily distinguishable from the background. Since the activity in the PL4B tile is distributed fairly uniformly within the bulk without showing any clear depth profile it is probably

located in the graphite macro porosity possibly retained by an isotope exchange mechanism.

No correlation between the concentration on the tile surface layer and that in the bulk of tiles is recognisable. The bulk concentration seems to be primarily determined by the ion flux.

It should be kept in mind that the measured tritium concentrations were obtained after the tiles had been subjected to numerous deuterium plasmas, glow discharge cleanings and other wall conditioning treatments. It is therefore probable that the measured values are below the steady state values reached after prolonged machine operation.

Table 2 summarises the impact of the tritium profiling results on the tritium inventory in the divertor region of JET. The large contribution of co-deposit layers on the shadowed edge of tile IN3_{S1}, previously identified as highest, is now less than that in the bulk of tile IBN4. Another observation is that the inner divertor tiles and floor constitute by far the most tritium-contaminated zone in the divertor.

The following general conclusions can be drawn from the first obtained experimental results:

- method for the detection of tritium on surfaces provided the tritium is distributed homogeneously. Under these condition a good correlation between the absolute amount in the bulk and on the surface is achievable. Possible applications of the technique are therefore the characterisation of the bulk of tiles and waste certification.

- While in isotropic graphite poloidal tiles the bulk concentration of tritium appears to remain at very low levels, i.e. about 0.2 % of that on the tile surface in a layer only a few 10 µm thick, in the case of CFC divertor tiles the tritium bulk concentrations can be as high as three times that found in the co-deposited/implanted surface layer.
- No straight forward correlation was found between the tritium co-deposited/implanted on the on the CFC tile surfaces and the tritium penetrated into bulk.
- The pin diode technique is a rather reliable and sensitive
- Some divertor tiles of CFC were found to contain a particularly large fraction of tritium in the bulk. This type of tritium retention, which comes in addition to implantation, co-deposition and the production of tritium by transmutation, had not been recognised previously. The bulk fraction is likely to increase with temperature and appears to be influenced by the ion flux on the divertor target tiles. Further investigation is required to elucidate the mechanism of hydrogen isotope retention.
- The existence of a significant tenaciously held tritium fraction in the bulk of first wall materials that accumulates and is released slowly represents an inventory with a long time constant. The saturation levels in a routinely operated machine are expected to be higher than those found in this work and still need to be determined.

Table 2: Comparison of the tritium fraction in the bulk of a TFTR and several JET tiles

Tile designation	Cylinder N°	Depth examined [mm]*	Total tritium in examined bulk depth [MBq]#	Total tritium in first mm depth [MBq]**	Fraction of total activity in the bulk %
TFTR 121-1 SNO11 HOC/95-2 [a]	many	12		0.0022	< 2
JET FTE/004/2-20	many	12		0.0066	< 1.1
Poloidal tile DTE1/PL4B Mod 7B TOP	2	18.2	0.67	275.93	0.20
Inner wall divertor DTE1/IN3 _{S1}	1	37.2	27.36	39.82	40.7
Inner wall divertor DTE1/IN3 _{S1}	2	31.2	18.06	29.40	38.1
Inner wall divertor DTE1/IN3 _{S1}	4	32.4	31.86	12.43	71.9
Divertor base tile DTE1/IBN4	1	35.3	185.44	99.30	61.6
Divertor base tile DTE1/BN7	3	31.70	34.94	28.61	18.1
Outer wall divertor DTE1/10N8	2	29.8		7.03	50.1

* The examined depth was limited by holes at the back or the tile itself.

The total tritium in the bulk was obtained from the sum of the tritium concentration in all the disks plus that estimated to be in the cuttings plus that obtained by extrapolation of all measured tritium concentrations to a depth of 0.2 mm.

** It was assumed that most of the activity in the first mm depth was in a layer < 50 µm thick.

- The large fraction of tritium present in the bulk of the divertor tiles is not recoverable with methods that only treat the surface, e.g. laser irradiation, exposure to an open flame or any gas/solid interaction treatment. Simple isotopic exchange with protium or deuterium is also not expected to be effective.

Staff:

N. Bekris
U. Berndt
J.P. Coad, JET-UKAEA
D. Knebel, HVT-HZ
R.-D. Penzhorn
H. Ziegler, HV-HZ

TR 5 Tritium Recovery from Liquid and Solid Wastes

Work on the detritiation of molecular sieve (MS) beds with the AMOR facility at the Tritium Laboratory Karlsruhe (TLK) is ongoing. So far almost 4 tons of MS's from the dedicated Tritium Retention Systems and from the Central Tritium Retention System of the TLK have been successfully regenerated without releases or contamination. The tritium levels of the water collected from the MS beds have fluctuated within the range $(4 - 40) \times 10^{10}$ Bq/l. The water content of the beds containing about 15 kg of MS is reduced from < 10 to about 1 % by weight. The recovered tritiated water is collected in a transportable 50 l vessel and after cementing disposed of by the Hauptabteilung Dekontaminationsbetriebe (HDB).

Valuable experience has accumulated at the TLK on the degree of tritium contamination of tubing, valves, components, sensors, etc. during the upgrading of the Isotope Separation System (ISS) by a new gas chromatographic displacement column manufactured at the workshops of FZK. Because essentially the components of the previous ISS were only contaminated by molecular hydrogen isotopes, the observed contamination levels, as determined by smear tests, were comparatively low. Most intervention activities were thus possible with the open glove box. Only when primary lines were opened was it necessary to work with a closed glove box while operating the dedicated Tritium Retention System.

The development of technology for the detritiation of oils from pumps employed during the operation of the experimental fusion machine JET is continuing. The effectiveness of noble metal catalysts finely distributed within the oil to promote the exchange with gaseous hydrogen bubbled through the oil was examined and found to be successful. More work, however, is necessary to optimise the procedure.

With the purpose of developing a water detritiation process for JET a new research activity was initiated in 2000 aimed at identifying a suitable hydrophobic catalyst for the exchange of hydrogen isotopes between molecular hydrogen and water. Three catalysts, manufactured in Russia, Romania and Belgium, are being compared in approx. 2 m long glass columns operated in counter current mode. The performance of the columns is being evaluated by analysing the effluent gaseous and liquid phase by mass spectrometry, infrared spectroscopy and conversion of deuterated water into deuterated molecular hydrogen species on a zinc bed. In addition, a model has been developed that allows comparison between experimental results and theory. For a better comparison the effect of gas velocity on the HETP's of the various columns is being examined in detail. After verification of the model it will be used for the optimised design of the large technical scale columns required for JET.

Staff:

H.-D. Adami
N. Bekris
U. Besserer
I.R. Cristescu (guest scientist)
I. Cristescu (guest scientist)
L. Doerr
R.-D. Penzhorn
S. Welte

TR 6 Tritium Extraction and Helium Purification

The ITER Helium Cooled Pebble Bed (HCPB) Test Blanket Module (TBM) will comprise helium loops for tritium extraction from the breeder zone and for purification of the coolant, both described in previous reports. One main component in these loops will be a cryogenic cold trap for the removal of tritiated water vapour. An existing cold trap has been installed in a pre-test facility in the TLK to investigate its efficiency to remove extremely small concentrations of water of the order of 10 ppm by volume.

The cold trap offers the following features:

two separately operated pre-coolers,

variable gas throughput and relatively small gas velocity in the freezing zone

electrical heating in selected regions of the cooling plates in the freezing zone to adjust the temperature profile (Fig. 1).

With this trap a series of tests was carried out. The first results obtained this year are presented below.

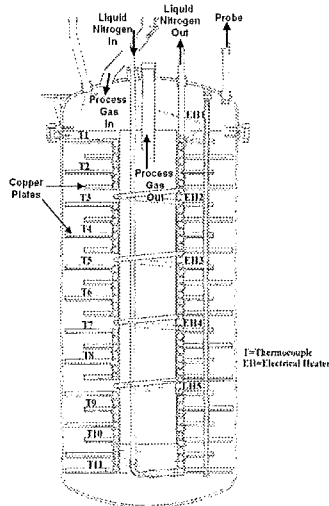


Fig. 1: The freezing zone of the cold trap

As shown in Fig. 2, under bypass conditions the three hygrometers show the same dew point temperature (point 1 Fig. 2) almost corresponding to the 10 ppm water certified by Messer Griesheim (gas supplier).

After the CT has reached a constant temperature, the helium gas flow was allowed to pass through the trap (point 2 in Fig. 2). The humidity level measured by the outlet hygrometer dropped and reached a stable dew point temperature of nearby -82°C corresponding to a water vapour concentration of about 0,4 ppm.

An increase of the LN_2 flow rate from 24 to 35 l/min improved the efficiency of the water retention of the trap. This is shown by the outlet hygrometer, which indicated a -86°C dew point temperature corresponding to 0,2 ppm of water vapour (point 4 in Fig. 2). The same experiment repeated with higher throughput of He containing about 160 ppm of water vapour (-38°C in DP), with maximum peaks at 305, 605 ppm and 550 ppm water, showed once again, that at the outlet an extremely dry gas leaves the CT containing less than 0,02 ppm of water vapour (-98°C in DP). In the most favourable case the resulting humidity reduction factor was approximately equal to 32 000 (Fig. 3).

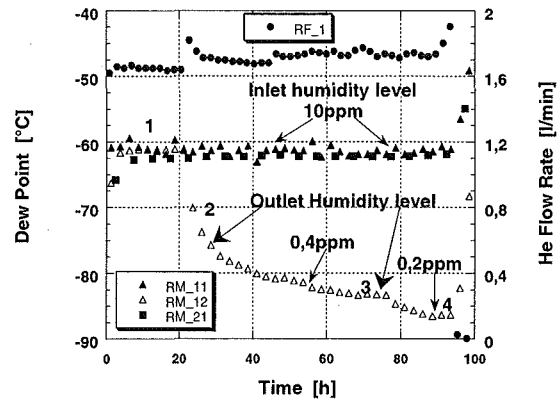


Fig. 2: Low He flow rate containing 10 ppm of water vapour

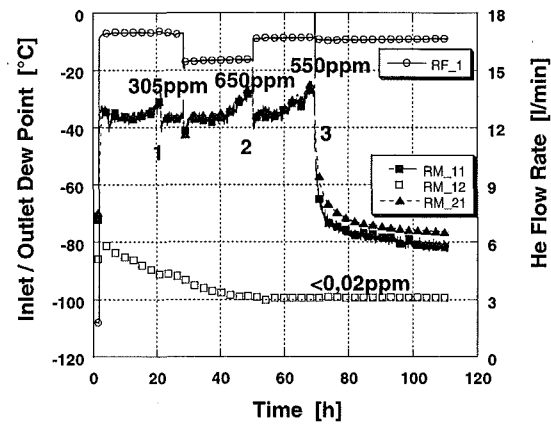


Fig. 3: High He flow rate containing high amount of water

The results of these first experiments have demonstrated the ability of the cold trap concept to reduce very effectively the water vapour content of a helium stream at high flow rates ($1\text{m}^3/\text{h}$), down to less than 0.02 ppm_v even when the inlet water concentration is about 300 ppm_v or higher. In such conditions the water reduction factor achieved was nearly 15 000.

In the HCPB test programme in ITER-FEAT the test of neutronic and tritium production (NT-TBM) is foreseen. For this phase a Tritium Measuring System (TMS) has been proposed:

In this process the carrier gas ($\text{He} + 0,1\% \text{H}_2$) will "rinse" the NT-TBM and exchange its hydrogen with the tritium produced in the breeder material. Then the hot gas passes through a reduction bed of Zr-Fe, Mn or Zn at a temperature of about 400°C where the reduction of water to the constituent gases, hydrogen or hydrogen isotopes, and oxygen occurs. The oxygen is fixed as an oxide on the metallic or intermetallic alloy in the reduction bed while the hydrogen (HT, T_2) is released downstream. After reduction the tritiated gas is cooled and the hydrogen isotopes are collected on appropriate Uranium or ZrCo beds. The tritium activity is measured either "on-line" or afterwards by calorimetry, by measuring the heat released by tritium decay.

Staff:

N. Bekris
E. Hutter

T 456 / 02 Development of a Tritium Compatible Roots Pump

Pumping Test of a Roots Pump under ITER Relevant Conditions

In present and future fusion devices large mechanical pump sets are needed to evacuate the plasma volume and to cope with the large gas amounts released during the regeneration of the cryo-pumps. Due to the large gas streams to be processed in ITER-FEAT Roots pumps with a pumping speed of a few thousand cubic metres per hour (two parallel Roots pumps of 4200 m³/h each with one Roots pump of 1200 m³/h in series) are proposed.

Large tritium amounts (in the average up to 100 Pam³/s) will pass through these Roots pumps. Therefore, an important requirement for their use is their adaptation for operation under ITER relevant conditions. The main aspects with respect to tritium compatibility are the achievement of a total leak tightness of better than 10⁻⁹ Pam³/s, the removal of any contact possibility between the radioactive gases and the oil needed for lubrication of the gears and bearings as well as the use of materials which do not change their properties in the presence of tritium. Commercially available Roots pumps do not fulfil the three conditions. Roots pumps are normally sealed by elastomer O-rings which will become brittle when in contact with gaseous tritium. Furthermore, the oil filled volumes of these pumps communicate with the pumping volume and as a consequence the oil will become tritium contaminated and the pumped gases oil contaminated.

A fully tritium compatible Roots pump can be designed in the following way:

1. The specified leak tightness can be achieved by the total replacement of the elastomer O-rings with metallic seals.
2. The transfer of gas between the oil filled volumes and the pumping volume is stopped by the use of special Ferrofluidic Vacuum Seals mounted 'inboard' of the four rotor shaft bearings. (In ferrofluidic seals the high leak tightness is achieved by a special ferrofluidic liquid kept in position by magnetic field lines. A ferrofluidic seal contains two components: a liquid with a very low vapour pressure and a colloid of approximately 100 Å magnetite (Fe₃O₄) particles equipped with surfactants to avoid clustering. Such seals can withstand large pressure gradients and are nowadays used in computer hard discs to stop dust entering and in ultra high vacuum equipment as rotary feed through.)
3. The use of only tritium compatible materials.

Many well known companies offering Roots pumps were contacted, but none was interested in installing ferrofluidic seals. Only one was willing to replace the O-rings by metallic seals. Finally, a special company producing Roots pumps for the oil and chemical industry was found with experience in using ferrofluidic seals in blowers at higher pressures.

As the companies selling the ferrofluidic seals were unable to guarantee the required leak tightness for ferrofluidic seals in the proposed application it was decided to build first an experimental test rig and to test the ferrofluidic seal under the conditions the Roots pump will be operated in. A tritium compatible Roots pump should be only designed and manufactured when the test proved the required leak tightness of the ferrofluidic seal.

This special test rig equipped with a magnetic coupling transmission, with metallic seals and a ferrofluidic seal was designed and constructed. The tests showed convincingly that

the ferrofluidic seal fulfilled the expectations. No He-4 leaks in the 10⁻⁹ Pam³/s range were detected at He-4 pressure up to more than 0.1 MPa(a) and independent of the rotation speed of the shaft up to the maximum speed of 3000 rpm. Indications of very small leaks of 1.5x10⁻¹¹ Pam³/s and 3x10⁻¹¹ Pam³/s were observed at 1500 rpm and 3000 rpm, respectively.

Quantitative leak determination in the 10⁻¹¹ Pam³/s range is quite difficult, but it can be stated with confidence that the installation of ferrofluidic seals and the addition of He to the oil filled volumes will stop the cross contamination between the oil filled volumes and the pumping volume. Further advantages are that the oil change and any maintenance to the bearings and other components can be done at a far lower risk as the tritium contamination is kept within the pumping volume. Finally the disposal of the oil will be far easier than when it is contaminated.

The next step will be a contract with industry for the design and manufacture of a tritium compatible Roots pump fulfilling the three requirements discussed above and the demonstration of this pump in a closed loop, initially filled with inactive gases, but finally topped up with tritium to simulate the deuterium-tritium exhaust gases for ITER-FEAT.

Staff:

H.-D. Adami
R. Lässer

**Safety Analysis
and
Environmental Impact**

SEA 3 Reference Accident Sequences – Magnet Systems (2)

Subtask 2: Magnet System Safety

Within the subtask 3.2 FZK investigates the thermal behavior of magnet systems during severe accidents.

In terms of code development the work concentrated on the development of a new module for MAGS to simulate conductor insulation failure in a toroidal field (TF) coil built with radial plates. The module named COnductor INSulation LOSS (COINLOSS) solves the Laplace equation for voltage for those coil areas and/or radial plates, which have contact to the conductor, caused by insulation failure. From the voltage field currents are calculated and the resultant power for each mesh element. The module is based on the mesh of MAGS for solution of the heat balance and handles mesh elements with different material properties, e.g. conductor, steel or insulation. Boundary conditions are given by a) intact insulation mesh elements b) the first conductor mesh element with failed insulation and c) the last conductor mesh element with failed insulation. In b) a current source is introduced with a source strength determined by the electrical circuit analysis of module MSCAP, in c) a voltage is placed, calculated by module OHM.

For insulation failure presently a simple model is used: Failure is identified if either the insulation temperature rises above an assumed failure temperature, e.g. 700 (K) or an adjacent metal mesh element reaches melting temperature, e.g. 1700 (K). The consequence of failure is that the thermal and electrical conductivity of these mesh elements are set to those of steel at this temperature. Ignition of arcs is not yet included. This is possible in a next step and requires definition of arc ignition criteria and calculation of arc voltage or resistance, respectively.

Parallel to the development of COINLOSS the material properties in MAGS for copper and steel were extended to cope now also with melting and evaporation.

COINLOSS has been used to analyze the unmitigated quench for ITER FEAT [1]. The complete coil including the coil case was modeled using about 110 000 mesh elements. Helium flow is not taken into account, see Figure below, quench front propagation was simulated with module HEXAN determining quench front location with a simple analytical formula.

The solution proceeds pretty slow, only about 50 (s) of problem time could be solved so far. Nevertheless some important results can be deduced: a) due to the winding technique of double pancakes insulation failure progresses towards the outer turns b) while insulation is intact current, i.e. heat source, and heat are kept in the cable space. c) if insulation has failed current and heat sources are relocated and the stored heat can be redistributed because of better heat conductivity of the insulation mesh elements.

For the ITER FEAT safety report a study of internal arcs has been performed considering the toroidal, poloidal and central solenoid coils [2]. It could be shown that the damage is limited to a small area in the coil. The scenarios with only one shorted turn show only some insulation destruction and dump can proceed regularly. In all other cases, where more turns are shorted, a shorting arc ignites and destroys the conductor over a certain length. As the jacket is able to carry the short current, no subsequent arcs are ignited and dump proceeds almost regularly with almost all magnetic energy dumped into the dump resistance and the inductively coupled structure parts. No noticeable heating of significant coil volumes is observed.

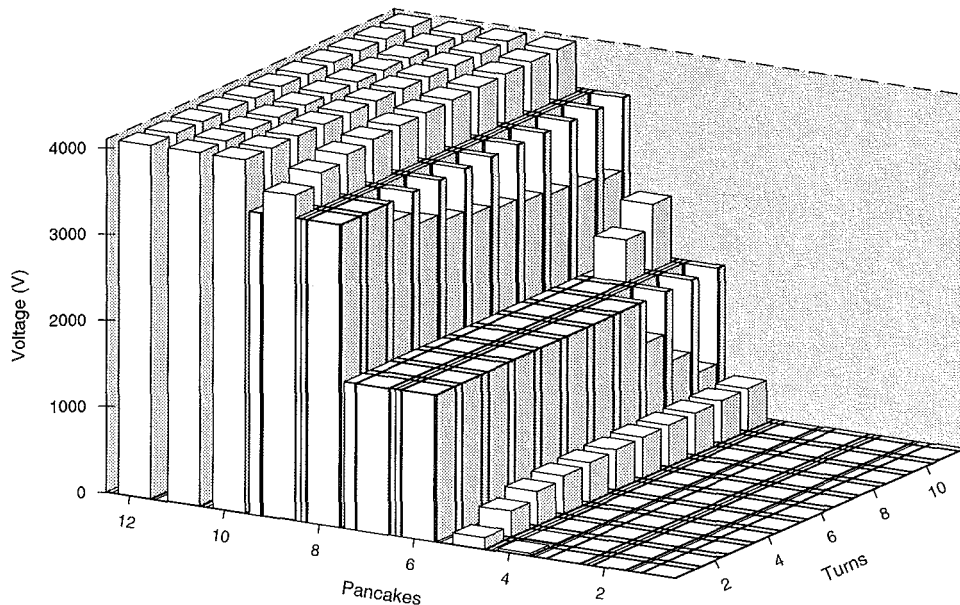


Fig. 1: Voltage distribution in a high field coil cross section. counted from right pancakes, 1 through 4, running in radial direction, are superconducting, pancakes 5 through 9 are normal conducting and pancakes 10 through 12 are superconducting. For pancakes 6 through 9 conductor insulation has failed. Insulation between radial plates, housing a double pancake each, is intact

Another study considered a shorting arc at the bus bar of a TF coil near the cryostat wall [3]. It could be shown that the hole in the cryostat wall, burnt by the arc is in the order of 0.1 (m²). This hole is so small that there are no concerns in the context of a release of radioactive material. The analysis shows that an important effect in this accident sequence is the quench of the shorted coil. Most of the energy initially stored in the coil and commuted to the coil can be dissipated in the large coil mass and only a small fraction is converted in the arc.

Literature:

- [1] R. Meyder: ITER-FEAT First Report on unmitigated quench August 2000 ITER Task G 81 TD 12 FE.
- [2] V. Pasler: Internal shorts and arcs in the ITER-FEAT tokamak. ITER Task G 81 TD 12 FE July (2000).
- [3] R. Meyder: ITER-FEAT Analysis of an arc shorting a TF coil during dump in the vicinity of the Cryostat June 2000 ITER Task G 81 TD 12 FE.

Staff:

R. Meyder
V. Pasler

SEA 5 Validation of Computer Codes and Models

Magnet analysis code MAGS

The validation of MAGS-module CRYOSTAT has been continued by predictions for the EVITA condensation experiments at Cadarache. A group of analysts from different labs accompany these experiments. Our results [1] were discussed and compared to the results of the other group members during a meeting with the EVITA staff, leading to an agreed test matrix for EVITA.

For the specified tests pre-test calculations have been performed by all participants. In these tests water steam at 0.7 (MPa) and 165 (°C) is injected into the vacuum vessel at a mass flow rate of 2.1 (g/s). Condensation takes place at the VV wall and / or on the cryogenic plate of 0.1 (m²) cooled with liquid nitrogen at different flow rates. The comparison and analysis of the results showed a big influence of heat transfer models and material properties data used. The CRYOSTAT results were in essence the same as found by the other codes. In some cases, however, especially where a frost layer is covered by a liquid layer differences showed up.

Therefore it was decided to extend the single layer condensation model of CRYOSTAT to a multi layer model. This will allow to handle frost layers near the cryogenic plate covered by a liquid layer with individual properties data for each layer.

Besides improvement of the MAGS code, for better analyses also meaningful experimental data have to be provided. In two areas work has been done: a) contact resistance between jacket and copper braids and b) electrical properties of insulation material at elevated temperatures.

Contact resistance experiments: In ITER the CS cable is surrounded for mechanical reasons by a thick steel jacket in the main coils. For the occurrence of arcs, MAGS calculates a rapid growth in arc length, and a high electric field strength. Hence, it must be investigated to which degree the electric current does not escapes into the steel jacket ('shunt effect'). For this parallel current to be calculated, not only the electric resistance of the jacket, but also the transition resistance between the cable and the jacket, also in the return direction, must be known. Therefore two experiments with a conductor piece of type CS1.2B, not heat treated, 100 (mm) long and rounded, have been done at temperatures between 20 (°C) and 320 (°C) to measure the transition resistance between cable and jacket as a function of temperature history. The experiment assembly is shown in the Figure below.

In the course of the experiments [2], it was found that in case of increase of the temperature of the conductor specimen, the transition resistance between cable and jacket is reduced. Simultaneously the structure of the cable will be altered. This can be seen by the fact, that the transition resistance at ambient temperature is changed after a temperature excursion to higher temperatures. If the temperature excursion leads to temperatures higher than 200 (°C), the transition resistance at ambient temperature will be enlarged.

Using the analogy between electrical and heat conduction and using a computer program like CATIA-ELFINI it is possible to calculate the shunt $R_{sh}(t)$ formed by the jacket in dependence of the length of the arc, the value of the transition resistance and the temperature t (°C). The experiments showed, that within an accuracy of about 20 % and in the temperature range of 20 (°C) and 320 (°C) the shunt formed by the jacket of a CS1 conductor parallel to an arc can be calculated in Ohms by the mathematical equation $R_{sh}(t(°C)) = 5.43 \cdot 10^{-10} \cdot t^2 - 3.78 \cdot 10^{-7}$

$\cdot t + 1.56 \cdot 10^{-4}$, assuming an arc of 20 (mm) length. The contribution of the jacket resistance is $2 \cdot 10^{-5}$ (Ω).

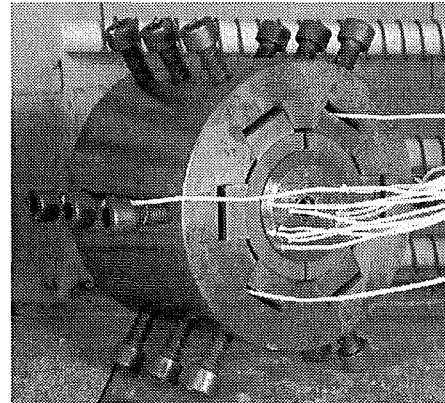


Fig. 1: Test apparatus to measure the transition resistance superconductor strands versus conductor jacket.

Two half shells of copper are pressed onto the cable jacket to provide a homogeneous current flow in radial direction.

Electrical insulation experiments: Insulators surround conductors in magnetic field coil systems. If unmitigated quenches occur, temperatures higher than 2000 (K) can be reached. In the case of ITER-FEAT the insulator is composed of polyimide film co-wound with pre-impregnated glass fibers. Because the behavior of such an insulation at temperatures higher than 300 (°C) is not well known, experiments were started, to measure the resistivity of such an isolation as a function of temperature.

First experiments done with a double-sided printed circuit board of FR-4-type and then with a layer of impregnated spun glass fabrics and with copper electrodes revealed, that already at a temperature of approximately 130 (°C) the resistivity of impregnated spun glass fabrics fell below $1 \cdot 10^8$ (Ωm), the beginning of the wide range of semiconductors ($1 \cdot 10^6 - 1 \cdot 10^8$ (Ωm)). The application seems sufficient. In the temperature range from 20 to 700 (°C) the resistivity ρ of the impregnated spun glass fabric in Ohms can be calculated by the equation $\rho(t(°C)) = \exp\{28 \cdot \exp[-(t/200)^2] + 20 \cdot \exp[-((t-450)/200)^2] + 9.5 \cdot \exp[-((t-700)/150)^2]\}$. To enlarge the knowledge to higher temperatures experiments with stainless steel electrodes and with specimens consisting of polyimide film co-wound with pre-impregnated glass are planned [3].

Literature:

- [1] G. Bönisch : "Report on first EVITA pre-test calculations with the MAGS-Module CRYOSTAT", Report GB8-SEA5A-M6 January 31, 2000
- [2] G. Schmitz, R. Meyder, "Report on contact resistance experiments", Report GB8-SEA5-M9, January 31, 2000
- [3] G. Schmitz, R. Meyder, "First report on electrical insulation experiments", Report GB8-SEA5A, August 22, 2000

Staff:

G. Bönisch
R. Meyder
G. Schmitz

SEP 2 Doses to the Public

Dose assessment for potential European ITER sites is an ongoing task. Dose assessments for releases into the atmosphere under routine and accidental conditions were summarised for the potential European candidate sites Cadarache, Greifswald and for an Italian site in [1]. Mainly potential individual doses and areas affected by protective measures were evaluated for three types of accidents, all of them placed in the event sequence categories IV ('extremely unlikely events') and V ('hypothetical sequences'). The results of both the accidental and routine release scenarios were also compared to site independent dose limits defined in the frame of ITER.

Annual doses from routine releases (CAT-I) are close to 1 $\mu\text{Sv/a}$ for the atmospheric source terms. In none of the release scenarios of category CAT-IV the ITER limits were exceeded. In addition, relevant characteristic quantities (e.g. 95% fractiles) of the early dose distributions from the hypothetical scenarios of type CAT-V are below 50 mSv or 100 mSv, values which are commonly used as lower reference values for evacuation in many potential home countries of ITER. These site specific assessments confirmed that the proposed release limits and thus the derived dose limits for a generic ITER site are unlikely to exceed the national criteria for evacuation.

As banning of contaminated feed- and foodstuffs has been identified as potential important, investigations have been performed to evaluate the present guidelines with respect to tritium [2]. For tritium, new maximum permissible levels of contamination are under preparation within the European Union. The proposed values are 10 times higher than those applied for cesium, the leading nuclide after the Chernobyl accident. However, the dose conversion factor of HTO is more than 100 times lower than that of Cs-137, thus the present proposal seems to be too conservative. A similar situation is valid for tungsten, an important nuclide in case of releases of activated dust. For tungsten, the same level of contamination as for cesium has to be applied whereas the dose conversion factor is more than 20 times lower.

Work has been started to evaluate the compliance of ITER source terms with dose targets for emergency, delayed and long term actions which might be initiated after a potential accidental release of tritium and activation products. A methodology is being developed which allows the easy scaling of potential ITER source terms with respect to national intervention levels. To this purpose the source term is subdivided into three parts, containing activated dust, activated corrosion products and tritium. Tungsten was selected as a first material to apply this approach. First results are expected by end of 2000 / beginning of 2001.

Within the BIOMASS (BIOSpheric Modelling and ASSESSment) project testing of tritium models for routine releases into the atmosphere and hydrosphere is nearly completed. Five different scenarios have been set up covering both fixed environmental conditions to test individual model features and using measured data from sites in Canada, Russia and France to test the overall performance of existing assessment codes for routine releases. NORMTRI [3] together with a computer code describing the water movement in the upper soil participated in four of the five scenarios. The evaluation demonstrated, that NORMTRI can be applied for nearly all atmospheric release situations despite its underestimation of the concentration in soil. For the scenario on the Canadian site, results obtained with NORMTRI were closest to the measured values.

Literature:

- [1] W. Raskob, I. Hasemann and L. Di Pace, Final Documentation on Dose Assessments for Three Potential European Candidate Sites with Updated Source Terms from ITER NSSR-2. Report FZKA 6404, Forschungszentrum Karlsruhe, March 2000
- [2] W. Raskob, Are the present maximum permissible activity concentration levels in feed- and foodstuffs appropriate for tritium? Internal report, Forschungszentrum Karlsruhe, October 1999
- [3] W. Raskob, Description of the Tritium Model NORMTRI for Releases under Normal Operation Conditions. Report KfK-5364, Kernforschungszentrum Karlsruhe, 1994

Staff:

J. Ehrhardt
I. Hasemann
W. Raskob

Studies for ITER

FU05-CT 2000-00003 (EFDA/99-514) ITER Tritium Plant Design

Design of the tritium fuel cycle of ITER-FEAT

The Tritium Plant of ITER-FEAT is essential for the operation of the machine after the initial hydrogen phase, as tritium will be produced from DD reactions. Within the fuel cycle of the tokamak deuterium and later also tritium will be provided to the fuelling systems and the unburned DT fraction recovered from the exhaust gases. The design of the fuel cycle has to be based upon well proven technology to assure the safe handling of tritium along with credible accountancy and a high reliability of all components throughout the lifetime of ITER-FEAT.

Despite the reduction in fusion power by a factor of about two between an earlier (1998) ITER design and ITER-FEAT, the DT flow rates for instantaneous fuelling remained essentially the same. The shorter pulse length together with the lower fraction of time spent in burn mode as compared to dwell time, however, dictates a complete re-examination of the previous design concepts for the fuel cycle.

The two fuelling scenarios currently considered are a short (450 s) and a long burn pulse (about 3000 s). In both cases the duty factor is specified to be 25 %, which leads to dwell times of 1350 s and 9000 s, respectively. The cryo-pumps will not be regenerated during the short burn pulse, consequently the complete amount of fuel (equivalent to about 120 g of tritium for a DT shot at the specified flow rate of $200 \text{ Pam}^3\text{s}^{-1}$) must be supplied and can only be recovered during the following dwell period. The long burn pulse, on the other hand, requires a semi-continuous recovery in accordance with the regeneration scheme of the cryo-pumps and also return of the unburned fuel topped up to the required flow rate after purification and isotopic separation, including the removal of any protium.

An outline flow diagram was developed at the Tritium Laboratory Karlsruhe (TLK) to provide a consistent design for the tritium fuel cycle of ITER-FEAT. This diagram is not only indispensable for the proper identification of all interfaces within the tritium fuel cycle, but also particularly for the preparation of clear and coherent drawings defining the links to other systems, such as the cryo-pumps, the fuelling manifolds or the detritiation systems.

Meanwhile, process flow diagrams and even detailed pipe and instrumentation diagrams have been prepared at TLK for certain subsystems of the fuel cycle, i.e. the Storage and Delivery System (SDS) including Long Term Storage and Load-in / Load out, Tokamak Exhaust Processing (TEP) system, Analytical (AN) system and auxiliary sections such as common vacuum manifolds or treatment of highly tritiated gaseous wastes.

Data sheets have been produced for the interfaces identified from the outline flow diagram and developed to reflect all the detailed information typically given in pipe and instrumentation diagrams and chemical flow sheets. The corresponding list currently comprises more than fifty interfaces between different subsystems of the tritium fuel cycle and to other systems of ITER-FEAT.

The initial version of the outline flow diagram of the tritium fuel cycle was used to develop a conceptual design of the entire loop and to make information about interfaces available to the different subsystem designers. With the highly detailed drawings and descriptions existing for Analytical (AN) system, Isotope Separation System (ISS), Storage and Delivery System (SDS) and Tokamak Exhaust Processing (TEP) system, the current overall flow diagram given in Fig. 1 now reflects all the essential features of the tritium fuel cycle. Some guidance for the eye is offered in Fig. 1 by different grey shading for the subsystems.

Details of the complex diagram can not be discussed in a rather short report. However, some key information about some subsystems designed by TLK are given in the following:

An experimentally validated mathematical model of the front-end permeators was used to calculate the effective Pd/Ag membrane surface area required for the short and the long burn pulse. For the short burn pulse scenario a single feed pump, type SRTI PBT 106 (France), and two front-end permeators with 1 m^2 each would be sufficient. However, a total surface area of 5 m^2 and two feed pumps, type SRTI PBT 106, are required for the exhaust flow rate from the sequential regeneration of the cryo-pumps during the long burn pulse. Since a slug of gas is expected each time the valve to a warmed-up cryo-pump is opened a small buffer vessel is used to smooth the flow rate. One permeate pump, type SRTI PBT 105, is required per m^2 of installed permeator surface area, giving a total of five permeate pumps for the long burn pulse.

The main tasks of the SDS of the tritium fuel cycle are the supply of the required hydrogen mixtures (DT flow rate $\leq 200 \text{ Pam}^3\text{s}^{-1}$, but T_2 flow rate $\leq 100 \text{ Pam}^3\text{s}^{-1}$) plus inactive gases (He, Ne, Ar, N_2 , H_2 , He + O_2) to the Torus for operation and also for the safe handling / storage of tritium in reservoirs and in ZrCo getter beds equipped with in-bed calorimetry.

Two ZrCo getter bed batteries are required to store the D product (with 0.6% tritium) and the 90% T/10% D product of the ISS respectively. These getter beds, each with a nominal storage capacity of 100 g tritium, together with associated reservoirs, supply the deuterium and tritium during the first minutes of the plasma until, at least for the long burn pulse, the hydrogen isotopes processed in TEP and ISS are recycled to the supply tanks and can be added to the gases from the getter beds. D-T mixtures of different concentrations are produced by actively mixing controlled flows from these reservoirs. A third ZrCo getter battery is used to store mainly D-T gases. Due to its low tritium concentration of less than 0.01%, the deuterium for Neutral Beam Injection is stored and supplied from a large tank. Ten further ZrCo beds of a simpler design (without in-bed calorimetry) are installed in the Long Term Storage Vault to accept, for example, the tritium recovered from co-deposits when the limit of the tritium inventory in the torus is reached.

The ZrCo beds of each battery have common inlet and outlet manifolds which permit different actions to be performed at the same time, such as supply of gas to torus, transfer of a sample from any getter bed to the AN system, pressure-volume-temperature and composition (pVT-c) measurements for accountancy purposes, absorption of gases from TEP or ISS, re-circulation of hydrogen to avoid blanketing of getter beds or simple transfer of the content of one bed to another one. Further tasks of SDS are the determination of the tritium supplied in special tritium shipping containers to the ITER site by dedicated calorimeters, transfer of that tritium to the 90% T/10% D getter beds and performance of (pVT-c) measurements, evacuation of the various volumes by pumps, collection of the tritium decay product helium-3, and determination of the decay heat by accurate measurements of the He flow and temperature at the inlet and outlet of each getter bed.

The final design package will be available for ITER JCT by March 2001.

Staff:

C. Caldwell-Nichols
L. Dörr
M. Giugla
R. Lässer
R.-D. Penzhorn
P. Schäfer

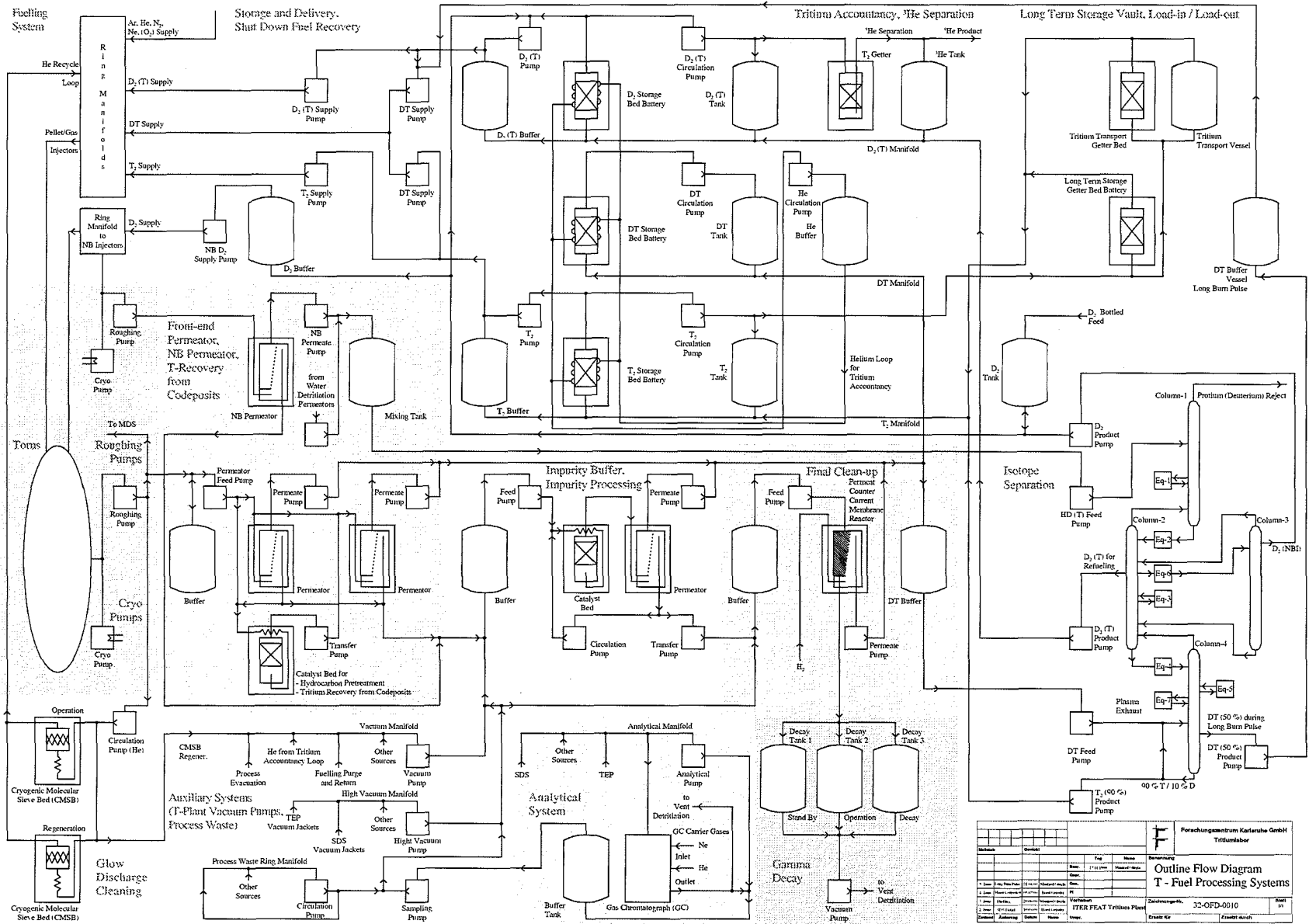


Fig. 1: Overall outline flow diagram for the tritium fuel processing systems of ITER-FEAT

Blanket HCPB Concept

TTBB-001 Test Blanket Module (TBM) Adaptation to Next Step

Assessment of Modified Machine Parameters on TBM Design and Testing

In order to reduce cost, a new concept of ITER ("ITER-FEAT") has been developed in 1998/99 leading to significant changes in design and operational conditions. This necessitated an assessment of blanket test program and objectives as well as a revision of the test module design and the test blanket subsystems. The related activities are reported in this contribution.

Objectives, test strategy and TBM design

The main objectives of testing tritium breeding blanket concepts in ITER-FEAT are as before:

- demonstrate tritium breeding performance and verify on-line tritium recovery and control systems;
- demonstrate high-grade heat extraction suitable for electricity generation;
- validate and calibrate the design tools and the database used in the blanket design process including neutronics, electromagnetic, heat transfer, and hydraulics;
- demonstrate the integral performance of blanket systems under different loading conditions;
- observe the influence of possible irradiation effects on the performance of the blanket modules.

These overall objectives are the frame for the specific test programme and objectives to be developed for the different blanket concepts taking into account the particular generic design features and issues, the capabilities and limitations of ITER-FEAT as test environment, and the alternatives to carry out particular tests in out-of-pile facilities or fission reactors at lower cost or under more relevant conditions.

The review of the Helium Cooled Pebble Bed (HCPB) blanket has led to a test concept consisting of four test blanket modules (TBMs), each devoted to a family of objectives. The first test module with the label "EM-TBM" serves to investigate the consequences of electromagnetic transients and ferromagnetic effects. The second module ("NT-TBM") is related to the test of blanket neutronics and tritium production. The third module ("TM-TBM") is to investigate the thermomechanical behaviour of pebble beds, a key issue of the HCPB blanket concept. The fourth module ("PI-TBM") is to demonstrate the integral performance of a complete HCPB blanket system under different loading conditions.

To reach the specific objectives of each TBM it is desirable or even mandatory to establish representative operational conditions ("act-alike" tests). Furthermore, the monitoring of the test modules, in particular of parameters relevant for the specific objectives, requires appropriate instrumentation. This is of particular importance with respect to the validation and calibration of the design tools, one of the main objectives of blanket testing in ITER-FEAT. Besides the data obtained by the on-line instrumentation, post-test examinations in the Hot Cells will deliver significant information on the operational behaviour and for code validation.

The envisaged test program and strategy (see below) allows to achieve most of the general objectives mentioned above. Restrictions have to be made mainly with respect to the last objec-

tive, the observation of possible irradiation effects: the maximum fluence of 31.5 MWd/m^2 expected at the end of the high duty D-T phase is too low to cause any significant radiation damage.

The arrangement of the HCPB-TBMs in the horizontal port of ITER-FEAT is shown in Fig 1. The port is shared with a Japanese helium-cooled solid breeder TBM which will be inserted in the upper compartment of the frame serving as support and interface between the TBMs and the ITER-FEAT environment. The given port size allows outer dimensions of the modules of 740 mm in poloidal, 1268 mm in toroidal and 600 mm in radial direction. The radial thickness of the breeding zone amounts to about 400 mm. This leaves a space of about 200 mm at the rear side of the module for the accommodation of the main headers and the connecting tubes. An additional space of 180 mm is available for the attachment of the module to the frame.

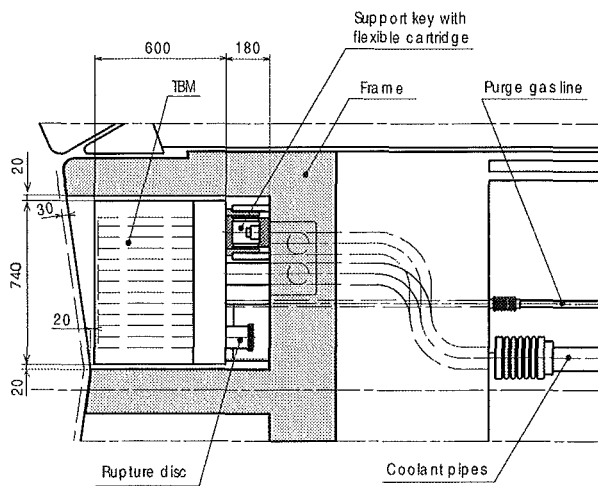


Fig. 1: Arrangement of the EU HCPB-TBM in a horizontal port of ITER-FEAT

The operation plan of ITER foresees a first operational phase extended over about 10 years. During this time, four different plasma phases follow one another: starting from the first plasma with hydrogen (H-phase), the operation goes on with the D-plasma phase, the low-duty DT-phase, and finally with the high-duty DT-phase. Neutrons will be involved from the beginning of the second phase with a D-plasma. Significant numbers of burn cycles of significant duration can be expected from the second half of the low-duty DT-phase.

The strategy for HCPB blanket testing is adapted to this schedule. The EM-TBM which does not need neutrons, will be installed in ITER at the beginning of operation. The NT-TBM should be inserted already in the D-D phase and unloaded at about the middle of the low-duty DT-phase; it will be replaced by the TM-TBM. This allows initial tests in the second half of this phase and final tests in the first half of the high duty DT-phase. The remainder of the latter phase will be devoted to tests with the PI-TBM.

A detailed plan for further operation beyond this period of 10 years has not been developed because it will depend on the plasma and operating experience obtained thus far. However, an accumulation of an average neutron fluence on the first wall of at least 0.3 MWa/m^2 at the end of a total 20-years operation program is envisaged. The PI-TBM can be installed again after about 2 years of refurbishment of the ITER machine to continue the test of the integral blanket system in the long term.

To avoid major irregularities of the plasma-facing first wall, and to assure the necessary shielding in the port region, test mod-

ules must probably be present at each port position during all the operation of ITER. To assure this for the HCPB test blanket, the following strategy is recommended: the normal procedure is that each TBM is replaced by the follower as envisaged in the test program if a significant test can be already carried out. If this is not the case (e.g. the NT-TBM during the H-H phase in which neutrons are not produced), a standard dummy module will provide the necessary stand-by. This dummy module must assure the base functions of cooling and neutron shielding in any operational phase of ITER.

Necessary changes, e.g. of instruments and sensors, as well as minor repairs (if possible), can be carried out during scheduled shut-down times. If in case of an unexpected failure repair during shut-down is not possible, then the follower will be inserted earlier than scheduled if a significant test can already be carried out. This is feasible because each TBM is compatible with the operational conditions of ITER during the preceding phase.

Helium cooling subsystem (HCS)

The HCS for the TBMs to be tested in ITER has been revised because of the reduced size of ITER FEAT compared to ITER EDA and as result of the changed testing strategy of the HCPB blanket, which involves now testing of four types of TBMs during the first 10-year period of ITER operation. The changes implied a number of modifications in the layout, affecting all design data of the helium cooling subsystem, while keeping the basic concept unchanged.

One significant difference compared to the original version is the reduction to a single loop design from the two-loop design used earlier for redundancy purposes. This became possible since safety assessment had shown that decay heat removal can be accomplished without any active cooling. Other major changes result from the relocation of the main components to the tokamak cooling water system (TCWS) vault, implying much longer piping. Furthermore, the concept of neutronics testing at low TBM temperatures (around 100°C) with subsequent tritium release at high temperatures (500°C) requires a much larger temperature range to be covered by the cooling system. The thermal-hydraulic conditions are summarised in Table 1 for the two bounding cases of TBMs, i.e., the plant integration PI-TBM and the neutronics and tritium production NT-TBM.

Table 1: Nominal Operating Conditions of the Helium Cooling System for two types of TBMs

	PI-TBM	NT-TBM
Total heat to be removed (MW)	1.08	1.08
Primary coolant	helium	helium
Number of loops	1	1
Temperature at TBM in/out (°C)	250/500	100/180
System pressure (MPa)	8	8
Mass flow rate (kg/s)	0.83	2.6
Total pressure loss (MPa)	0.07	0.43
Helium inventory (kg)	15	20.6
Typical tritium inventory (g)	10 ⁻³	10 ⁻³
Secondary coolant	water	water
Temperature at HX in/out (°C)	35/75	35/75
System pressure (MPa)	2	2
Mass flow rate (kg/s)	6.5	6.5

Main components are the heat exchanger, circulator, electrical heater and dust filter (Fig. 2). The pipework with a total length of 180 m takes more the 50 % of the helium inventory. The pressure control equipment is connected to several sets of tanks. All together requires a foot print size of 16 m².

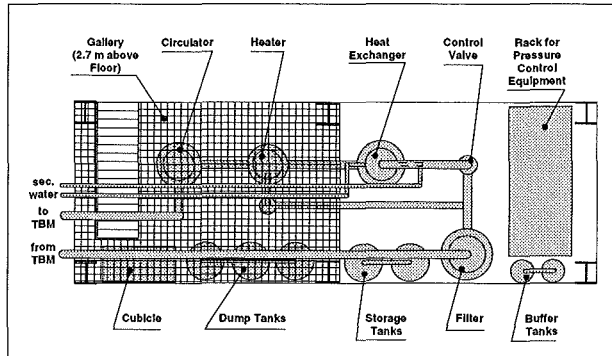


Fig. 2: HCPB helium cooling system arrangement (plan view) in the TCWS vault (footprint size 16 m², height ca. 5 m)

Coolant purification subsystem (CPS)

The cooling subsystem for the TBM has been reduced to a single loop. The consequences for the layout of the components of the CPS have not yet been investigated. As the mass flow rate of both the CPS for the NT-TBM and for the PI-TBM are expected to be nearly the same as of ITER-FDR (Final Design Report), the space requirements remain in the specification of the previous ITER-FDR version.

Tritium extraction (TES) and measurement system (TMS)

As the helium mass flow of the TES at PI-TBM does not change substantially the original design of TES remains valid. An additionally implemented task is the assessment and removal of the tritium produced in the breeder of the NT-TBM. For the operation of the NT-TBM instead of the TES a special system is installed in the vault near the vacuum vessel door in order to remove and accurately measure the tritium produced in the TBM. The flow diagram of this system, called Tritium Measurement system (TMS), is shown in Fig. 3.

The tritium extraction is achieved by purging the breeder with He containing 0.1% H₂ in view to facilitate the tritium release by isotopic exchange. However, purging with He the pebble bed will release also some water. The later could also undergo isotopic exchange and give tritiated water.

As tritium in water (HTO) is estimated to be 10 000 times more hazardous than tritium gas, it is reduced to hydrogen or hydrogen isotopes and the tritiated gas is collected in appropriate Uranium or ZrCo beds. Subsequently, the tritium activity is measured calorimetrically by measuring the heat released by the tritium decaying.

To achieve a very high reduction of water (>90%) the use of an appropriate bed containing a getter alloy such as Zr-Fe-Mn or Zn is required. The advantage of such a method is that the hazardous water production is avoided.

Humidity sensors before and after the reduction bed as well as tritium monitors control the efficiency of the whole process. After water reduction the tritium accountancy could be performed by using a ZrCo bed coupled to a gas flowing calorimetry system. The method provides sufficient accuracy and possesses a detection limit of about 10mCi of tritium (10⁻⁷ mol). Such a bed could be used for "in-line" measurements, or after it is filled up with tritium it could be removed and transported to a separate facility where the tritium is released by heating and measured.

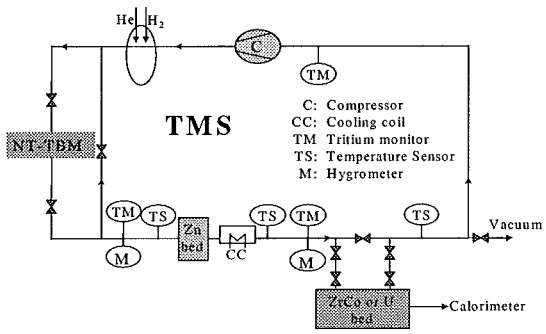


Fig. 3: HCPB Tritium measurement system for NT-TBM operation

Staff:

- N. Bekris
- L. Boccaccini
- S. Gordeev
- S. Hermsmeyer
- E. Hutter
- K. Kleefeldt
- S. Malang
- K. Schleisiek
- I. Schmuck
- H. Schnauder

TTBB-002 Blanket Manufacturing Techniques

TTBB-002/1 Second Cooling Plate Specimen Manufactured with Improve HIP Parameters

Two-step HIP experiments

The diffusion welding experiments using two-step hot isostatic pressing (HIP) [1] to produce fusion blanket components out of MANET II with internal cooling channels were continued with specimen plates of the same first-wall and cooling plate geometry, while the welding preparation was modified. This experiment [2] (internal designation: the 6th series) were carried out using the same procedure of "Two-step HIP Process" as applied in the previous experiment series, i.e. first by pressure plates protected and encapsulated with relatively low gas pressure at max. 120 bar (1050 °C, about 2 h) and afterwards with open cooling ducts and a high pressure at 2000 bar (1050 °C, about 2 h). With this second HIP step the still existing defect zone in the HIP joint are pressed together and the strength of the HIP joints can be improved by further diffusion procedures.

Specimens preparation

The joining surfaces of the specimens had been dry milled to a surface roughness of $R_t \leq 3 \mu\text{m}$. Cleaning took place in an ultrasonic bath with acetone. As getter material, zirconium wires had been inserted into the cooling channels of every second plate. Quartz glass mats of a fine structure were used as separators between the specimens, the pressure plates and the encapsulating jacket during the first HIP step.

Experimental results

Post-welding examinations showed a still permissible deformation of the channel webs in both types of plates. For the first time, good strength values were achieved for both types of plates, with and without getter material after encapsulated HIP (1st step, Fig. 1) already [2]. Particularly for specimens with getter material higher strength values were reached in each case. Mean values of yield and ultimate tensile strength of 539 / 684 MPa could be achieved for the first wall specimens and 550 / 664 MPa for the cooling plate specimens, respectively. These strength values were further increased by open HIP (2nd step, Fig. 2) to 722 / 760 MPa for the first wall specimens and 645 / 750 MPa for the cooling plate specimens, respectively. They were found to be in the range of the strength of the basic material. Ultimate elongation of specimens with getter material amounted to about 7 % for first-wall specimens and to about 12 % for the cooling plates and, hence, by far exceeded the values reached by specimens without a getter material.

Conclusion and Outlook

These diffusion welding experiments with "two-step HIPing" [2] for the first time succeeded in reaching a good quality of the welds for both types of plates. After this successful 6th experiment series further specimens were manufactured for the following 7th experiment to verify the good results and to further improve the HIP parameters. Furthermore, the specimens preparation will be modified, e.g. using ground joint surfaces instead of milled surfaces and sealing the outside edge of welding seam by EB welding. As the latter for the first time also specimens made from EUROFER will be diffusion-welded. The 7th experiment will probably start in the third quarter of 2000.

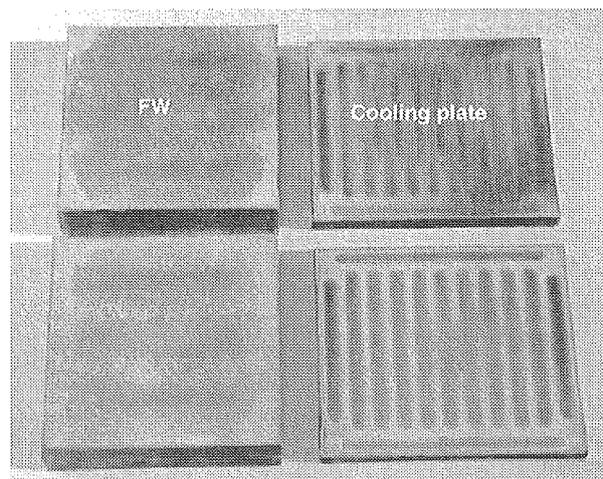


Fig. 1: Test specimens (FW and cooling plate) after the first HIP step

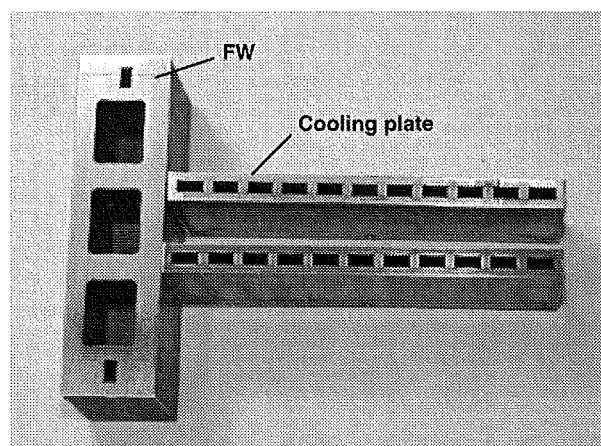


Fig. 2: Test specimens (FW and cooling plate) after the second HIP step

Literature:

- [1] G. Reimann, Diffusionsschweißversuche in Heißisostatischen Pressen zur Herstellung von Plattenbauteilen mit inneren Kühlkanälen für Fusionsblankets, FZK-PKF Report, August 1999.
- [2] G. Reimann, Diffusionsschweißversuche in Heißisostatischen Pressen zur Herstellung von Plattenbauteilen mit inneren Kühlkanälen für Fusionsblankets - sechste Versuchsreihe -, FZK-PKF Report, August 2000.

Staff:

P. Norajitra
G. Reimann

TTBB-002/2 Blanket Box Section with HIP-Joined Stiffening Plate

a) Determination of Optimum Diffusion Welding Parameters

The basic tests to determine the optimum conditions for diffusion welding of ferritic-martensitic (FM) steels by hot isostatic pressing (HIP) were completed. The final tests have shown that the parameters found optimum for MANET are likewise suited for EUROFER and allow to produce joints with mechanical properties (strength, ductility, fracture toughness) in the range of the base material. On the other hand a HIP specimen with welding surfaces machined by wet grinding had a significantly reduced fracture toughness. This result confirms that dry machining, e.g. dry milling, is favourable for obtaining high quality HIP joints.

b) Joining of FW and Cooling Plate by Diffusion Welding

With respect to joining of the blanket box and the cooling/stiffening plates, a small-scale mock-up representing a 90° bend of the First Wall (FW) and a corner of a plate was welded successfully in 1999 applying the HIP parameters found optimum in the tests mentioned above. Tensile and impact samples showed perfect mechanical properties of the joint.

As a final demonstration of the feasibility of this technique, a second mock-up with a U-shape FW (see Fig. 1) has been manufactured and is presently being investigated in non-destructive and destructive tests. This mockup consists of a U-shaped 60 mm segment of a 300 mm wide blanket box with one cooling plate. Cooling channels were omitted to reduce cost. So the FW plate was machined of massive MANET II and bent to give it the required U-shape.

After measuring and modelling by CAD it was machined to the intended shape. The cooling plate including the arched flange towards the FW was machined equally – the last milling step (joining surface) was carried out without coolant/lubricant to prevent any contamination of the joining surfaces. Both pieces fitted practically with zero gap and were joined after the usual cleaning procedure. Seal-welding in a evacuated electron beam (EB) facility caused some problems due to remaining magnetization of a handling device. After several efforts the flange surrounding seam could be completed. As the leak tests result was better than 10^{-4} mbar · l · s⁻¹ the diffusion welding process was done in a HIP facility at 100 MPa and 980 °C for 3 hrs. Good bonding was achieved and stated by ultrasonic test.

The shrinking of the FW plate during HIP and thermal treatment was zero which was expected since the joining of the two pieces was done without remaining gap. Now mechanical tests (tensile and charpy impact) are done to investigate the bonding quality.

c) Manufacturing of a Semi-scale Mock-up

The manufacturing of a semi-scale mock-up (SSM) is an integral demonstration of the feasibility to manufacture the structural parts of a HCPB blanket according to the reference fabrication procedure.

A first mock-up with a size of 500x250x280 mm including 8 FW cooling channels and five dummy cooling plates was designed in 1998. Manufacturing was started in 1999. However, insufficient bonding of the diffusion-welded FW caused the plate to break during bending before reaching the bending angle of 90°. Subsequently, it was decided to manufacture a second SSM, however with reduced dimension, and only two cooling channels

and three cooling plates. In spite of these restrictions, the mock-up included the most important steps of the reference HCPB blanket manufacturing sequence.

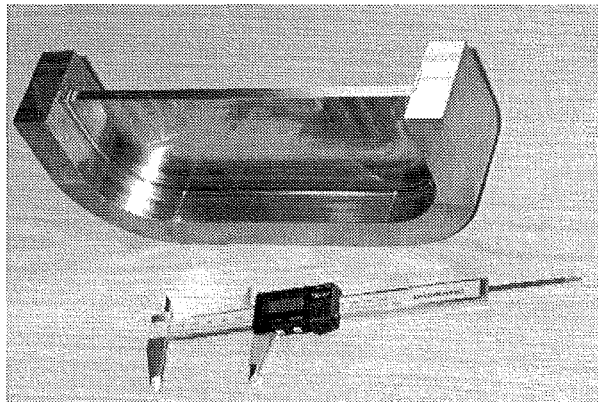


Fig. 1: Second mock-up with diffusion-welded joint between FW and cooling plate

As for the first mock-up, the two plane plates of the first wall were machined including the grooves representing the cooling channels. The rib between the cooling channels was tungston inert gas (TIG) welded from both sides with overlapping seams whereas the massive borders were only seal-welded by TIG and EB, respectively. Leaktightness of the seal weld was tested by He bombing test and found to be better than 10^{-4} mbar · l · s⁻¹. This was sufficiently low to allow diffusion welding of the two half plates of the FW by HIP in a single step without encapsulation. Ultrasonic tests confirmed the correct bonding of the plates.

Subsequently, bending was carried out without any problems. The bending angles were both within the specified tolerance of $90^\circ + 0.5^\circ/0^\circ$.

Based on measurements on a coordinate measuring device, a complete 3D model of the bent plate was established by CAD allowing to design the final shape including the wedges and weld preparation. Machining was carried out on a CNC milling machine. Finally, the three dummy cooling plates were TIG-welded to the U-shape FW in a fully mechanized welding facility (see Fig. 2).

After completion of the manufacturing steps, the mock-up is presently inspected. The accuracy achieved is within 0.3 mm for the distance and better than 0.2 mm for the parallelism of the plates. The shrinkage of the mock-up box in toroidal direction due to the 6 welding seams of the three cooling plates of 0.75 mm is in agreement with earlier tests. The results of the destructive tests are expected until the end of 2000.

This report includes also work carried out in Oct. – Dec. 1999 under former Task B3.1.1.

Literature:

- [1] K. Schleisiek, T. Lechler, L. Schäfer, P. Weimar: Diffusion Welding Parameters and Mechanical Properties of Martensitic Chromium Steels. ICFRM 9, Colorado Springs, USA, Oct. 1999.

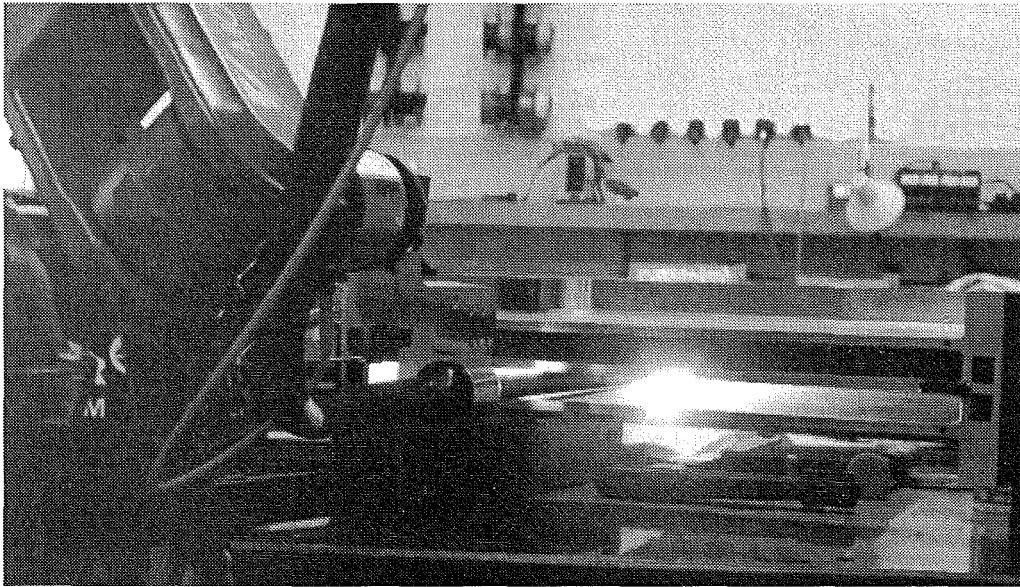


Fig. 2: Fully mechanized TIG welding of the cooling plates into the U-shape FW of the semi-scale mock-up

[2] G. Reimann, T. Lechler: Diffusion Welding Experiments Using Hot Isostatic Pressing to Manufacture Components for HCPB Blankets (Subtask B 3.1.1). FZK Internal Report IRS-Nr. 2/00, Febr. 2000.

Staff:

H.-J. Fiek, Fa. Ingenieurbüro Fiek
S. Gordeev
P. Graf
R. Vouriot
H. Kempe
T. Lechler
E. Nold
L. Schäfer
K. Schleisiek
P. Weimar
H. Zimmermann

**TTBB-003
Pebble Bed Assembly Development and
Testing**

**TTBB-003/1, 2
Operation and Analysis of HEBLO Test Section**

First experiment series under steady-state condition

After intensive preparations for the Helium Blanket Test Loop (HEBLO) experiment containing layout calculations, construction, fabrication and assembly of the test section as well as the preceding tests of components [1] the first experiment series under steady-state conditions was accomplished successfully. Simulation calculations for this experiment were carried out in parallel which showed a good agreement with the measurements [2, 3]. In the following, steps of work are described and the experimental and calculation results are discussed.

1. Pre-selected thermohydraulic conditions

According to the DEMO layout condition [4, 5] different He temperatures in the neighboring FW coolant channels are simulated for the achievement of the maximum temperature stresses at the hot spot with the largest FW surface heat flux of 50 W/cm² which is realized in HEBLO by a high performance heating plate of 3.6 kW maximum power. In the HEBLO facility there are two possible split flow conditions I and II. For the condition I a smaller amount of the hot He gas is passed through the half channel and the larger amount of cooler He gas is passed through the full channel or another way around for the condition II (larger amount of hot He gas for the larger full channel). The thermohydraulic pre-checks in the HEBLO facility have shown, that only the split flow condition I can be fully realized as predicted, but for the split flow condition II about 80% of the theoretical flow rate could be achieved because of the uncertainty of the pressure losses especially in the gas heaters that increase strongly with the mass flow and with the higher gas temperature. This uncertainty will only have a negligible effect

on the temperature distribution in the pebble beds and in the test section during the experiments.

2. Instrumentations

In each pebble bed four thermocouples (TC) are installed across the poloidal thickness (Fig. 1) and are shifted arranged in toroidal direction especially for the ceramic pebble bed in order to reduce the mutual influence and disturbance between the TCs because of the small dimension of the pebble bed height. In addition, because of the difficult spatial accessibility for the TC assembly it was not possible to place the TCs axes ideally on the isothermal lines (equidistance to the cooling plate and heating plate) at expense of the accuracy of the temperature measurements due to the temperature gradients along the TC axes themselves.

3. Experimental results

A series of experiments with altogether 61 measurements under various steady-state conditions with split flow mode I and II were carried out. For safety reasons not to over-strain the heating plates in these first experiments, the maximum heating plate temperatures were limited at 700°C and should be increased to 900 °C at the end of the experiment series in 2001. All measurement data (temperature, flow rate, heat power, purge gas flow and pressure drop, etc.) are full-automatically online recorded. Comparisons of repetition experiments show that the results of the temperature measurements are reproducible, an indication that the pebble beds and heating plates are still intact.

For example the measured temperatures according to the thermocouples (TC) arrangement (a-d) in the Be and Cer pebble beds are shown in Fig. 1 for split flow mode II under stepwise increasing of heating plate powers. Because of the rather small bed heights the numbers of the TCs are limited and are not large enough for a more detailed temperature measurement across the pebble beds. With the extensions of the temperature slope within the middle range of the pebble beds (dotted lines)

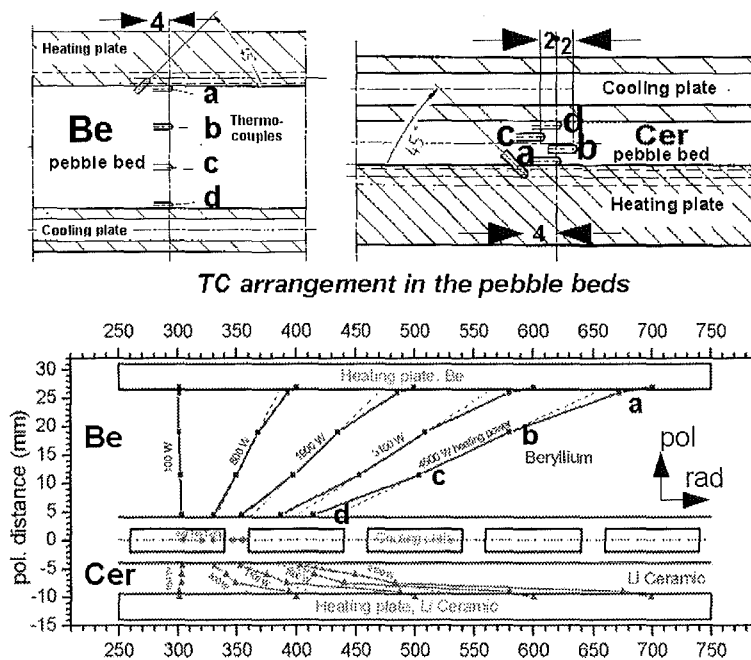


Fig. 1: Steady-state experiment, measured temperatures across the Be and cer. pebble beds. (Measurement positions: a: NW-HP, b: PB, c: PB, d: NW-CP; CP = cooling plate, FW = first wall, HP = heating plate, NW = near-wall, PB = pebble bed)

towards to the heating plates (HPs) and cooling plate (CP) the near-wall temperature differences at the HP and CP can be well recognized. The maximum FW temperature in this experiment series reaches a value of 453 °C and is lower than the expected DEMO value of 550 °C. That is because of the fact that a 1 mm thin graphite layer was necessary between the FW and the heating plate for heat flux equalization and so to avoid the hot spots on the FW heating plate.

4. Simulation calculations

The two-dimensional temperature and stress calculations were carried out with the finite element (FE) program ABAQUS. For the stress calculations the steel structure containing the diffusion welded FW and CP and the outer frame is considered explicitly. The ground rules and the material data used for the calculations, i.e. thermal conductivity and the near-wall heat transfer coefficient of the binary beryllium and the ceramic pebble beds as well as thermal conductivity and strength data for MANET, are described in detail in the DEMO blanket layout in [5]. Generally, the heat transfer coefficient of the intermediate graphite layer mentioned above depends strongly on the contact pressure and on the sort of the gas atmosphere. The calculations for this experiment (high contact pressure by compression bars in He atmosphere) showed that a value of over-all heat transmission coefficient of 3000 W/m²K would give the best fit of the calculated FW temperature in comparison to the measured value. For the helium gaps between the inner frame carrying the heating plates and the surrounding outer structural frame in the test section heat transfer by gap conductance and gap radiation was taken into account.

5. Calculation results

Fig. 2 shows for example the calculated temperature distribution for a measurement with split flow mode II with poloidal temperature gradients across the Be and Cer pebble beds through the location of their maximum temperatures and the measured values at the respective thermocouples location. For the Be pebble bed there is a good agreement (within a range of about 10 K) between the calculation and the measurement. For the Cer pebble bed the measured temperatures are definitely lower than the calculated ones, in particular a remarkable strong difference of about 100 K for the value at the thermocouples position b. This discrepancy is to be due to the fact that a large number of thermocouples (Ø 1 mm) with a relatively large steel portion and much higher thermal conductivity than that of the ceramic in addition are densely accommodated in a close Cer pebble bed (4.5 mm high). Another explanation could be the positioning accuracy of the thermocouples and the fact that their axes do not lie on the isothermal lines but partially even along the relative cooler wall of the cooling plate.

For the 2D stress calculations with ABAQUS the external load on the cooling plate possibly caused by the differential thermal expansion between the pebble beds and the surrounding steel structure was not taken into account here because of the lack of calculation methods and formulas. The evaluation of the stresses is based on the ASME ground rules used in the DEMO calculations [3]. As calculation results, the maximum primary stresses amount to 54 MPa for the FW and 61 MPa for the cooling plate and are far below the allowable values of 230 and 308 MPa, respectively, with respect to the local temperatures. For the calculation of the secondary stresses for some experimental cases with highest FW temperature attained the individual temperature distributions in the steel structure achieved from the temperature calculations above are used as input. The maximum primary plus secondary stresses here amount to 440 MPa for the first wall, 579 MPa for the cooling plate and 348 MPa at the TIG welding joint (cooling plate/first

wall). In all cases, the total von Mises stresses are well below the allowable values, with respect to the local temperatures.

Conclusion and outlook

The first experiment series under steady-state condition with altogether 61 measurements with different flow modes and temperature levels up to a maximum temperature at the pebble bed heating plates of 700 °C was accomplished successfully. All components of the HEBLO test section and of the HEBLO facility functioned well and withstood so far all thermal-mechanical loads. The maximum helium mass flow in the HEBLO test loop predicted in a layout and adaptation of the HEBLO loop for these experiments could be achieved. Comparisons of repetition experiments show that the results of the temperature measurements are reproducible, an indication that the pebble beds and heating plates are still intact. The results of 2D simulation calculations for the first series of the HEBLO experiment show good agreements between calculated and measured temperatures.

The following HEBLO experiment series under temperature transient condition was defined and started successfully. By means of cyclic power control of the gas heaters and the pebble bed heaters a maximum temperature ramp of about 200 K within the pebble beds could be achieved (Fig. 3). These temperature cyclic tests for the pebble beds will continue till the end of 2000. Detailed calculations and evaluation of the experimental results are planned. The following experiments planned for 2001 concern transient experiments under the simulated boundary conditions for accidental case (e.g. loss of flow).

Literature:

- [1] P. Norajitra, H. Lehning, D. Piel, G. Reimann and R. Ruprecht, State-of-the-art of the third HEBLO experiment based on the EU Helium-cooled pebble bed blanket concept, Proceedings of the 20th Symp. on Fusion Technology, Sept. 7-11, 1998, Marseille, France, Vol. 2, pp 1187-1190.
- [2] P. Norajitra, D. Piel, G. Reimann and R. Ruprecht, The First Series of the HEBLO Experiment with the HCPB Small-scale Test Section, FZK-PKF Report, 2000.
- [3] P. Norajitra, D. Piel, G. Reimann and R. Ruprecht, First HEBLO Experiments Based on the Eu HCPB Blanket Concept, 21th Symp. on Fusion Technology, Sept. 11-15, 2000, Madrid, Spain, to be published in Fusion Engineering and Design.
- [4] M. Dalle Donne, U. Fischer, P. Norajitra, G. Reimann and H. Reiser, European DEMO BOT Solid Breeder Blanket: The Concept Based on the Use of Cooling Plates and Beds of Beryllium and Li₄SiO₄ Pebbles; Proceedings of the 18th Symposium on Fusion Technology, Karlsruhe, Germany, August 22-26, 1994, vol. 2, pp. 1157-1160.
- [5] P. Norajitra, Thermohydraulics Design and Thermo-mechanics Analysis of Two European Breeder Blanket Concepts for DEMO; FZKA 5580, 1995.
- [6] VDI Wärmeatlas, VDI-Verlag, Düsseldorf, 1988.

Staff:

P. Norajitra
D. Piel
G. Reimann
R. Ruprecht

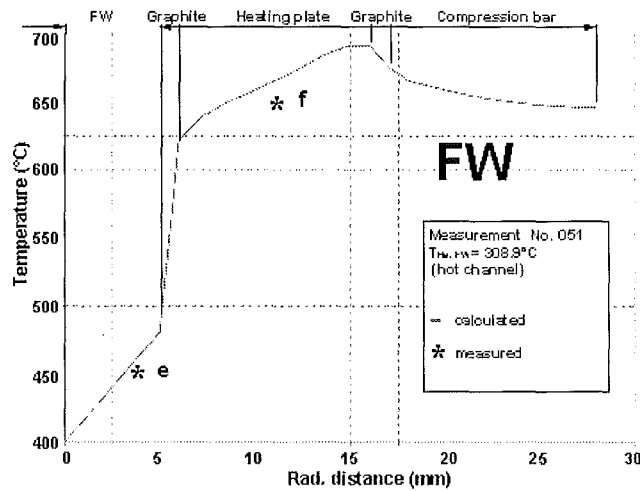
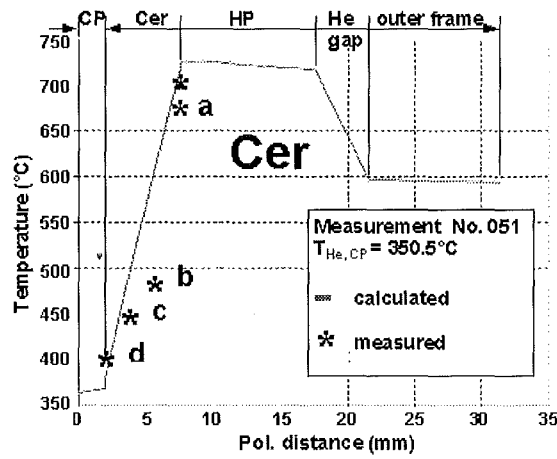
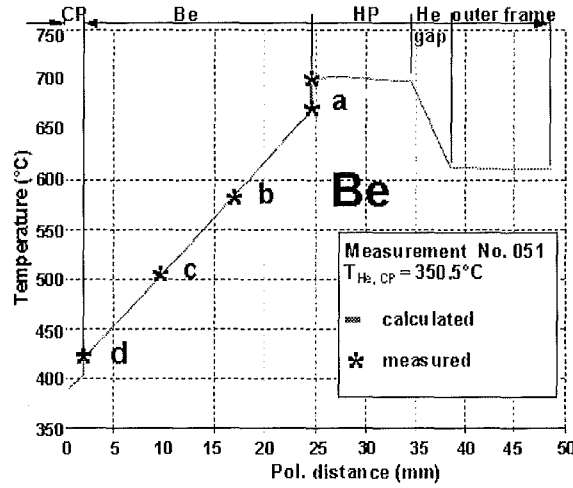
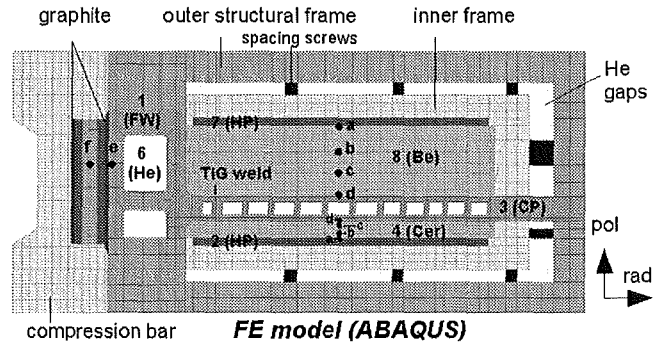


Fig. 2: Steady-state experiment, calculated temperatures across the Be and cer. pebble beds

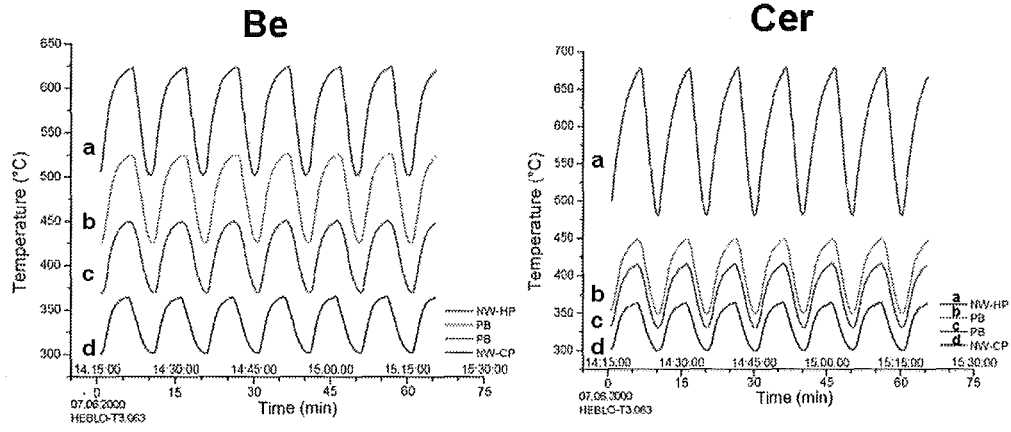


Fig. 3: First cyclic temperature transient experiment, measured temperatures within the pebble beds

TTBB-005 Development of Ceramic Breeder Pebble Beds

TTBB-005/1 Characterisation of Li_4SiO_4 Pebbles

In the period 1998-2000 a campaign of three long time annealing experiments (aging) was carried out at Forschungszentrum Karlsruhe (FZK) in order to study the behaviour of ceramic breeder pebbles in HCPB-blanket relevant temperature and atmosphere ($\text{He} + 0.1\% \text{H}_2$). The experiment were performed with lithium orthosilicate ($\text{Li}_4\text{SiO}_4 + \text{SiO}_2$ from FZK) pebbles, fabricated by the melting-spraying method, lithium metatitanate ($\text{Li}_2\text{TiO}_3 + \text{TiO}_2$ from CEA) and lithium metazirconate ($\text{Li}_2\text{ZrO}_3 + \text{ZrO}_2$ from CEA) pebbles, fabricated using either an extrusion-spheronization-sintering or the agglomeration-sintering process. To achieve representative HCPB blanket End-of-Life conditions for the pebbles, a temperature of 970 °C and an annealing time of 96 days was chosen. In April 2000 the third long time annealing experiment was concluded. In this aging the following materials were tested:

- Lithium orthosilicate ($\text{Li}_4\text{SiO}_4 + \text{SiO}_2$) pebbles supplied by Forschungszentrum Karlsruhe and fabricated by SCHOTT Glaswerke by melting-spraying process. Fig. 1 shows the pebbles in initial conditions. Agglomerations of several small pebbles on the surface of larger ones originated during the spraying phase in the production process, and the number of such agglomerations can be reduced. The pebbles had natural ^6Li -enrichment and the diameter was in the range 0.25-0.63 mm. No pre-annealing of the pebbles was performed.
- Lithium orthosilicate ($\text{Li}_4\text{SiO}_4 + \text{SiO}_2$) pebbles supplied by Forschungszentrum Karlsruhe and fabricated by SCHOTT Glaswerke by melting-spraying process. The pebbles had 50% ^6Li -enrichment and the diameter was in the range 0.25-0.63 mm. No pre-annealing of the pebbles was performed.
- overstoichiometric $\text{Li}_2\text{TiO}_3 + \text{TiO}_2$ pebbles supplied by CEA and fabricated by extrusion and sintering process (Fig. 2). The diameter of the pebbles was in the range about 1 mm. For this material a pre-annealing of 10 hours at 500 °C in air was performed before starting the long time annealing.

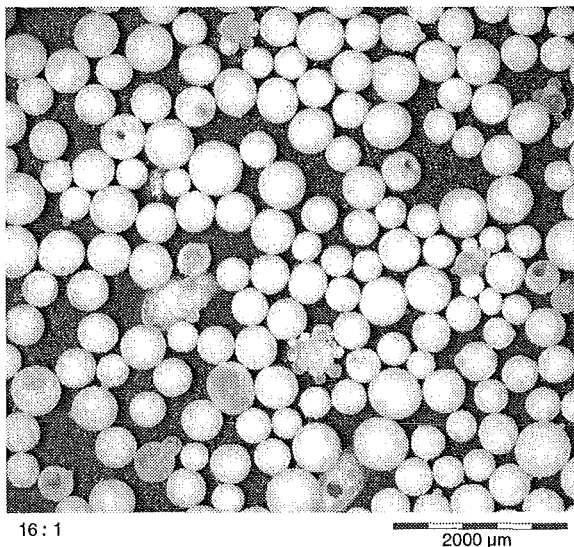


Fig. 1: Li_4SiO_4 pebbles (natural enrichment)

The experiment was performed in an oven consisting of three tubes of Al_2O_3 , one tube for each specimen, with separate purge gas flow (Fig. 3). At the tube inlets the pressure of the purge flow and its H_2O content were measured. The moisture content in the purge flow was also measured at the outlets together with the mass flow. Sintered steel filters were used at the tubes outlets to have a qualitative indication of the vaporisation of lithium from the pebbles. The purge flow was 99.9 % $\text{He} + 0.1 \text{ vol}\% \text{H}_2$ (0.6 l/h).

Samples of all the specimens were analysed before, during and after the aging. To characterise the ceramics following analyses were performed:

- Measurements of Li-content (atomic emission spectroscopy) and of Si- and Ti-content (X-ray fluorescence analysis) in the pebbles.
- X-ray diffraction analysis (XRD) for the phase composition analysis;
- scanning electron microscopy (SEM) and light-microscopy for the microstructure analysis;
- He-pycnometry and Hg-porosimetry for density and porosity measurements;
- Brunauer, Emmet and Teller (BET) method for the specific surface area measurement;
- crush load determination;

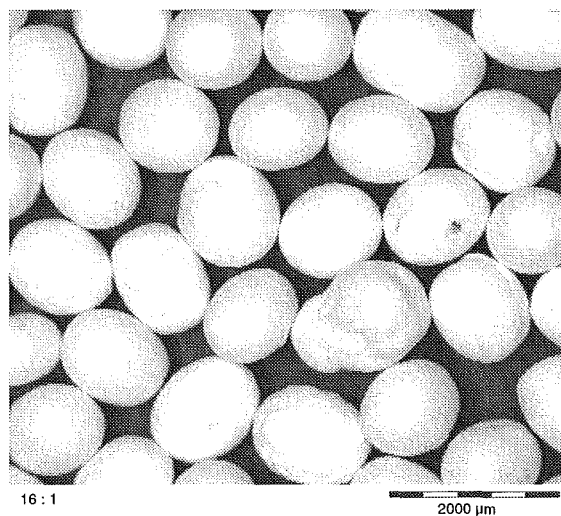


Fig. 2 Li_2TiO_3 pebbles

During the experiment 2 vpm of moisture were measured in the purge flow at the inlet of each pipe. After an increase at the beginning of the experiment (the oven was opened to put inside the specimens), stationary values of water content were reached at the outlet of each pipe after several weeks. About 3 vpm were measured for both lithium orthosilicate specimens, and about 18 vpm for the lithium metatitanate.

Results

The results from the above mentioned analyses are:

- In Li_4SiO_4 pebbles with natural enrichment the results of previous agings were substantially confirmed [1,2]. During the annealing there was recrystallization of the dendrite

microstructure with increase in the roughness of the pebble surface, rearrangement of the void volume in round pores and diffusion of metasilicate through the material with formation of metasilicate particles (1 – 4 µm size). Particles with larger dimensions were present in microcracks and at the boundary of grains. After 96 days of annealing there was a reduction of the specific surface area from 0.17 m²/g to about 0.07 m²/g. The density increased from about 90 % to about 93 % T.D. (T.D. = 2.4 g/cm³). Crush load tests were performed on 80 pebbles with 0.5 mm diameter. The initial average value of about 9.48 ± 3.54 N was reduced to 4.91 ± 2.74 N at the end of the annealing.

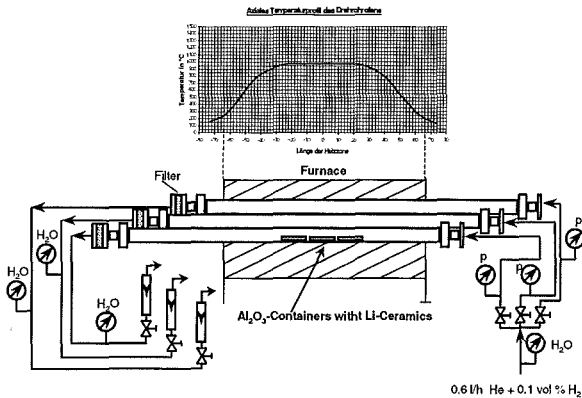


Fig. 3: Schematic of the equipment used in the annealing experiments

- In Li₄SiO₄ pebbles with 50 % ⁶Li-enrichment there was, during the annealing, recrystallisation of the dendrite microstructure with increase in the roughness of the pebble surface and rearrangement of the void volume in round pores. Metasilicate diffused through the material with formation of metasilicate particles. After 96 days of annealing there was a slight reduction of the specific surface area from 0.13 m²/g to about 0.09 m²/g. The density decreased from about 86 % to about 82 % T.D. (T.D. = 2.4 g/cm³). Crush load tests were performed on 80 pebbles with 0.5 mm diameter. The initial average value of about 8.88 ± 2.60 N was reduced after 96 days to 1.69 ± 0.47. The differences in the density values in the enriched and not enriched pebbles might be explained by considering that the not enriched pebbles are produced by melting a mixture of Li₄SiO₄ and SiO₂, whereas for the production of the enriched pebbles also Li₂CO₃ powder has to be mixed. In this case lithium carbonate could be still present in the produced pebbles, leaving, during the aging, the material as CO₂, and causing the density reduction. Also the strong reduction of the crush loads could be attributed to the presence of carbonate in the produced pebbles.
- In Li₂TiO₃ the pre-annealing at 500 °C had no significant effect on the structure of the material. During the aging there was an increase in the grain size (it was about 1.5 µm at the beginning and, after 96 days, it grew up to about 25 µm). After the aging the pebbles were black. This colour change did not correspond to any change in the microstructure of the pebbles, and no additional phase could be detected. The colour change was caused by a slight oxygen sub-stoichiometry of the material. After the annealing in Li₂TiO₃ there was no significant reduction of the density which remained about 90% of the theoretical density. The closed porosity in initial conditions was larger than the open one, after 96 days the situation was reversed and the open porosity was the larger one. An explanation for this could be

that the change of the microstructure during the aging caused the opening of pores. The initial specific surface area of 0.23 m²/g was reduced to 0.07 m²/g after 96 days. The average crush load was measured on 40 pebbles with diameter ≥ 1 mm. The average crush load decreased from 49 ± 5 N at the beginning to 39 ± 14 N.

In the aging the purge flow moisture content at the inlet was well under control and the atmosphere was strong reducing. This accelerated the reduction of the ceramics which rapidly changed their colour. As far as the not enriched lithium orthosilicate and the lithium metatitanate are concerned, there is good agreement between the results from this aging and those from the previous ones. On the other side the results with the enriched lithium orthosilicate showed the need of further development in order to optimise the production of enriched pebbles (addition of lithium carbonate).

Literature:

[1] G. Piazza, M. Dalle Donne, H. Werle, E. Günther, R. Knitter, N. Roux, J.D. Lulewicz, "Long term Annealing of Ceramic Breeder Pebble for the HCPB DEMO Blanket". Proceedings of the CBBI-7, 14-16 Sept. 1998, Petten, the Netherlands.

[2] G. Piazza, J. Reimann, E. Günther, R. Knitter, N. Roux, J.D. Lulewicz, "Behaviour of Ceramic Breeder Materials in long time annealing experiments". Proceedings of the SOFT 21st, 11-15 Sept. 2000, Madrid, Spain.

Staff:

- C. Adelhelm
- E. Günther
- R. Knitter
- G. Piazza
- J. Reimann
- R. Rolli
- O. Romer

TTBB-005/7 Thermal-mechanical Pebble Bed Tests

Present ceramic breeder blanket designs are based on ceramic breeder and beryllium pebble beds. During operation, thermal stresses arise from different thermal expansions of the pebble beds and structural materials, and pebble bed swelling due to irradiation. The knowledge of this bed-structure mechanical interaction (BSMI) is important for the assessment of the blanket lifetime.

The BSMI is predicted by finite element codes with appropriate pebble bed modules which as input require data on mechanical pebble bed characteristics such as relationships for the modulus of deformation, E, to describe the start-up and power cycling phases, and thermal creep strain, ϵ_{cr} , relationships for extended phases of operation.

Experiments were carried out in an uniaxial test facility at temperatures up to 850 °C and pressures up to 9 MPa with FZK-orthosilicate (Li_4SiO_4) pebble beds (pebble diameters $d = 0.25\text{-}0.63$ mm), and metatitanate (Li_2TiO_3) pebble beds delivered both by CEA ($d = 0.8\text{-}1.2$ mm) and JAERI ($d = 0.85$ mm). The experiments were performed in the frame of the EFDA Programme and within an IEA Implementing Agreement.

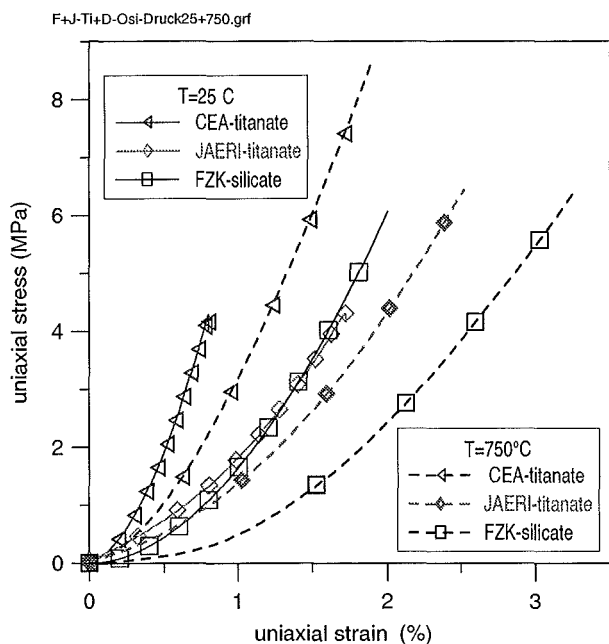


Fig. 1: Comparison of stress-strain dependence at $T=25^\circ\text{C}$ and $T=750^\circ\text{C}$

Figure 1 shows characteristic results for the different granular materials for stress-strain dependences at different temperatures for the first loading of the pebble beds which are used to determine the moduli of deformation, $E = f(\sigma)$. With increasing temperature the strains increase, mostly caused by thermal creep occurring during the loading period (load ramp ≈ 1 MPa/min). Table 1 shows the correlations for the moduli of deformation at ambient temperature (As input in BSMI codes these correlations are recommended, all temperature effects are taken into account in the corresponding creep correlations).

Figure 2 shows characteristic results for thermal creep strains of the different materials for a constant stress between 4.5

and 6.5 MPa at 750 °C. The data are quite close together for all materials except for the CEA titanate which was not long term annealed (l. t. ann.). The creep strain results were fitted by an expression of the type

$$\epsilon_{cr} = A \exp(-B/T) \sigma^p t^n, \text{ see Fig. 3}$$

Table 2 contains the values of the different coefficients. The temperature influence is, as expected, quite pronounced, the stress influence, however, is very small compared with homogeneous materials.

Table 1: Moduli of deformation for 1st stress increase

Granular material	$E(\text{MPa}) = C \sigma(\text{MPa})^m$	
	C	m
FZK- Li_4SiO_4	130	0.47
CEA- Li_2TiO_3	239	0.38
JAERI- Li_2TiO_3	154	0.32

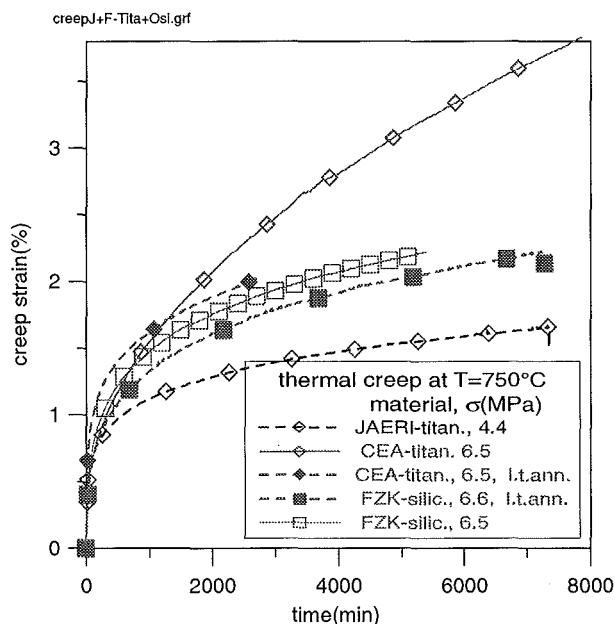


Fig. 2: Comparison of thermal creep data at 750°C

Table 2: Thermal creep correlations

Granular material	$\epsilon_{cr}(t) = A \exp(-B/T(K)) \sigma(\text{MPa})^p t(s)^n$			
	A	B	p	n
FZK- Li_4SiO_4	4.5	9320	0.65	0.2
CEA- Li_2TiO_3 (l.t.ann.)	2.0	8760	0.65	0.18
JAERI- Li_2TiO_3	0.23	6428	0.65	0.19

The proposed correlations represent a first complete set of pebble bed input data required for future calculations of the mechanical behaviour of ceramic breeder blanket components.

Literature:

- [1] J. Reimann, G. Wörner, Thermal creep of Li_4SiO_4 pebble beds, 21th Symp Fusion Technology, Madrid, Spain, Sept. 11-16, 2000.
- [2] J. Reimann, G. Wörner, Thermal creep of ceramic breeder pebble beds, 9th Int. Workshop on Ceramic Breeder Blanket Interactions, Toki, Japan, Sept. 27-29, 2000.
- [3] L. Bühler, Continuum models for pebble beds in fusion blankets, to be published as FZKA report, 2000.

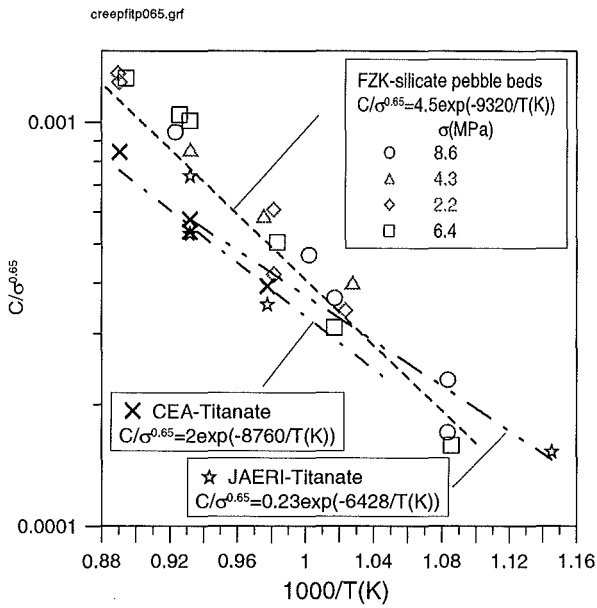


Fig. 3: Fit of temperature and stress dependence for FZK- Li_4SiO_4 and JAERI and CEA- Li_2TiO_3 pebble beds

Staff:

J. Reimann
G. Wörner

**TTBB-005/8
Calculations for Particle Flow in Biaxial
Geometry**

The modeling of the mechanical behavior of solid breeder pebble beds for applications in fusion blankets is based on the finite element code ABAQUS for the use of which the required material properties have to be extracted from experiments (calibration of the models). The models are those commonly used in soil mechanics. The granular material is considered as a continuum, which can undergo reversible elastic and irreversible plastic deformations. Important variables during modeling are the pressure stress p and the Mises equivalent stress q .

A porous elastic model that relates the volumetric deformation to the pressure stress describes the elastic part of the deformation. Granular particle flow is described by the Drucker-Prager Cap model. The deformation due to shear failure is related to the internal friction angle β of the material while the volumetric compaction depends on the cap position $p_b(\epsilon_{vol})$. The deformation during shear failure and consolidation is prescribed by flow potentials for both mechanisms.

Uniaxial compression

The coefficients required for the model data have been adjusted in order to find best agreement with experimental data. One example is the oedometer test shown in Fig. 1. The agreement between calculated and measured data during the compression phase is acceptable. However, since vibrated beds behave qualitatively different than loosely filled beds it is necessary to use two different sets of parameters for the modeling. The material is very sensitive to the filling procedure so that future experiments should use initial conditions as close as possible to blanket applications in order to create a realistic data base for computational models. In addition, experiments should be repeated to ensure reproducible results.

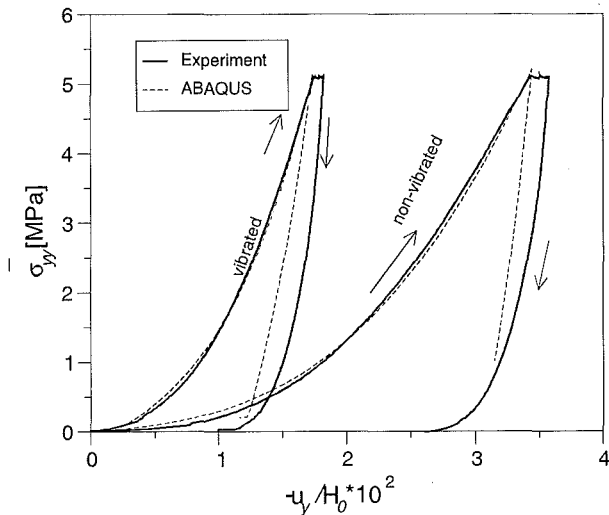


Fig. 1: Uniaxial compression. $\bar{\sigma}_{yy}$ versus u_y for loosely filled and initially vibrated beds

Granular flow of particles

The granular flow of particles has been experimentally and numerically examined for a plane strain geometry as shown in Fig. 2. For investigating the biaxial particle movements the vertical load $\bar{\sigma}_{yy} = F_y / (L_x L_z)$ is increased monotonically while the horizontal load $\bar{\sigma}_{xx} = F_x / (L_y L_z)$ can not exceed a certain

value. The volumetric compaction of the bed is measured by recording at the plate the vertical and horizontal displacements u_y and u_x .

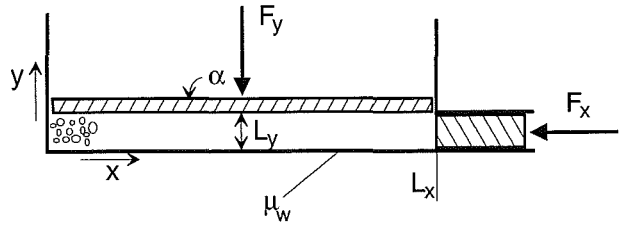


Fig. 2: Sketch of the plane strain experiment

The results shown in Fig. 3 are normalized by the initial height H_0 of the bed. The biaxial particle flow experiments were performed in such a way that the vertical load was increased up to the maximum value of about $\bar{\sigma}_{yy} = 5\text{MPa}$ in a given time period; then the load was kept constant for 2h and finally, the force was reduced to zero during 15min. When the vertical force is increased above a certain value, depending on $\bar{\sigma}_{xx}$ the horizontal piston starts to move. It moves more or less linearly with increasing vertical force over a wide range. The experimental observations are compared with ABAQUS calculations using an internal friction angle of $\beta = 44^\circ$. The agreement is satisfactory and deviations are within the range of experimental uncertainty

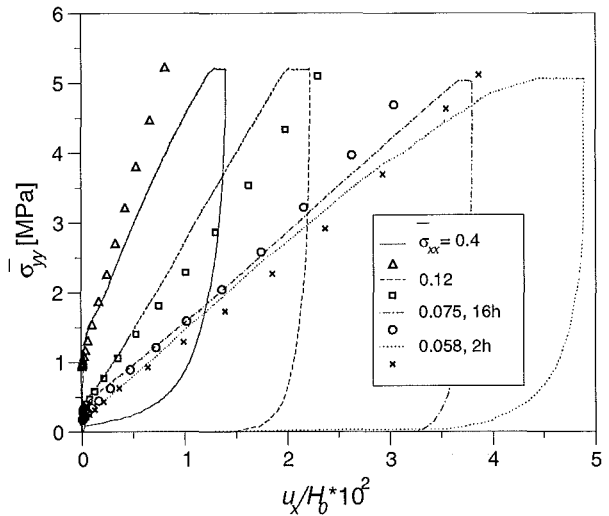


Fig. 3: Biaxial granular flow

During simultaneous vertical compression and lateral expansion the measured inclination angle α of the top plate has been recorded. The calculated values of α are compared with the measured data. A perfect agreement could be found with the carefully performed experiment for which the load was increased very slowly over 16h. For other experiments, which are performed faster, the agreement is only qualitatively (see Fig. 4).

Thermal creep

Recent experiments showed that thermal creep of granular breeder materials becomes important at higher temperatures. If for example a bed of Li_4SiO_4 at 800°C is compressed by a uniform vertical load of $\sigma_{yy} = 4.2\text{MPa}$ the thermal creep strain

already after one day exceeds the plastic and elastic strains so that thermal creep is essentially important for a realistic description of the long-term behavior of a fusion blanket with pebble beds. Calculations using the ABAQUS standard creep laws reproduced the experiments only during a short initial stage. For modeling of the long-term behavior a new flow potential is proposed for consolidation creep as $G_c = (p^2 + q^2)^{1/2}$ from which the creep strain tensor is determined as $\dot{\epsilon} \sim \partial G_c / \partial \sigma$. The magnitude of creep strain is chosen to such a value that the volumetric creep consolidation follows a law $\dot{\epsilon}_c = A(T)p^n t^m$ with a coefficient A depending on temperature T as $A = A_0 \exp(Q/RT)$. Q is the activation energy and R is the gas constant. For stress and time dependence a power law with exponents n and m is used. If the load varies during the creep phase a formulation as $\dot{\epsilon}_c = \dot{\epsilon}_c(\epsilon)$ according to a strain hardening mechanism is preferred instead of the time hardening law shown above where $\dot{\epsilon}_c = \dot{\epsilon}_c(t)$.

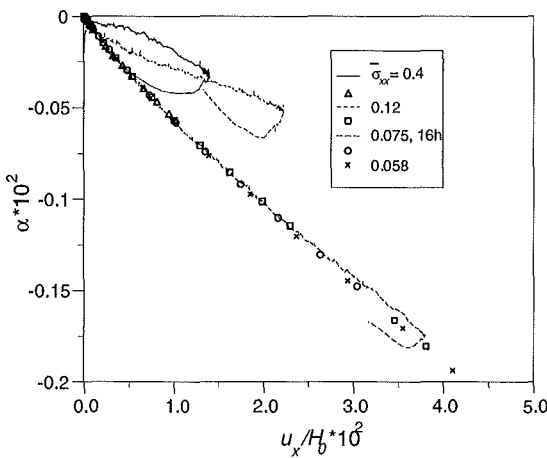


Fig. 4: Inclination angle α versus horizontal displacement

During creep compaction the contact surfaces between particles increase so that the material becomes stiffer for subsequent compression. This effect has been taken into account by modeling *creep hardening* as $p_b(\epsilon_{vol}, \epsilon_c)$. The new creep laws have been implemented in a user-defined subroutine of the ABAQUS code. Results are compared with an experiment as shown in Fig. 5. It is possible to reproduce the experimental data obtained at $T = 800^\circ\text{C}$ almost perfectly with $n = 0.705$ and $m = -0.82$. Even if the load is increased a second time at $t > 5605$ min to a higher value the agreement is surprisingly good. The results shown for other temperatures have been obtained by using the value $Q/R = 9741\text{K}$ as proposed by Reimann and Wörner (2000).

A technical report which outlines the details of the modeling and which shows additional results and comparisons with experiments is in preparation (Bühler (2000)).

Literature:

[1] Bühler, L. 2000, Continuum models for pebble beds in fusion blankets. *Technical report*, Forschungszentrum Karlsruhe, in preparation.

[2] Boccaccini, L., Bühler, L. Hermsmeyer, S., Wolf, F. 2000, Modeling of thermal and mechanical behavior of pebble beds. CBB1-9 conference, Sept. 27-29, 2000, Japan.

[3] Reimann, J. Wörner, G. 2000, Thermal creep of Li_4SiO_4 pebble beds. SOFT conference, Sept 2000, Madrid.

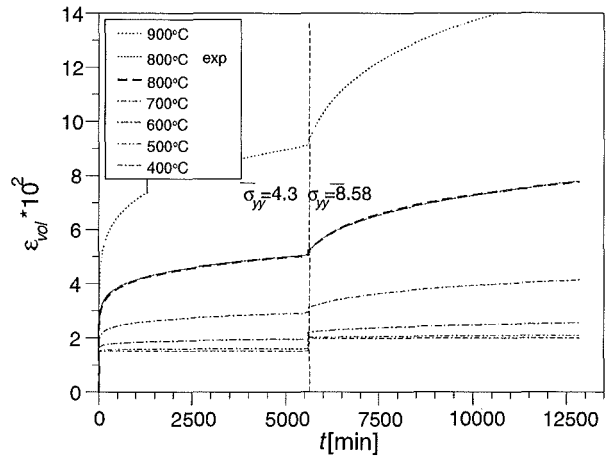


Fig. 5: Creep strain versus time. The load is increased rapidly to $\bar{\sigma}_{yy} = 4.3$ MPa, kept constant for 5600 min and increased a second time to $\bar{\sigma}_{yy} = 8.58$ MPa for the rest of the experiment

Staff:

L. Boccaccini
L. Bühler

**TTBB-006
Irradiation of Ceramic Breeder Pebble Beds**

**TTBB-006/2
Contribution to the PIE of EXOTIC-8 Pebbles**

The EXOTIC-8 irradiation experiment in the HFR Petten provides, in comparison with the previous 7 EXOTIC's experiments, a higher flexibility of breeder irradiation testing [1]. The new design (4 legs being operated independently) allows to perform experiments with dedicated objectives:

- Tritium-release behaviour by performing in-pile thermal transients and post irradiation inventory measurements;
- High burn-up for integrity of pebbles and obtain large quantity for post irradiation testing of mechanical and thermal properties;
- Permeation studies;
- Sweep gas chemistry.

In June 1997 EXOTIC-8 was started with two FZK capsules containing orthosilicate pebbles with a small addition of TeO₂:

- Capsule E8/3 containing Li₄SiO₄ + 2wt% TeO₂ pebbles with 50% ⁶Li-enrichment. In this capsule the behaviour of the material at high burnups (about 10%) should be studied;
- Capsule E8/4 containing Li₄SiO₄ + 2wt% TeO₂ pebbles with natural enrichment. This capsule should give information on the behaviour of lithium orthosilicate at burnups up to 3%, and on the tritium release characteristics and tritium residence time.

Unfortunately it turned out that these pebbles are not suited as breeder material because the tellurium is released at higher temperatures. Therefore the material in the capsules was replaced with pebbles without tellurium. In particular other two capsules were inserted in the HFR Petten:

- Capsule E8/8 containing Li₄SiO₄ pebbles with 50% ⁶Li-enrichment substituting E-8/3;
- Capsule E8/10, containing Li₄SiO₄ pebbles with natural enrichment, substituting E-8/4.

The lithium orthosilicate pebbles containing tellurium from capsules E-8/3 and E-8/4 were sent back to Forschungszentrum Karlsruhe to be examined.

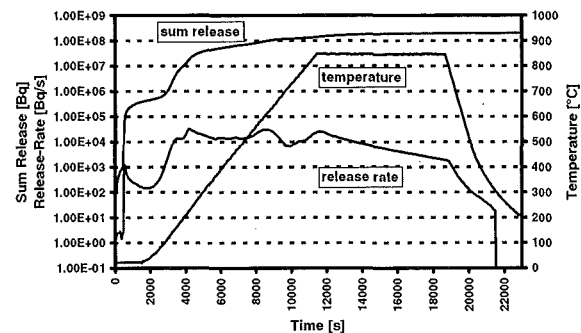


Fig. 1: Tritium release kinetics

Results

Post irradiation examinations of lithium orthosilicate pebbles containing tellurium are being completed at hot cells and preliminary results can be given. Optical microscopy showed no significant change in the microstructure of the pebbles, which is plausible because, due to the substitution, the pebbles were irradiated for short time and the lithium burnup is very small. The tritium release kinetics of the pebbles of capsule E-8/3 (enriched material) was measured (Fig. 1). Pebbles were heated with a temperature ramp of 7 °C/min from 20 °C up to 850 °C. Helium with 1vol% of H₂ was used as purge flow. Fig. 2 shows the tritium release rate as function of the temperature. There are three main peaks of release rate at about 200 °C, 600 °C and 850 °C.

Literature:

[1] J. G. van der Laan, K. Bakker, R. Conrad, A. Magielsen, G. Piazza et alii, "Performance of ceramic breeder pebbles to DEMO representative lithium burnups". Proceedings of the 21st SOFT, Sept.11-15, 2000, Madrid, Spain,.

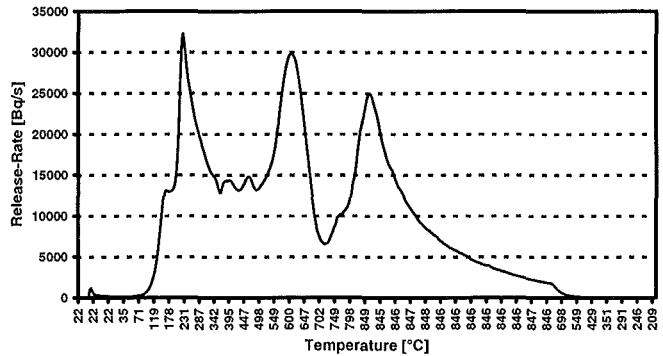


Fig. 2: Tritium release rate as function of the temperature

Staff:

- E. Damm
- H. Kleykamp
- D. Knebel
- G. Mangai
- B. Neufang
- G. Piazza
- R. Rolli
- O. Romer
- C. Sand
- F. Scaffidi-Argentina
- H. Ziegler

TTBB-006/3 Thermomechanical Pebble Bed Analysis for High Fluence Irradiation (HFI)

Nuclear analyses have shown that high flux fission test reactors are well suited to simulate fusion power reactor irradiation conditions and that representative ratios of dpa and burn up can be achieved provided that the neutron spectrum is well tailored and the ${}^6\text{Li}$ -enrichment is properly chosen, [1]. Based on this finding, high fluence irradiation experiments of ceramic breeders in the HFR Petten were suggested with the main objective to investigate the impact of neutron spectrum and the influence of constraint conditions on the thermo-mechanical behaviour of breeder pebble-beds. In the frame of the EFDA Technology Work Programme 2000, FZK carried out some preliminary design and analytical studies to develop a concept for achieving the required constant axi-symmetrical temperature distribution in the ceramic breeder pebble bed and the constraint conditions. The studies were carried out for Li_4SiO_4 as current reference material but apply basically for other ceramic breeders, too.

Design recommendations

The overall design of the HFR irradiation device consists of a TRIO type rig with Cd-shield as near as possible to the outer control gas gap [2].

The analyses have shown that the desired irradiation conditions can be achieved by simple design measures, and by using materials with appropriate properties. Cover plates at the axial ends of the pebble bed made of Nb foam, possibly combined with an additional heat source placed on the central region of the plates, allow to establish an axially constant temperature distribution and to minimize the disturbance of the temperature field by the thermocouple guide tube. The volumetric differential thermal expansion between the pebble bed and the Nb structure amounts to 3.8 %, which would lead, without creep, to a bed pressure of 8.8 MPa. To provide a weak constraint it is suggested to replace the stiff distance tubes between the bed cover plates and the caps of the capsule by a plastically deformable tube.

A confirmation of the thermal calculations is necessary when more reliable data are available on the thermal conductivity of the Nb foam. Furthermore, additional analyses are necessary to determine the influence tube on the precision of the temperature measurement of the heat generation inside the thermocouple and the guide. For a complete thermal-mechanical analysis of the capsules, pebble bed models are necessary which describe the elastic and plastic pebble bed compression, pressure relaxation by creep, the corresponding thermal conductivity and bed to wall heat transfer coefficients. Such models are presently being developed.

Literature:

- [1] U. Fischer et alii, "Comparison of nuclear irradiation parameters of fusion breeder materials in high flux fission test reactors and a fusion power demonstration reactor". J. Nucl. Mat. 280 (2000) 151-161
- [2] J. G. van der Laan, R. Conrad et alii, "On the irradiation performance of HCPB candidate ceramic breeder materials to DEMO-like conditions. An approach with neutron and particle Irradiations". Proceedings of the 8th Workshop on ceramic breeder blanket Interactions, Colorado Springs, USA, Oct. 6-8, 1999.

Staff:

S. Gordeev
G. Piazza
K. Schleisiek

TTBB-007 Development of Beryllium Pebble Beds

TTBB-007/1 Characterization of Be Pebbles

The Rotating Electrode Process (REP) is one of the candidate methods for producing beryllium pebbles for use as a neutron multiplier in the European Helium Cooled Pebble Bed (HCPB) blanket. This method consists of arc melting the end of a long cast cylinder, which is rotating about its axis in a vacuum chamber filled with an inert gas (e.g. helium). Molten droplets of metal are thrown off the end of the rotating cylinder and solidify in flight. The size and quality of the REP beryllium pebbles depends essentially on the material used and on the production process parameters (e.g. electrode impurity content, electrode diameter, electrode angular velocity, cooling velocity, etc.). Usually, this method produces almost perfectly spherical pebbles with a very small surface roughness the mean size of which ranges from 0.2 mm to 2 mm or more.

REP beryllium pebbles with 1 mm diameter produced by the NGK Insulators Company were investigated before and after thermal annealing by means of optical microscopy.

Macroscopically, the pebbles look almost perfectly spherical with a very smooth external surface. As usually expected the pebbles are covered by a beryllium oxide layer the thickness of which was estimated to be about 50-150 nm. The optical microscopy of the as-fabricated pebbles show an almost fully dense metallographic structure characterized by the presence of large grains (average grain size 100-300 μm). However, a quite large number of pebbles exhibit a big pore (up to 0.1-0.2 mm) at their center together with a fully dense region near the external surface. This kind of pebble structure (which has been already observed in other types of pebbles subjected to fast thermal treatments) is typically generated during the cooling phase of the fabrication process.

After a stepwise heating process in a flowing helium atmosphere up to 790 $^{\circ}\text{C}$ for several hours, the external surface of the pebbles look still "metallic" (probably because of the relatively small oxide content of the pebbles). Furthermore, the pebble microstructure does not change significantly and only a small amount of new porosity has developed as a consequence of the annealing process (Fig. 1).

Staff:

E. Damm

E. Kaiser

F. Scaffidi-Argentina

H. Ziegler

F. Weiser

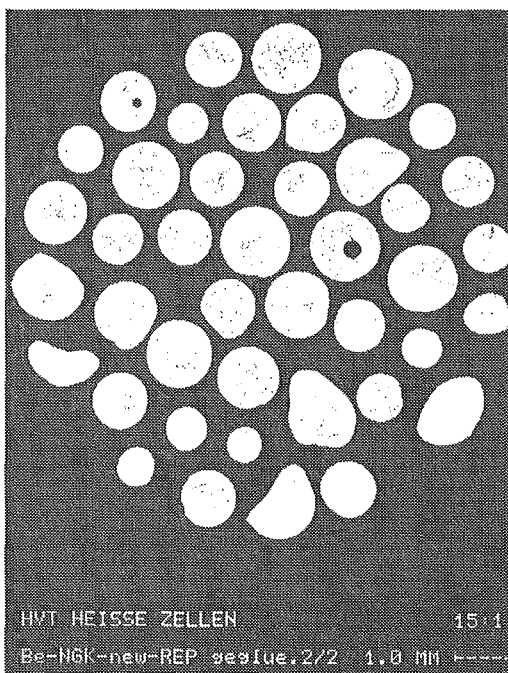
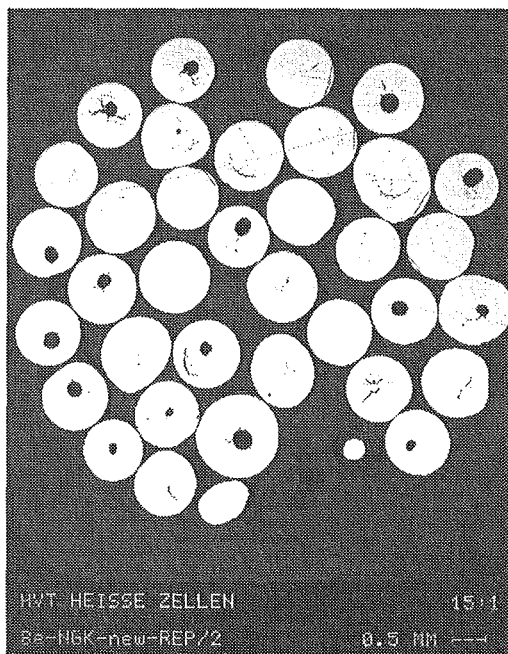


Fig. 1: Metallographic structure of both as-received (top) and thermally treated (bottom) REP beryllium pebbles

TTBB-007/2 Evaluation of Tritium Release and Swelling under Irradiation (ANFIBE-Code)

In order to better understand the physical mechanisms governing swelling and tritium and helium release behavior in beryllium, as well as to generate confidence in the results provided by the code ANFIBE [1] and to assess its prediction capabilities, some experimental results on density change and tritium and helium release for beryllium pebbles irradiated in the EBR-II test COBRA-1A [2, 3] have been compared with the code predictions.

Swelling calculations were performed for both 1-mm and 5-mm C03 and D03 material as well as for 3-mm C03 material. The calculated volumetric swelling for C03 material ranges from 0.61% to 0.91% depending on the respective helium content. On the other hand, the resultant calculated swelling in case of D03 material is up to about 25% higher than in case of C03 material and ranges from 0.83% to 0.98%. The agreement between the calculated swelling data and the experimental estimated value of 0.83% is satisfactory. The calculated diameter of the homogeneously distributed intragranular helium bubbles is 16.8 nm and the corresponding bubble density is $2.4 \times 10^{15} \text{ cm}^{-3}$. These values are in reasonable agreement with those estimated by means of transmission electron microscopy (TEM) examinations (mean bubble diameter 11.9 nm, mean bubble density $2.0 \times 10^{16} \text{ cm}^{-3}$). This fact confirms the assumption that beryllium swelling under neutron irradiation is predominantly due to the development of internal helium bubbles, so that void formation from radiation damage can be neglected.

Helium release calculations were also performed on pebbles of both 1-mm C03 and D03 material. The calculated helium inventory after annealing as a fraction of the total helium in the sample was 7% and 29% for C03 and D03 material respectively.

A comparison in terms of cumulative tritium release as a function of the annealing time between experimental data and predictions of ANFIBE for the C03 stepped-anneal test is shown in Figure 1. In agreement with previous studies it has been found that the release starts at about 500-550 °C and becomes significant for temperatures higher than 700-750 °C.

The total cumulative released tritium at 350-850 °C has been calculated 883 MBq/g which represents 71% of the 1240 MBq/g total inventory. These values are in reasonable agreement with the experimental results.

The experimentally observed different tritium release behavior between 1 mm and 3 mm pebbles of both C03 and D03 materials is essentially due to the different helium release kinetics during the in pile irradiation. Calculations indicate in fact that, for both small and large pebbles, most of tritium produced during in-pile irradiation at about 390 °C is trapped into relatively small intragranular helium bubbles. During the irradiation at this relatively high temperature the bubbles move into the lattice and tend to coalesce, thus forming bigger bubbles. Because the bubble diffusion coefficient decreases strongly with the bubble radius ($\propto 1/r^4$) the integral migration distance

$$x(t) = \sqrt{6D_b(r)t}$$

covered by a growing bubble will attain rapidly an asymptotic value which is determined by the distance migrated during the early bubble lifetime. Therefore, tritium trapped in helium bubbles will reach the sample free surfaces much easier in the case of small pebbles than in the case of larger ones.

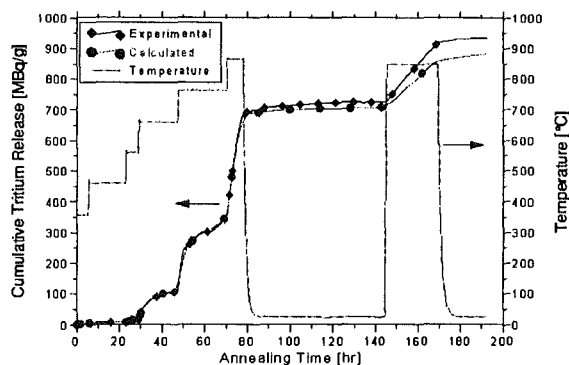


Fig. 1: Comparison between calculated and experimental tritium release by stepped temperature anneal for C03 Be pebbles

This "particle size" effect explains why in-reactor loss of tritium is dependent upon pebble diameter size, with greater loss in the 1-mm pebbles than for the 3-mm pebbles.

Literature:

- [1] F. Scaffidi-Argentina et al., Fusion Technology 32 (1997) 179-195.
- [2] M.L. Hamilton et al., in: Fusion Materials SemiAnnual Progress Report DOE/ER-0313/14 (1993) 3-13.
- [3] L.R. Greenwood and R.T. Ratner, in: Fusion Materials SemiAnnual Progress Report DOE/ER-0313/21 (1996) 225-228.

Staff:

F. Scaffidi-Argentina

TTBB-007/4 Heat Transfer Parameters of Pebble Beds

In a helium cooled pebble bed blanket (HCPB) for power reactors the neutron multiplier and the breeder material are arranged as pebble beds between flat cooling plates. The maximum temperatures in the breeder and the beryllium pebble beds are in the range of 900°C and 650°C, respectively. Because of large temperature differences between pebble beds and the structural material, different thermal expansion coefficients and irradiation effects, constrained strains occur. The large compressive stresses in the pebble beds might result in plastic deformations of pebbles. These deformations influence the thermal conductivity of the bed which determines the temperature distribution. Therefore, for the thermal-mechanical blanket design, the relationship between bed stress and bed strain as well as the thermal conductivity as function of strain and stress must be known.

Compression tests

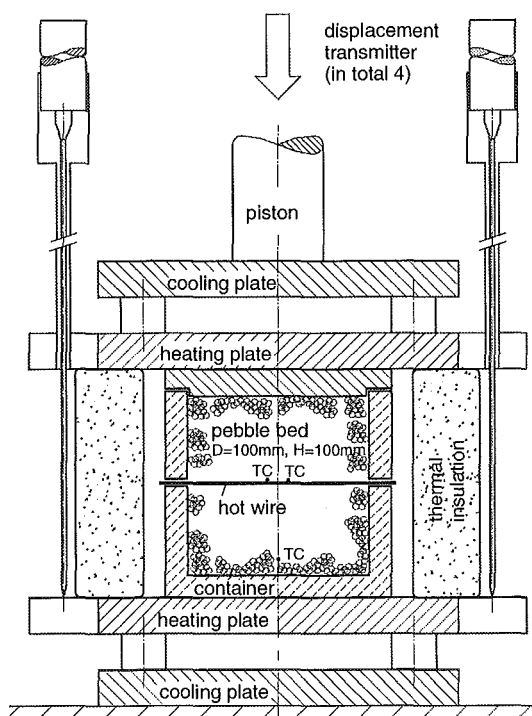


Fig. 1: Experimental set-up

At present, a considerable amount of data exists in respect to the mechanical behaviour of pebble beds (stress-strain relationships, thermal creep) at blanket relevant conditions, obtained by uniaxial compression tests (UCTs) [1,2]. The measurements of thermal conductivity, however, concentrated either on uncompressed pebble beds [3] or on pebble beds where a small degree of compression was reached due to temperature differences in the test section [4,5]. There is only one experimental investigation [6], performed at ambient temperature, where the conductivity was determined as a function of an external load (varied up to 1.5 MPa), however, without recording the corresponding bed strains. Therefore, a considerable lack of data exists in respect to the knowledge of the thermal conductivity of deformed beds in relevant temperature range as a function of bed strain and stress. Presently, the HECOP facility is being built at Forschungszentrum Karlsruhe for investigating the thermal parameters of strongly deformed Be pebble beds [7]. In order to have in short term data for the design of irradiation test

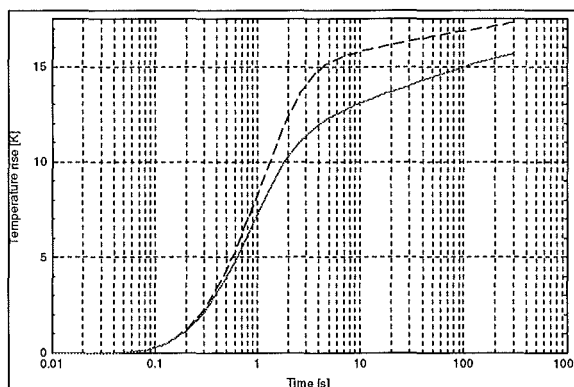


Fig. 2: Heater surface transient temperature (3D FE model): continuous curve: $k = 6.7 \text{ W/mK}$, $\alpha = 1500 \text{ W/m}^2\text{K}$; dashed curve: $k = 12 \text{ W/mK}$, $\alpha = 1000 \text{ W/m}^2\text{K}$.

capsules, an activity was started to measure thermal parameters of deformed pebble beds by using the hot wire technique [8].

Experiments with the "Hot Wire" method

The Hot Wire (HW) experiments were performed with an uniaxial compression test (UCT) facility in a He filled glove-box used already for previous UCTs (Fig 1). After filling the pebbles into a cylindrical container (the filling is supported by vibration in order to obtain a high packing factor), the container is positioned in the press. The pebble bed has inside an indirectly heated electrical heater with 1mm outer diameter. The hot wire consists of an inner electrically heated wire (0.3 mm diameter), MgO insulator (0.3 mm thickness) and outer stainless steel tube (thickness is 0.1 mm). For experiments at elevated temperatures the bed is first heated up without bed compression by means of the heating of the press. When the temperature in the bed has reached the selected value and is in steady state, the pressure on the bed is gradually increased, and, reached the at selected values, an external voltage is applied to the hot wire. On the basis of the measured time dependent hot wire's temperature increase (measured by 0.25 mm thermocouples brazed on the hot wire surface), the effective thermal conductivity of the pebble bed can be calculated.

In order to test the experimental equipment, first experiments were carried out in air with aluminium pebble beds (pebble diameter 2 mm) and orthosilicate pebble beds (pebble diameters between 0.25 and 0.6 mm). For the beryllium pebble bed tests, 1 mm pebbles were used manufactured by the Japanese company NGK and 2 mm pebbles produced by Brush and Welman.

As this method was intended to be used for bed conductivity larger than normally recommended for (1 W/m K), and because of the relatively small dimensions of the wire length and pebble bed diameter, also a modelling work of the thermal response of the hot wire supported the experimental activity. The experimental conditions were modelled in two steps. In the first step, a one dimensional heat conductance model was used assuming an infinitely long hot wire and axis-symmetry of the surrounding bed. The finite bed dimensions were taken into account by assuming a bed radius of 50 mm (the heat resistances and heat transfer coefficients, respectively, between heater surface and pebble bed and between bed and container wall were simulated by thin layers with small values of the heat conductivity). In the second, a three dimensional modelling was done taking into account realistically all geometric conditions described above. The results of the modelling showed that the Hot wire method is still applicable for beryllium pebble beds. Fig. 2 shows the heater surface transient temperature predicted by the 3D Finite Element model. Two different couples of bed

conductivity and heat transfer coefficient were assumed: $k = 6.7$ W/mK, $\alpha = 1500$ W/m²K (continuous curve), $k = 12$ W/mK, $\alpha =$

curve in the half-logarithmic plot develops (after about 20s for

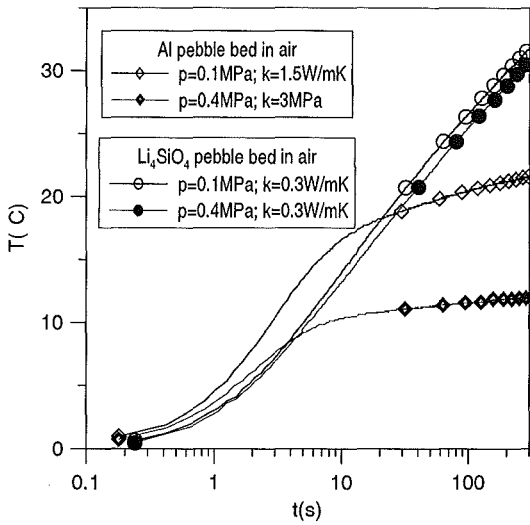


Fig. 3: Measured temperature response for Li₄SiO₄ and Al pebble beds

1000 W/m²K (dashed curve).

Experimental results

Fig. 3 shows characteristic HW temperature signals for two types of pebble beds:

- the aluminium pebble bed which is characterised by a large thermal conductivity of the pebbles and significant plastic pebble deformations during compression;
- the orthosilicate pebble bed, characterised by a small thermal pebble conductivity and negligible plastic pebble deformations during compression.

After switching on the electrical power in the hot wire, its thermal response is first dominated by heat conduction through the MgO insulation around the metallic wire and the outer stainless steel tube and the heat resistance between heater and pebble bed. After a certain time period the heat conductivity of the surrounding material becomes dominating and a fairly straight

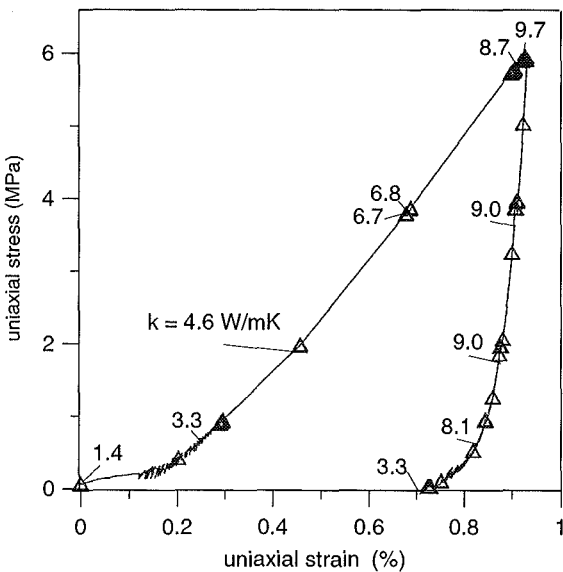


Fig. 4: Thermal conductivity for UCT at ambient temperature

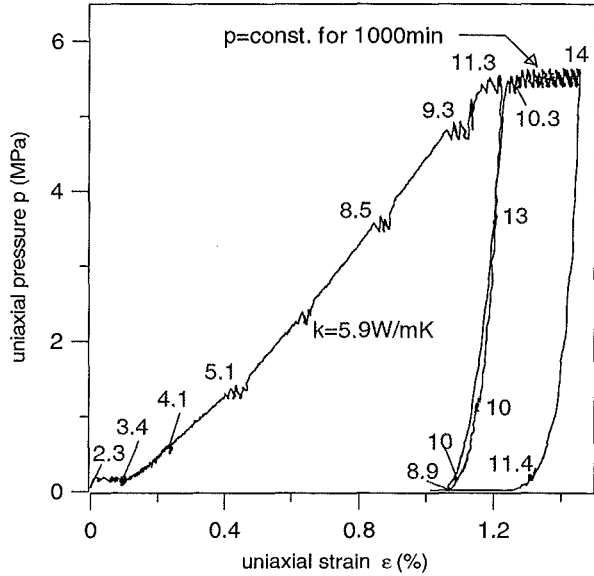


Fig. 5: Thermal conductivity of Be pebble bed for UCT at T=475°C

the Al pebble bed). For the orthosilicate pebble beds fairly constant slopes of the curves are obtained after less than 10s. For the orthosilicate beds there is no significant influence of pressure on the bed conductivity and the influence of the heat resistance is not so clearly observed because of the small thermal conductivity. For large conductivity (Al beds at high pressures), the slope of the curve becomes quite flat which is unfavourable for the accuracy of the conductivity evaluation (this is the main reason why the HWM is recommended to be used for small conductivity). The slope can be increased to a certain extent by increasing the voltage applied to the wire. Analysing in more detail the measured slopes for large values of k , one observes that the slopes are not exactly constant in the time range between 20 and 300 s. This effect has the consequence that the evaluated conductivity depends somewhat on the time where the slope is taken. For this reason detailed modelling of the thermal response was done. Assuming thermal parameters characteristic for the experimental results, the 3d modelling

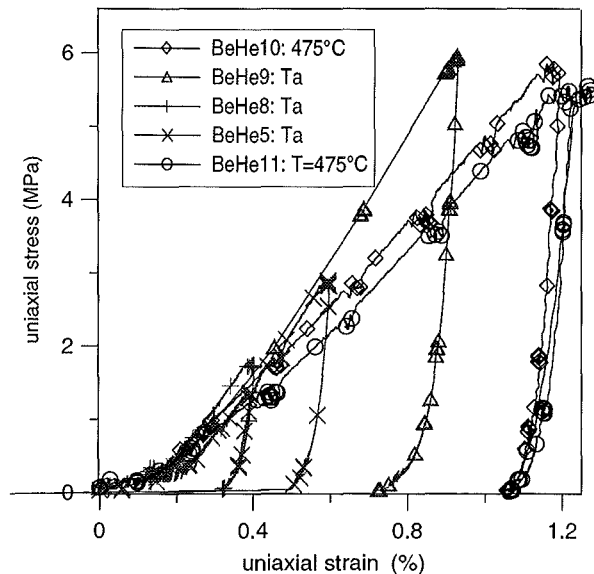


Fig. 6: UCTs of beryllium pebble beds at different temperatures

shows that, for conductivity evaluation, the slope is to be taken at about 50 s.

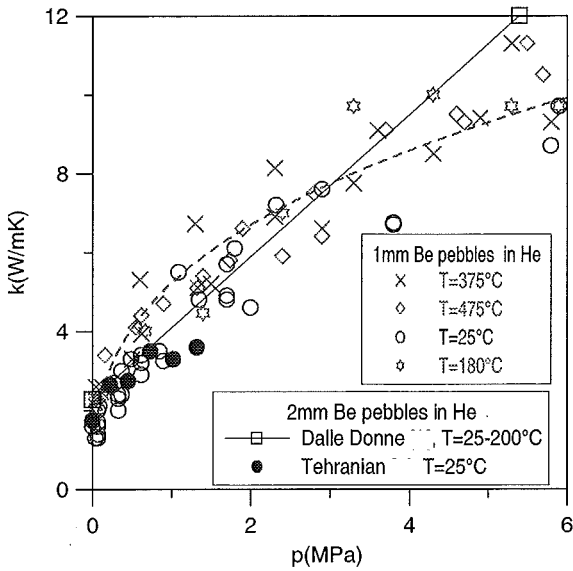


Fig. 7: Thermal conductivity of Be pebble beds as a function of stress

Results of beryllium pebble bed tests

Fig. 4 shows the stress-strain dependence measured during the UCT for a Be pebble bed at ambient temperature and the evaluated conductivities at different pressure levels. The first HW measurement was performed before the bed was compressed. During the pressure increase period, the stress-strain dependence is determined mainly by the relocation of pebbles and, to a smaller degree, by elastic and plastic pebble deformation. The increasing elastic and plastic pebble deformation, however, is the reason for the increase of conductivity with increasing pressure. During the pressure decrease period, the pebbles can merely change their position, there are minor movements due to elastic deformations. The conductivity essentially keeps the value reached at the highest pressure; only at very small pressure the values become significantly smaller. This tendency indicates that the increase of conductivity during pressure increase is mainly caused by plastic deformations.

With increasing temperature, the conductivity of He and Be increases and decreases, respectively. At elevated temperatures the bed conductivity should be, therefore, larger

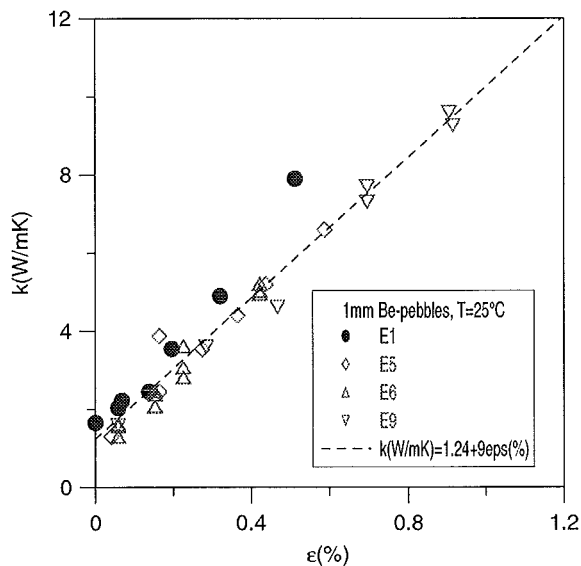


Fig. 8: Thermal conductivity of Be pebble beds as a function of strain (room temperature)

for negligible compressions but considerably smaller for larger compressions. On a first glance, the results for a bed temperature of 475°C (Fig. 5), appear to be contradictory: for given pressures, the values of k are quite close or even larger than those for ambient temperature. The reason is that, at higher temperature, the strains for a given pressure are larger, and, if this difference is mostly caused by plastic pebble deformations, then the effect of increased contact areas overcompensates the effect of the Be conductivity decrease (Fig. 6). In the experiment with thermal creep at 475°C, a distinct increase of the thermal conductivity during creep was observed.

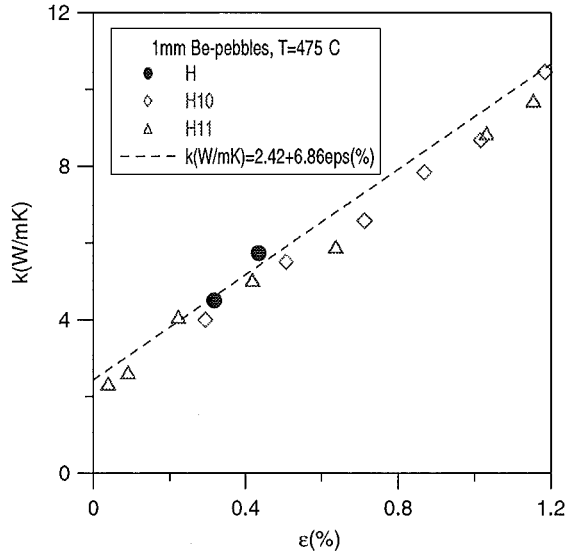


Fig. 9: Thermal conductivity of 1 mm Be pebble beds as a function of strain (475 °C)

The thermal conductivity k can be correlated as a function of both stress σ and strain ϵ . Fig. 7 shows the measured data as a function of σ : There is a non linear dependence between k and σ , and the temperature effect is not very expressed. This figure contains also the linear data fit for 2 mm Be pebbles from [5] which exhibits an increasing discrepancy to the present data

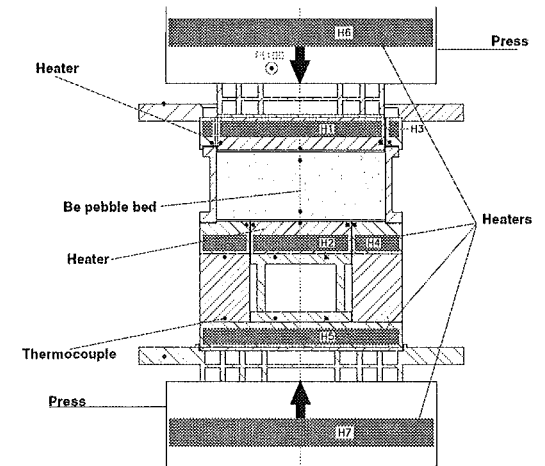


Fig. 10: Schema of the HECOP test facility

with increasing pressure. The results from [5] are representative for a temperature range between 25 and 200°C. The results from [6] again for 2 mm Be pebbles for ambient temperature agree fairly well with the present data.

Figs. 8 and 9 show the correlation $k = f(\epsilon)$ at two different temperatures. This kind of presentation is more appropriate for the determination of the beryllium structural material interaction

in blanket elements. In fact, the strain can be directly determined from the temperature field (at least for the beginning of blanket operation).

The present data can be fairly well fitted by relationships of the type $k = k_0 + A(T) \epsilon$, where k_0 is the conductivity t without bed compression.

HECOP experiment

The HECOP test facility (Fig.10) [7] has been completed and tests out of glove box have started. The design of the machine aimed to minimise uncontrolled heat losses, in order to allow reliable measurement of the temperature gradients in the bed, and of the heat flux flowing through the bed. Presently the hardware and software for the control of the experiment and the data acquisition is being checked: all thermocouples were calibrated and also the response of the heating and controlling system to a transient is being tested.

Till the end of this year HECOP will be built-up in a glove box already used for beryllium experiments (Fa. Goraieb Versuchstechnik). It is foreseen to have the first results on the heat transfer parameters of a beryllium single size pebble bed in the first months of the next year.

Literature:

- [1] J. Reimann, E. Arbogast, M. Behnke, S. Müller, K. Thomauske, Thermomechanical Behaviour of Ceramic Breeder and Beryllium Pebble Beds, 5th Int. Symp. Fusion Nuclear Technology, Roma, Italy, Sept.19-25, 1999.
- [2] J. Reimann and G. Wörner, Thermal Creep of Li_4SiO_4 Pebble Beds, 21st Symp Fusion Techn., Madrid, Spain, Sept. 11-15, 2000.
- [3] G. Piazza, M. Enoeda, A. Ying "Measurements of effective thermal conductivity of ceramic breeder pebble beds". 21st Symposium on Fusion Technology, Madrid, September 11-15, 2000.
- [4] M. Dalle Donne et al, "Measurement of the heat transfer parameters in infiltrated binary beryllium pebble beds. Comparison between the results of PEHTRA and SUPER-PEHTRA". 4th IEA Int. Workshop on Beryllium Techn. For Fusion, FZK, Karlsruhe, Germany, Sept. 15-17, 1999.
- [5] M. Dalle Donne et al, "Experimental investigation on the thermal and mechanical behaviour of single size beryllium pebble beds". 4th IEA Int. Workshop on Beryllium Techn. For Fusion, FZK, Karlsruhe, Germany, Sept. 15-17, 1999.
- [6] F. Tehranian and M. Abdou, Experimental study of the effect of external pressure on particle bed effective thermal properties, Fusion Techn. Vol. 27, May 1995, pp 298-313.
- [7] Nuclear Fusion Project Annual Report of the Association Forschungszentrum Karlsruhe/EURATOM, October 1998-September 1999, December 1999.
- [8] J. Reimann, S. Hermsmeyer, G. Piazza, G. Wörner "Thermal conductivity measurements of deformed beryllium pebble beds by hot wire method". Proceedings of the CBBI-9, Sept 27-29, Toki, Japan.

Staff:

Fa. Goraieb Versuchstechnik
S. Hermsmeyer
G. Hofmann
G. Piazza
J. Reimann
G. Wörner

TTBB-007/5 Model Development of Beryllium Pebbles Beds

The granular character of Beryllium pebble beds used in the Helium Cooled Pebble Bed (HCPB) blanket affects both their thermal and mechanical behaviour. Modelling that behaviour and using experimental results for calibration is essential for a prediction of conductivity and an engineering blanket design.

1. Modelling of the mechanical behaviour in ABAQUS

The mechanical Beryllium pebble bed behaviour has been reproduced successfully using a Drucker-Prager cap model approach. Recently, experimental data on the dependence of the thermal conductivity on bed deformation, and temperature, (sub-task TTBB-007/4) have been implemented in the finite-element code ABAQUS. Now, local deformations can be translated into local thermal conductivity. A coupled thermal/mechanical analysis [1], with mechanical interaction of Beryllium and ceramic breeder pebble beds, was carried out for the HCPB sub-module irradiation experiment that is pursued under Task TTBB-004. The figure depicts the locally varying Beryllium bed conductivity, with no structure or ceramic breeder bed plotted. Under the present conditions, the bed deformation guarantees a near-constant conductivity value for the largest part of the bed, despite a sharp axial temperature drop of about 300 K.

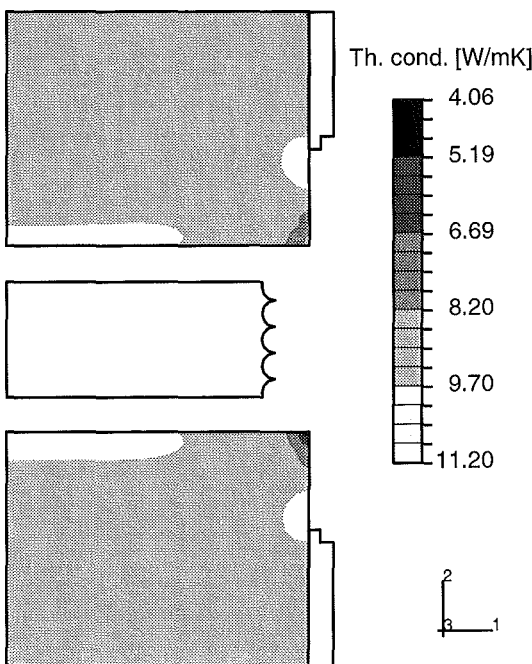


Fig. 1: Beryllium bed conductivity in the HCPB sub-Module

2. Modelling of thermal conductivity

The conductivity of Beryllium pebble beds is strongly affected by bed stress, and strain. Modelling this behaviour requires relevant experimental data; results from three independent experimental campaigns described in the literature were employed to develop a model that predicts bed conductivity during the first loading of the pebble bed knowing bed pressure. To this end, a correlation between external loading pressure and

pebble contact was developed and the Schlünder conductivity model used to isolate the contribution of contact deformation to the increase in bed conductivity [2]. A reasonable agreement of all data was achieved, and open issues in the prediction at temperatures far above room temperature highlighted. It was pointed out that two of the three experimental data series used did not offer strain data for the pebble bed, and that such data are needed to develop a model covering the range of operation that a pebble bed sees during its life time.

Literature:

- [1] F. Wolf, "Strukturmechanische Berechnungen für das Submodul des HCPB-Blankets", Internal report, Forschungszentrum Karlsruhe, October 2000.
- [2] S. Hermsmeyer, "Conductivity modelling of mechanically loaded Beryllium pebble beds", Internal report, Forschungszentrum Karlsruhe, June 2000.

Staff:

L. Bühler
S. Hermsmeyer
K. Schleisiek
F. Wolf

TTBB-007/6 PIE of Be Pebbles Irradiated in EXOTIC-8

The beryllium specimens consist of spherical beryllium powder with a diameter of 0.1-0.2 mm made by inert gas atomization (IGA) and centrifugal atomization at Brush Wellman Inc. The production process involves break up and rapid cooling of a molten metal stream to form powder. This powder has the purity level of other commercial beryllium products and is usually very close to spherical in shape. However, there are a large number of variables which can theoretically affect sphericity of the particles, therefore the sphericity of the IGA pebbles is not always guaranteed.

The specimens were irradiated for 200 days in the High Flux Reactor (HFR) in Petten at temperatures ranging from 500 °C to 600 °C with a fast (>1 MeV) neutron fluence of about $5 \cdot 10^{24} \text{ m}^{-2}$ [1].

1. Gas release measurements

Annealing and gas-release measurements for the irradiated beryllium specimens were carried out with a flow-through tritium release facility installed in the hot-cell laboratory of the Forschungszentrum Karlsruhe. The system essentially consists of an inlet gas manifold, a sample furnace chamber connected by a short, heated line ($T \approx 300 \text{ °C}$) to a zinc-reducer ($T \approx 390 \text{ °C}$) which transforms any tritium water to tritium gas, and an ionization chamber downstream from the furnace for analysis of the purge gas tritium activity. The use of the zinc-reducer avoids problems with tritium water absorption on the inner wall of the release facility pipes, thus allowing quantitative tritium measurements. The total released tritium is determined by integrating the measured release rate over the time.

The release kinetics and total amount of released tritium are determined by annealing the specimens with temperature ramps at a constant heating rate of 7 °C/min from room temperature up to 1000 °C . The final annealing temperature of 1000 °C was kept constant for about 3 hours. Either a $50 \text{ cm}^3/\text{min}$ high-purity argon with 1vol% H_2 or helium with 0.1vol% H_2 was used as a purge gas for the annealing experiments to facilitate the tritium transport.

Tritium release rates are measured with an in-line ionization chamber, while the gas composition in the process line as well as helium release rates are measured with a quadrupole mass spectrometer (QMS) connected downstream from the specimen furnace. QMS signature were mass-2 for H_2 , mass-4 for ^4He and mass-40 for ^{40}Ar . Based on previous studies [2] the contribution of HT to the QMS mass-4 peak can be considered as negligible.

The QMS was calibrated with gas standard mixtures flowing in the process line, while the ionization chamber was calibrated with a standardized tritiated gas mixture. Before a tritium release experiments is started a dummy release measurement is performed in order to determine the background of the system, which is then subtracted from the measured tritium release rate.

2. Results

According to previous studies [3, 4, 5], the result of the measurements indicated that helium and tritium release behavior is a complex function of both irradiation temperature and time at temperature. Anyhow, in agreement with the studies reported in Refs. 3 and 4, all beryllium specimens do not show any significant tritium release at temperature of 600 °C and below. Although tritium is released between 600 °C and 900 °C , no helium release is observed in that temperature range. In all investigated samples, the tritium release rate starts to increase significantly above about $600\text{-}650 \text{ °C}$, reaches a maximum at

about 900 °C and than starts to decrease monotonically quite slowly with the time when the annealing temperature is kept constant at 1000 °C . In all cases, at the time when the largest peak of tritium release occurred a peak of helium release was always observed. Figures 1 and 2 show quite clearly that tritium and helium are unambiguously released concurrently from the beryllium specimen, thus leading to the conclusion that tritium and helium reside in common bubbles in the irradiated material. In fact, the gas release is due to the migration of the helium bubbles to form interconnected grain-edge tunnels to the specimen-free surfaces. The tritium trapped in the helium-filled bubbles follows the destiny of the bubbles and will be released concurrently to the helium only after their migration and venting from an open-porosity network. Strong oscillations in the helium release rate curves have been usually observed.

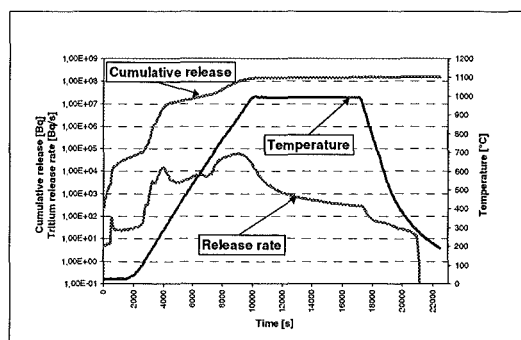


Fig. 1: Tritium release from 0.1-0.2 mm beryllium pebbles heated on a linear ramp to an anneal temperature of 1000 °C

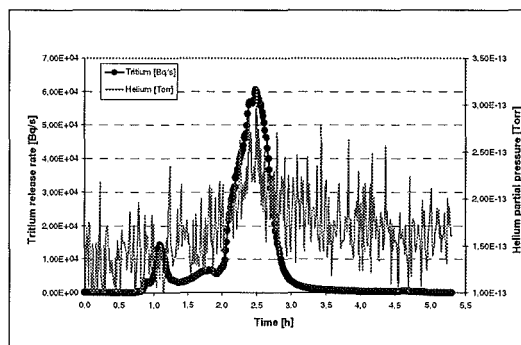


Fig. 2: Tritium and helium release from 0.1-0.2 mm beryllium pebbles heated on a linear ramp to an anneal temperature of 1000 °C

Literature:

- [1] J.G. van der Laan, Personal communication.
- [2] R.A. Anderl et al., Fus. Techn. 28 (1995) 1114.
- [3] R.A. Anderl et al., "Tritium and Helium Retention and Release from Irradiated Beryllium", in: Proc. 3rd IEA International Workshop on Beryllium Technology for Fusion, Mito City, Japan, October 22-24, 1997.

- [4] F. Scaffidi-Argentina and H. Werle, "Tritium Release from neutron Irradiated Beryllium: Kinetics, Long-Time Annealing and Effects of Crack Formation", in: Proc. 2nd IEA International Workshop on Beryllium Technology for Fusion, Jackson Lake Lodge, Wyoming, September 6-8, 1995.
- [5] F. Scaffidi-Argentina et al., "Beryllium R&D for Fusion Applications", in: Proc. 5th International Symposium on Fusion Nuclear Technology, Rome, Italy, September 19-24, 1999, to be published.

Staff:

E. Damm

C. Sand

F. Scaffidi-Argentina

H. Ziegler

TTBB-007/7 Contribution of Basic Layout of Test Capsules

In order to investigate the beryllium behaviour under End-of-Life (EOL) HCPB blanket conditions, an irradiation test at high helium production rates (at least 3000 to 6000 appm/year) and, at the same time, high temperatures (up to 700 °C) would be strongly required. A preliminary conceptual study has been carried out by looking at the potential use of either the Russian fast reactor BOR-60 or the European High Flux Reactor (HFR).

The main objective of the study was to investigate which reactor is the more suitable for such irradiation as well as to estimate the irradiation time required for obtaining the desired EOL HCPB blanket conditions.

The result of neutron calculations in terms of He production vs. neutron damage for the HCPB blanket, the BOR-60 and the HFR reactors are shown in Fig. 1.

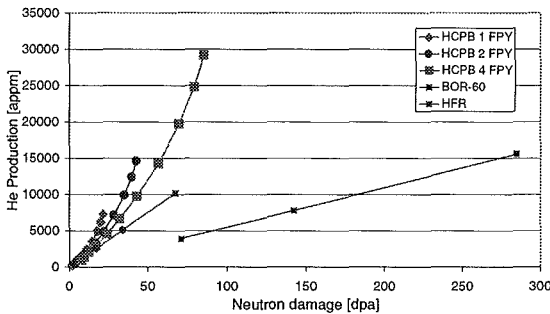


Fig. 1: Beryllium He production vs. neutron damage in the HCPB blanket as compared with the BOR-60 and HFR reactor

Although neither the BOR-60 nor the HFR reactor are able to fully reproduce the conditions expected in the HCPB blanket, the HFR seems to be more suitable than the BOR-60. In fact, the intrinsic disadvantage of the HFR with respect to the BOR-60 in term of required irradiation time is compensated by its higher availability (i.e. 77% and 55%, respectively). Furthermore, the "harder" neutron spectrum of the BOR-60 would produce a much higher neutron damage than that expected in the HCPB blanket. According to that calculation and taking into account the reactor availability, the effective irradiation time necessary to produce 10000 appm helium in beryllium has been evaluated in 4.3 and 5.1 calendar years for the BOR-60 and the HFR, respectively.

In order to estimate the gas-driven swelling expected during the irradiation, calculations with the ANFIBE code have been carried out. As shown in Fig. 2, a swelling ranging from 2.5% to 7.5% would be expected after 4 full power years (FPY) viz. 5.1 calendar years (i.e. 10000 appm He) irradiation in the HFR in a temperature range of 350-700 °C.

In any case, it is quite clear that it is extremely difficult to reproduce irradiation conditions similar to those expected in the HCPB blanket in a reasonable time with the presently available fission reactors. Similar conditions could probably be easily obtained if an appropriate fusion material irradiation facility (e.g. IFMIF) would be available.

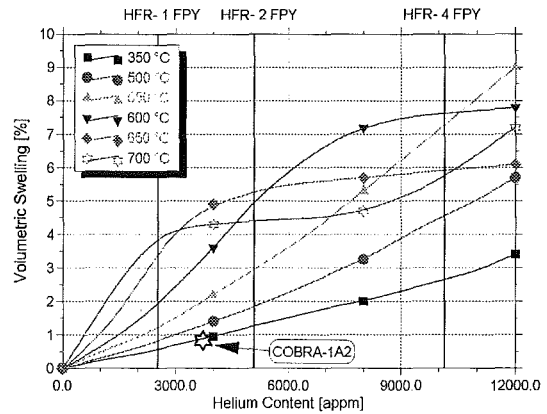


Fig. 2: Swelling vs. He content in beryllium

Staff:

U. Fischer
D. Leichtle
F. Scaffidi-Argentina
H.-J. Tsige-Tamirat

**Blanket
WCLL Concept**

TTBA-002 Blanket Manufacturing Techniques

TTBA-002/3 Forming and Form Stability of Solid HIP FW and Cooling Tubes

A small-scale diffusion welding test of MANET plates with Cu compliant layer of 0.1 mm thickness was successfully carried out. The mechanical testing evidenced rupture strength values of about 587 MPa. This is rather high for Cu, but below the yield strength of MANET. The total elongation at rupture of the 18 mm long tensile test sample with the 0.1 mm Cu layer in the axial center was found to be about 1.4 %. In total the results of this test are considered fully satisfactory for the envisaged application.

After failure of bonding in the first attempt, HIPping of the medium-scale FW plate with three cooling tubes and Cu compliant layer was repeated. In the subsequent ultrasonic test, again insufficient bonding was detected. As neither a leak of the seal welds nor of the tubes could be found, it is assumed that the welding surfaces were contaminated during the numerous handling, testing, and machining operations. In parallel the manufacturing of a second FW plate with only one cooling tube was started. Plate and tube material is now EUROFER. Presupposing successful diffusion welding, bending is envisaged for Oct. 2000.

This report includes also work carried out in Oct. – Dec. 99 under Task A 3.2.

Literature:

T. Lechler, K. Schleisiek, H.-J. Fiek: FZK Contribution to the Development of FW Manufacturing Techniques for the EU-WCLL Blanket. FZK Internal Report IRS-Nr. 3/00, Febr. 2000

Staff:

H.-J. Fiek, Fa. Ingenieurbüro Fiek
S. Gordeev
T. Lechler
K. Schleisiek

**TTBA-003
Coating Qualification and Irradiation Tests
TTBA-003/2**

Fabrication and Characterisation of Hot-Dip Specimens, Delivery of Hot Dip Specimen

Tritium permeation can be significantly reduced by a suitable coating of the structural material. Previous experiments have proved that hot dip aluminised and heat treated steel sheets fulfil the goals required for a tritium permeation barrier (TPB). A further improvement of the coating structure was anticipated by HIPping of the specimens during the heat treatment.

Hence, the hot dip aluminised samples were HIPped in an argon atmosphere at 1, 250, 500 and 750 bar, the temperatures and times chosen correspond to the instruction for austenisation and tempering for F82H-mod. steel: 1040 °C / 30 min, 750 °C / 1 h.

Metallographical cross sections of the samples revealed the formation of three layers. A band of pores is only observed on the specimen heat treated under 1 bar. The specimens heat treated with superimposed pressure showed no vacancies, pores or holes in their layers. The formed phases analysed by means of EDX line scans (see fig. 1) were the same on each specimen. The brittle Fe₂Al₅ phase formed during the hot dip aluminising process was completely transformed after heat treatment into three new compounds. The external layer consists of the FeAl₂ phase with an Al content of around 46 wt%. Just beneath the FeAl₂, a region of FeAl phase was found. The concentration profiles for Fe, Al and Cr show a sharp change from the FeAl₂ phase to FeAl which reflects the missing compounds between 36 and 58 wt% Al in the Fe-Al phase diagram at 1040 °C. According to the binary Fe-Al phase diagram the FeAl phase is stable between 18 and 36 wt% Al at 1040°C. Beneath the FeAl phase the Al concentration decreases continuously from 18 to 0 wt%. This composition corresponds to α-Fe(Al).

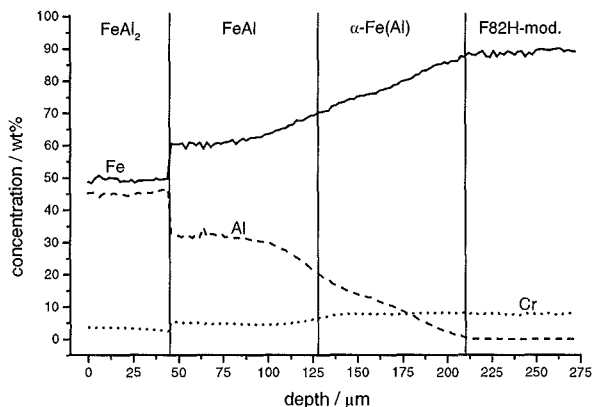


Fig.1: EPMA line scans of a hot dip aluminised F82H-mod. sample sheet after heat treating (1040 °C / 30 min, 750 °C / 1 h) under 750 bar.

The micro hardness determined on the three phases FeAl₂, FeAl and α-Fe(Al) of all specimens are comparable. With decreasing Al content the micro hardness value decreases in all Fe-Al phases. Hence, the pressure has no influence on the micro structure.

The thickness of the layers were measured in different zones of the samples. The thickness revealed for the FeAl and α-Fe(Al) layers is shown versus the superimposed pressure in fig. 2. The

specimens heat treated with superimposed pressure showed only a little change in thickness of about 10 μm in maximum for each phase. In the case of the 1 bar specimen the range measured is bigger because the porous band did not allow an exact distinction between the two phases. It can be shown very well by linear fitting of the data that the thickness of the FeAl layer increases with increasing superimposed pressure, the thickness of α-Fe(Al) layer show the opposite trend: it decreases with increasing pressure.

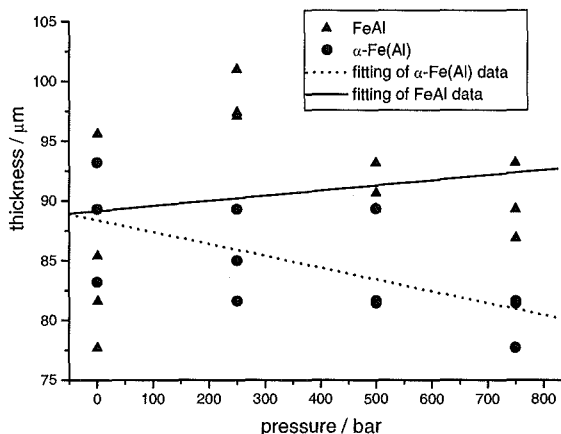


Fig. 2: The thickness of the FeAl and α-Fe(Al) phases versus the superimposed pressure existed during the heat treatment.

It is obvious that the transformation rate of Fe₂Al₅ into the phases FeAl₂, FeAl and α-Fe(Al) gets slower with increasing pressure. High pressure influences the number of vacancies, holes and cavities in a lattice, i.e. increasing pressure leads to a decrease in vacancies. This fact has led to a decrease in the diffusion rate which can be seen in the slower transformation of Fe₂Al₅ and FeAl₂ and the absence of Kirkendall pores.

Heat treatment with superimposed pressure has a significant influence concerning the scale structure of hot dip aluminised steels sheets. Two effects were observed on the HIPped samples:

- With increasing pressure the thickness of the FeAl phase increases and the thickness of the α-Fe(Al) phase decreases.
- The formation of pores were suppressed successfully.

The absence of the pores could have a positive influence on the reduction of the permeation rate. Hence, permeation measurements of HIPped samples have to be done.

Literature:

[1] H. Glasbrenner, J. Konys, 21st SOFT conference, 11 – 15 September 2000, Madrid, Spain.

Staff:

- H. Glasbrenner
J. Konys
Z. Voß
O. Wedemeyer

**TTBA-006
Magneto Hydrodynamics (MHD)**

**TTBA-006/1, 2, 3
Test and Modelling of Forced Convection MHD**

Introduction

In currently investigated liquid-metal (LM) blankets for fusion reactors the LM - a lithium-lead alloy - serves mainly as breeding material [1] and not as coolant.

1. Thus the externally forced flow required for a continuous circulation of the breeding material is very weak within the breeding zone reaching there typically mean velocities on a scale of a few mm/s. Therefore, buoyant flow may become dominant in the whole blanket influencing heat transfer and the distribution of the concentration of the tritium generated within the liquid metal breeder [2].
2. However, in the blanket header high flow velocities appear which due to the large amount of structural material in the header generate high pressure drops. An even more peculiar feature of the MHD flow in the header is that uneven flow rates in the individual feeding and draining ducts appear, which are caused by the electric coupling of channels via the electrically conducting structural material. New fabrication technologies allow an electrical separation of the individual feeding/draining ducts and hence drastically reduce the MHD pressure drop and avoid uneven flow rates (the so called multi-channel effect). The electrical separation is performed via an electrically insulating coating being plasma-sprayed on the ducts. Afterwards the individual ducts are hipped to a full header module.
3. A third feature of the EU-WCLL design is that the structural material being considered is MANET which is ferro-magnetic, having a magnetic permeability significantly larger than unity ($\mu_r \approx 50$). This ferro-magnetism may lead to changes of velocity profiles within the duct and probably to reduced MHD pressure drops, due to the modified electromagnetic boundary conditions at the liquid-solid interface. This effect becomes most apparent especially if the magnetic saturation field strength is exceeded, which holds for the blanket.

These features of the EU-WCLL blanket have been investigated within the R+D program and the results achieved are discussed below.

1.1 Natural convection experiments

Buoyant flow in breeding blankets can be caused by temperature differences within the LM due to volumetric heating and the heat removal through the cooled walls and/or tubes. The knowledge of the velocity distribution is important for the evaluation of the heat transfer and it is of special interest with respect to the concentration distribution of the tritium generated within the LM [3]. In order to avoid tritium hot spots in the corner near the first wall a transport velocity of at least 10^{-6} m/s is necessary. Out of pile experiments on natural convection of volumetric heated LM under MHD-conditions cannot be realized because any electrical heating would interact with the MHD phenomena to be investigated. Therefore we decided to restrict our experiments to the investigations of the natural convection flow between a heated and a cooled plate. With the experimental verification of numerical results reliable predictions of the flow patterns appearing in the blanket can be made.

The most relevant case in the EU-WCLL blanket concept is the configuration shown in fig 1a. There, in principle a vertically

arranged box heated and cooled from the sides is exposed in a horizontally oriented magnetic field.

The experiments are conducted in in the superconducting solenoid magnet of the MEKKA laboratory [4] which allow to measure in magnetic fields of up to 3.5 Tesla.

A cross section through the test apparatus is shown in Fig. 1b. The heated side wall - a 20 mm thick copper plate - is heated by 20 electrical heater rods embedded and brazed in grooves in order to improve the heat transfer. This heater allows to operate with an electrical power up to 12 kW corresponding to a heat flux of up to 15 W/cm² and enables Rayleigh-numbers up to 105. The cooled side wall - again a copper plate - is cooled and kept at constant temperature of about 100 °C by a boiling pool of water. The other walls are of 1.5 mm stainless steel. To homogenize the boiling heat transfer a particle bed of glass spheres with a diameter of 5 mm is used. The vapor from the boiling pool is recondensed on water cooled heat exchanger located outside the magnet. A more detailed description can be found elsewhere e.g. [2,3,5] .

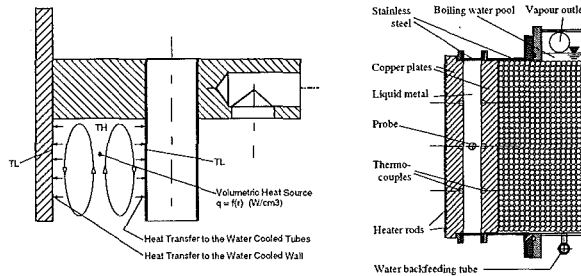


Fig. 1: a.) Natural convection in substructures of the WCLL and the influence on tritium concentration.
b.) Schematics of the convection experiment performed in the MEKKA facility

1.2 Theory: Two-dimensional (2D) formulation of the problem

In 3D magnetohydrodynamic flows the energy of vortices whose axes are inclined to the direction of the magnetic field is immediately removed by Joule's dissipation and the vortices will be strongly damped (see e. g. [4-9]). Vortices whose axes are aligned with the direction of the magnetic field are not affected by the field as long as the fluid is of infinite extent in the direction of the magnetic field. So if the magnetic field is strong enough a 2D flow pattern of convective rolls aligned with the direction of the magnetic field will evolve. If the fluid is of finite extent in the direction of the magnetic field, electric currents induced by the fluid motion can close in the viscous Hartmann layers and in the electrically conducting Hartmann walls. Thus, the fluid motion is damped by an additional Lorentz force. Integrating along magnetic field lines, taking into account symmetry conditions and the thin wall condition, these 3D currents can be taken into account and the problem can be described by 2D equations (B is parallel to the x -axis):

$$\frac{1}{Pr} \left[\partial_t \omega + \partial_y \psi \partial_z \omega - \partial_z \psi \partial_y \omega \right] = \left(\partial_{yy} + \partial_{zz} \right) \omega + Ra \partial_y T - \frac{\omega}{\tau}$$

$$\partial_t T + \left(\mathbf{v} \cdot \nabla \right) T = \left(\partial_{yy} + \partial_{zz} \right) T$$

$$\frac{1}{\tau} = \frac{\sqrt{Q}}{b} + \frac{Q \cdot c}{b+c}$$

Here x, y, z is a Cartesian coordinate for which the distance h between the heated and the cooled plate is taken as a characteristic length scale. The magnetic field is orientated in x -

direction and the two dimensional flow evolves in the y,z-plane. The velocity components v and w are expressed in terms of a 2D stream function ψ with $v=\partial_z\psi$ and $w=-\partial_y\psi$ and $\omega=(\nabla\times v)\cdot e_x$ is the vorticity component in the direction of the magnetic field. T is the dimensionless temperature obtained from scaling with the temperature difference across the layer ΔT . The effect of magnetic field is accounted for by the last term of equation (2). The dimensionless parameter τ is a characteristic time scale for the decay of vorticity by the effect of Hartmann braking. Its inverse $1/\tau$ is called the magnetic damping parameter, defined from equation (3) where b is the half dimensionless extension of the layer in the direction of the magnetic field, c is the wall conductance ratio defined as $c=s\sigma_W/(h\sigma)$ with the thickness of the wall s and the electrical conductivities σ an σ_W of the fluid and the wall respectively. The magnitude of the applied magnetic field is expressed in terms of the Chandrasekhar number $Q=h^2B^2\sigma^{-1}\nu^{-1}$ which is related to the more common Hartmann number like $Ha=0.5Q^{0.5}$. Other dimensionless groups in these equations are: The Prandtl number $Pr=\nu/\kappa$ with ν the kinematic viscosity and $\kappa=\lambda/(\rho c_p)$ the thermal diffusivity, calculated from the thermal conductivity λ , the density ρ and the specific heat capacity c_p . The Rayleigh number $Ra=\alpha g\Delta Th^3\kappa^{-1}\nu^{-1}$ where α is the cubic thermal expansion coefficient and g the magnitude of the acceleration of gravity.

1.3 Results of the convection experiments

The heat transfer across the layer is denoted in dimensionless form by the Nusselt number $Nu=q''h\lambda^{-1}\Delta T^{-1}$ with q'' the applied heat flux. In Fig. 2 the Nusselt-numbers are shown for different Hartmann-numbers Ha as a function of the Rayleigh-number Ra . For all Hartman numbers, the Nusselt numbers are increasing continuously with increasing Rayleigh numbers. Consistent with the concept of increased Joule's dissipation at higher magnetic fields the Nusselt numbers for the high Hartmann numbers $Ha=800$ and $Ha=1600$ are significantly lower than at ordinary hydrodynamic (OHD) flow at $Ha=0$. However, for moderate strengths of the applied magnetic field $50<Ha<400$ higher Nusselt numbers than without Magnetic field are observed. This can be explained by an ordering effect of the magnetic field on the convective flow patterns. The non-isotropic character of the electromagnetic forces gives rise to the transition of three-dimensional convective vortex structures into increasingly two-dimensional ones in the sense that vortex axes become aligned with the direction of the applied magnetic field. The reduced non-linearities of local non-isotropic flow cause the formation of large-scale coherent structures which exhibit much simpler temporal dynamics and higher convective heat transport than under ordinary hydrodynamic (OHD) conditions.

In Fig. 2b typical time recordings of the fluctuating part of the temperature signals recorded by the probe are shown. At a constant heating power of 7200W the magnetic field is varied in the range $0<Ha<1600$. Due to the variation of the convective heat transport the Rayleigh numbers vary in the range $5\cdot 10^4<Ra<8.7\cdot 10^4$. At OHD flow ($Ha=0$) large amplitude random fluctuations of the temperature, typical for turbulent convection, are observed. The imposition of moderate magnetic fields in the range $50<Ha<200$ causes a significant increase of the governing time scale and even larger amplitudes of the fluctuations. These findings are related to convective motions with larger scales. If the magnetic field is increased beyond $Ha=400$ the flow undergoes a fast transition from high organized temporal structures to stationary flow as it is indicated for the highest Hartmann numbers. In Fig. 3(a) the Nusselt numbers obtained from the measurements shown in Fig. 2b are compared with predicted values obtained for $Ra=10^4$ from a numerical solution of the 2D model equations. The strength of the applied magnetic field here is expressed in terms of the magnetic damping parameter $1/\tau$. The calculations are well reflecting the tendency of decreasing heat transfer at higher magnetic damping parameters. Additional information on the flow is obtained from the distribution of the stream function ψ plotted in figure 3(b). As the magnetic damping parameter is increased from left to right the time dependent convective flow pattern of multiple rolls evolves into a stationary one characterized by one single convective cell. At this stage the contribution of convective heat transport becomes negligible and the asymptotic behaviour $Nu=1$ is obtained. However this does not mean a full suppression of any convective motion and significant tritium transport in the blanket due to thermal convection may be expected nevertheless.

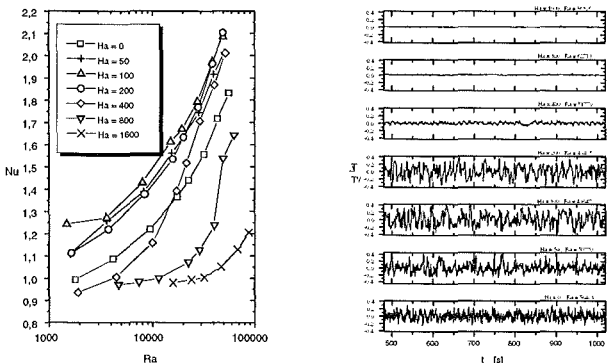


Fig: 2 a.) Measured Nusselt-numbers versus Rayleigh numbers Ra for different Hartmann-numbers Ha . b.) Fluctuating part of the temperature signals recorded by the probe, $0<Ha<1600$, $5\cdot 10^4<Ra<8.7\cdot 10^4$

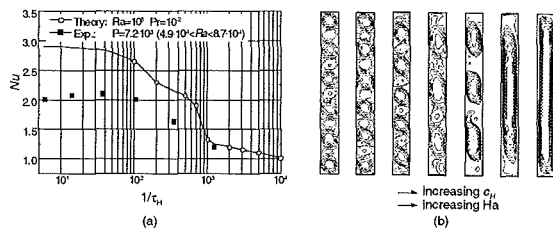


Fig. 3 : (a) Comparison of measured Nusselt numbers with values obtained from a numerical solution of 2D model equations. (b) flow patterns of the 2D numerical solution. The effect of increasing magnetic damping parameters $1/\tau$.

1.4 Summary of the natural convection experiments

Natural convective flow of liquid metals under the influence of externally applied magnetic fields as they may occur in fusion blankets may be investigated in well defined experimental set-ups. From the experimental results, complemented by the theoretical analysis it is concluded, that under fusion relevant conditions (Hartmann numbers $Ha\approx 5000$, Rayleigh numbers $Ra\approx 5\cdot 10^7$) thermal convection is reduced to large scale stationary motions that do not significantly contribute to the heat transfer in the blanket. Nevertheless, the existence of the remaining marginal motion is crucial to avoid tritium hot spots.

2.1 Forced convective flow in the ducts of the Blanket header

One important question for the design of liquid metal blankets is availability of a long term reliable electrical insulation of the duct walls, which is capable to withstand the high neutron fluxes present in the reactor. The research to develop such electrically

insulating materials is still an ongoing task although the insulation requirements for such a material with respect to MHD are far below the ones setup by the electric industry. In the absence of an electric insulation of the duct walls global electric currents induced by the fluid motion can circulate within the blanket structure. This effect known as multi-channel effect (MCE) may lead especially for self-cooled blankets to pressure drops exceeding the allowable material stresses. But also the actually discussed Water-Cooled-Lead-Lithium (WCLL) blanket can be significantly affected by the MCE since it yields uneven flow distributions in the individual ducts.

The pressure drop caused by MHD flows in most of the relevant duct geometries may be minimized by the use of thin conducting walls or by direct insulations (coatings or ceramics). Thin conducting walls can be achieved by the use of so-called Flow-Channel Inserts (FCI), where an electrically insulating ceramic sheet is sandwiched by thin steel plates. These FCI's are fitted loosely in the ducts. The physical effect leading to the reduced MHD pressure drop is that the electric current density is minimized, because the thin steel sheets represent a higher ohmic resistance than a thick wall facing the liquid metal. A second advantage are the low requirements on the FCI's with respect to their stiffness, since the pressure level in- and outside the FCI is nearly the same. Nevertheless, the usage of FCI's in long geometries requires the insertion of several FCI's. At the junctions where the FCI's overlap three-dimensional MHD flows appear due to the jump of the electrical conductivities.

Another technical method to overcome the disadvantage of the overlapping of FCI's and their fitting into the ducts bores is discussed in the frame of the manufacturing of the WCLL test blanket module (TBM) for ITER [10]. This specific type of FCI is illustrated in figure 4 and the manufacturing of such a FCI is performed as follows:

- a.) Fabrication of semi-circular grooved thick MANET steel plates (using the hot isostatic pressing or HIP method).
- b.) Spark-erosion of a thin-walled MANET steel tube and final machining of this tube.
- c.) Plasma spraying of the thin walled MANET tube with alumina oxide Al_2O_3 .
- d.) Seal welding of the thick plates with the thin tube using an electron beam
- e.) Finally, diffusion bonding of the semi plates in a HIP facility at 50MPa and 980°C for three hours.

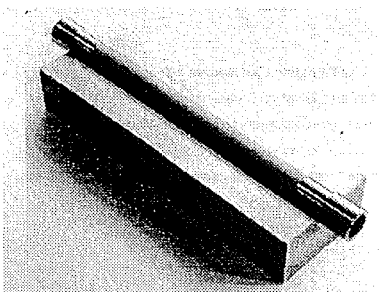


Fig. 4: Photograph of the semi-fabricated specimen foreseen for MHD flow tests in the MEKKA-facility of the FZK [10].

2.2 Results of the Electrical Decoupling

The module shown in figure 4 has been embedded in the MEKKA-Facility. In the pretesting phase of the test section the

eutectic InGaSn alloy has been used as liquid in order to measure the quality of the electrical insulation of the plasma sprayed alumina oxide Al_2O_3 layer between the inner duct and the massive hiped MANET structure.

The measurements showed that no electrical separation between the MANET and the stainless steel tube was achieved, although the inner tube was completely leak tight to the ambience. A metallographic investigation for this quite disappointing effect revealed that the glue necessary for attaching the alumina oxide on the stainless steel tube contained carbon. During the high temperature hiping procedure carbon and graphite crystals are formed, because of the carbon concentration difference between glue and the MANET. The crystals penetrated through the alumina oxide layer in such a way that they formed an electrical contact. Unfortunately, the crystals are spread dense and quite regularly over the whole hiped domain. Thus no significant increase of the ohmic resistance between the thin steel tube and the massive MANET block could be measured.

A new test section using a different method of plasma spraying alumina oxide layer onto the steel tube is currently under fabrication. First tests of the specimen have shown a high degree of electrical separation.

3.1 Forced convective flow in ferromagnetic ducts

The structural material considered in the EU-WCLL blanket as in many other blanket types is the ferro-magnetic steel MANET a magnetic permeability μ_r far above unity ($\mu_r \approx 50$). This ferromagnetism leads probably to reduced MHD pressure drops, due to the modified electro-magnetic boundary conditions at the liquid-solid interface. This effect becomes most apparent if the magnetic saturation field strength of MANET is exceeded, which is about 1.65 Tesla. In the blanket, however, this magnetic field strength is by far exceeded.

As a consequence the electro-magnetic boundary conditions at the liquid metal-duct interface are different than in the case of non-ferromagnetic materials. Especially, the magnetic field produced by the electric current (which originates from the interaction of moving liquid and plasma confining magnetic field) circulating within the liquid metal and the magnetic field lines compressed in the ferro-magnetic duct interact with each other, leading to other current paths. This modification of the boundary condition leads to different MHD flow features than investigated in the past.

Thus, new models have to be derived and verified by experiments in order to ensure a high performance of the blanket module. These models have not only to treat the fluid dynamics and the electrical properties of the fluid/ wall system but also the magnetic field, which can now not be treated as a constant field property. This magnetic field is a function of space when ferromagnetic duct walls are used.

In order to quantify the effect of a ferromagnetic material on the MHD flow, two geometrically identical thick-walled test sections, one consisting of stainless steel ($\mu_r \approx 1$, see fig.5) and one being ferromagnetic (made of construction steel S355) have been fabricated. Both test modules have circular cross-sections. A photograph of the stainless steel section is shown in figure 5.

A diagram of the magnetisation of the ferro-magnetic steel is shown in graph 6, where the externally applied magnetic field is shown as a function of the field within the duct. The graph shows that the ferro-magnetic material shields up to field strength of up to 0.8 Tesla. Above this range the inner field grows linearly with the outer one. The implementation of the test sections in the MEKKA facility is scheduled for October 2000.

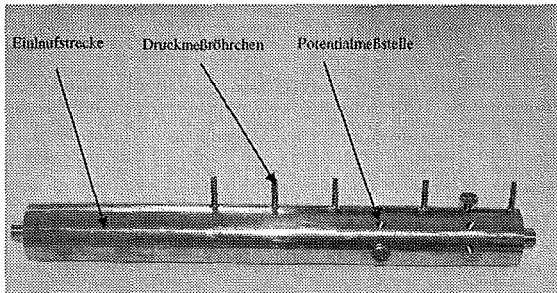


Fig. 5: Photograph of the stainless steel test section being fabricated at the FZK-IKET. The length is about 500mm

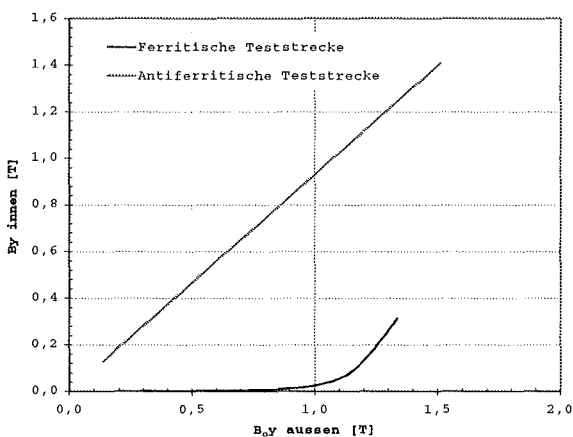


Fig. 6: Magnetisation diagram of the ferritic test section

Literature:

- [1] Giancarli, L. et al. (1992), Water-cooled lithium-lead blanket design studies for DEMO reactor, Fusion Technology 21, 2081
- [2] Stieglitz, R.; Barleon, L. (1997), MHD aspects and experimental activities in fusion blanket designs, Proc. IEA Intern. Workshop on Liquid Metal Blanket Experimental Activities, Paris, France, Sept. 16-18, 1997
- [3] Barleon, L.; Burr, U.; Mack, K. J.; Müller, U. (1997) Natural Convection Phenomena in Magnetic Fields of Liquid Metal Fusion Blankets, Ref. [2]
- [4] Barleon, L.; Mack, K. J.; Stieglitz, R. (1996) The MEKKA-facility a flexible tool to investigate MHD-flow phenomena, FZKA-5821
- [5] Barleon, L.; Jochmann, P.; Mack, K.-J.; Burr, U.; Stieglitz, R. Experimental Investigations on the Magneto-Conductive Flow in a Vertical Gap, Proc. 4th Int. PAMIR Conf., 1, p. 309-315.
- [6] Lehnert, B. (1956), An instability of laminar flow of mercury caused by an external magnetic field, Proc. R. Soc. London, A 233, 299-310
- [7] Kolesnikov, Y., Tsinober, A. (1972), An experimental study of two-dimensional turbulence behind a grid, Fluid Dynamics 9, 621-624
- [8] Sommeria, J. Moreau, R. (1982) Why, how and when MHD turbulence becomes twodimensional, Journ. of Fluid Mechanics 118, 597-618
- [9] Chandrasekhar, S. (1961) Hydrodynamic and Hydromagnetic Stability, Oxford University Press, Dover Publications, Inc. New York
- [10] Fütterer, M.; Giancarli, L. (1996) Design Description Document for the European Water-Cooled Pb-17Li Blanket. DMT 96/349 SERMA/LCA/1911.

Staff:

L. Barleon
 L. Bühler
 U. Burr
 M. Frank
 R. Vollmer
 K. J. Mack

Structural Materials

TTMS-001 Irradiation Performance

HFR Irradiation Programs

HFR Phase IB

The HFR Phase IB programme was performed at irradiation temperatures from 250 – 450 °C and a dose level of 2.4 dpa. It concentrated mainly on technological studies. Due to numerous problems and delays (politically motivated delayed granting of transport permits), the examinations will start in November 2000 instead of October 1999. The following results are expected:

- A study of EB and TIG weldings with F82Hmod and of diffusion weldings with MANET II.
- A characterisation of the F82Hmod HIP base material and the influence of the notch root.
- The influence of different annealing treatments on the mechanical properties of OPTIFER and F82Hmod.
- Further insights for the improvement of the chemical composition (OPTIFER without boron, JLF1).

HFR Phase IIB (SPICE)

The layout and details of the new irradiation programme (SPICE) in the HFR have been completed. The sample holder fabrication has started, specimen fabrication is completed by the end of September. Irradiation is planned to start in December 2000.

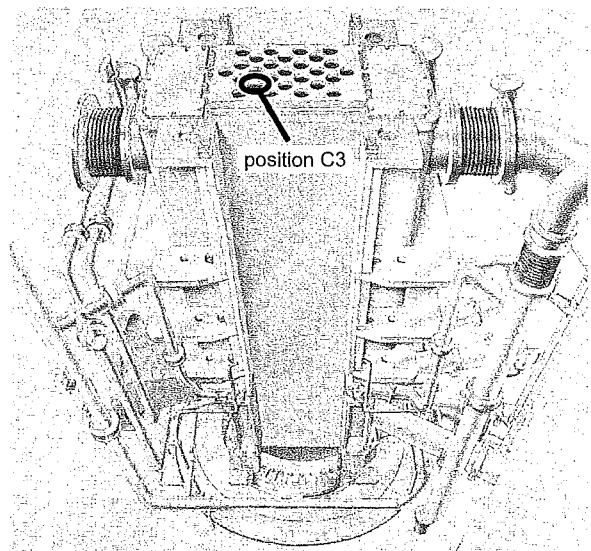


Fig. 1: Reactor vessel of the HFR. The position of the SPICE capsule, which is surrounded by fuel assemblies, is marked

The final design after thermodynamic calculations provides space for 130 charpy, 91 tensile, and (for the first time simultaneously) 160 fatigue specimens. The irradiation temperatures are 250/300/350/400/450 °C and the dose level is 15 dpa, reached in a central core position of the reactor (see Fig. 1). Activation detectors in the sample holders and temperature control by sodium are additionally applied to ensure the high quality level of HFR irradiations even at higher doses (see Fig. 2).

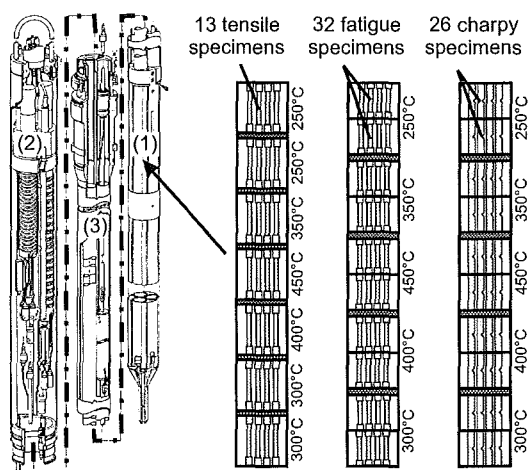


Fig. 2: Irradiation capsule with sample holders. (1): sample holders, (2): vertical displacement unit for neutron flux control, (3) temperature control unit

In the SPICE programme, the new low activation alloy EUROFER 97 - the result of the development from OPTIFER I to OPTIFER VII - will be investigated in different variations: Different heat treatments, a HIP powder steel, and various boron contents to investigate the effect of He embrittlement. A few samples will serve as a reference to former irradiations and to complete the data for several formerly investigated alloys. Regarding the EUROFER steel, an embrittlement behaviour comparable to the best alloys investigated in former irradiation programmes is expected, accompanied by good mechanical properties. The higher irradiation dose of 15 dpa will be a step towards fusion-relevant doses.

Staff:

J. Aktaa
B. Dafferner
W. Kunisch
H. Ries
O. Romer
H.-C. Schneider

Work on OPTIFER- and F82H mod.-Alloy

A series of martensitic developmental alloys has been investigated after irradiation in the HFR. These 7-10%CrWV/Ta alloys have been optimised towards long-term activation and the properties are compared with the conventional 9-12%CrMoNb steels.

The irradiation in HFR was carried out in the temperature range of 250 – 450 °C up to an accumulated dose of 2.4 dpa. The tensile specimens were manufactured of the alloys OPTIFER II, OPTIFER IV and the Japanese steel F82H mod.. The chemical compositions are given in Table 1. The heat treatments are collected in Table 2.

Table 1: The chemical components of the irradiated alloys

Elements	OPTIFER II	OPTIFER IV	F82H mod.
Cr in wt.% ↓	9.5	8.5	7.61–7.64
C	0.125	0.11	0.09
Mn	0.49	0.57	0.16
V	0.28	0.23	0.16
Ta	0.018	0.15	0.02
W	0.006	1.16	1.94–1.97
Ge	1.2	-	-
P in ppm ↓	43	40	20
S	20	40	10-20
B	59	40	2
N	159	600	60-80
O	90	35	-
Nb	-	-	1
Ce	<10	-	-

Table 2: The heat treatments of the irradiated alloys

Alloy	Heat Treatment
OPTIFER II	950 °C 0.5 h + 780 °C 2 h
OPTIFER IV	900 °C 0.5 h + 750 °C 2 h
F82H mod.	1040 38 min + 750 °C 1 h

The tensile specimens were tested in the Hot Cells of the Forschungszentrum Karlsruhe. The tests were performed with a static mechanical tensile testing machine with a strain rate of 1% min⁻¹. The unirradiated specimens have also been tested at RT (Room Temperature). The irradiated specimens were tested at their irradiation temperature of 250, 300, 350, 400 and 450 °C. The results of the yield strength ($R_{p0.2}$), ultimate tensile strength (R_m), and the total elongation (A) are plotted vs. the irradiation and test temperature, Fig. 1-3.

The influence of the irradiation is quite obvious by an increase of the strength in all materials at 250 and even more at 300 °C. At the higher test- and irradiation temperatures, the strength of all alloys decreased again. This is not only due to the irradiation, there is the influence of the increasing test temperature, too. The tensile tests with unirradiated specimens show the thermal effect as a continuous softening. The highest strengthening due to the irradiation was found at 300 °C and with lower values at

350 °C. The total elongation, a measure of ductility, confirms the behaviour of the strengthening at 300 °C, too. All three alloys have a similar mechanical behaviour after irradiation. In this series, OPTIFER II has the weakest strength and highest ductility.

The influence of strengthening by the irradiation (0.8 dpa) could be explained by former microstructural investigations. Irradiation induced loops, fine precipitates and He-bubbles contribute to the strengthening in the material. They block the movement of the dislocations during the deformation of the material.

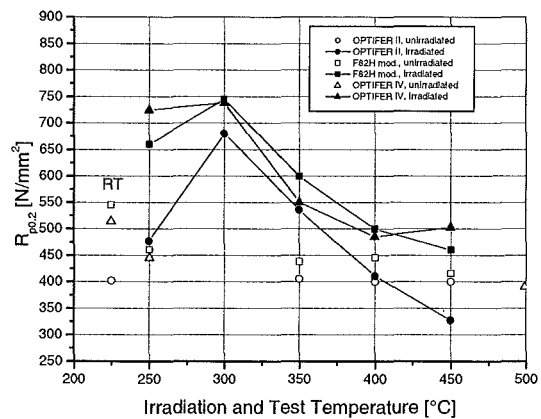


Fig. 1: The yield strength, $R_{p0.2}$

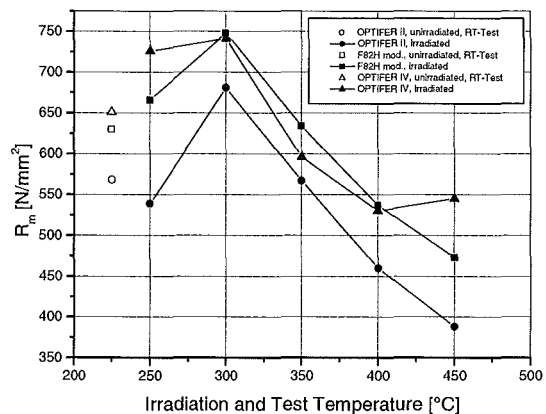


Fig. 2: The ultimate tensile strength, R_m

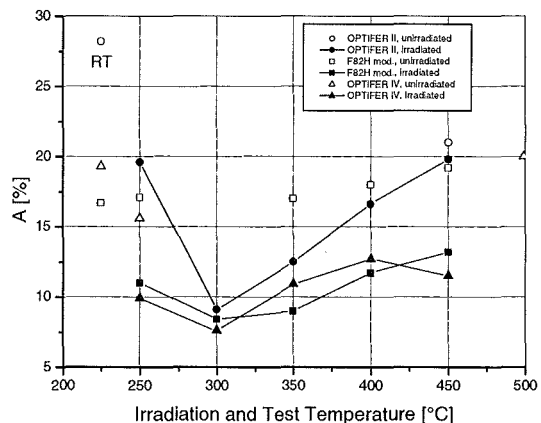


Fig. 3: The total elongation, A

Literature:

E. Materna-Morris, M. Rieth and K. Ehrlich: Mechanical Properties and Microstructure of HFR-irradiated Ferritic/Martensitic Low-Activation Alloys. Effects of Radiation on Materials: 19th Int. Symp., ASTM STP1366, March 2000, p. 597-611.

Staff:

B. Dafferner

K. Ehrlich

M. Holzer

W. Kunisch

E. Materna-Morris

B. Neufang

H. Ries

R. Rolli

O. Romer

Correlation between Microstructure and Mechanical Properties

Overview

The correlation between microstructure and the form of ductile - brittle transition as well as the tensile properties of martensitic 9-12CrMoVNb and 7-9CrWVTa steels have been analysed by physical models [1, 2]. Particularly the superimposed effects of helium [3, 4] and hydrogen [3] isotope generation with displacement damage, as well as precipitation hardening and strain rate have been considered. Additionally, the possible contribution of second particles to enhance irradiation resistance by suppression of point defect (PD) concentration have been examined [4].

Irradiation hardening and DBTT

In accordance with model predictions for stress induced fracture appearance, the irradiation induced shift of ductile brittle transition $V = \Delta DBTT / DBTT_0$ observed in Charpy impact tests increases. This is combined with a pronounced widening of ductile-brittle transition interval mainly increasing with athermal strengthening, strain rate sensitivity of thermal strength and initial DBTT₀ value [1, 2]. An embrittlement with reduction in fracture stress by a probably irradiation enhanced, coarse Laves phase formation at higher irradiation temperatures and doses or coarse prior austenitic grains increase embrittlement shift V . Both, irradiation strengthening $\Delta\sigma_{irr}$ and embrittlement shift V increase logarithmically with displacement damage dpa at 300°C as shown in Figs.1, 2 for 11CrMoVNb steels (MANET-I,II), and particularly of steel F82H. No saturation is observed in both properties below 34 dpa for F82H. Such behaviour is expected by a weak decrease in defect nucleation rate with increasing damage in absence of strong irradiation induced recovery processes. Mainly due to stronger defect hardening, shift V for MANET-I,II is larger and the dose dependence is more pronounced compared to 7-9CrWVTa steels. It correlates linearly with tensile strength. The strength dependence $V(\Delta\sigma)$, however, is somewhat stronger for 7-9CrWVTa steels due to additional effect from thermal strengthening. As the analysis has further shown, irradiation strengthening above around $T_i = 300^\circ\text{C}$ is mainly athermally caused by larger defects like loops, He- bubbles and α' -precipitates. Below that temperature, however, progressive stronger thermal hardening occurs due to generation of a high density of small PD clusters (vacancy-helium-hydrogen) with size below 1 nm. Thus, in this low temperature region $T_i \leq 300^\circ\text{C}$, helium and even more stronger hydrogen [3] can enhance thermal cluster nucleation and hardening by increasing their density.

Effect of He and H

Fig. 3 shows the yield strength dependence of total elongation $\epsilon_R[\alpha(T)]$ of unirradiated and neutron-irradiated 7Cr2WVTa steel F82H without and with helium generation (≤ 120 appm) by ^{10}B doping in addition to displacement damage of $< 2,4$ dpa. For unirradiated material a sharp minimum of $\epsilon_{R,min}$ is observed around 300°C . The 120 appm helium generated at $T_i = 250^\circ\text{C}$ and 0.7 dpa reduces the tensile ductility strongly, whereby only a weak effect of a variation in the test temperature between RT and 400°C is visible. In contrast, a very strong irradiation temperature dependence of tensile ductility ϵ_R results, as indicated by the HFR irradiation data at $T_i = T_T = 250-450^\circ\text{C}$, 0.8-2.4 dpa with $\approx 20-40$ appm He. Similar, like in unirradiated material a very sharp minimum in ductility occurs around $T_i = T_T = 300^\circ\text{C}$ by formation of a distinct He-induced „nose“ which propagates with increasing He content respectively damage dpa. This minimum is caused by a high density of small He-bubbles formed at coarser $M_{23}C_6$ precipitates enhancing micro-

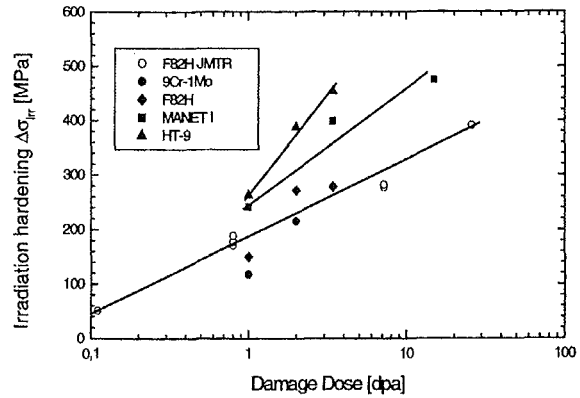


Fig. 1: Irradiation defect strengthening in dependence of logarithmic dose $\ln(\text{dpa})$ at $T_i = T_T = 300^\circ\text{C}$ for 7-12Cr steel

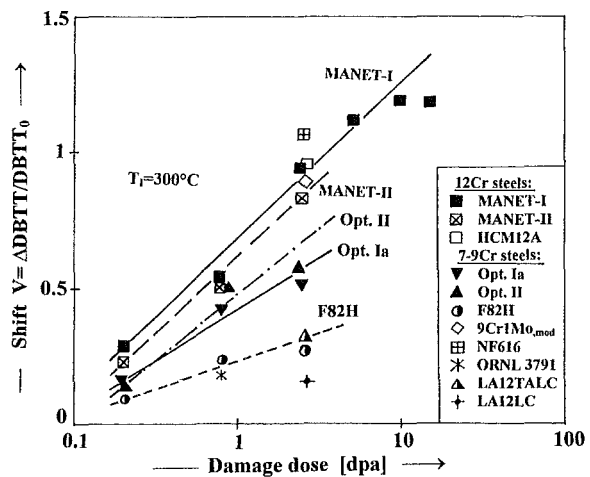


Fig. 2: The embrittlement shift V in dependence of logarithmic dose for various 7-12Cr steels at $T_i = T_T = 250-300^\circ\text{C}$

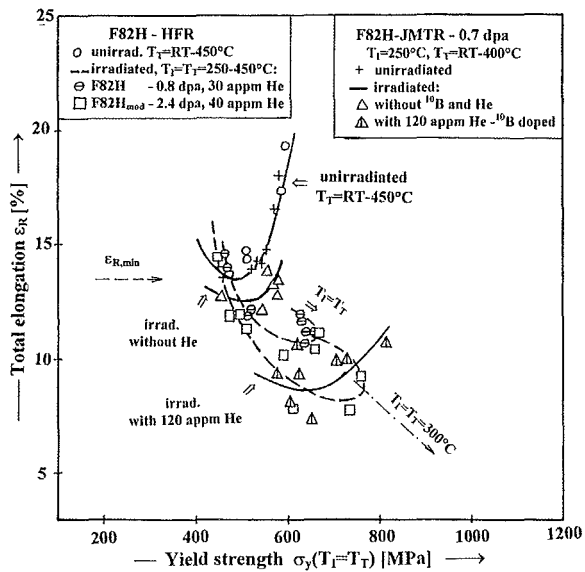


Fig. 3: Effect of superimposed helium generation by ^{10}B doping to lattice damage 0.7-2.4 dpa on the yield strength dependence of total elongation of steel F82H for $T_i = 250-450^\circ\text{C}$

crack nucleation and reducing the ductile fracture stress. Above and also below $T_I = 300^\circ\text{C}$, ductility ϵ_R decreases more strongly due to enhanced bubble growth and probably interfacial stress relaxation by vacancy absorption at these coarse precipitates involved in the ductile fracture process. This mechanism can exceed He-induced ductility reduction at higher temperatures and contribute to an irradiation-induced ductilisation. Such He-induced nose formation was found at all 7-12 steels irradiated in HFR to 0.8-15 dpa where ~ 20 -85 appm He are generated. This demonstrates Fig. 4 which shows the effect of helium content generated via ^{10}B on the relative ductility degree $D = \Delta\epsilon_R^{\text{He}} / \epsilon_{R,\text{min}}$ for constant temperatures $T_I = T_T = 250$ - 475°C and 0.7-15 dpa, ≤ 120 appm He. The ductility reductions are below $D \leq 0.5$ and clearly tend to increase with increasing helium content, possibly somewhat stronger at higher irradiation temperatures. Particularly for steel F82H it becomes positive at higher $T_I = 400$ - 450°C and lower helium contents. This might indicate that vacancy absorption at precipitates enhances interfacial stress relaxation at coarser M_{23}C_6 precipitates and reduces microcrack nucleation and increases ductile fracture stress. Summarising, a neutron-induced helium generation via ^{10}B transmutation causes tensile ductility loss by a high density of small helium bubbles formed at coarser M_{23}C_6 precipitate interfaces. That is enhanced by segregation of boron in precipitates producing „locally“ a high helium content. This explains, why He-implantation, where helium is distributed more uniformly within the matrix, only reduces tensile ductility to a lesser extent but not upper shelf energy of Charpy tests for 300 appm He. The generated matrix helium mainly contributes to thermal cluster hardening below $T_I = 300^\circ\text{C}$, which enhances in addition to displacement damage embrittlement shift V , but comparably weaker than athermal strengthening by larger defects.

Literature:

- [1] D. Preininger, „Modelling of irradiation damage and helium effects on the dynamic embrittlement of 7-12Cr steels“, ICFRM-9, submitted to J. Nucl. Mater.
- [2] D. Preininger, „Characterisation of microstructural effects on the ductile to brittle transition of 9-12CrMoVNb and 7-9CrWVTa steels“, ICFRM-9, submitted to J. Nucl. Mater.
- [3] D. Preininger, „Modelling of superimposed effects of irradiation damage and hydrogen, helium generation on impact behaviour of ferritic-martensitic 7-12%Cr steels“, 5th International Workshop on Hydrogen Isotopes in Solids, Stockholm, 17/19. May 2000, Book of abstracts submitted to Physica Scripta.
- [4] D. Preininger, „Modelling of the effect of microstructure on the shape of cleavage fracture transition in martensitic 7-12Cr steels“, Intern. Congress Materials Week 2000, 25/28. Sept. 2000, Munich, appear in the proceedings

Staff:

D. Preininger

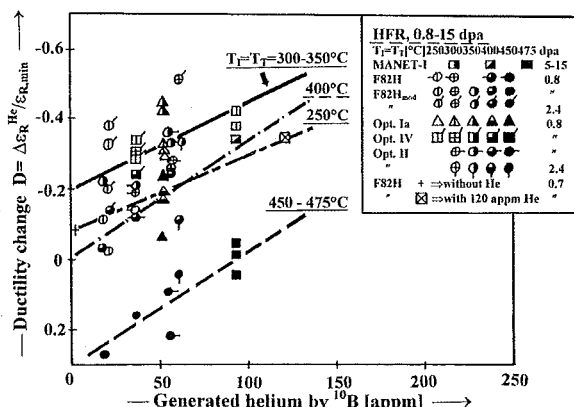


Fig. 4: Effect of helium content generated by ^{10}B on tensile ductility degree D of various 7-12Cr steels for constant temperatures $T_I = T_T = 250$ - 475°C

Effect of second particles

Furthermore, it is frequently found that a high density of small second precipitates reduces strongly swelling similar as cold working by suppression of PD supersaturation. Regarding this, there is a clear different behaviour of coherent and incoherent precipitates. For ferritic 7-12Cr steels as shown by rate theory calculations of defect absorption at defects, against incoherent particles, coherent precipitates can reduce PD concentration only within mean irradiation temperatures of 360 - 490°C and lower defect generation rates by the enhancement of point defect recombination. Thus, coherent precipitates could contribute to reduction of irradiation hardening below 450°C .

**TTMS-002
Metallurgical and Mechanical Characterisation
of RAFM Steels**

**Transformation Behaviour and Tensile, Creep
and Impact Toughness Properties**

Within the framework of the European Technology Programme, the Japanese steel F82H mod. is being investigated parallel to the European steels OPTIFER and the new common European steel EUROFER.

Work on F82H mod.

The characterisation work has been completed and documented (see Annual Reports 97/98 and 98/99). The latest and longest creep test over a duration of 40311 hours at 550°C and 160 MPa marked the completion of creep data collection [1, 2].

Work on OPTIFER

Work with regard to the mechanical properties (tensile and toughness tests) of various OPTIFER types has now been completed [3]. Investigations regarding the creep strength and creep behaviour of annealing states at a reference hardening temperature of 950°C have been completed largely (except for individual long-term experiments). The same applies to the experiments for determining the ageing behaviour following stabilisation annealing. Usually, test durations of $\geq 10^4$ h were applied in the test temperature range. The experimental data obtained allow to determine the design characteristics of $R_{p1\%/20000h}$ and $R_{m/20000h}$ at a temperature of 400 - 600°C with the ageing behaviour taken into account. The curves obtained for the 1% W and W-free types of OPTIFER under reference annealing conditions at a hardening temperature of 1075°C are shown in Fig. 1a. The values obtained at a reduced hardening temperature of 950°C are represented in Fig. 1b [4].

Using OPTIFER-IVc, numerous thermal treatment states and stabilisation annealings were investigated at variable T/t combinations with a view to determine the ageing behaviour [5]. It was found out that annealings of 580°C/3300 h and 600°C/1050 h led to nearly the same results in tensile, notch impact toughness, and creep strength experiments. According to the approach of Hollomon-Jaffe ($P = T_K \cdot (18 + \log t)$), these temperature/annealing time combinations correspond to a load of 550°C/20000 h.

Work on EUROFER

Since the middle/end of 1999, rod material of 100 mm \varnothing and 14 mm sheet material has been made available for characterisation experiments. To determine the transformation behaviour, a continuous CCT diagram was plotted at an austenitisation temperature of 980°C (Fig. 2). The behaviour largely corresponds to that of the OPTIFER alloys [6]. Hardening experiments in the T range of 800 - 1150°C and tempering experiments in the T range of 300 - 850°C allowed conclusions to be drawn with regard to the annealing behaviour and grain size formation. The hardness values following hardening and tempering above all depend on the C content and correspond accordingly to the OPTIFER alloys and F82H mod. [6, 8]. Grain size mainly depends on the Ta content. At 0.14% Ta, a fine-grained structure of 15 - 23 μm is achieved in the hardening temperature range of 950 - 1050°C [6, 8]. It was demonstrated by first metallographic studies that a fully martensitic structure exists without δ -ferrite. Additional structural investigations are presently being performed with various heat treatments being applied. Tensile and notch impact toughness tests have been performed using specimens as delivered and specimens subjected to two different thermal treatments. The tensile test values obtained at a test temperature of RT - 700°C are found to be in the range of those measured for the alloys of OPTIFER (W) and F82H mod., whereas the A_v -T curves of EUROFER are shifted to smaller temperatures as compared to F82H mod. [7, 8]. The results obtained in first creep strength tests at T = 450 - 650°C over maximum periods of 4000 h correspond to the values reached by F82H mod. [9]. As far as ageing stability is concerned, results have been obtained from annealing tests in the T range of 550 - 750°C and at annealing times of 20-3300 h. It is obvious from Fig. 3 that the hardness of the tempered structure is hardly modified as compared to the initial state up to a design parameter of 550°C/20000 h. This means that EUROFER as well as the alloys of OPTIFER and F82H mod. possess a good structural stability over the planned duration of use.

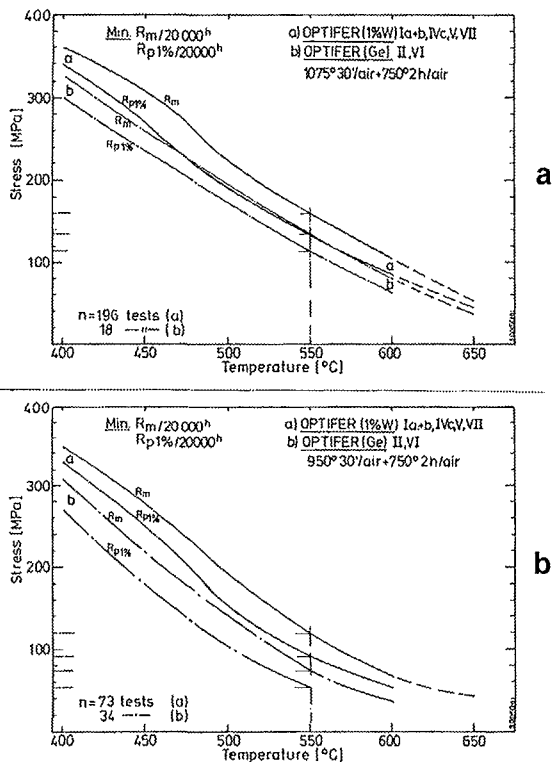


Fig. 1: Design values for $R_{p1\%/20000h}$ and $R_{m/20000h}$

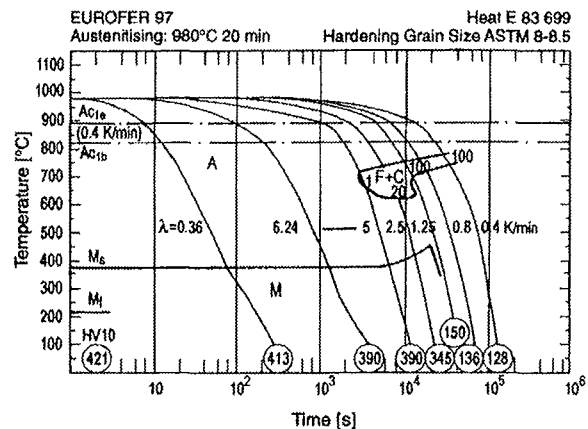


Fig. 2: Continuous Cooling Transformation (CCT) diagram

Material assessment and development strategies

A comprehensive assessment of structural materials for nuclear fusion was elaborated which summarised the present status of knowledge of the different material groups, identified possible feasibility issues and proposed appropriate R&D activities for their further development [10]. An internationally harmonised strategy for fusion material development including necessary irradiation facilities was formulated as a guideline for further collaboration [11] and the development of steels and other materials for future fusion reactors was reviewed [12,13].

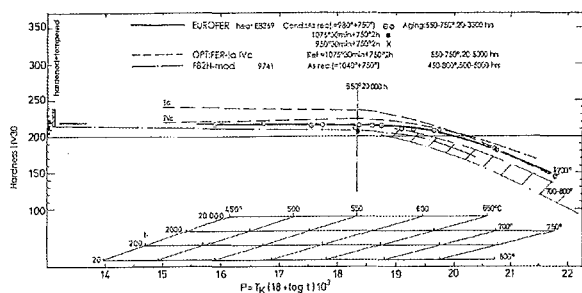


Fig. 3: Annealing Master-Curve Hollomon-Jaffe-Parameter)

Literature:

[1] M. Schirra, S. Heger, A. Falkenstein; Das Zeitstandfestigkeits- und Kriechverhalten des niedrigaktivierenden Stahles F82h-mod, Abschlussbericht, FZKA 6265, Mai 1999

[2] P. Fernández, J. Lapeña, A.M. Lancha, D. Gómez-Briceño, M. Schirra, "Characterización Metalúrgica del Acero Martensítico de Baja Activación F82H Modificado", Informe Tecnico Ciemat 912-diciembre, 1999

[3] Annual Report 98/99 FZKA 6400, Dez. '99, p. 137, Metallurgical and Mechanical Characterization of RAFM Steels

[4] M. Schirra et al., Final Report FZKA 6464 (at work), "Das Zeitstandfestigkeits- und Kriechverhalten der OPTIFER-Legierungen"

[5] M. Schirra et al., Interner Bericht 6/2000, "Untersuchungen an 4 Chargen der W-haltigen Legierung OPTIFER-IVc"

[6] M. Schirra et al., Interner Bericht 3/2000, "Einfluss der Härtetemperatur auf physikalische und mechanische Eigenschaften von niedrigaktivierenden martensitischen Stählen"

[7] M. Schirra et al., Interner Bericht 9/2000

[8] R. Lindau, M. Schirra, "Erste Ergebnisse zur Charakterisierung einer Großcharge des niedrigaktivierenden ferritisch-martensitischen Stahls EUROFER 97", Jahrestagung Kerntechnik 2000, Bonn, 23.-25. Mai, Beitrag 1212, S. 613-616

[9] R. Lindau, M. Schirra, "First Results on the Characterisation of the Reduced-Activation-Ferritic-Martensitic Steel EUROFER", SOFT 21, 11.-15. Sept., Madrid, Spanien

[10] K. Ehrlich; "Structural Materials Assessment", FZKA-Report 6332, August 1999

[11] K. Ehrlich, E.E. Bloom and T. Kondo; "International Strategy for Fusion Materials Development", Proc. ICFRM-9, Oct. 10-15, 1999, Colorado Springs, USA, to be published in J. Nucl. Materials (Invited)

[12] K. Ehrlich and W. Dietz; "Development and Qualification of Steels for Future Fusion Reactors", Proc. VDEH-Vortragsveranstaltung, 26. November 1999, Düsseldorf, Germany, p. 114-127

[13] K. Ehrlich; "Materials Research towards a Fusion Reactor", Proc. 21st Symposium on Fusion Technology, Sept. 11-15, 2000, Madrid, Spain, to be published in Fusion Engineering and Design

Staff:

- E. Daum (until 07/2000)
- P. Graf
- K. Ehrlich
- A. Falkenstein
- R. Lindau
- S. Heger
- E. Materna-Morris
- M. Schirra
- H. Zimmermann

Thermal and Isothermal Fatigue Properties of Base Metal

1. Introduction

Structural components of a DEMO-blanket are subjected during service to alternating thermal and mechanical stresses as a consequence of the pulsed reactor operation. Of particular concern is the fatigue endurance of Reduced Activity Ferrite-Martensite (RAFM) steels like the Japanese steel F82H mod., the German steel OPTIFER IV and the European heat EUROFER 97 under cyclic strains and stresses produced by these temperature changes. In order to design such structures, operating under combined mechanical and thermal cycling, fatigue life has to be examined in isothermal fatigue tests for materials data generation and in thermal fatigue for verification of design codes.

In this report isothermal mechanical (LCF) data with hold time of the RAFM steel F82H mod. is compared to those of MANET II ferrite-martensite steel. First results of thermal low-cycle fatigue (TCF) experiments without hold time of EUROFER 97 are compared to F82H mod. and OPTIFER IV.

2. Experiments

Solid cylindrical samples of F82H mod. have been used for the LCF-experiments. Hollow cylindrical samples of EUROFER 97 have been used for TCF-experiments.

The LCF tests have been performed with computer-controlled MTS servohydraulic testing machines operating in strain controlled push-pull mode. Triangle wave forms are applied with constant strain rates of 3×10^{-3} 1/s in case of LCF tests.

For the LCF experiments, solid specimens of 77 mm length and of 8.8 mm diameter in the cylindrical gauge length of the specimen have been used, where 21 mm is the initial gauge length of the axial extensometer.

The TCF test rig consists of a stiff load frame for mechanical clamping of the sample, which is directly heated by the digitally controlled ohmic heating device. Cylindrical specimens are used with similar outer dimensions as the above mentioned solid specimens, but with a wall thickness of 0.4 mm. Variable strain rates are applied at TCF test mode, due to the constant heating rate of 5.8 K/s and variable temperature changes.

Since both, temperature and mechanical strain cycling are taking place, mechanical strain is available only after subtraction of the thermal strain from the net strain.

In case of LCF tests F82H mod. samples have been cycled in as received conditions and compared to MANET II in reference condition.

In case of TCF samples of EUROFER 97 have been tested in as received thermal treatment. The results are compared to data from F82H mod. samples, which were tested in the tempered as received condition (normalizing 1040°C and tempering 750°C) and to OPTIFER IV with heat treatment of: normalizing 1075°C and tempering 750°C.

3. Results

The LCF tensile hold-time tests on F82H mod. have been extended to 450°C and compared to MANET II results. Fig. 1 shows, that for this temperature the numbers of cycles to failure of both materials are nearly equal up to tensile hold-times of 10 minutes. At the higher temperature of 550°C, F82H mod.

samples had shown better fatigue lives for hold-times being equal or larger than three minutes.

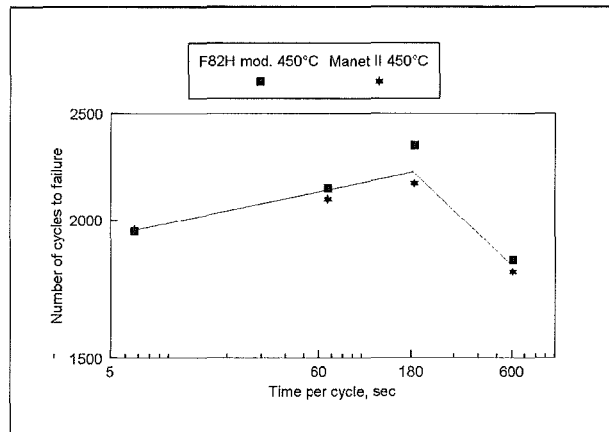


Fig. 1: Comparison of isothermal creep-fatigue behavior between the RAFM-steel F82H mod. and MANET II

TMF-experiments on OPTIFER IV in the optimized annealing condition (normalized at 950°C, 31 min/air and tempered at 760°C, 120 min/air), lead in the temperature range between 200 and 550-650°C to a small reduction in life time compared to the (1075°C/30') - condition of OPTIFER IV.

First TMF results of as received EUROFER 97 in the temperature range between 100 and 500-600°C show a remarkable reduction in life time (a factor of 2) compared to F82H mod. and OPTIFER IV. TMF-experiments with hold times of 100 and 1000 sec are continued on F82H mod. and on OPTIFER IV.

The installation of a modified TMF-test facility for postirradiation TMF experiments on so called German samples (hollow specimens of 77 mm length and of 8.8 mm diameter in the cylindrical gauge length) to be performed in the hot cells of CRISM „PROMETEY“, St. Petersburg, Russia, is still delayed due to licence problems of a binational contract between Germany and Russia.

Literature:

G. Filacchioni, C. Petersen, F. Rézaï-Aria and J. Timm: „A European Round Robin in Thermo-mechanical Fatigue Behavior of a 9%Cr Low Activation Ferrite-Martensite Steel“, *Thermo-mechanical Fatigue Behavior of Materials: Third Volume, ASTM STP 1371*, H. Sehitoglu and H.J. Maier, Eds., American Society for Testing and Materials (2000) pp. 239 – 256

L. A. Belyaeva, A. A. Zisman, C. Petersen, V. A. Potapova and V. V. Rybin: “Thermal Fatigue Crack Nucleation in Ferritic-Martensitic Steels before and after Neutron Irradiation” to be published in the ICFRM 9-issue of Journal of Nuclear Materials.

Staff:

J. Aktaa
M. Klotz
C. Petersen
M. Pfeifenroth
D. Rodrian
R. Schmitt

TTMS-003 Compatibility with Hydrogen and Liquid

Thermal Fatigue Scoping Tests under Hydrogen Atmosphere

1. Introduction

During service structural components of a DEMO-blanket are subjected - under corrosive atmospheres - to alternating thermal and mechanical stresses as a consequence of the pulsed reactor operation. Of particular concern is the thermal fatigue endurance of Reduced Activity Ferrite-Martensite (RAFM) steels under test conditions and in atmospheres close to that operating in the reactor.

2. Test facility

The Vacuum Thermal Cycling Fatigue (VTCF) test facility consists of a stiff load frame, built in a vacuum vessel, for mechanical clamping of the sample, which is directly heated by the digitally controlled ohmic heating device. To apply a hydrogen partial pressure of 10^{-3} to 10^{-1} mbar, valves, transducers and the pump was modified and first calibration tests have been performed.

3. State of the art

The hydrogen feeding system to operate an existing vacuum facility for thermal fatigue tests under hydrogen atmosphere is installed.

The laboratory safety system that has to be specified according to the regulations of the FZK's safety authorities will be installed.

Staff:

C. Petersen

D. Rodrian

Corrosion of Reduced Activation Ferritic Martensitic (RAFM) Steels in Pb-Li

The eutectic melt with 83 at% lead and 17 at% lithium is considered as an attractive breeding material for future fusion reactors. The corrosion of structural materials is one of the issues to be investigated for the water-cooled liquid lead-lithium (WCLL) blanket concept. Therefore long-term exposure tests have been made on the martensitic low activation steels MANET I, Optifer IVa and F82H-mod. up to 10000 h in a forced convection Pb-17Li loop named PICOLO (Pb-Li corrosion loop).

The beginning of the corrosive attack was found to be inhomogeneous by means of metallurgical investigations. Unattacked areas which still showed the original surface of the specimens and areas which were already heavily attacked by the eutectic are visible. This fact is due to the presence of passivating oxide scales on top of the surfaces. The oxide scales have to be firstly dissolved before the basic material can be attacked. The time needed for this process is called incubation period. With a flow rate of 0.3 m/s at 480 °C an incubation period of about 3000 h was found.

As published previously [1, 2] a porous layer was found on the steel surface after exposure to Pb-17Li. This remaining layer is enriched with steel elements which have a low solubility in Pb-17Li, e.g. W, V, and Mo. Only small spots of such layers were observed by Electron Microprobe Analysis (EMPA). Up to now in literature only the uniform dissolution of ferritic steels was mentioned. In order to clarify the mechanism some of the exposed specimens were not cleaned after testing and were examined with the remaining Pb-17Li on the surface.

EMPA line scan analyses have been carried out on the cross sections of specimens exposed to Pb-17Li. An enrichment of tungsten was found in the near surface region on nearly all scans across the cross section of Optifer IVa and F82H-mod. specimens independent of exposure time and post treatments (see fig. 1 and 2; solidified Pb-17Li was not removed). The thickness of the enriched porous zone was about 5 µm and the layers were characterised by a strong iron depletion and by lead and lithium penetration into the porous area. The adherence of the porous layer on the steel surface is low and no protecting character can be ascribed to it. The thickness of this zone is dependent of the flow velocity of the liquid melt. The higher the flow velocity the higher is the probability that this zone is removed by erosion.

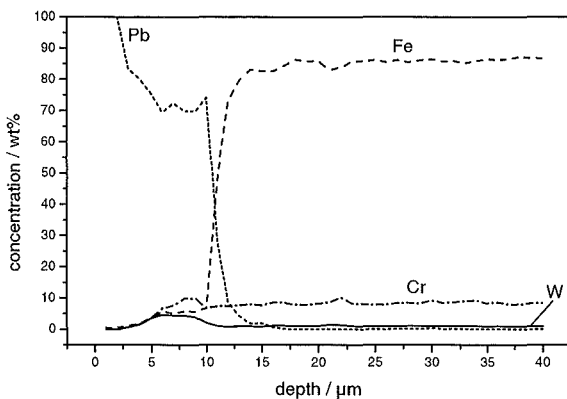


Fig. 1: EMPA line scan across the cross section of Optifer IVa after 4000 h of exposure to Pb-17Li at 480 °C.

On MANET I steel sheets, no enrichment of Mo or V was observed independent of the exposure time to the specimens. A possible reason for this might be the content of tungsten which is much higher in F82H-mod. and Optifer IVa than that of Mo in MANET I.

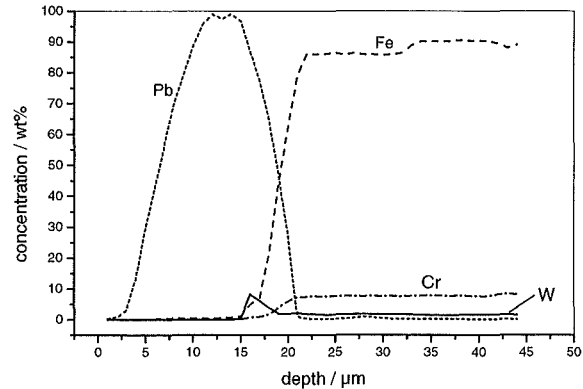


Fig. 2: EMPA line analysis of F82H-mod. after 10000 h exposure to Pb-17Li at 480 °C.

It was found that two processes are responsible for the corrosive attack: firstly, the dissolution of the oxide scale during the so-called incubation period, which is dependent on temperature and flow velocity of the melt. Secondly, the main corrosion attack consists of a strong depletion of iron from the steel resulting in a porous low adherent layer on the surface of the steels in which Pb-17Li could penetrate easily in. The remaining porous zone shows a low adherence to the steel matrix and can be easily eroded from the surface by the flowing melt. The thickness did never exceed 5 µm. Hence, no protecting character can be ascribed to this layer.

Literature:

- [1] K. Stein-Fechner, J. Konys, H. Glasbrenner, Z. Voß, Tagungsbericht Jahrestagung Kerntechnik '99, 18.-20. Mai, Karlsruhe (1999), 677.
- [2] K. Stein-Fechner, H. Glasbrenner, J. Konys, Z. Voß, EUROCORR 99, 30 August – 2 September 1999, Aachen, Germany.
- [3] H. Glasbrenner, J. Konys, Z. Voß, J. Nucl. Mater., to be published.

Staff:

H. Glasbrenner
Z. Voß

TTMS-004 Qualification of Fabrication Processes

Mechanical Properties of Diffusion Weldments

The influence of the roughness of joining surfaces on notch impact toughness was studied in a diffusion welding experiment. It is represented in Fig. 1. The surface roughness range below 1 μm cannot be used for technical purposes. An optimum notch impact toughness is obtained at a surface roughness of about $R_z = 4 \pm 1 \mu\text{m}$. Another experiment performed at a surface roughness of $R_z = 33 \mu\text{m}$ exhibited notch impact toughnesses which were far better than those at $R_z = 8 \div 9 \mu\text{m}$. Apparently, other parameters (e.g. cold deformation, oxide layer, etc.) also play a certain role.

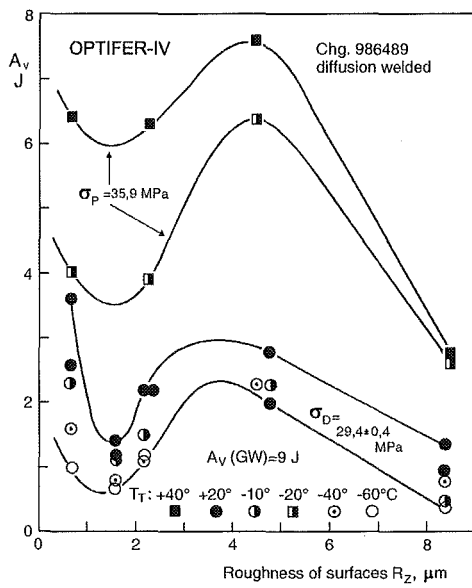


Fig. 1: Impact energy A_v of diffusion welded steel OPTIFER-IV in dependence of the roughness of joining surfaces

Investigation of various martensitic chromium steels revealed an increasing weldability in the following order: (based on the measured notch impact toughness) MANET-II; F82H mod.; OPTIFER-IV; EUROFER97.

Staff:

L. Schäfer

**TTMS-005
Rules for Design, Fabrication and Inspection**

Local Fracture Criteria for EUROFER in the Ductile-to-Brittle Transition Regime

Objective

The objective of this subtask is the development and application of methods that enable the generation of design-relevant fracture mechanics material parameters on the basis of micromechanical failure models.

A characteristic feature of these models is the utilisation of a 'hybrid' approach, which means extraction of material parameters for brittle or ductile fracture from (fracture) mechanics experiments by accompanying Finite Element Stress analyses.

The main advantage of this so-called 'Local Approach' with respect to global failure criteria is the fact that a mechanism-based fracture description is combined with a numerical stress analysis. Geometrical size effects are thus already accounted for within this approach. Limitations of the local approach originate from different fracture mechanisms. Knowledge of fracture mechanisms is therefore essential, so that fractography invariably is an essential part of the evaluation of the experiments.

Local fracture criteria establish a link between metallurgy and mechanical engineering and they are currently being incorporated into design codes such as the R6 code of British Energy, where Local Approach methodology is covered in a special appendix issued in 1999 [1].

Experimental results, fractography

A summary of the cleavage fracture parameters obtained on notched tensile specimens is given in Fig. 1 together with the respective 90%-maximum-likelihood confidence intervals.

T/°C	r / mm	m	90% ML-CI	C _{II} / MPa	90% ML-CI
-150	1	11.6	[8.2, 16.6]	1943	+/- 76
	2	10.7	[7.5, 16.5]	2107	+/- 90
	5	78.9	[51, 125]	1913	+/- 13
-75	1	107.5	[70, 170]	1941	+/- 14
	2	78.8	[51, 124]	1764	+/- 12

Fig. 1: Weibull stress analysis results (r-notch radius, m, C_{II}-Weibull parameters of cleavage stress)

Two groups of results can be identified. The first group, associated with small fracture strains, exhibits moderate values of m, whereas for the second group, associated with large fracture strains, m attains values of about 80-100. Complementary fractographic investigations on flat notched tensile specimens at ambient temperature revealed that, with increasing plastic deformation, martensite laths tend to orient themselves in load-

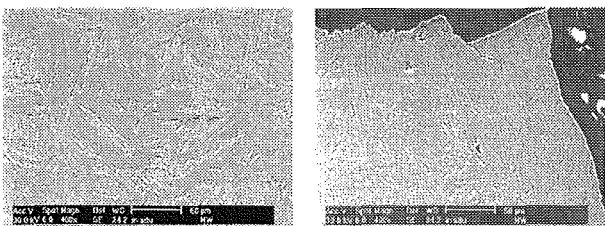


Fig. 2: Orientation of martensite laths.

ing direction. This is shown in Fig. 2 for two different regions located in the vicinity of the notch (right) and in an undeformed part of the specimen (left), respectively. This behaviour is felt to be the cause for the formation of axial cracks in case of large plastic strains, corresponding to the shaded regions in Fig. 1. A typical view of the fracture surface in the presence of axial cracks is shown in Fig. 3.

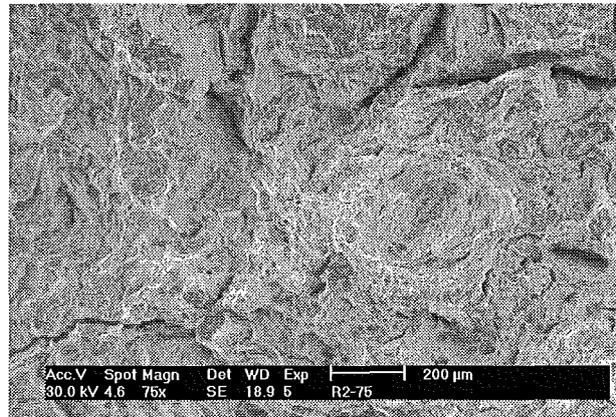


Fig. 3: Fracture surface for 2mm notched specimen (-75°).

For the transferability assessment, tests on pre-cracked specimens were performed. Pre-cracking was done by rotation bending with continuous monitoring of crack depth. It was possible to obtain a circumferential pre-crack with no significant eccentricity. A fractographic analysis showed differences in type and spatial distribution of fracture origins compared to notched specimens. Numerical evaluation of the results is pending.

Statistical inference

Transferability assessment requires statistical assessment of the uncertainty of the cleavage fracture parameters. Usually applied confidence intervals as given in Fig. 1 do not take into account that m and α_v are correlated. A bootstrap approach was used to generate appropriate confidence intervals [2]. Results of the bootstrap simulation procedure (see Fig. 4) clearly reveal the statistical dependency of m and α_v.

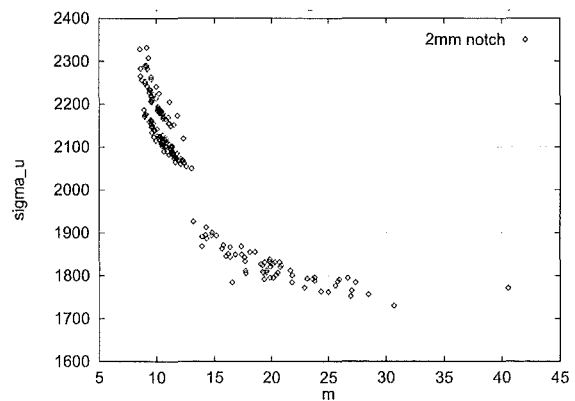


Fig. 4: Pairs of (m, α_v) from bootstrap simulation (-150° C).

Perspective

The local approach methodology provides a framework to apply fracture mechanics based design rules for RAFM steels in the spirit of R6 [1] or similar rules as currently developed e.g. in the framework of the European Structural Integrity Society (ESIS).

Irradiation effects will be a subject of future investigations after generation of experimental data.

Literature:

- [1] British Energy Generation Ltd, Assessment of the integrity of structures containing defects R/H/R6, Rev. 3, Appendix 17 'Guidance on Local Approach Methods', 1999.
- [2] H. Riesch-Oppermann, M. Walter, Fractographic evidence and statistical inference for cleavage fracture modelling of F82Hmod low activation steel, Proc. 13th European Conference on Fracture, 6-9 Sept. 2000, San Sebastian (CD-ROM).

Staff:

E. Diegele
M. Klotz
C. Petersen
H. Riesch-Oppermann
G. Rizzi
M. Walter

Life Time Prediction Rules for RAFM Steels

To describe damage at high temperatures of reduced activation ferritic martensitic (RAFM) steels, the linear accumulation rules by Robinson for creep and by Manson-Coffin for fatigue and their linear and non-linear combinations for creep/fatigue interaction suggested in the ASME and RCC-MR design codes as well as the continuum damage model ISRM (Inelastic Strain Rate Modified) presented in the recent literature were selected. The ISRM model has been applied successfully to several high temperatures alloys, among others the austenitic steel AISI 316 L(N) in the pre- and post-irradiated states.

For applications on F82H mod., data from isothermal creep and low cycle fatigue tests performed up to failure at 450 and 550 °C have been collected. In a closer look to this data some important aspects have been recognised with respect to the applications of the life time rules: F82H mod. exhibits up to failure cyclic softening, which is not necessarily caused only by damage. Furthermore, the representative saturation cycle can not be a priori identified, because there is no saturation in the sense of finished softening. Therefore, the application of the life time rules selected needs proper criteria, which are presently being investigated.

Staff:

J. Aktaa

Development of Miniaturized Push-Pull (Creep-) Fatigue Specimen

As long as Tokamak type facilities are the primary path towards commercial fusion power reactors, (creep-)fatigue remains one of the main lifetime limiting failure modes of structural materials as the limited data from reactor and higher energy accelerators have shown. The development of a miniaturised push-pull (creep-)fatigue specimen is essential in order to minimise flux gradients within the gauge volume and to fully utilise the available irradiation region of an intense neutron source like IFMIF. The requirements for a suitable miniaturised specimen include (i) data that represent material specific properties for widespread loading conditions, (ii) ability for fully remote handling operation before, during and after (creep-) fatigue testing, and (iii) universality, that is one common specimen design for different fatigue behaviour (e.g. cyclic softening/hardening) or loading conditions (e.g. thermal/isothermal fatigue). The early availability of a suitable miniaturised specimen helps also to use limited fission reactor volume in a very effective manner.

Based on long-term experience with fatigue properties, neutron and charged particle irradiation as well as hot cell handling, a specimen geometry has been developed and optimised with finite element calculations. The proposed fatigue specimen has a cylindrical geometry with a gauge width of 2 mm, a gauge length of 7.6 mm and a total length of 27.0 mm. Special emphasis has been put on the radius of curvature at the end of the gauge length to achieve throughout the gauge volume homogeneous stress-strain fields under uniaxial push-pull fatigue conditions (fig. 1).

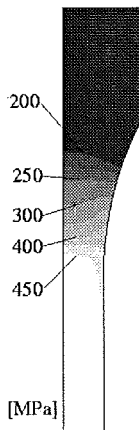


Fig. 1: Axial Stress (MPa); symmetry part (upper half and positive r) of the miniaturised creep-fatigue specimen

Parallel to the specimen development a high performance extensometer has been successfully adapted that shows a resolution of less than $0.1 \mu\text{m}$ and can be clamped on gauge lengths larger than 5 mm even in vacuum chambers and under high temperature. It is also completely remote controlled and can be adjusted with high precision on cylindrical miniaturised gauge volumes even under hot cell conditions.

LCF-tests in high vacuum have been performed using a universal testing machine equipped with a high vacuum chamber, an integrated vacuum load cell and a high performance extensometer. Miniaturised fatigue specimens made of F82H mod. steel were push-pull fatigue tested between room temperature and $450 \text{ }^\circ\text{C}$ under strain controlled conditions in a limited strain range at $R = -1$ and compared with standard push-pull fatigue specimens having a cylindrical geometry. For

specimens tested in high vacuum at $250 \text{ }^\circ\text{C}$ and a total strain range of 0.8 % typical examples for the stress behaviour are shown in figure 2 and for the related stress-strain hysteresis loops in figure 3. It is relevant to note that the tensile and compressive stresses are symmetric throughout the fatigue test and that at least under LCF conditions the fatigue life of this miniaturised samples is in the range of massive fatigue specimens. Also the elastic and plastic fraction of the total strain are exactly in the range of conventional specimens.

Fig. 2: Stress vs. fatigue cycles showing the continuous cyclic softening of F82H mod measured by miniaturised specimens.

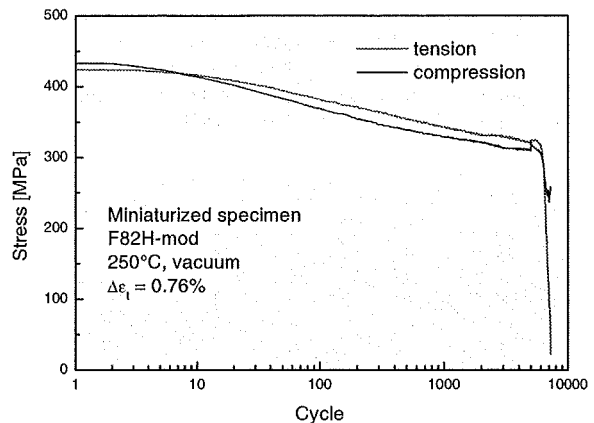
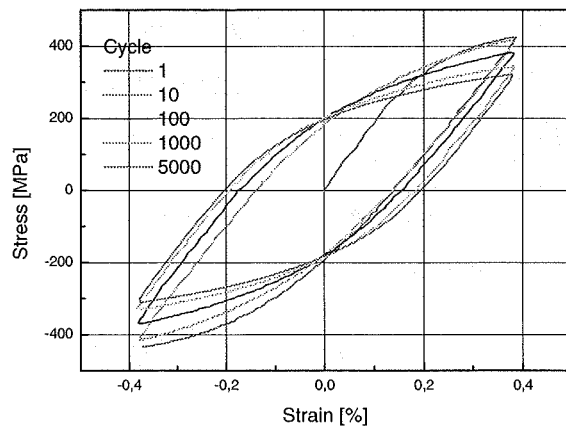


Fig. 3: Stress strain hysteresis loops of miniaturised fatigue specimen made of F82H-mod.



Meanwhile several hundred of these fatigue specimens made of different type of RAFM steels are fabricated and surface polished for neutron irradiation in the mixed spectrum reactor HFR, and in the fast breeder reactor BOR60. In both reactors start of irradiation is scheduled end of 2000.

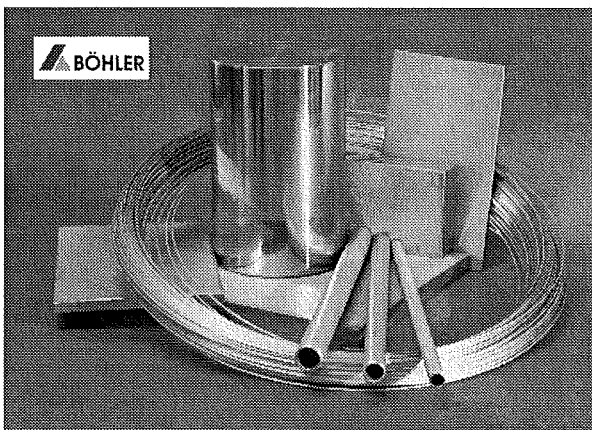
Staff:

- S. Baumgärtner
- G. Bürkle
- E. Diegele
- A. Möslang
- G. Rizzi

Quality Control and Distribution of EUROFER 97

Production and distribution

Reduced activation ferritic/martensitic (RAFM) steels are being considered for structural application in potential fusion energy systems. Based on the substantial experience with RAFM developmental steels of OPTIFER type, produced as laboratory melts of 25 kg, a RAFM steel of the 9CrWVTa type, called EUROFER 97 had been specified under the leadership of FZK in close co-operation with another European Association (CEA). BÖHLER EDELSTAHL GmbH in Austria had finally been selected as manufacturer for about 3.5 tons semi-finished products (plates, forgings, filler wire material and tubes). Besides different technological goals the question of transferability of properties from laboratory to industrial scale melts was of major interest. Fig. 1 shows the product range of EUROFER 97.



Product	Size	Length/Area	Mass
Forged bar	Ø 100 mm	~ 10 m	800 kg
Plates	d = 1.5, 8, 14, 25 mm	~ 5 or 7.5 m ²	2500 kg
Filler Wire	Ø 1 mm		200 kg
Tubes	10x1, 13x1.25, 17x1.5 mm	~ 140, 100, 60 m	90 kg

Fig. 1: Product range of EUROFER 97

The production of EUROFER 97 is now finished, the final inspection and approval of all products took place in October 1999 (bar, plates, wire) and February 2000 (tubes). The different semi-finished products have been delivered to the associated laboratories and a small reserve has been laid in stock.

The production of EUROFER 97 has revealed, that at present the technical limits of metallurgy have been reached concerning raw materials, the melting processes and analytical methods due to the strict requirements for impurity levels of specific chemical elements.

From the technological point of view, the fabrication of the different semi-finished products by means of traditional manufacturing processes like rolling, forging, milling and drawing did not pose real problems for this new type of alloy.

Quality Assurance and Characterisation Programme

Tensile tests

A quality assurance and characterisation programme has been launched to determine the relevant mechanical properties. The results are being compared to the previous conventional reference steel MANET II and the Japanese RAFM steel F82H mod. and a precursor alloy with similar composition OPTIFER V. All examinations have been undertaken on specimens prepared from either a forged bar with 100 mm in diameter (Heat E 83699) or rolled plate material (Heat E 83698) of 14 mm thickness.

The results of the tensile tests on cylindrical specimens of 5 mm diameter and 25 mm gauge length are given in Fig. 2.

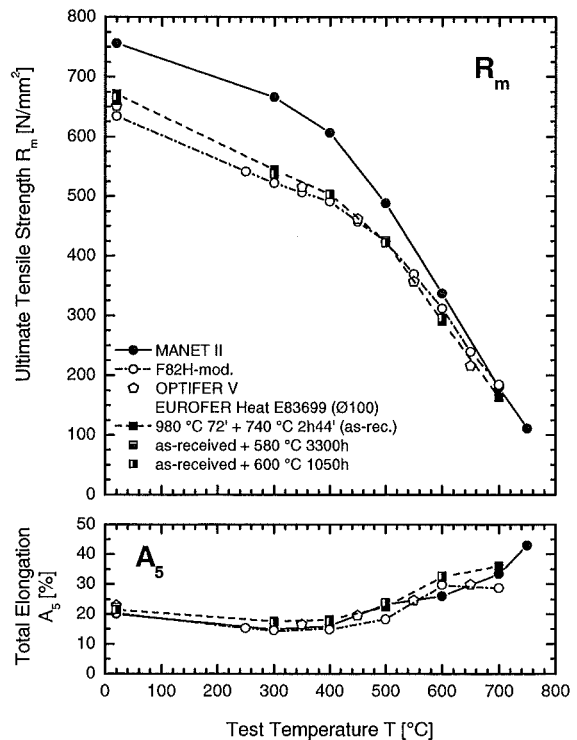


Fig. 2: Ultimate tensile strength and total elongation of different RAFM steels in dependence of test temperature

From these results following can be concluded:

- Up to a test temperature of 500 °C EUROFER reaches higher, at 600 and 700 °C slightly lower strength values than F82H mod.
- The strength values coincide very well with those of the developmental precursor alloy OPTIFER V.
- The strength and ductility values of Ø100mm bar (E83699) and 14mm plate (E83698, not diagrammed) are almost congruent.
- Raising the austenitising temperature to 1075 °C leads to lower strength values, most pronounced at lower test temperatures, whereas the ductility is less affected. This loss in strength is accompanied by higher ductile-brittle transition temperatures (DBTT) in the impact test.

- Ageing at 580 and 600 °C up to 3300 hours causes only a marginal decrease in tensile strength.
- The total elongation is similar for all alloys >15%.
- This applies also for the uniform elongation A_u and reduction of area Z (not shown).

Impact bending tests

Standard ISO-V Charpy-specimens have been machined from the 14mm plate material. The specimen orientation was transverse (T-L), additionally in one case longitudinal (L-T) with respect to the final roll of the plates. BÖHLER BLECHE applies the so-called cross rolling technology to achieve isotropic mechanical and physical properties, what has been verified here in an excellent way. Figure 3 shows the absorbed energy in dependence of the test temperature for EUROFER 97 compared with F82H mod. .

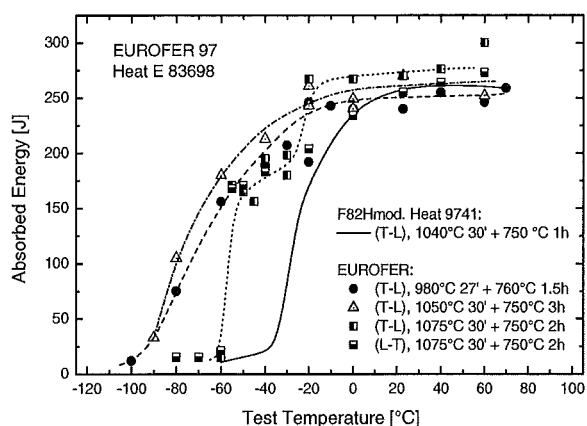


Fig. 3: Absorbed energy vs. test temperature of EUROFER 14 mm plate material compared with F82H mod., sampling transverse (T-L) or longitudinal (L-T) to final rolling direction

The upper shelf energy of both alloys with different heat treatments is roughly between 240 and 300 J. The Ductile to Brittle Transition Temperature (DBTT), which is an important measure for the suitability of RAFM alloys for structural applications in a fusion reactor, is for all EUROFER-variants remarkably better than for the Japanese steel F82H mod. (solid line) in the as-received condition (1040 °C 30 min + 750 °C 1 h). One reason for the higher DBTT (-20°C) of F82H mod. is the larger grain size (55 µm) which depends on the austenitisation temperature, another reason could be the higher oxygen content (124 ppm) compared to 10 ppm for EUROFER which for the as-received condition (980 °C 27 min + 760 °C 90 min) exhibits a DBTT of -70 °C. Increasing the austenitisation temperature to 1050 °C leads to a slightly better DBTT (-73 °C) although the grain size increases to 26 µm. A further increase to 1075 °C however increases the DBTT to -56 °C and -57 °C for the transverse (closed squares) and longitudinal specimens (open squares) respectively. The shift in DBTT can be related to a further increase of the grain size (45 µm), the shape of the energy curve not. The energy-temperature-curve (dotted line) shows in the transition region between upper and lower shelf energy a step-like behaviour which, more or less pronounced, could be observed frequently at this type of alloys. This behaviour in the transition region will be subject of further investigations.

Conclusions

The first results of the quality assurance and characterisation programme show that it is possible to transfer the good

mechanical and structural properties of precursor laboratory melts to an industrial scale melt. The short term mechanical properties fully comply with the requirements. Concerning the activation behaviour it could be demonstrated, that it is possible to produce an industrial scale RAFM steel with low contents of radiologically undesired tramp elements. Nevertheless a further reduction into the sub-ppm-range is necessary on the way from reduced to real low activation alloys.

Literature:

- [1] R. Lindau und M. Schirra, Erste Ergebnisse zur Charakterisierung einer Großcharge des niedrigaktivierbaren ferritisch-martensitischen Stahls EUROFER 97, Annual Meeting on Nuclear Technology 2000 of the Kerntechnische Gesellschaft, May, 23-25, Bonn, pp 613-616, ISSN 0720-9207.
- [2] R. Schneider, P. Würzinger, G. Lichtenegger und H. Schweiger, Metallurgie an den technischen Grenzen höchster Reinheitsgrade und niedrigster Spurenlementgehalte, Berg- und Hüttenmännische Monatshefte BHM 145 (2000) 199-203, ISSN 0005-8912.
- [3] R. Lindau and M. Schirra, First Results on the Characterisation of the Reduced-Activation-Ferritic-Martensitic Steel EUROFER, 21st Symposium on Fusion Technology, Sept. 11-15, 2000 Madrid, Spain

Staff:

- P. Graf
- H. Kempe
- M. Klotz
- R. Lindau
- M. Schirra
- H. Zimmermann

TTMS-006 Qualification of High Performance Steels

Specification and Characterization of a Reduced Activation (RA) Heat

The efficiency of future fusion power plants is strongly dependent on the operating temperature. Presently considered conventional RAFM steels for structural applications limit the operating temperature to around 550 °C. Oxide Dispersion Strengthened (ODS) materials would allow to increase the operating temperature by about 100 K. Therefore it seems to be necessary to develop Reduced Activation ODS alloys on the basis of the 9%Cr RAFM steels using the results of prior activation calculations.

Reduced activation ODS steels are not available commercially at present. As a first step in developing a RAFM-ODS-steel an existing 9%CrWVTa-RAFM steel, called EUROFER 97 was chosen as base material. H.C. Starck was charged to produce about 150 kg of steel powder by gas atomisation after preceding vacuum melting. The EUROFER powder has a spherical morphology and a grain size between 0 and 180 microns (Fig. 1). The oxygen content of the powder which is of some importance for the properties of the later consolidated material could be kept below 200 ppm. The structure of the atomised powder is martensitic.

PLANSEE was selected for the manufacturing of 2 batches of ODS-EUROFER with 0.3 and 0.5 wt-% Yttria content. The steel powder was mechanically alloyed with the corresponding amount of Yttrium-Oxide in ball mills, which are commonly used in industry. Hot Isostatic Pressing (HIP) was chosen as the appropriate consolidation process for the production of bars with 60 mm in diameter and 300 mm in length. The Hipping process is regarded as the most promising production route for nearly end-shaped structures for future fusion reactors.

Specimens from the as-received furnace-cooled bars were subjected to a heat-treatment program similar to that applied for the base material EUROFER in order to study the hardening and tempering behaviour. It turned out, that furnace-cooling, which corresponds to a cooling rate of approximately 3-4 K/min, is not fast enough to cause a martensitic transformation. Air cooling was also not sufficient to produce martensite, the prerequisite for a subsequent tempering treatment. On the other hand, the measured hardness values after austenitisation, air cooling and tempering showed only a moderate decrease up to temperatures of 900 °C, that gives a hint on a good structural stability. After water quenching it was possible to surpass the air-hardening EUROFER in Vickers hardness, but there is no doubt, that such a heat treatment cannot be performed on large reactor components with complicated structures.

The microstructure of the different powders and consolidated materials in different heat treatments is being examined by appropriate methods like optical microscopy, SEM and TEM. Fig. 2 shows a TEM micrograph of a specimen in the as-received condition. Concerning the Yttria particles, that are among others responsible for the strengthening of ODS-EUROFER it can be stated, that there is a relatively uniform distribution of smaller and larger particles. Neither depletion nor enrichment, especially on the grain boundaries, could be observed.

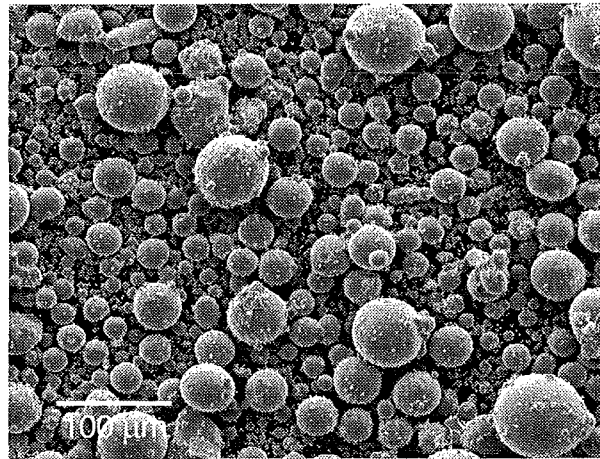


Fig. 1: SEM micrograph of EUROFER steel powder

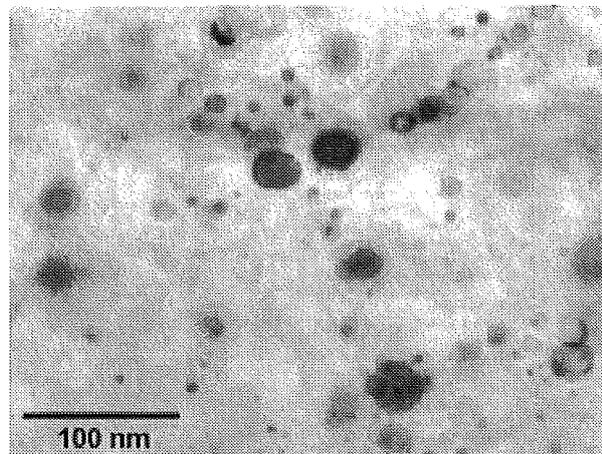


Fig. 2: TEM micrograph of ODS-EUROFER (0.5wt-% Yttria)

First results of preliminary tensile tests in the furnace-cooled, as-shipped state are very encouraging. Ultimate Tensile Strength R_m (1000 MPa) and Total Elongation A (16%) at room temperature are in the same order as for some commercial ODS Fe base alloys.

The work on the mechanical behaviour (tensile, creep, impact) will be continued. Further studies will be necessary to understand the deviating transformation behaviour compared to conventional RAFM steels with similar composition. This includes the determination of relevant physical properties and the creation of a continuous cooling transformation diagram. Complementary microstructural examinations shall complete the knowledge.

Staff:

P. Graf
M. Klotz
R. Lindau
U. Schanz
D. Rodrian
P. Schloßmacher
H. Zimmermann

Irradiation in a Temperature Controlled Test Rig of BOR 60

1. Objectives

In an energy generating fusion reactor structural materials will be exposed to very high levels of irradiation damage of about 100 dpa. Due to the fact, that fast reactor irradiation facilities in Europe are not available anymore, a cooperation with the Russian institution: State Scientific Centre of Russian Federation Research Institute of Atomic Reactors (SSC RIAR) has been implemented.

2. Irradiation project "ARBOR"

The project has the name "ARBOR" (the latin name for tree) for Associated Reactor Irradiation in BOR 60. The negotiations between State Scientific Centre of Russian Federation Research Institute of Atomic Reactors (SSC RIAR), Dimitrovgrad, and Forschungszentrum Karlsruhe GmbH Technik und Umwelt, Institute for Materials Research II (FZK, IMF II) about a cooperation in the field of irradiation in a test rig with temperature measurement of BOR 60 for reduced activation ferritic-martensitic (RAFM) steels led to the following contractual terms and the contract has been signed by both institutions.

150 mini-tensile/low cycle fatigue specimens and 150 mini-charpy (KLST) specimens of different RAFM steels have been delivered to SSC RIAR and will be irradiated in a special designed irradiation rig of BOR 60 at a temperature less than 340°C. After hydraulic tests in distilled water, the irradiation will first start in position D-23, where temperature measurement is possible and later up to 30 dpa in an identical position of the the 5th row of BOR 60.

The irradiation rig will be instrumented with neutron monitors in the central tube on three of ten levels of specimen positions as well as with three temperature detectors also on three of ten levels. This rig is ready to be filled with specimens at SSC RIAR.

For tensile and low cycle fatigue testing a small size cylindrical specimen and for charpy testing the KLST specimen have been accepted by both sides. Tensile, low cycle fatigue and charpy specimens of the following materials have been prepared, controlled and delivered by FZK, IMF II: EUROFER 97, as received; EUROFER 97, normalised at 1040°C; F82H mod., as received; OPTIFER IVc, normalised at 950°C EUROFER 97 with 82 wppm nat. B, as received; EUROFER 97 with 83 wppm B10, as received; EUROFER 97 with 1160 wppm B10, as received; EUROFER 97 with ODS as received; EUROFER 97 electron-beam welded and reference bulk material, from NRG, Petten.

The postirradiation tests together with microscopy will be performed in the hot cells of SSC RIAR beginning in 2003.

Staff:

C. Petersen
D. Rodrian

Neutron Source

Neutron Source

ERB 5005 CT 990061 (EFDA/99-507) IFMIF Test Cell and Accelerator Optimization and Cost Reduction

Test Cell Design

At the recommendation of the Fusion Power Coordination Committee (FPCC), January 1999, the IFMIF project focussed on exploring reduced-cost options during the reporting period. Reduced-cost strategies elaborated during related workshops in Lausanne and Colorado Springs and Karlsruhe are the basis for significant design changes. The activities carried out included (i) assessment to what extent test cells, access cells, service cells, PIE hot cells, shielded glove boxes and related inventory and auxiliary systems could be reduced without losing the capacity of a "full performance IFMIF", (ii) Redesign of access cell and test cell based on two co-planar accelerator lines, and (iii) determination of new costs according to the methodology outlined during the conceptual design activity (CDA) phase.

The need to develop a structural material that can withstand the high-energy neutron flux environment expected for the first wall and blanket regions of deuterium-tritium (D-T) fusion reactors is recognized as one of the key challenges remaining in the program aimed at producing commercial fusion power. IFMIFs mission is (i) to provide a neutron source with an energy spectrum simulating that of fusion neutrons at sufficient intensity and irradiation volume to test samples of candidate materials up to about full lifetime of anticipated use in a fusion DEMO reactor in a reasonably short operation time, and (ii) to calibrate data generated from fission reactors and particle accelerators. Initial studies have indicated that a volume of about 0.5 L is required in a region producing a flux equivalent to 2 MW/m^2 ($0.9 \times 10^{18} \text{ n/m}^2\text{-s}$) or greater. A fraction of this volume, about 0.1 L would be available at a flux equivalent to 5 MW/in^2 for accelerated testing. The design concept consists of a 40 MeV deuteron accelerator. The deuterons interact with a flowing liquid lithium target (D-Li) producing high energy neutrons with a peaked flux around 14 MeV. The resulting high energy neutrons will interact with a set of test assemblies located immediately behind the Li-Target. Designs for the four major technical subsystems

- Accelerator System
- Lithium Target System
- Test Facility System, and
- Conventional Facilities

has been developed in parallel during the CDA phase and extended during the conceptual design evaluation (CDE) phase (1997-98). In 1999, progress was reviewed and checked by meetings of each of the three main facility groups (Accelerator, Target and Test Facilities).

The Forschungszentrum Karlsruhe (FZK) has undertaken to contribute to the IEA project for the conceptual design evaluation of an International Fusion Materials Irradiation Facility (IFMIF) within the frame of the contract EFDA/99-507. In line with the recommendations of the FPCC, Paris January 1999 and 2000, the FZK activities concentrated on key cost reduction items of the test facility systems. Below, the activities of the reporting period are summarized [1-7].

1. Redesign and cost reduction of Test Facilities

In principle, the total capital costs are besides cost acceleration almost independent on the time scale of the construction. To obtain a flatter budget profile, a stepwise construction might be

appropriate. The work included (i) specification of costs for different scenarios and cost-benefit evaluation, and (ii) implication of the one-beam-on-target option on operation requirements.

With respect to test facilities, major outcomes of the cost-reduced design changes are:

- Reduction of the total construction cost by elimination of the previous plan for a potential upgrade beyond user requirements ($4 \times 125 = 500 \text{ mA}$ at 40 MeV). The total configuration of the system is now rearranged by limiting the maximum number of accelerators from 4 to 2. As a result, size and complexity of the facility could be significantly reduced. These design changes imply a complete rearrangement of the test facilities.
- Elimination of the second test cell, including the Li-target station, as well as elimination of a dedicated test cell for beam calibration. Consequently, the IFMIF project has in the present version only one test cell.
- Test cell size reduction
- A scenario for staged construction was explored. Three construction stages were suggested at request of Japan to best fit a spending profile that could be assumed for Japan. Presently the staged construction includes a first (50 mA, 40 MeV) and second phase (125 mA, 40 MeV) with only one beam on target. Although the final goal of a full performance IFMIF ($2 \times 125 \text{ mA} = 250 \text{ mA}$ at 40 MeV) will be achieved in the third stage, the impact of having only one beam for a long time on user strategy and test matrixes are considered to be significant.

It is important to note, that these cost reducing design changes are not for free, but are connected with (i) the risk of a certain reduction in robustness and redundancy of the design, (ii) a likely reduction in reliability and availability, and (iii) increased time for assembling and reassembling of vertical test assemblies (VTA), as well as for unscheduled maintenance. That is, independent of staging scenarios, the total annual neutron fluence to be achieved in the irradiation experiments is potentially reduced compared to the original CDA design. Whether these findings can be compensated by future design improvements and general progress (e.g. accelerator technology) is of course not yet clear.

1.1 Assessment of cell reduction

Practically all rooms and cells were involved in the redesign of the entire IFMIF plant. In the light of potential cost savings, during the reporting period, function, size and inventory of the following rooms and cells were evaluated: Test cells, test assemblies, test cell technology rooms, test facility control room, access cell, service cell, test module handling cell, PIE hot cell, shielded glove box laboratory and maintenance systems. Major design changes were made in the

- access and service cell,
- remote handling procedures and equipment
- test cell areas.

The essential basis of the design modifications are the elimination of the 500mA upgrade option as well as the elimination of the second test cell and the beam calibration station including elimination of the related Li-target stations. As a consequence, the area above the test cells could be reduced significantly. In addition, a reassessment of all handling and

maintenance procedures resulted in the conclusion that a combination of the former access cell and service cell to a multipurpose access cell seems possible with significant impact on cost savings due to greatly reduced hot cell area and volume.

With respect to the remote handling procedures and the involved devices, it is now suggested to have only one universal robot system being responsible for any remote handling inside the multipurpose access cell. While in the CDA reference design two completely independent systems have shared the actions, namely a universal robot system and various power master/slave manipulators in connection with through wall windows. The original purpose of the universal robot system was (i) routine VTA removal and reloading operations, (ii) removal and insertion of the shield plugs and test cell removable cover, (iii) maintenance operations in the access cell and test cells including removal and replacement of Li-target components. The purpose of 5+3 power master-slave manipulators in the wall of the access and service cells was mainly the assistance of the universal robot system and independent handling of devices and maintenance operations. In the present design the universal robot system is upgraded by additional tools and features in order to allow completely independent operations in the multipurpose access cell and to compensate the elimination of the master/slave manipulators.

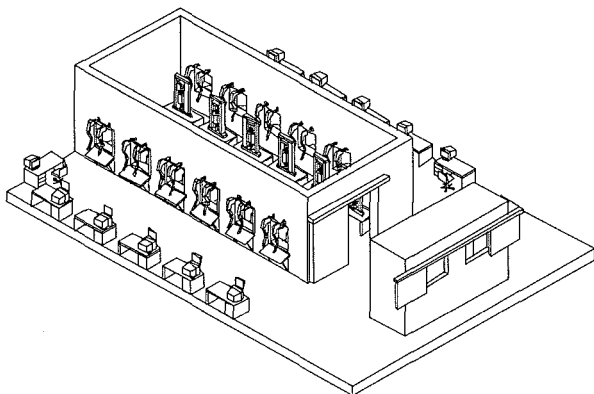


Fig. 1: Bird view of the redesigned and instrumented PIE hot cell

1.2 Cost assessment

Based on the updated IFMIF KEP design and the related size reduction of the Test Cell, a revised cost estimate has been done by the same German Industry company which has already outlined a significant fraction of the former IFMIF CDA design. In order to allow a direct comparison with the CDA cost report, all costs were established on the basis of January 1996. That is, the cost estimate done by the German industry partner is done (i) assuming stable costs since January 1996 and (ii) assuming a DM/\$ conversion ratio of 1.52 as it was valid at that time. Because this rate of exchange increased substantially since that time (presently about 2.00), the costs in this document would become smaller if they would be specified based on actual rate of exchange.

The same standard spreadsheet formats of the CDA phase have been used to categorize the costs in terms of on-side and off-side costs with a strict differentiation between industrial and institutional contributions. For the explanation of "industrial" and "institutional" as well as for the explanation of various abbreviations used in this chapter, see "IFMIF Conceptual Design Activity Cost Report, compiled by M.J. Rennich, Dec 1996, ORNL/M-5502". Only those Test Cell and VTA related

spread sheets have been updated which were significantly changed as a consequence of the Test Cell modifications. For the significantly modified design of the cells (access cell, service cell) and related inventory the Japanese estimate seems to be realistic. According to the original work breakdown structure (WBS), mainly the following devices have been considered:

- Helium gas cooled high flux test assembly including related test module
- Encapsulated specimens
- Test module
- VTA shielding body
- Electrical cabling and piping for He-gas coolant loop
- Test cell shielding plug
- Test cell removable cover
- Sealing plates
- PIE facilities

The Test Facility costs evaluated together with the industry are shown in fig. 2 by comparing the CDA reference case (115.2 Mio\$) with the original assessment of the cost-reduced CDE version (89.5 Mio\$). The final cost estimate from Dec 1999 amounts to 95.4 Mio\$, because a complete 2nd set of VTAs and related test modules has been added. Please note also, that in the cost reduced CDE design the service cell and the access cell has been unified to one common access cell. Significant cost savings are related to the elimination of the second test cell and related VTAs as well as to the elimination of the NaK cooled option. The most remarkable cost saving is due to a reassessment of the tritium laboratory costs, based on the argument that experience with existing tritium labs becomes more and more available. The abbreviations in fig. 2 are as follows: VTAs = Vertical Test assemblies, Technol = Test cell technology room, ContrR = Users control room, Acc Cell = Access cell, Serv Cell = Service cell, Han Cell = Handling cell, PIE HZ = Post irradiation examination hot cell, PIE Lab = Shielded glove box laboratories for PIE, Trit Lab = Tritium laboratory, Mainten = Maintenance room.

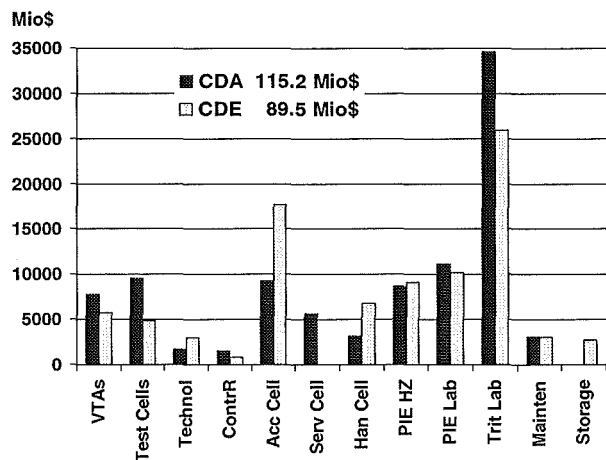


Fig. 2: Test facilities costs, normalized to Jan. 1996; Comparison between CDA and cost-reduced CDE assessment

2. User group area

For the full performance facility (10MW, 40MeV, 250mA) detailed neutronic calculations have been carried out during the CDA and CDE phases. These results can be found in detail in the supplementary neutronics report for the CDA phase and in the publications of the references listed in the previous FZK-contract report (ERB5004 CT 970072 NET, NET/97-453, February 1999, PKF Nr. 132). During the reporting year considerations were taken to reduce the IFMIF facility cost and therefore also the IFMIF performance. As one part of the IFMIF cost reduction study, the impact of the beam power reduction on the irradiation conditions in the IFMIF test cell had to be evaluated. Following the conditions based on the three stage proposal, starting with 50 mA, upgrading to 125 mA and achieving finally a performance of 250 mA, the main parameters of interest are the irradiation volume as a function of dpa, the spatial dependence of the neutron flux and the derived variables like H- and He-gas production, displacement damage, nuclear heating etc.

The presented results are estimated from the detailed neutronic calculations which were carried out for the full performance facility. In principle there are two options if beam power gets reduced: Option one is the case of leaving the beam footprint size constant and reducing the beam current density on the target. Option two is the case of reducing the beam footprint size and leaving the beam current density constant. In comparison, for both options the available irradiation volumes as function of the dpa is estimated. For option two the beam footprint height was set to 5 cm as in the full performance case and only the beam footprint width is varied corresponding to the beam current reduction.

2.1 50 mA option

A series of calculations has been performed dedicated to (i) irradiation volume considerations, (ii) to beam footprint and target back wall loading, as well as (iii) to irradiation conditions in the cost reduced IFMIF test cell. As example, for the first stage, the "50 mA option" calculations of the He/dpa ratio, the dpa distribution, and the dpa gradients are summarized in fig. 3. The right half of the high flux volume is represented, showing above the abscissa a vertical cut through the front of the high flux test volume (HFTV), and below the abscissa a horizontal cut through the center plane of the HFTV. It is either possible to reduce the beam footprint at the expense of volume or to reduce the beam current density at the expense of available damage. From the users point of view, there are arguments that the available dpa rate and thus the beam current density is more relevant than volume. Having a beam current density of 2.5 mA/cm² would allow the development of very few heats in the same time than under CDA-design conditions. Following these arguments it would be more attractive to have high dpa rates in a small volume than low dpa rates in a larger one. This is why in the following for the 50mA option a reduced volume is considered by keeping the beam current density at "reference conditions" of 2.5 mA/cm².

2.2 Staged approach strategies from the users point of view

It is certainly clear that the overwhelming majority of the international users would prefer getting a "full performance IFMIF source" with 250 mA beam current as soon as possible. On the other hand, on request of Japan a spending profile must be developed that meets also their national requirements. As a result, a concept for a staged facility deployment was developed in the second half of 1999 consisting of the three stages already mentioned before: 50 mA (stage 1, one accelerator at 40 MeV)

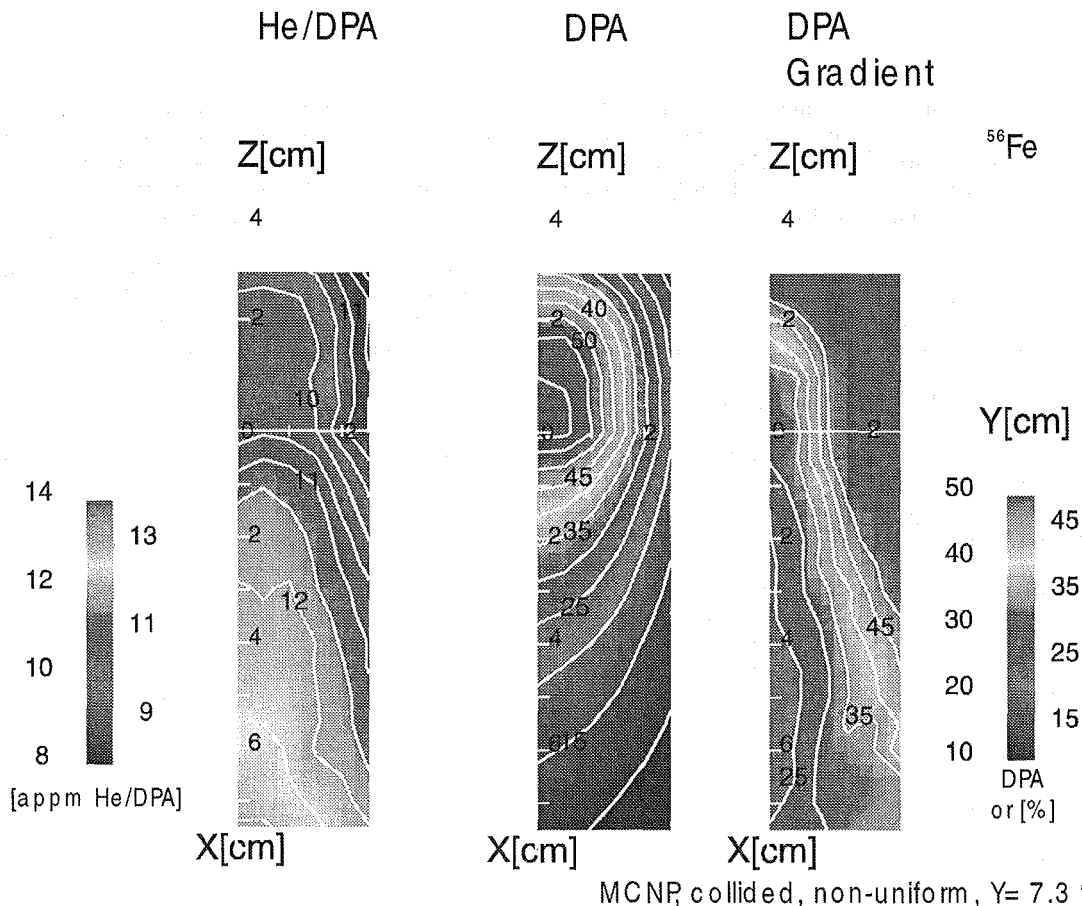


Fig. 3: He/dpa ratio, dpa/fpy and dpa gradients for a reduced beam footprint of 4 cm width by 5 cm high for 50mA, 40 MeV and 2 MW on target.

→ 125 mA (stage 2, one accelerator at 40 MeV) → 250 mA (stage 3, 2 accelerators at 40 MeV). Such staging would result in certain cost increase compared to a single stage construction. As advantage from a technical point of view, it has been claimed that staging with three dedicated stages would reduce some of the technical risks.

During discussion with the majority of users, no strong reason was found why to do a first 50 mA step for a longer time period. Therefore, a fraction of the international user community suggested not to do a three step but a two step approach starting with a full performance 125 mA single beam line. From a technical point of view it is anyhow clear, that the beam would not start from scratch with 125 mA but begins with very low current and then smoothly increases by fully controlling the Li-target and the instrumented test modules. The advantages of a "2step strategy" will be discussed below. When doing cost reduction to an existing facility design, a major problem is to minimize any drawbacks for the overall facility performance both from the users point and the technical point of view. Therefore, assessing the impact of the cost reduction opportunities on the neutronics performance requires to go through all options in detail. The strategy used here is to go from accelerator through the target to the test modules. For each beam current setup, 50 mA, 125 mA and 250 mA several possibilities for irradiation scenarios come up. A detailed discussion of the different approaches can be found in Ref [8].

2.3 Consequences of staged approach

Especially during the CDA phase various test matrixes have been developed for the high and medium flux test volumes and for a variety of materials and test conditions. In the case of structural materials the test matrixes include especially those heats and alloys that have priorities for the next 10 years and that are developed in the frame of related IEA programs in Europe, Japan, USA and Russia. Therefore the test matrixes are dedicated mainly to reduced activation ferritic/martensitic steels, vanadium alloys and SiC/SiC composites. The irradiation of these material classes implies that at any time the individual rigs must be able to allow temperatures between about 280 °C and 1000 °C and removal at intermediate fluence levels. As a consequence, test module and VTA architecture are designed from the early beginning to accommodate for major changes in test matrixes, be it materials, irradiation temperatures or time schedules.

For the HFTM comprehensive test matrixes have been developed for 11 different heats of primary candidate structural materials to be irradiated under "full performance conditions" (250 mA, 40 MeV) based on a footprint of 20x5 cm². With respect to the reduced cost IFMIF, a staged approach proposal for the 1st stage (50 mA, footprint variations) is governed by basic investigations and ITER related irradiations due to the limited dpa levels. In the 2nd stage (125 mA, 20x5 cm² footprint) higher dose irradiations come up at the expense of basic investigations, while in the 3rd stage DEMO oriented high dose irradiations would dominate as in the original CDA reference test matrixes. Already from the quality of irradiation (e.g. flux and related property gradients) it becomes immediately clear that any reduction in flux should go along with a related volume reduction. That is, a 50 mA beam should be focussed on a beam footprint of e.g. 5x4 cm² in order to keep constant the dpa/fpy rates. Dpa/fpy rates significantly below the original mission are not adequate at all for an intensive neutron source, they would not meet the mission requirements and therefore would also not be attractive for an international user community. Therefore, we suggest to keep constant the original dpa/fpy values for any stage. This implies for a 1st stage, 50 mA facility:

- (i) beam footprint of 5x4 cm²
- (ii) irradiation of typically 6 rigs (instead of 27); 2 rigs with about 40 dpa/fpy, 2 rigs with 30 dpa/fpy and 2 rigs with 20 dpa/fpy

It is important to note that this strategy would still allow to get for about two different materials or heats the most relevant properties in almost the same time as for the "full performance" CDA reference facility. In the CDA reference case (250 mA, 27 rigs) it was foreseen to create a database up to at least 150 dpa for 11 different materials or heats within 12-15 years of operation.

As already said, the concept of a staged facility deployment consists of three stages, one accelerator with two operation phases at 50 and 125mA (Stage 1 and 2) with reduced test capacity and thereafter the installation of a second accelerator with another 125mA to achieve the full test capability of 2x125mA in Stage 3. Consequences of such a strategy on available test capacities and research activities are outlined in ref. [8]. In essence, the research activities which would allow an aggressive search for high performance materials have - in comparison with the initial planning - to be postponed by roughly ten years into Stage 3, whereas in the initial Stage 1 questions like fusion-fission data correlation, fundamental radiation damage studies and the above discussed material concept confirmation for DEMO Test Breeding Blankets could be addressed. On the other side the expanded schedule would reduce the annual investment costs, relieve the financial burden, and would give more time to solve some of the technical risks during the development of the facility.

3. Neutronics

3.1 Source term of d-Li reaction: preparatory work for evaluating d+Li cross sections

For validating the physics basis of the McDeLi neutron source routine, an evaluation of deuteron cross sections on Li-6 and Li-7 for the deuteron energy range 40 ... 0 MeV is required. The nuclear models employed in the known cross section calculation codes, however, are not valid for very light target nuclei such as the lithium isotopes. Therefore, development of suitable methods was undertaken, again in co-operation with INPE, Obninsk, Russia. An extended version of the cross section calculation code DISCA/3 was produced, DISCA/3D, which permits calculation of deuteron cross sections. The difficulty of selecting optical potentials for target nuclei as light as Li was avoided by using a diffraction approximation. The methods are described in a forthcoming publication [4].

3.2 20-50 MeV data evaluation

3.2.1 Preparatory work for evaluating n+Li and n+Be cross sections

An approach to calculate neutron-lithium interactions for intermediate neutron energies was developed together with the development work for calculating d+Li cross sections (see above). It is described together with the d+Li work in Ref.[4]. Calculating the interaction of neutrons with lithium is required not so much for effects in the lithium target of IFMIF (where the deuteron interactions will dominate), but in view of IFMIF irradiations of breeding materials. Beryllium, the important neutron multiplier material, is a similarly light nucleus as the lithium isotopes. The new method will be useful as well for obtaining neutron-beryllium cross sections.

3.2.2 Preparatory work for evaluating activation cross sections for light nuclides

In order to complement the Intermediate Energy Activation File (IEAF), development of suitable calculational methods for target nuclides with $Z < 6$ has been started at INPE, Obninsk, Russia. The goal is, to have in the future a complete activation/transmutation library for all target nuclides having a half life of 10 hours or longer, $Z = 1$ to 83, for neutron energies up to 150 MeV.

3.2.3 Experimental benchmarking of IEAF cross section evaluations

An activation experiment with structural material samples in an IFMIF-like neutron spectrum was reported previously. Since the IFMIF spectrum has more than 80% of the neutrons at energies less than 20 MeV, and the data in the IEAF library below 20 MeV have been taken from the standard European Activation File (EAF), the experiment as a whole inevitably constitutes a test of mainly the EAF cross sections and only to a lesser extent a test of the new evaluations beyond 20 MeV.

However, a test for the intermediate energy activation file (IEAF) evaluations proper can be obtained from these experimental data by considering only those activation reactions not contained in EAF, i.e., $(n,p\alpha)$ and $(n,d\alpha)$ reactions as well as any reactions having thresholds above 20 MeV. Our results for these 10 products, 12 C/E values, are given in Table 1, together with reactions and minimum thresholds. Seven among these twelve C/E results (= 58%) do not deviate from unity by more than a factor of 2 if their experimental uncertainties are taken into account. This is considered to be a satisfactory first test result. However, more specific experimental benchmarking for some materials as well as future improvements to IEAF will be required.

Table 1: Products of activation reactions not covered in EAF-97. In case of several possible reaction channels, only the one with minimum threshold is given.

E_{thr} : Threshold neutron energy
 C/E : Calculated activity/experimental activity

Product	Sample	Reaction	E_{thr} MeV	C/E	Exp. Unc. %
Ca-47	V-pure	V51(n,p α)	11.7	0.71	10
Sc-43	V-alloy	Ti46(n,nt)	23.4	0.02	30
V-48	V-pure	V50(n,3n)	21.3	1.14	10
Cr-48	SS-316	Cr50(n,3n)	24.1	4.54	30
Cr-48	F82H	Cr50(n,3n)	24.1	3.25	30
Fe-52	SS-316	Fe54(n,3n)	24.5	2.49	50
Fe-52	F82H	Fe54(n,3n)	24.5	2.33	15
Ni-56	SS-316	Ni58(n,3n)	22.9	1.61	10
Y-87	SS-316	Mo92(n,d α)	11.4	0.30	20
Y-88	SS-316	Mo92(n,p α)	4.2	1.01	35
Zr-86	SS-316	Mo92(n,3n α)	27.9	0.03	25
Mo-90	SS-316	Mo92(n,3n)	23.0	1.69	60

Literature:

[1] P.P.H. Wilson, *Neutronics of the IFMIF Neutron Source: Development and Analysis*, FZKA 6218 (1999)

[2] E. Daum, *How to Improve the Irradiation Conditions for the International Fusion Materials Irradiation Facility*, Conference ICFRM-9, Colorado Springs, US, October 1999, to appear in J. Nuc. Mat.

[3] F. Maekawa, U. von Möllendorff, M. Wada, P. P. H. Wilson and Y. Ikeda, *Determination of neutron spectra formed by 40-MeV deuteron bombardment of a lithium target with multi-foil activation technique*; Proceedings ISFNT-5, Rome, Sept. 1999 (to appear in Fus.Eng.Des.)

[4] Yu. Konobeyev, Yu. A. Korovin, P. E. Pereslvtsev, U. Fischer and U. von Möllendorff, *Development of methods for calculation of deuteron-lithium and neutron-lithium cross sections for energies up to 50 MeV*; Submitted to Nucl. Sci. Eng.

[5] U. von Möllendorff, F. Maekawa, H. Giese and P. P. H. Wilson, *Experimental test of structural materials activation in the IFMIF neutron spectrum*; Proceedings ISFNT-5, Rome, Sept. 1999 (to appear in Fus.Eng.Des.).

[6] Möslang, K, Ehrlich et. al; *Suitability and feasibility of the International Fusion Irradiation Facility (IFMIF) for fusion materials studies*; Nucl. Fusion, 40; No. 3Y, (2000) p. 319-327.

[7] K. Ehrlich, E.E. Bloom, and T. Kondo, *International Fusion Materials Strategy*, ICFRM-9, Oct. 10-15, 1999, Colorado; Journ. Nucl. Mater. in press.

[8] E. Daum, K. Ehrlich, U. Fischer. U.v. Möllendorff, A. Möslang and S. Gross; *FZK Contribution to IFMIF Test Facility Optimization and Cost reduction*; Final Report for the Contract ERB5005 CT 990061, FZK internal report, May 2000.

Staff:

G. Bürkle
 E. Daum
 K. Ehrlich
 U. Fischer
 A. Konobeyev (INPE Obninsk)
A. Möslang
U. von Möllendorff
 P. Pereslvtsev (INPE Obninsk)
 P. Wilson (Univ. of Wisconsin)

Accelerator Design

I. Ion Source

I.1 Introduction

In 1998/99 a new high current ion source has been developed and tested. This ion source is of a volume type and delivers **200 mA H⁺** (corresponds to 140 mA D⁺, according to the Child Langmuir law) in continuous wave with a **H⁺ fraction of about 93 %** [1,3]. The used triode extraction system has an aperture of 8 mm in diameter and is designed for voltages up to 55 kV. Consequently, the beam energy is also 55 keV. For the following accelerator systems (RFQs) it is necessary to postaccelerate the 55 keV proton (deuteron) beam to an energy of 100 keV. Therefore, a new so-called tetrode system has been designed and calculated.

I.2 100keV extraction system

The following figure 1 shows a schematic drawing of the tetrode system. It consists of four electrodes: plasma-, puller-, screening- and ground electrode. In difference to the triode system another so-called puller electrode is installed between plasma and screening electrode. Other geometric parameters (aperture radius, thickness of the electrodes, aspect ratio, gap field strength) are the same as in the experimental proved triode system.

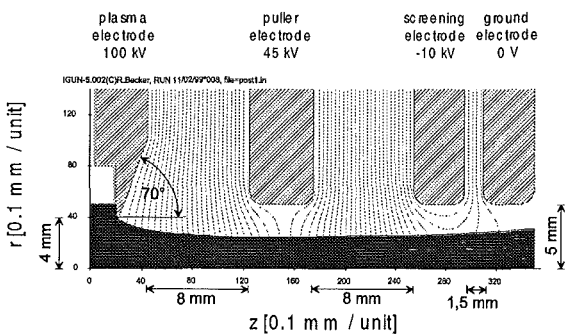


Fig. 1: Igun plot of the post accelerated 140 mA @ 100 keV deuteron beam

An important step in the design study of the extraction system is the choice of the potential of the puller electrode and the distance between puller-, plasma-, and screening electrode. Both, the electrical field strength and the distances between the electrodes should be carefully adapted to the proved values of the triode system. The neutral gas flow in the extraction system is responsible for voltages break throughs. Consequently, the maximum field strength in the extraction system is a function of the aperture radius, the neutral gas flow and the gap distances. For the triode system we determined a maximum field strength of 7.75 kV/mm for gap distances up to 8 mm. In course of the design of the tetrode system we used a more moderate gap field strength of 6.8 kV/mm to be **sure that the probability of voltage break troughs** are reduced. As shown in figure 1 the distance between plasma and puller electrode is 8 mm with a potential difference of 55 kV. The distance between puller- and screening electrode is also 8 mm with a potential difference of 55 kV.

Conclusions

With the computer code Igun[2] we designed a 140 mA @ 100 keV extraction system. The ion beam is extracted in matched case with a radius of 2.9 mm (80%) and a divergence angle of 35 mrad at the end of the extraction system. The normalised

rms-80%-emittance is 0.008π mm mrad and fulfils the IFMIF requirements with a value of 0.2π mm mrad at the entrance of the first RFQ. This value is much better as we expected according to theoretical considerations.

I.3 Influences of different auxiliary gases

In a second step, the influence of different auxiliary gases on the H⁺ fraction and on the beam noise was investigated. The goal was to reduce the beam noise and to enhance the H⁺ fraction at low arc powers. Figure 2 illustrates the H⁺ fraction as a function of the auxiliary gas pressure for different auxiliary gases. It was found that the **H⁺ fraction increases from 75 % to above 92 % by increasing the auxiliary gas pressure from 0.02 to 0.8 Pa**. The effect is stronger for higher atomic masses of the auxiliary gases. Helium has nearly no influence, xenon on the other hand has the strongest effect. Note, in all measurements, the extracted auxiliary ion fraction in the beam was below 1%. It is assumed that the enhancement of the H⁺ fraction is caused by the reduction of the mean electron energy. In contrast to electron collisions with hydrogen atoms and molecules, the cross sections for vibrational and rotational excitations of the investigated auxiliary gas atoms are higher. A higher cross section leads to a shorter mean electron path with the consequence of a higher number of inelastic collisions, resulting to a reduction of the mean electron energy as well as a reduction of the electron temperature. From this it follows that the fraction of the generated H⁺ ions rises. As shown in theoretical considerations, low energy electrons in the plasma are favourable for high H⁺/D⁺ fractions. Moreover, the use of a trace amount of an auxiliary gas **reduces the beam noise level from 4 % (without auxiliary gas) to less than 1 % (with xenon,** figure 3) [3].

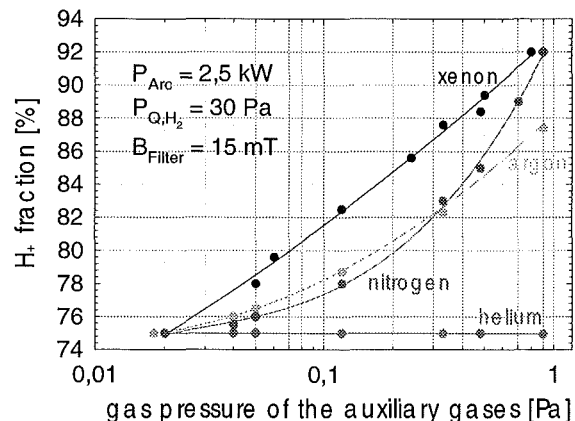


Fig. 2: H⁺ fraction as a function of the pressure for several auxiliary gases

Conclusions

Density fluctuations of the ions at the plasma sheath are dc coupled with density fluctuations of the electrons. As shown in basic plasma investigations with a 127° cylinder spectrometer, traces of xenon in the plasma reduces the electron temperature. This results in lower electron density fluctuations. Consequently, the ion density fluctuations and noise reduces, too. Moreover, the use of xenon allowed the operation of the ion source with 50 % (2.5 kW) of the conventional necessary arc power[3].

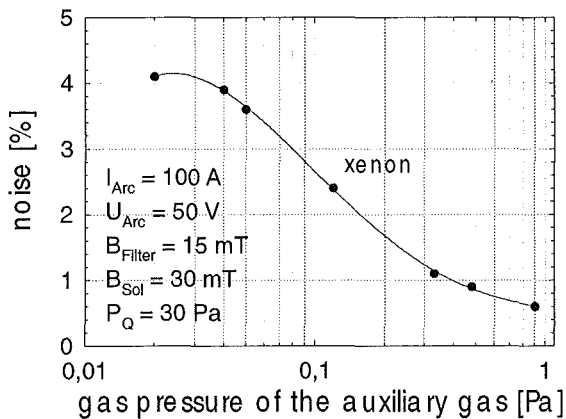


Fig. 3: Noise level as function of the auxiliary gas pressure xenon

1.4 Lifetime

Besides a high current and a low beam emittance an appropriate ion source lifetime is another important requirement. The ion source lifetime is determined by the lifetime of the filament. During the operation the filament the material wear is exposed due to the positive ion bombardment out of the plasma. For a given filament arrangement and operation gas, the lifetime is approximately antiproportional to the duty cycle, the arc power and the arc voltage (energy of the ions). In order to obtain a long ion source lifetime, one should employ several filaments with large cross sections. With the configuration used in these experiments (one tungsten filament with a diameter of 1.8mm) the ion source was operated 100 h at full arc power. During this time, the filament thickness was reduced from 1.8 mm at the beginning to 0.9 mm. For filament diameters smaller than 0.8 mm the arc discharge burns more and more unstable. An operation with such filaments isn't recommendable.

Conclusion

With the used arrangement the lifetime is about 100 h [3]. As it is possible to use up to four filaments the life time will be four times higher, if the ion source is equipped with four filaments. Due to low arc powers (2.5 kW) the use of the auxiliary gas xenon increases the lifetime of the ion source, too.

II Low energy beam transport

II.1 Introduction

Varying space charge forces due to current fluctuations, source noise and rise time of space charge compensation negatively influences the low energy beam transport and the injection into the RFQ. Rotation of the emittance pattern as a function of time increases the time integrated emittance and varying twist parameters of the emittance inhibit proper injection into the RFQ and therefrom decrease the transmission. Numerical simulations have been performed for electrostatic and magnetic transport (including space charge compensation and Gabor lens systems) for a beam current variation of $\pm 2\%$ at frequencies from 20 kHz up to 5 GHz.

II.2 Electrostatic (decompensated) transport

Simulations on the influence of varying beam current on beam transport have been performed using the IGUN code under assumption of varying plasma density in the ion source as the main course for the current fluctuation. Therefore the beam extraction simulations have been included into the simulation as well. Figure 4 shows the emittance at the beginning of the

electrostatic LEBT for the 3 different ion currents (137.2 mA, 140 mA, 142.8 mA). Due to the space charge forces the beam radius and angle increases slightly with the current. The decrease of the RMS-emittance indicates that the extraction system is optimised for a slightly higher current than 140 mA.

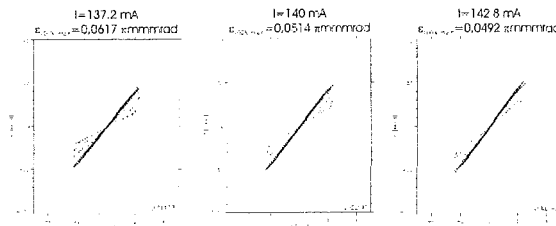


Fig. 4: Emittances at the entrance of the LEBT system for varied extracted beam currents gained by simulations using the computer code IGUN

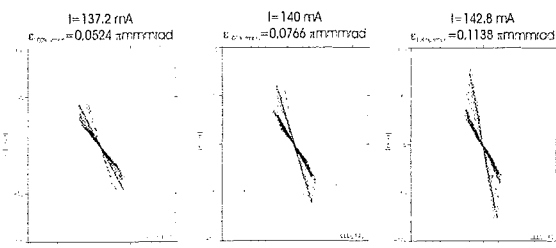


Fig. 5: Emittances at the exit of the LEBT system (RFQ entrance) for varied extracted beam currents. The simulations have been performed using the computer code IGUN

Figure 5 shows the emittance at the exit of the electrostatic LEBT for the 3 different cases. Due to the space charge forces the beam radius decreases slightly (1.6 mm, 1.5 mm, 1.3 mm) and the envelope angle increases stronger (50 mrad, 60 mrad and 80 mrad) with the current. This increase in angle can be explained also with the increasing space charge leading to a higher degree of lens filling in the last electrode leading to a stronger deflection. The increase of the RMS-emittance shows the effect of higher lens aberrations due to the increased degree of lens filling.

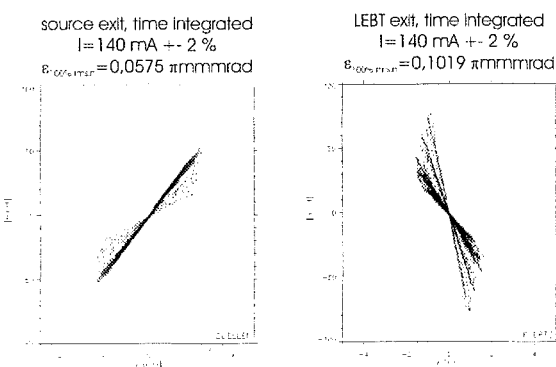


Fig. 6: Input (left) and output (right) Emittance of the electrostatic LEBT gained by simulations of 3 different ion currents (source noise) and superposing them for time integration

Conclusions:

Figure 6 shows the effective (time integrated) emittance at the entrance (left) and the exit (right) of the electrostatic LEBT. Due to the current fluctuations the RMS-emittance at source exit is slightly (12 %) higher than for the nominal current. At the LEBT exit the RMS-emittance growth has already increased to 33 %

(total 77 %) compared with the nominal current. The additional 21 % is mostly due to the higher space charge in the 142.8 mA case. This leads to extensive redistribution due to lens aberrations.

II.3 Magnetic (space charge compensated) transport

For the simulation of the influence of varying beam current on space charge compensated beam transport the knowledge of the time scale of the disturbance (fluctuation frequency) and the reaction time of the compensated beam plasma is necessary. Therefrom two frequencies can be defined. The maximum frequency (f_{max}) is given roughly by the plasma frequency (for IFMIF $f_{max} \approx 0.5$ GHz) and the minimum frequency (f_{min}) defined by the production mechanisms of the compensation. Below f_{min} the compensation is adiabatic and can be neglected for beam transport properties above f_{max} the compensation can not follow the disturbance.

II.3.1 Measurements of the rise time of compensation

For IFMIF f_{min} has been determined from rise time measurements at the H⁺ injector in Saclay [4]. Figure 7 shows the development of the beam current (for a pulsed ion source) as a function of time.

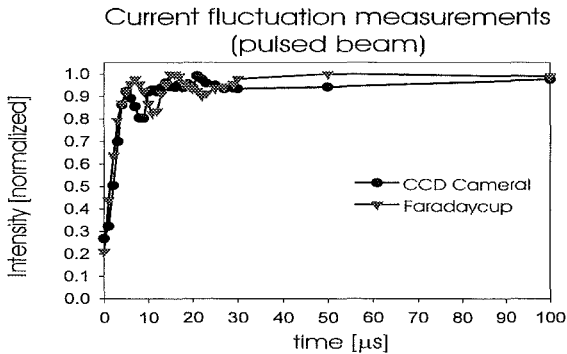


Fig. 7: Normalised ion current measurements as a function of time gained by faraday cup and CCD camera measurements on a pulsed ion beam

The rise time of the ion current (given by the ion source) can be estimated by measurements of an faraday cup and by CCD camera measurements to be approximately 7 µs. Fig. 8 shows the reaction of the beam radius on the changing space charge as a function of time. The time constant is again dominated by the source physics and pulsforming electronics.

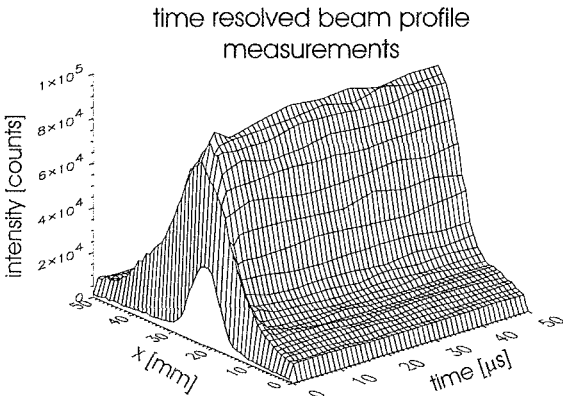


Fig. 8: Transversal ion beam intensity distribution as a function of time determined by CCD camera measurement

Fig. 9 shows the development of the beam potential on beam axis as a function of time for different residual gas pressures

and therefrom for different theoretical rise times of compensation (2.3-10 µs). The rising potential for the first 2-3 µs is due to the rise time of the source, the falling potentials after 3 µs is already the effect of the establishing space charge compensation (for 100 % variation of the space charge I).

Conclusions

For IFMIF the lower boundary frequency (f_{min}) for preservation of space charge compensation will be $200 \text{ kHz} > f_{min} > 20 \text{ kHz}$ (depending on the residual gas pressure). Noise above this boundary will negatively influence the compensation degree and emittance growth might occur.

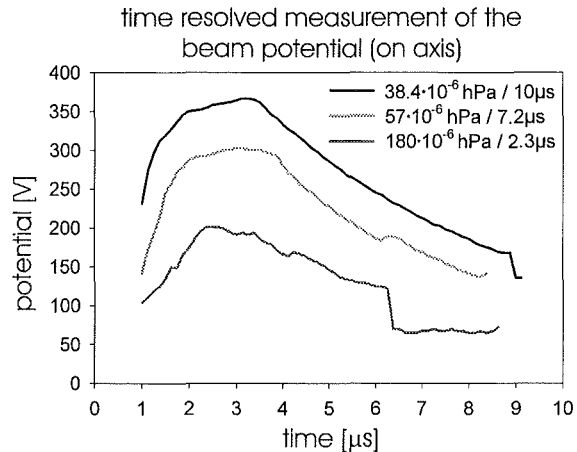


Fig. 9: Development of the beam potential as a function of time for different residual gas pressure, determined by time resolved residual gas ion energyspectrometry

II.3.2 Beam transport calculations

Therefore simulations have been performed using the LINTRA [5] code for 3 different scenarios ($f_{noise} < 20 \text{ kHz}$; $f_{noise} \approx 100 \text{ kHz}$; $f_{noise} > 500 \text{ MHz}$). Figure 7 shows the results of simulations gained from the LINTRA code under assumption of source noise frequencies below 20 kHz (constant space charge forces, see chapter II.3.1). The variation of the emittances at the exit of the magnetic LEPT section is due to the varying input emittances delivered by the ion source (see fig. 4).

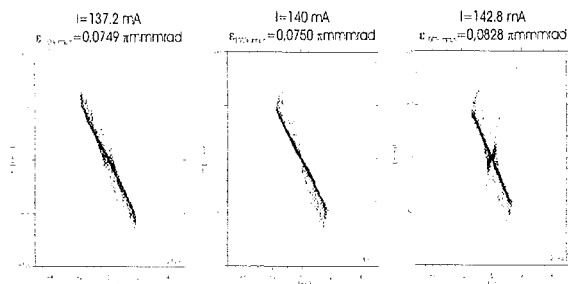


Fig. 10: Simulation of beam transport for space charge constant ($f_{noise} < 20 \text{ kHz}$) using entrance emittances according to fig. 1

Figure 11 shows the results of simulations gained from the LINTRA code under assumption of source noise frequencies of 100 kHz (space charge fluctuations are partly compensated the resulting variation is +- 1.2 %, see chapter II.3.1). The variation of the emittances at the exit of the magnetic LEPT section is still mainly influenced by the variation of the input emittance delivered by the ion source (see fig. 4) only the simulation with a space charge higher than nominal show a minor reduction of emittance growth.

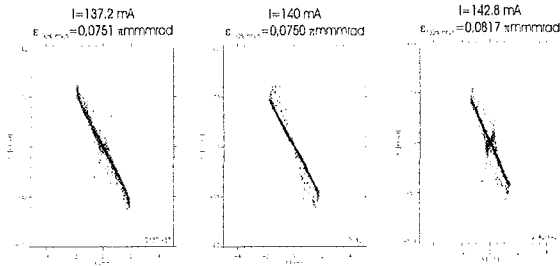


Fig. 11: Simulation of beam transport for app. $\pm 1.2\%$ space charge variation ($20 \text{ kHz} < f_{\text{noise}} < 100 \text{ kHz}$) using entrance emittances according to fig. 4

Figure 12 shows the results of simulations under assumption of source noise frequencies above 500 MHz (space charge fluctuations are $\pm 2\%$). The variation of the emittances at the exit of the magnetic LEBT section is still mainly influenced by the variation of the input emittance delivered by the ion source (see fig. 1), in this case the simulation using the low space charge shows a minor increase (1%).

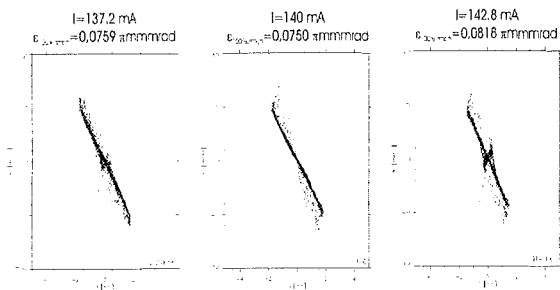


Fig 12: Simulation of beam transport for space charge variation of $\pm 2\%$ ($f_{\text{noise}} > 500 \text{ MHz}$) using entrance emittances according to fig. 4

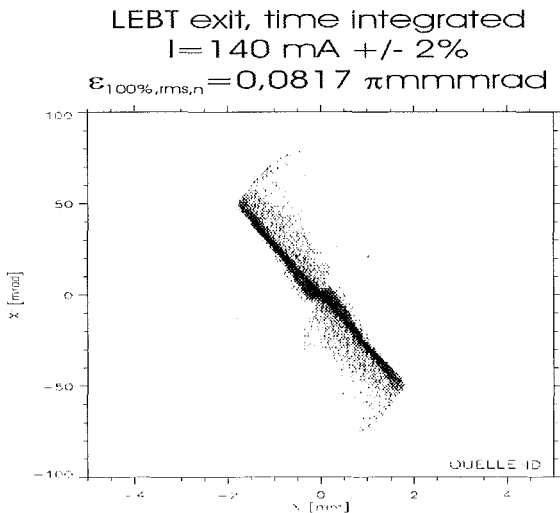


Fig. 13: Time integrated emittance gained from a simulation of beam transport for constant space charge ($f_{\text{noise}} > 20 \text{ kHz}$) using entrance emittances according to fig. 4

Conclusions

For a variation of the beam current of $\pm 2\%$ minor changes in beam transport have been found. An overall growth of the time integrated emittance of 9% from the nominal 0.075 πmmrad to 0.0817 πmmrad (see fig. 13, overall all emittance growth 42%) is not significant and mostly caused by the variation of the

input emittance delivered by the ion source. Under the consideration that the necessary focussing field strength for space charge compensated transport is mostly a function of ion energy and mass and not the space charge forces a variation of $\pm 2\%$ is not dominant for transport properties and therefore this result was not too surprising.

II.4 Beam transport using a Gabor lens

Gabor lenses used for beam transport not only deliver strong cylinder symmetric focussing but also totally compensated the space charge of the beam within the lens. This is valid up to the plasma frequency (app. 5 GHz). Outside the lenses the degree of compensation is reduced compared with magnetic focussing [6,7]. This is due to the heating of the electrons inside the lens. On the other hand this exchange of lens electrons and compensation electrons increase the boundary frequencies for fluctuations also outside the lens. An magnetic field for electron enclosure below 0.2 T and an electrode potential of 15 kV is necessary to fulfil the injection requirements at RFQ entrance. The degree of lens filling was 84% for the chosen geometry. Figure 14 shows the results of transport simulations for IFMIF for an variation of beam current of $\pm 2\%$. An overall emittance growth of 54% (0.088 πmmrad) is prognosted. The additional emittance growth due to current fluctuations is mainly caused by the variation of the input emittance. An additional emittance growth of 15% is found. This is valid for frequencies up to 5 GHz.

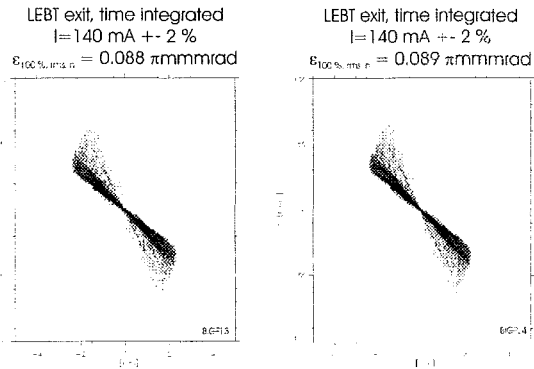


Fig. 14: Time integrated emittances gained from a simulation of beam transport using Gabor lenses) using entrance emittances according to fig.1. Left for space charge variation of $\pm 1.2\%$ ($20 \text{ kHz} < f_{\text{noise}} < 500 \text{ MHz}$) right for a variation of $\pm 2\%$ ($500 \text{ MHz} < f_{\text{noise}} < 5 \text{ GHz}$)

Conclusions

For a variation of the beam current of $\pm 2\%$ minor changes in beam transport have been seen. An overall growth of the time integrated emittance of 15% is not significant and mostly caused by the variation of the input emittance delivered by the ion source.

Summary

The influence of current fluctuations of $\pm 2\%$ on low energy beam transport has been determined numerically for 3 different transport systems. For electrostatic systems the largest growth of the time integrated emittance has been found (77%, at app. 50% degree of lens filling) partly caused by the variation of the delivered source emittance and the varying space charge in the lens. Space charge compensated transport shows better results (42% for solenoids below a frequency of 20 kHz at 50% degree of lens filling, and 54% for Gabor lenses below a frequency of 5 GHz at 84% degree of lens filling). For compensated transport the main source of emittance growth is the variation of the

source emittance. Comparison between magnetic systems and Gabor lenses show only at very low frequencies a slightly better performance of the solenoid systems. On the other hand the magnetic field strength is reduced by at least a factor of 7. Therefore the investment costs for Gabor lenses is app. 50% of the solenoid solution. **Both fulfil the requirements for IFMIF even at a current variation of +- 2%.**

III. Beam Dynamics Calculations

III.1 Introduction

Beam dynamics calculations have been performed for the RFQ and DTL in the IFMIF scenario to study the effects when

- a) the electrode voltage is lowered in the RFQ, leading to a lower sparking risk, which is essential for the required cw operation of the IFMIF accelerator.
- b) the output energy of the RFQ is lowered from 4.0 MeV/u to 2.5 MeV/u, giving a shorter RFQ
- c) the DTL has to start with an injection energy of 2.5 MeV/u only.

Calculated RFQ output emittances have been injected into the DTL instead a somehow idealized input distribution like waterbag or K-V type, mismatch and filamentation have been observed.

III.2 RFQ

In the RFQ design the electrode voltage has to be distributed in an appropriate way to achieve both: strong transverse focusing as well as sufficient beam bunching and acceleration at the same time. Lowering the electrode voltage and by that the sparking risk means in the first approximation either less transverse focussing which is not possible for high currents, or less acceleration and a longer RFQ. The planned lower end energy of the RFQ of 2.5 MeV/u is therefore complementary to the simultaneous reduction of the electrode voltage.

A lot of parameter sets have been studied to when the electrode voltage in the RFQ is lowered to a value corresponding to 1.7 Kilpatrick, which is considered to be sufficiently safe. First simple estimations show, that for a high current limit a high input energy of the RFQ is favourable, which again increases the length of the RFQ. But from the technical view new results show, that voltages up to 400 kV can be used for ion source operation [8]. Table 1 shows a parameter set found with the use of CURLI and RFQUICK for a non equipartitioned RFQ for 1.7 Kilpatrick and a transmission of 95.3%. The rms emittance growth is with 30% moderate.

From the table 1 we can see two special design features'. First is, in our RFQ design study we used 6 RMS-in cells which gave the best match to the RFQ acceptance and for a better transition of the beam into the following Alvarez DTL, we used as a matching out cell a Crandall cell. In such a Crandall cell the modulation of the RFQ goes to 1 and the focussing strength B goes to zero which leads to a good beam quality at the entrance of the following DTL [9].

The next three figures 15, 16 and 17 show beam dynamic calculations which were made with the multi particles program called PARMTEQM, we used 5000 macro particles, a 2d space charge solver and a matched 4d waterbag input distribution. The calculations includes multipoles and image charge effects which are very important for high current and high intensity applications like IFMIF.

Table 1: Structure parameter of 175MHz 1.7 IFMIF RFQ

Ion	D ⁺
Design	Non EP
Frequency f [MHz]	175
Number of particles	5000
Input distribution	4d Waterbag
W _{in} / W _{out} [MeV/u]	0.125 / 2.5
Voltage V [MV]	0.136
Bravery factor b	1.7
Focussing factor B	3.551
Cells / Length [m]	633 / 14.85
RMS-in	6 cells
RMS-out	Crandall cell
Aperture [cm]	0.815 – 0.595
Av. aperture r ₀ [cm]	0.774
Phase [°]	-90- -35
I _{in} [mA]	140
I _{out} [mA]	133.2
Transmission	95,3 % (Mult.+Imag.)
Modulation m	1 – 1.55
Input- / Output ε ^{N,RMS} _{trans} [cm×mrad]	0.020 / 0.026 (0.04)
Input- / Output ε ^{N,RMS} _{long} [MeV×Deg]	0.0 / 0.199 (0.4)

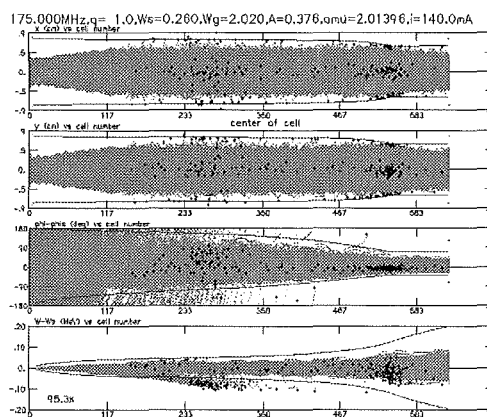


Fig. 15: Transverse and longitudinal phase profiles of the 1.7 IFMIF RFQ

In figure 15 the phase profiles of the RFQ are plotted. From the transverse plane we can see that the most losses are at the beginning of the Buncher at an energy of $W_s \approx 0.3$ MeV which are uncritical and 1% at the end of the Buncher at his "bottle neck" with an energy of $W_g \approx 2$ MeV which is still tolerable. In the energy area over 2 MeV we have nearly no losses which is quite important for the maintenance of the structure. From the phase space profiles we can see some longitudinal losses during the bunching process of RFQ. These losses are uncritical as long as the particle do not hit the wall.

Figure 16 shows the input and output emittances of the RFQ. For matched 4d waterbag input distribution with the IFMIF N-RMS emittance of 0.02 [cm×mrad] the output distribution looks satisfying. No halo in the transverse plane and in the longitudinal we have only a small energy spread of $\Delta W = \pm 1.5$ % and in phase of $\Delta \phi = \pm 30^\circ$ and no filamentations.

The figure 17 shows the real space of the beam at the end of the RFQ and the longitudinal phase space again. From the real space we can see that the beam has a nearly round shape, no halo and is centred. This output distribution was used for injection into the DTL in our test calculations.

III.3 DTL

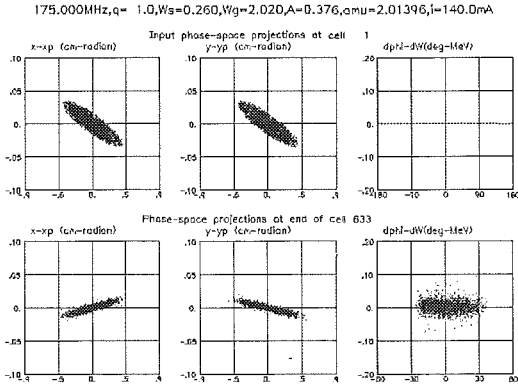


Fig. 16: Matched input and output distribution of the 1.7 IFMIF RFQ

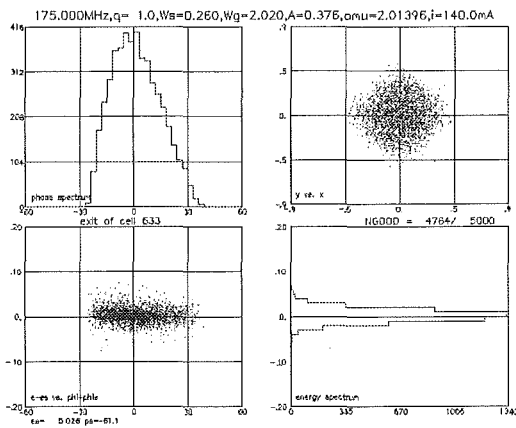


Fig. 17: Real space and energy-phase distributions at the end of the 1.7 IFMIF RFQ

The studies of the costs of an 4-Rod-RFQ showed a considerable reduction in comparison with the 4-Vane-structure which is of the order of 30%. This calculation is based on our experiments with the 4-Rod-RFQ; many of those have been built in the last years by Prof. Schempp and his team in the IAP and by close cooperation with the industry. For example, weeks ago an RFQ has been delivered to the Rutherford Lab in Great Britain, which has a high duty cycle of 20%. But to get an exact price for a 4-Rod-RFQ working in cw operation mode is still difficult at the moment. We have to make a complete and detailed layout of the system, before, for example, taking into account the cooling system for the high power losses. The costs of the power supplies, the ion source and the LEBT could not be reduced, the old prices are correct. Maybe in the case of the power supplies a reduction can be done in the future, if the ongoing development for the American Spallation-Neutron-Source (SNS) will be successful. We are in contact with our American colleagues, first results can be expected at the end of the year.

Conclusions

A new RFQ design was made with a new set of parameters (1.7 Kilpatrick, $W_{in}=0.125$ MeV/u, $W_{out}=2.5$ MeV/u). The design study fulfils the key requirements of the IFMIF project (low sparking risk through cw operation with 1.7 Kilpatrick, high transmission > 94 % , nearly all losses in a energy area of ≤ 2 MeV to prevent the structure to get radioactive and guarantee hands-on maintenance, low emittance growth and small energy and phase spread for a good transition into the next structure).

The new set of design parameters of the IFMIF RFQ requires a new set of design parameters for the IFMIF DTL. Therefore a new design with a lower input energy of 2.5 MeV/u and an unchanged output energy of 20 MeV/u was necessary. The other design issues could be taken from the former design (1 Kilpatrick, normal conducting, FoDo structure, an electric field gradient of 2 MV/m). The type of the LINAC assumed as before, a conventional normal conducting Alvarez DTL. The new input energy of 2.5 MeV/u leads to an input beta of $\beta = 0.072$. The cell length determines the drift tube length and therefore the length of the magnetic quadrupole lenses which are inside the drift tubes. In our case the first cell of the DTL is $\beta\lambda = 12.4$ cm with a quadrupole length of 7 cm and a magnetic field strength of 0.97 T in the FoDo lattice case. This is still in the normal conducting area of the magnetic field which is a design issue too and in addition we can take the conventional FoDo focussing scheme.

Table 2 shows the structure parameter of the new 175 MHz Alvarez DTL for IFMIF.

Table 2: Structure parameter of the 175 MHz Alvarez DTL for IFMIF

Mass A	2 (D^+)	
Charge q	1	
Current I	125.0	mA
Transmission	100 % (+Multi)	
Number of particles n	5000	
Input distribution	6d Waterbag	
Frequency f_{rf}	175.0	MHz
Focussing lattice	FODO	
Number of tanks	1	
Power (Cu + Beam)	6.15	MW
Injection energy W_{in}/A	2.5	MeV/u
Extraction energy W_{out}/A	20.0	MeV/u
Energy gain $\Delta W/A$	17.5	MeV/u
Cells N_c	101	
Cell length $\beta\lambda$	12.5 ... 34.12	cm
Quadrupole length L_q	7.0	cm
Total length L_{tot}	23.87	m
Electric field amplitude E_0	2.0	MV/m
Total electric field amplitude $E_0 T$	1.65 ... 1.75	MV/m
Synchronous phase ϕ_s	-50 - -30 (20 cells)	deg
Aperture radius r_0	1.2	cm
Quadrupole gradient G_{max}	8.19 - 4.10	kG/cm
Gap length gl	1.88 - 8.6	cm
Effective shunt impedanz $\langle Z_{eff} \rangle$	45.8	M Ω /m
Bravary factor b	1.0	
Input- / Output $\epsilon_{n,rms}^{trans}$	0.025 / 0.027 (0.04)	cm \times mrad
Input- / Output $\epsilon_{n,rms}^{long}$	0.178 / 0.213 (0.4)	deg \times MeV

The cavity design was made with the field solver programme SUPERFISH. In the cavity design we paid attention to some important engineering constraints. This means we used in the cavity design a face angle to provide some space for the cooling devices and the electromagnets [10]. Table 3 shows the SUPERFISH output with the most important cavity parameters

of the first two cavities with a beta of $\beta=0.072$ and beta of $\beta=0.145$.

Table 3: SUPERFISH output of the first two cavities of the new 175 IFMIF DTL

Quantities	Cavity 1	Cavity 2
FREQuency	175	175
BETA	0.0728503983913	0.145998502737
LENGTH	12.48	5
DIAMeter	113.5898447282	25.011
G_OVER_Beta_lambda	0.1602564102564	113.5898447282
GAP_Length	2	0.202205335320
E0_Normalization	1.654133274768	9
E0T_Normalization	1.2	5.05735764171
CORNER_radius	1.2	2
INNER_nose_radius	1.2	1.791810912179
OUTER_nose_radius	1	1.2
FLAT_length	15	1
FACE_angle	16	1
DRIFT_TUBE_Diamet	0	34
er	0	16
BEAD_radius	3	0
GAP_Change	1	0
STEM_Diameter	1.2	3
STEM_Count	180	1
BORE_radius		1.2
PHASE_length		180

The next two figures 18 and 19 show the results of the beam dynamics calculations done with multi particle program PARMILA. The calculations were made with 5000 macro particles, a matched 6d waterbag input distribution and a 2d space charge solver. The multipole effects of the magnetic quadrupoles were included. The matching of the input distribution was made with the envelope program TRACE3D.

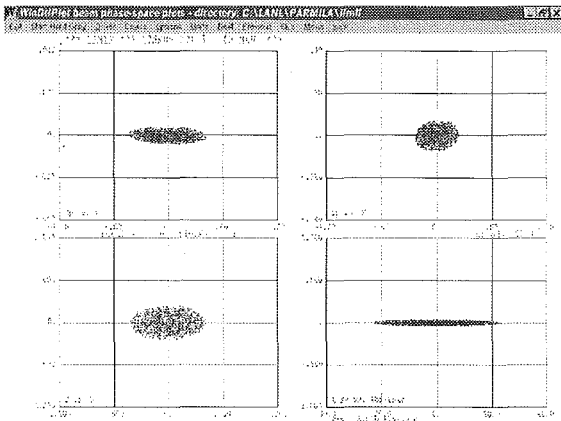


Fig. 18: Matched input distribution of the 175 MHz IFMIF DTL

In figure 18 the matched input distribution of the of the IFMIF DTL is plotted. In the transverse plane the DTL requires a beam in the focus which means the twiss parameter α is nearly zero. For the simulation we used a input RMS-N-emittance of 0.025 [cm \times rad] which is in the area of the output emittance of the RFQ (see table1). The matched energy spread and phase spread is with $\Delta W = \pm 1\%$ and $\Delta\phi = \pm 21^\circ$ smaller than the output of the RFQ. This is an indicator for some difficulties for the direct injection from the RFQ into the DTL.

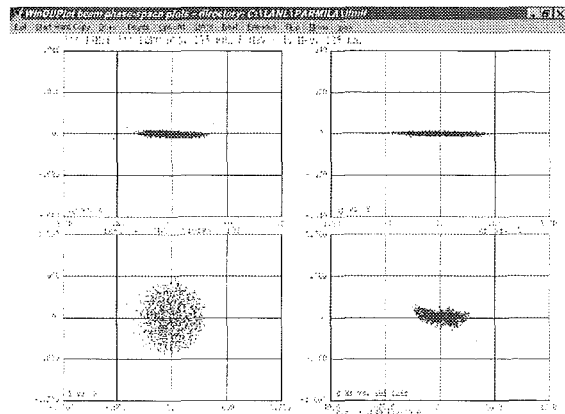


Fig. 19: Matched output distribution of the 175 MHz IFMIF DTL

Figure 19 shows the matched output distribution of the DTL. It looks quite satisfying. No halo appears in the transverse planes. 100 % transmission which is very important because of the activation of the structure due to deuteron-copper collision with energies over > 2 MeV and the beam is on axis. In the longitudinal plane we have nearly the same situation. No halo, the beam has no great filamentations and is on axis too. The spreads are $\Delta W = \pm 2\%$ in energy and $\Delta\phi = \pm 12^\circ$ in phase. As a consequence the emittance growth is quite low (see table 2).

III.4 Transition studies between RFQ and DTL

After simulations with a standard input distribution for the new parameter sets of the two structures, we tried a direct injection from the RFQ into the following DTL without some matching procedures inside the DTL or between the two structures. This method was favoured from the LANL group to prevent some emittance growth through the lenses of a MEBT [11]. We only varied the drift space between the two structures from 19.1 cm where the beam have a focus in the x-x' plane, to $\beta\lambda=12.4$ cm, $\beta\lambda/2=6.2$ cm and finally direct after the fringe field of the RFQ which we assumed with 3.9 cm. The preliminary results were quite promising. Without a special matching procedure between the two structures we got with a drift smaller than $\beta\lambda/2=6.2$ cm and greater than 3.9 cm 100 % transmission in the DTL. We only recognised some small halo production in both phase space planes and some filamentation in the longitudinal plane.

Conclusions

A new DTL design was made with a new set of parameters ($W_{in}=2.5$ MeV/u, $W_{out}=20.0$ MeV/u, 1 Kilpatrick, normal conducting, 175 MHz, FoDo lattice)

The design study fulfil the requirements of the IFMIF project (no losses in the linac (< 1 nA/m) due to the activation of the structure, small emittance growth to produce a good beam quality for the following HEPT and the Li target)

Even with no special matching procedures we achieved with a direct injection from the RFQ into the DTL with a drift $< \beta\lambda/2=6.2$ cm a transmission of 100 % which is an important constrain of IFMIF too.

Literature:

[1] R. Hollinger, P. Beller, K. Volk, M. Weber und H. Klein, The Frankfurt 200 mA Proton Source, Proc. ICIS 99, Kyoto, September 1999, in Print.

- [2] R. Becker, W.B. Hermannsfeldt, IGUN-A program for the Simulation of Positive Ion Extraction Including Magnetic Fields, Rev. Sci. Instruments., 63 (41), 2756-2758, 1992
- [3] R. Hollinger, Thesis, Institut für Angewandte Physik, University of Frankfurt, 2000, (in print)
- [4] Jakob, P-Y. Beauvais, R. Gobin, H. Klein, J-L. Lemaire, P-A. Leroy, J. Pozimski, „Time Resolving Diagnostics of Compensation process of Pulsed Ion Beams at SILHI“, Proc. 8 th ICIS Conf. 1999 Kyoto, Japan, to be. Publ.
- [5] J. Pozimski, O. Meusel “LINTRA ein Computerprogramm zur Berechnung des Strahltransportes teilkompensierter, hochperveanter Ionenstrahlen” , GrakoNews 1/99 , Graduiertenkolleg Physik und Technik von Beschleunigern, grako@ikp.tu-darmstadt.de
- [6] J. Pozimski “Untersuchungen zum Transport raumladungskompensierter niederenergetischer und intensiver Ionenstrahlen mit einer Gabor Plasma Linse” , Dissertation, Institut für Angewandte Physik der Johann Wolfgang Goethe Universität, 1997
- [7] O. Meusel, J. Pozimski, A. Jakob, A. Lakatos, “Low Energy Beam Transport for HIDIF” , Proc.HIDIF 2000 Meeting. 2000 San Diego, USA, to be. Publ. (NIM)
- [8] U. Ratzinger, Private communication, March 2000, GSI Darmstadt
- [9] K.R. Crandall, Proc. 1994 Linac Conf., August 1994 Tsukuba, Japan, p227
- [10] J.L. Merson, „Preliminary ATW DTL Dimensions, December 1991, AT-7:TM-91-33-35
- [11] J. Billen, A Room Temperature Design Option, September 1995, New Mexico, USA, La-UR-95-4416

Staff:

H. Deitinghoff
R. Hollinger
A. Jakob
H. Klein
A. Lakatos
A. Maaser
O. Meusel
I. Müller
J. Pozimski
A. Sauer
K. Volk

Nuclear Data Base

**TTMN-001
EFF/EAF Data File Update, Processing and
Benchmark Analyses**

TTMN-001/5, 6, 8

The European Fusion File / Activation File (EAF) projects aim at developing a qualified data base for nuclear calculations of fusion reactors. The related Task TTMN-001 of the EFDA technology work programme is devoted to the evaluation, processing, application and benchmarking of required nuclear cross section and uncertainty data.

The focus of the FZK contribution to Task TTMN-001 is on the qualification of new and updated EFF data evaluations by means of computational benchmark analyses. This includes sensitivity and uncertainty analyses and the processing of the related co-variance data. In addition, advanced computational schemes are being developed for sensitivity calculations based on the Monte Carlo technique.

**Integral Data Testing and Sensitivity/Uncertainty Analyses
for EFF-3 Ni Data Evaluations**

New EFF-3.0 data evaluations were provided over the reporting period for Ni-58 and Ni-60. They have been extensively tested through benchmark analyses of two 14 MeV neutron transmission experiments performed previously on spherical nickel shells at the Oktavian facility (University of Osaka, Japan) and the Institute for Physics and Power Engineering (IPPE), Obninsk, Russia. The analyses included calculations of the neutron leakage spectra using the MCNP code, sensitivity calculations for specified neutron flux integrals using MCSEN, a local version of MCNP4A with the capability for sensitivity calculations with the point detector technique, and assessments of the uncertainty on the basis of the newly processed EFF-3.0 co-variance data [1,4]. For the IPPE transmission experiment, Fig.1 compares the calculated and the measured neutron leakage flux spectra; Fig.2 shows the corresponding comparison of calculated and measured neutron flux integrals.

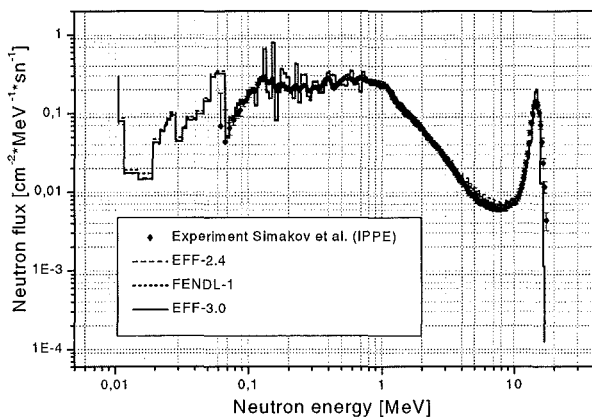


Fig. 1: Comparison of calculated and measured neutron leakage spectra for the IPPE spherical nickel shell (7.5 cm thickness).

The resulting good agreement with the new EFF-3 data has been achieved only after a reduction of the inelastic scattering cross-section around 14 MeV as had been suggested by the sensitivity and uncertainty calculations with MCSEN.

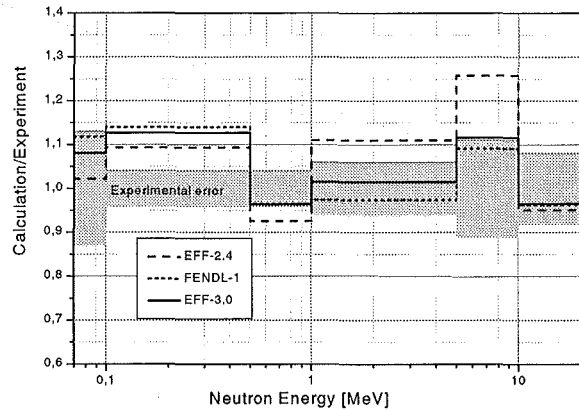


Fig. 2: C/E (calculation/experiment) comparison for neutron flux integrals of the IPPE Ni transmission experiment

Processing of co-variance data with extended options

Co-variance data with extended options for secondary distributions are being introduced in EFF-3 data evaluations to enable corresponding uncertainty calculations. Over the reporting period, co-variance data for Ni-58 and Ni-60 (file 33 for excitation functions and file 34 for angular distribution data) have been provided. The co-variance matrices have been processed in the VITAMIN-J group structure and applied in sensitivity/uncertainty calculations of the IPPE and Oktavian nickel integral experiments. A considerably reduced uncertainty has been obtained with the Ni EFF-3.0 co-variance data. As compared to FENDL-1 data, the uncertainty of the calculated neutron flux integrals is reduced by a factor 2 to 3, see Table 1.

Table 1: Calculated uncertainties of neutron flux integrals due to Ni-58 cross-section uncertainties (IPPE nickel spherical shell experiment)

E [MeV]	0.1-0.5	0.5-1	1-5	5-10	E> 10	Total
FENDL-1						
Uncertainty [%]	2.45	2.52	2.76	6.58	3.82	1.76
EFF-3.0						
Uncertainty [%]	0.93	0.84	0.88	2.59	0.91	0.40

A few problems were encountered when processing the co-variance matrices for Ni-58 [3,5]. A problem with negative eigenvalues for the total and the capture cross-section co-variance data was resolved in co-operation with the evaluators of IRK Vienna. Unphysical spikes appear in the elastic co-variance matrices due to the fact that they are derived by subtraction of the total and non-elastic co-variances.

The spike problem was shown to be eliminated by using an improved unified energy group structure in which the evaluated covariance data are provided, and/or using smaller values of the LB=8 parameter which represents the uncorrelated short range variance that scales inversely proportional to the energy group width.

Benchmark for sensitivity and uncertainty calculations

A computational benchmark on probabilistic and deterministic sensitivity and uncertainty calculations has been conducted with the objective to check and validate the novel Monte Carlo technique for calculating point detector sensitivities as being implemented in MCSEN. A suitable 14 MeV neutron benchmark problem on an iron assembly has been considered to this end. After removal of some minor bugs in MCSEN, good agreement has been achieved for the calculated individual sensitivity profiles, the uncertainties and the neutron flux spectra as well. For the 28 cm thick spherical iron shell, Table 2 compares the uncertainties as calculated for the neutron flux integrals at the location of the detector. Nuclear cross-sections and co-variance data were taken from the EFF-3.1 Fe-56 data file. It was concluded that the Monte Carlo technique for calculating point detector sensitivities and related uncertainties as being implemented in MCSEN is well qualified for applications to sensitivity and uncertainty analyses of fusion neutronics integral experiments [6].

Table 2: Uncertainties of neutron leakage flux integrals as calculated for a 28 cm thick iron spherical shell with the Monte Carlo (MCSEN) and the deterministic (ONEDANT/SUSD) approach

E [MeV]	1-5	5-7.4	7.4-10	10-13.8	E> 13.8	Total
Uncertainty [%]						
MCSEN	1.43	12.1	7.46	5.73	4.35	0.72
SUSD	1.59	12.4	7.45	5.74	4.54	0.72

Algorithm for Monte Carlo calculation of sensitivities to secondary angular distributions

The Monte Carlo calculation of sensitivities with the point detector technique is currently restricted to the excitation functions of the considered nuclear reactions. With the running EFF-programme, development work was started on computational schemes for secondary distributions with the objective to implement them into the MCNP code. The first part of the development work is devoted to the secondary angular distributions (SAD).

Over the reporting period, suitable algorithms have been developed for the Monte Carlo calculation of SAD sensitivities based on the differential operator method [2]. A general algorithm was designed which enables to calculate the sensitivity independently on the actual representation of the SAD on the nuclear data file. Variants thereof were derived making use of special features of specific SAD such as the Kalbach-Mann representation of the energy- angle distribution. Finally, suitable formulae have been elaborated that can be implemented into the MCNP code to allow the calculation of these sensitivities with the point detector tally. Work on the coding of the SAD algorithms developed for implementation in MCNP is currently in progress.

Literature:

- [1] C. Konno, U. Fischer, R. Perel, Monte Carlo Benchmark Analyses for Ni EFF-3.0 Including Sensitivity/Uncertainty Calculations, EFF-Doc-702 (November 1999).
- [2] R.L. Perel, Algorithm for Monte Carlo Calculation of Sensitivities to Secondary Angular Distributions, EFF-Doc-703.
- [3] I. Kodeli, Report on 1999 Activity on ND-1.2.1 Subtask: Processed Multigroup Covariance Files with Extended Options for EFF-3, EFF-DOC-698 (November 1999).
- [4] C. Konno, U. Fischer, R. Perel, Supplementary Benchmark Analyses for New and Revised Ni EFF-3.0 Ni Data , EFF-DOC-733 (May 2000).
- [5] I. Kodeli, EFF-3 Covariance Matrices – A User’s Point of View, EFF-DOC-732 (May 2000).
- [6] U. Fischer, I. Kodeli, C. Konno, R. Perel, Inter-comparison of Monte Carlo and S_N Sensitivity Calculations for a 14 MeV Neutron Benchmark, Int. Conf. Advanced Monte Carlo for Radiation Physics, Particle Transport Simulation and Applications, October 23-26, 2000, Lisbon, Portugal.

Staff:

- U. Fischer
- C. Konno (FNS, JAERI)
- R. Perel (Hebrew University of Jerusalem)
- I. Kodeli (Josef-Stefan Institut, Ljubljana)

**TTMN-002
Benchmark Experiments to Validate EFF/EAF
Data**

**TTMN-002/4
Activation Experiments in Fusion Peak
Spectrum**

11. Activation experiments in fusion peak neutron field

Safety and environmental assessments are essential parts of fusion power plant development to ensure the attractiveness of fusion power. A central topic of safety-related investigations is the radioactivity induced by neutrons in the materials of the assembly. Radionuclides with a broad range of half-lives have to be included in the corresponding analyses. The short-term radioactivity (half-life, $t_{1/2}$, ranging from the order of magnitude of minutes to weeks) is mainly of interest with respect to heat production and shut-down dose rates, whereas long-term radioactivity ($t_{1/2}$ of the order of 10 – 100 years or more) determines the waste management.

The European Activation System (EASY) [1] is a complete tool for the calculation of activation in materials exposed to neutrons. It represents the reference system for corresponding analyses of the ITER design. In order to validate EASY, several integral experiments are carried out. Complementary to investigations at Karlsruhe with a white spectrum of fast neutrons ranging up to energies of 20 MeV, 14-MeV neutrons (fusion peak) are used by TU Dresden, in collaboration with CCA Sergiev Posad and RRC „KI“ Moscow, for activating the same materials. After experiments with steels (SS316, MANET, F82H) [2] and vanadium alloys (V3Ti1Si, V4Ti4Cr, V5Ti2Cr) [3], in 1999 the investigations were extended to the low-activation structural material SiC and to Li_4SiO_4 , which is used as tritium-generating material in the European Helium-Cooled Pebble Bed blanket design [4].

In a calculation with EASY-99 the materials were taken to be irradiated with 14-MeV neutrons of a flux density corresponding to the power of 1.0 MW, for a period of one year. The results are shown in Fig. 1. The dominant radionuclides are ^{28}Al , ^{29}Al and ^{27}Mg , mainly produced on Si. Already for decay times of $t_D > 1$ h, radionuclides originating from impurities determine the dose

rate. At about 10 years the recycling limit is reached. For $t_D > 100$ y, more than 99% of the dose rate come for both materials from ^{26}Al ($t_{1/2} = 7.2 \cdot 10^5$ y) produced by $^{27}Al(n,2n)$.

The obtained dose rate profiles suggested carrying out two experimental runs with each of the materials. After a short irradiation the activities of ^{27}Mg , ^{28}Al and ^{29}Al were measured and analysed (previous Annual Report [5]).

To determine activities originating from impurities, neutron fluences of $3 \cdot 10^{14}$ cm⁻² were applied in a second irradiation at the high-intense neutron generator SNEG-13 [6] at Sergiev Posad. The sum of the measured and of the calculated activities are compared in Fig. 2.

SiC: The underestimation at $t_D = 2.4$ h and 4.1 d is mainly due to the ^{24}Na activity, which contributes 99% and 89%, respectively, to the total one. It is all produced by the $^{27}Al(n,\nu)^{24}Na$ reaction. Using the ratio of calculated-to-experimental value for ^{24}Na , the Al content of the material can be estimated to 0.72 wt-%. This amount of Al in SiC leads, under fusion power plant conditions, to a dose rate of the SiC of 274 :Sv/h at $t_D = 100$ y. To meet the hands-on level, the Al content has to be reduced by a factor of 1/27.

A large underestimation was found for the ^{92m}Nb activity produced by $^{93}Nb(n,2n)$. The measured value indicates a Nb content of at least 0.0003 wt-%. That has no significant influence on the long-term radioactivity induced by 14-MeV neutrons. For thermal neutrons the situation may be changed, as ^{94}Nb , produced by $^{93}Nb(n,\gamma)$, has a $t_{1/2}$ of $2 \cdot 10^4$ y.

Li_4SiO_4 : The agreement of the measured with the calculated sum seems to be satisfactory. But underestimations are compensated in the sum by overestimated values for the Sc activities. As all Sc activities are produced by reactions on Ti, its elemental content is estimated to be 0.054 wt-%, instead of 0.021 wt-% as determined by X-ray fluorescence analysis. A ^{92m}Nb activity was measured, but not predicted. The experimentally determined activity results in a Nb content of about 0.003 wt-%, with possible influence on the long-term radioactivity of an assembly, if thermal neutrons are present. The weak ^{59}Co activity is overestimated by a factor of 5.8 due to uncertainties of the Ni and Co content of the sample.

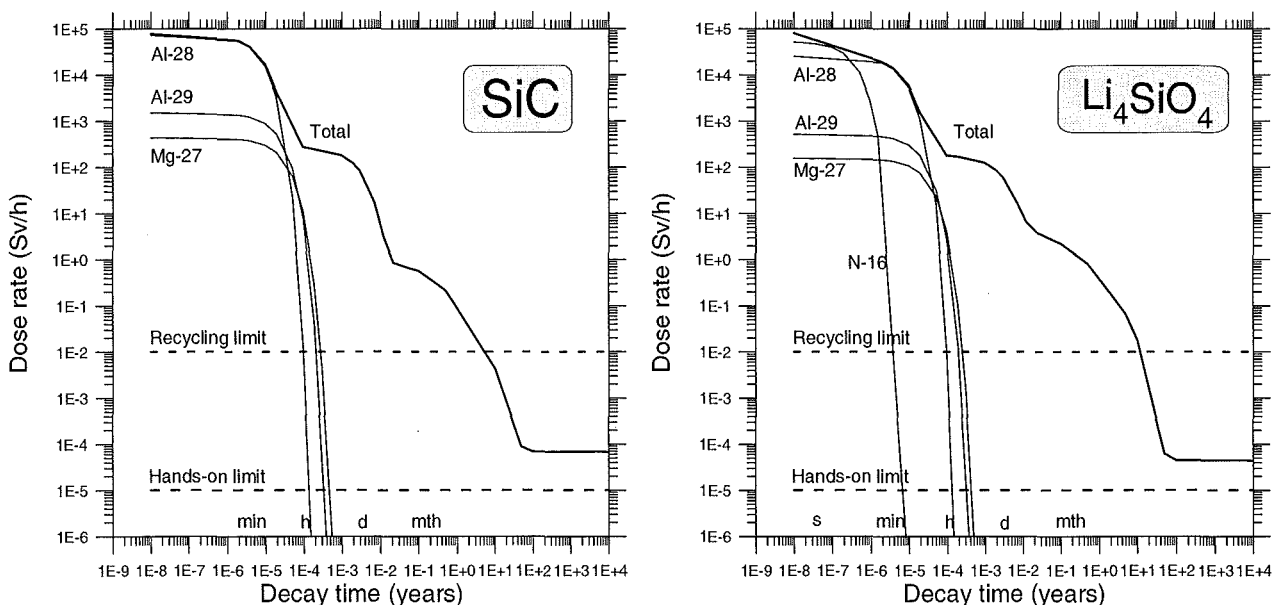


Fig 1: Contact dose rates from the (-emitting radionuclides in SiC and Li_4SiO_4 after irradiation with 14-MeV neutrons of 1.0 MW power for one year as function of the decay time. Full line - total dose rate; thin line - contribution of the radionuclide indicated; dashed line - recycling limit by remote handling and hands-on recycling limit as recommended by ICRP

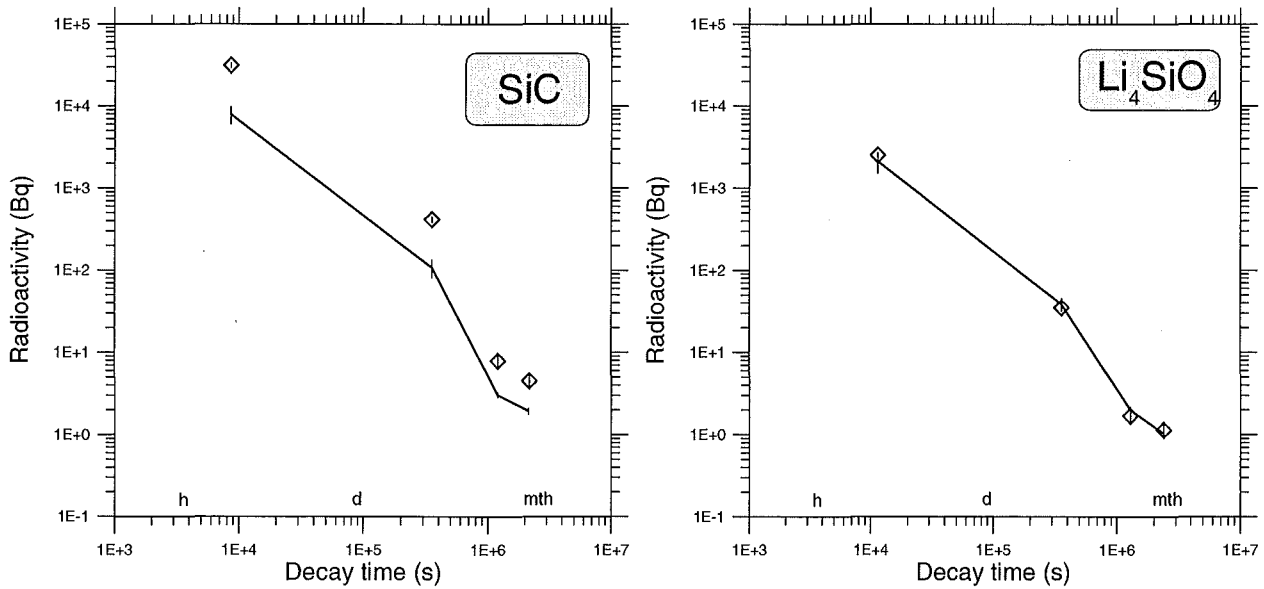


Fig. 2: Measured sum of (-activities () in SiC (^{24}Na , ^{46}Sc , ^{47}Sc , ^{48}Sc , ^{51}Cr , ^{54}Mn , ^{56}Mn , ^{57}Co , ^{58}Co , ^{89}Zr and $^{92\text{m}}\text{Nb}$) and in Li_4SiO_4 (^{24}Na , ^{46}Sc , ^{47}Sc , ^{48}Sc , ^{51}Cr , ^{54}Mn , ^{56}Mn) in comparison to the corresponding calculated activities (solid line) at the decay times of measurement

Literature:

[1] R. A. Forrest, J.-Ch. Sublet and J. Kopecky, The European Activation System, Proc. Int. Conf. On Nuclear Data for Science and Technology, Trieste, May 19-24, 1997, ed. by G. Reffo, p. 1140.

[2] H. Freiesleben, V. Kovalchuk, D. Markovskij, D. Richter, K. Seidel, V. Tereshkin and S. Unholzer, Experimental investigation of radioactivities induced in fusion reactor materials, Fusion Engineering and Design 42(1998)337; Nuclear Fusion Project, Annual Report of the Association Forschungszentrum Karlsruhe/EURATOM, Oct. 1996 – Sept. 1997, comp. by G. Kast, FZKA 6050, 1997, p. 131.

[3] K. Seidel, R. A. Forrest, H. Freiesleben, V. D. Kovalchuk, D. V. Markovskij, D. Richter, V. I. Tereshkin and S. Unholzer, Measurement and analysis of radioactivity induced in vanadium alloys by 14-MeV neutrons, Proc. of the 20th Symposium on Fusion Technology, Marseille, Sept. 7-11, 1998, p. 1361; Nuclear Fusion Project, Annual Report of the Association Forschungszentrum Karlsruhe/EURATOM, Oct. 1997 – Sept. 1998, comp. by G. Kast, FZKA 6200, 1998, p. 149.

[4] L. V. Boccaccini, et al., The European HCPB Test Blanket Module to be irradiated in ITER, Proc. of the 20th Symposium on Fusion Technology, Marseille, Sept. 7-11, 1998, p. 1255.

[5] Nuclear Fusion Project, Annual Report of the Association Forschungszentrum Karlsruhe/EURATOM, Oct. 1998 – Sept. 1999, comp. by G. Kast, FZKA 6400, 1999, p. 165.

[6] V. D. Kovalchuk, et al., Neutron generator SNEG-13; Neutron and photon field characteristics, Report IAE-5589/8, Russian Research Centre "Kurchatov Institute", Moscow, 1992.

Staff:

H. Freiesleben
 D. Richter
K. Seidel
 S. Unholzer

TTMN-002/5 Activation Experiments in White Neutron Spectrum

1. Lithium Orthosilicate

A sample of Li_4SiO_4 in the form of a solid disc of 10 mm diameter and 1.5 mm thickness (produced by hot pressing/sintering) was activated in the Karlsruhe d-Be neutron field at a flux density of about 10^{11} n/cm²/s for 48 hours. The chemical composition, as analyzed before the hot processing process, is given in Table 1. Gamma spectrometry with an efficiency calibrated HPGe detector was performed after 8 different cooling times ranging from 15 minutes to 112 days. A total of 20 product radionuclides were identified. A corresponding calculation was performed using EASY-99 (European Activation System), which is the combination of the FISPACT inventory code and the EAF-99 cross section and decay data library. The calculation yielded 15 of the product nuclides, so that C/E ratios can be derived. These C/E are given in Table 2 below. The remaining 5 nuclides, all found in low concentration, were not predicted by EASY. They have mass numbers beyond A=90. Impurities of such high mass numbers were not expected in Li_4SiO_4 , consequently, not sought for in the chemical analysis and therefore not specified in the input to the calculation. The main conclusions from the results in Table 2 are:

- Be-7, produced by the sequential (p,n) nuclear reaction on Li-7, is relatively important, as it is the only gamma emitting product with half-life beyond 21 hours produced from Li_4SiO_4 itself, not from impurities. Improving the prediction quality of EASY for this special case of a sequential charged-particle reaction may be worthwhile.
- The important short lived products from Si are all somewhat overestimated.
- Even a small Al impurity in Li_4SiO_4 leads to significant Na-24 activity. The Al impurity should be minimized.

Table 1: Composition of Li_4SiO_4 granulate

Element	weight %
Li	22.12 ±0.13
Si	23.30 ±0.03
O	54.29
C	0.108 ±0.0005
Na	0.0033 ±0.0010
Mg	0.0029 ±0.0006
Al	0.115 ±0.023
K	0.0076 ±0.0005
Ca	0.0059 ±0.0001
Ti	0.0214 ±0.0004
Cr	< 0.0006
Mn	0.00030±0.00004
Fe	0.0143 ±0.0001
Co	< 0.0004
Ni	< 0.0006
Cu	< 0.0004
Zn	< 0.0002
Zr	0.0046 ±0.0002

2. Eurofer-97

A sample of the low activation steel Eurofer-97 was activated in the same neutron field for 43 hours at a similar flux density as above. Gamma spectrometry on this sample is in progress.

3. Re-analysis of Nickel and Copper Experiment

The neutron fluence in the activation of pure Ni and Cu samples reported previously was re-determined by analyzing the nickel foils, which in the experiment originally served only for monitoring the flux density decrease across the sample. Also, a chemical analysis of the Cu sheet used was made for impurities of Fe, Co and Ni. A new calculation with EASY-99 yielded C/E ratios, that for the more important products are now compatible with unity within uncertainties. Exceptions are Cu-64 from Cu and Co-61 from Ni. Two more nuclides are not properly calculated by EASY because their production reactions, Cu-63(n,pα)Fe-59 (neutron energy threshold 6.7 MeV) and Cu-63(n,2nα)Co-58 (neutron energy threshold 16.5 MeV) are missing in EAF.

Staff:

H. Giese
U. von Möllendorff
H. Tsige-Tamirat

Table 2: Results of Li₄SiO₄ activation compared with EASY-99

Measurement and calculation at eight different cooling times, 15 min ... 112 d
C/E averaged over cooling times where applicable

f₀: Max. fraction of sample γ dose rate at any one of these cooling times

\pm_e : experimental uncertainty

\pm_s : EASY uncertainty

Prod.	$\approx T_{1/2}$	<i>f₀</i> EASY %	<i>C/E</i>	\pm_e %	\pm_s %	Generic pathways EASY	Remarks
Be-7	53 d	4.8	0.68	10	----	⁷ Li(p,n) 100%	<i>p induced</i>
Mg-27	9.5mi	8.4	1.49	10	9	³⁰ Si(n, α) 71% ²⁷ Al(n,p) 27% ²⁸ Si(n,2p) 2%	
Mg-28	21 h	0.07	0.39	12	199	²⁹ Si(n,2p) 99% ³⁰ Si(n,h) 1%	
Al-28	2.2mi	53.1	1.54	25	25	²⁸ Si(n,p) 100%	
Al-29	6.6mi	25.6	1.68	15	25	²⁹ Si(n,p) 98% ³⁰ Si(n,d) 2%	
Na-22	2.6 a	2.5	1.36	60	24	²³ Na(n,2n) 100%	
Na-24	15 h	97.4	0.83	20	22	²⁷ Al(n, α) 96% ²⁴ Mg(n,p) 4%	
Ca-47	4.5 d	3.0	6.9	70	89	⁴⁸ Ca(n,d) ⁴⁷ K(β) 89% ⁴⁸ Ca(n,2n) 5% ⁵⁰ Ti(n, α) 6%	
Sc-46	84 d	56.3	2.79	10	23	⁴⁶ Ti(n,p) 90% ⁴⁷ Ti(n,d) 10%	<i>Ti content incorrect?</i>
Sc-47	3.4 d	0.6	2.69	10	12	⁴⁷ Ti(n,p) 64% ⁴⁸ Ti(n,d) 33% ⁴⁹ Ti(n,t) 1% ⁴⁸ Ca(n,d) ⁴⁷ K(β) ⁴⁷ Ca(β) 2%	
Sc-48	44 h	21.8	2.66	10	5	⁴⁸ Ti(n,p) 99% ⁴⁹ Ti(n,d) 1%	
Cr-51	28 d	0.2	<1.82	25	36	⁵² Cr(n,2n) 58% ⁵⁴ Fe(n, α) 42%	
Mn-54	312 d	13.3	0.98	10	4	⁵⁴ Fe(n,p) 87% ⁵⁵ Mn(n,2n) 13%	
Y-88	107 d	0.01	1.8E-3	20	60	⁹⁰ Zr(n,t) 100%	<i>Y impurity?</i>
Zr-89	78 h	1.0	6.93	10	25	⁹⁰ Zr(n,2n) 100%	

T 426 Experimental Validation of Shut-down Dose Rates

The neutronics design of ITER is based on calculations with sophisticated codes and nuclear data with inherent uncertainties. Experimental validation is required for design parameters which affect the feasibility and the safety. Present dose rate calculations for a complex geometry suffer from high uncertainties which are unacceptable for guaranteeing occupational safety during hands-on maintenance inside the ITER cryostat. Therefore, a neutronics experiment is being performed at the Frascati Neutron Generator (FNG) [1] with the objective to validate dose rate calculations for a radiation field similar to that outside the ITER vacuum vessel and inside the cryostat. The related ITER Task T 426 is conducted in co-operation of ENEA Frascati, TU Dresden and FZK. The task of TU Dresden (TUD) is to provide the experimental data for the decay gamma spectra and the dose rates while the task of FZK is devoted to the computational analysis of the experiment and the development of the required computational tools.

Measurement of spectra and dose rates (TUD)

An ITER-specific material assembly was irradiated with 14 MeV neutrons at FNG to create a level of radioactivity which can, after shut-down of the neutron source, be followed by dose meters for a time period of at least two weeks. This is a typical waiting time assumed to be required for ITER-like machines to allow personal access to the cryostat.

The assembly consisted of a block of stainless steel (SS316) and water equivalent material with a total thickness of 70 cm and a lateral size of 100 cm x 100 cm. The detectors were positioned in a cavity (12 cm x 12 cm x 15 cm) at about 23 cm of shield thickness. Between neutron source, located in front of the assembly, and cavity, a void channel of a diameter of 2.7 cm was realised to include the effect of a streaming path in the bulk shield.

Complementary to experimental methods applied by the team of ENEA Frascati, the group of TU Dresden measured:

- the neutron flux spectrum during the irradiation with a NE213 scintillation spectrometer [2]
- the photon flux spectrum of the induced radioactivity with NE213 scintillation spectrometer,
- the dose rate with a tissue-equivalent scintillator.

The neutron fluence applied during two days of irradiation (1.8×10^{15} source neutrons produced) was sufficient to measure the dose rate and the photon flux spectrum over three weeks of cooling with acceptable effect-to-background ratio.

The experimental campaign was finished on September 21. The evaluation of the data obtained is in progress.

Development of computational tools (FZK)

The calculation of dose rate distributions requires the following computational steps: (i) neutron transport calculation for the neutron flux spectra distribution, (ii) activation calculation for the decay gamma source distribution and (iii) decay gamma transport calculation for the decay gamma spectra and the dose rate distribution. As for step (iii), various approximation methods are in use to enable these calculations for a complex geometry like the ITER machine.

In the framework of T 426, a computational procedure has been developed at FZK that allows a rigorous calculation of the shut-down dose rate distribution for full three-dimensional geometrical configurations. It is based on the use of the use of the computer code MCNP (calculation of neutron and photon transport) for the transport calculations (neutron and decay gammas) and the computer code FISPACT (for activation calculation) for the inventory calculation (decay gamma source). A suitable coupling scheme has been devised to enable an automated routing of the MCNP neutron flux spectrum distributions to FISPACT (interface MCFISP) and the FISPACT decay gamma source distributions to MCNP (interface FISPACT), see Fig. 1. The decay gamma source distribution is sampled in a source routine linked to MCNP according to the distribution provided by the preceding MCNP neutron transport and FISPACT inventory calculations. This proceeding allows to apply the procedure for any complex geometry without restrictions. Therefore, it will also be used to check the approximate dose rate calculations for ITER inside the cryostat.

Verification calculations so far have been performed for different models of the mock-up assembly being under investigation in the framework of T 426.

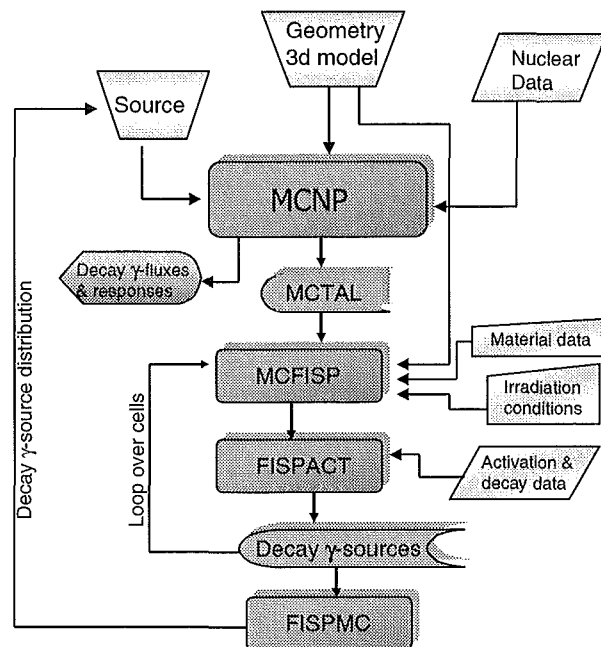


Fig. 1: Flow scheme for MCNP based shut-down dose rate calculations

Literature:

- [1] M. Martone, M. Angelone and M. Pillon, The 14 MeV Frascati neutron generator, Journal of Nuclear Materials, 212 (1994) 1661-1664.
- [2] S. Guldbakke, H. Klein, A. Meister, J. Pulpan, U. Scheler, M. Tichy and S. Unholzer, Response matrices of NE213 scintillation detectors for neutrons, Reactor Dosimetry ASTM STP 1228, p. 310, ed. by H. Farrar, American Society for Testing Materials, Philadelphia, 1995.
- [3] Y. Chen, U. Fischer, Dose Rate Calculation Methodology under Development at FZK, ITER Technical Meeting "Nuclear Analysis for the Final Report", Garching, 24-25 February, 2000.

- [4] Y. Chen, U. Fischer, Rigorous Method for MCNP Based Dose Rate Calculations, Progress Report July 2000, ITER Progress Meeting "Neutronics for the Final Report", Garching, 4-5 July, 2000.

Staff:

Y. Chen (Institute for Plasma Physics, Hefei)

U. Fischer

H. Freiesleben

D. Richter

K. Seidel

S. Unholzer

Socio-economic Research on Fusion

Socio-economic Research on Fusion (SERF 2)

International Power Supply Policy Globalisation of Research: The Example of Fusion Research

Contribution 2000

Within the scope of the SERF 2 Macrotask 4: "Politics and mega-science: the global scale of fusion", Task Title: "International Power Supply Policy and the Globalisation of Research: The Example of Fusion Research", the activities of our group at the Institute for Technology Assessment and System Analysis (ITAS) are focused on the following research goals:

- Which contribution does fusion make toward a "sustainable energy and research policy", which is slowly establishing itself at the national and international levels in the shape of the principle of efficiency and prudent use of resources. Here, fusion is regarded as a strategy of future sources of energy in comparison to existing energy resources.
- Fusion, as a project which can only be tackled internationally, is a manifestation of the globalisation of research at the organisational level. Here, we should examine how
 - a) Communication forms emerge in the "scientific community" and
 - b) New forms of cooperation and organisation of research processes are developed, to unite scientific research (fundamental research) and technological development in a single project.

At the present state of our information, based on a literature review, we can affirm that fusion research, as far as the necessary financial expenditures and their political justification are concerned, is being politically controversially debated.

In the political arenas, projects like controlled nuclear fusion are discussed primarily with regard to the controllability of complex technical systems and the sustainability of our future supply of electric power.

The attempt to discuss this problem will have to consider:

- on the one hand, already established concepts of sustainability,
- and on the other, the – according to the present state of our knowledge – foreseeable characteristics of a system of power generation and supply based on fusion reactors.

Not only do the goals of global technology projects have to be embedded in patterns of universally accepted legitimisation (sustainability), but the organisation of research and development is also changing into networks acting globally. In this sense globalisation means not only the world-wide linking of financial markets and the permanent availability of information and communication networks, but above all the creation of global organisations of research and innovation processes. The globalisation of research and development of technology has several dimensions:

- the recognition and treatment of global problems,
- the transformation and evolution of new forms of organization and cooperation in a global community of researchers,
- the constitution of Global Change Research.

Fusion is playing a "pathfinder role" for these processes and is at the same time itself an expression of the globalisation of the production of technology.

Results were presented at the 21st Symposium on Fusion Technology, September 11 - 15, 2000 – Madrid, Spain

Staff:

G. Bechmann
F. Gloede
E. Lessmann

Preparatory Work for Power Plant Conceptual Study

Power Plant Conceptual Studies

Task TRP 2 Economic and Operational Requirements

TRP 2-D 1 Critical Review of Economic-related Objectives Used in Earlier European, USA, and Japanese Power Plant Studies

A number of Fusion Power Plant Studies performed in USA, Japan and Europe during the last 10 years have been reviewed. Main emphasis has been placed on the economic related objectives and assumptions of these studies.

The overall impression is, that, compared to the usual strategy in Europe, in the USA as well as in Japan larger advances are anticipated in the areas of plasma physics and technology before a commercial power plant will be built. This leads to considerably higher wall loads, higher thermal efficiencies, and, related to the neutron wall load, lower heat fluxes to the divertor plates.

Other important differences are in the area of power core replacement. In Europe the replacement methods are based on the ones investigated in more detail in the frame of NET and ITER. In USA and Japan fast replacement methods are considered as an important key for a sufficiently high plant availability. For this reason, large replacement units (mostly entire torus sectors) are selected in order to allow for a replacement time of 1-2 months for the entire power core.

In a number of USA studies the blankets are subdivided in radial direction into two or three regions in order to take benefit for the potential increase in lifetime of the outer blanket zones. In ARIES-AT for example, the inner blanket zone (30 cm thick) has to be replaced after about 3 years, whereas the outer part is a lifetime component

Ferritic steels and SiC-composites are selected in USA and JA for solid breeder blankets, Vanadium alloys for Li-blankets, and SiC-composites for a self-cooled Pb-17Li blanket. There is one hybrid concept (ARIES-ST) with a self-cooled Pb-17Li breeding zone, helium-cooled steel structure and SiC flow channel inserts serving as electrical and thermal insulator (similar to our PPA 2.5 concept) . SiC is considered in USA and JA as low activation waste material in agreement with their regulations.

Staff:

L. Boccaccini
K. Kleefeldt
S. Malang
K. Schleisiek

Underlying Technology

Underlying Technology

Operation and Upgrade of the Hot Cells and the Chemo-Analytical Laboratories of FZK

The Hot Cells and the Chemo-Analytical Laboratories provide the infrastructure for the performance of tasks defined in the EFDA workprogramme related to the characterisation of irradiated and non-irradiated materials using methods such as optical and electron microscopy, He-pycnometry and Hg porosimetry, crush-, micro-hardness- and charpy tests as well as long time annealing tests.

Investigations on the ductile-to-brittle temperature of OPTIFER alloys and ORNL steel after irradiation (2.4 dpa) and the influence of trace elements such as boron and tantalum have been performed in the frame of the materials development programme. Furthermore the impact properties of a Vanadium alloy after irradiation has been investigated.

In the framework of the Breeding Blanket Task Area experiments for the characterisation and post-irradiation examination on ceramic breeding materials have been performed aimed to control the quality and to characterise lithium orthosilicate pebbles (diameter 0,25 – 0,63 mm) before and after irradiation. The aim is to determine properties such as microstructure, porosity and density, deformation and hardness, and tritium and helium release which are essential for the further development of the HCPB concept. For detailed results on the analysis of short time irradiated Li_4SiO_4 pebbles which have been performed in the reporting period see TTBB-006: „Irradiation of ceramic breeder pebble beds“.

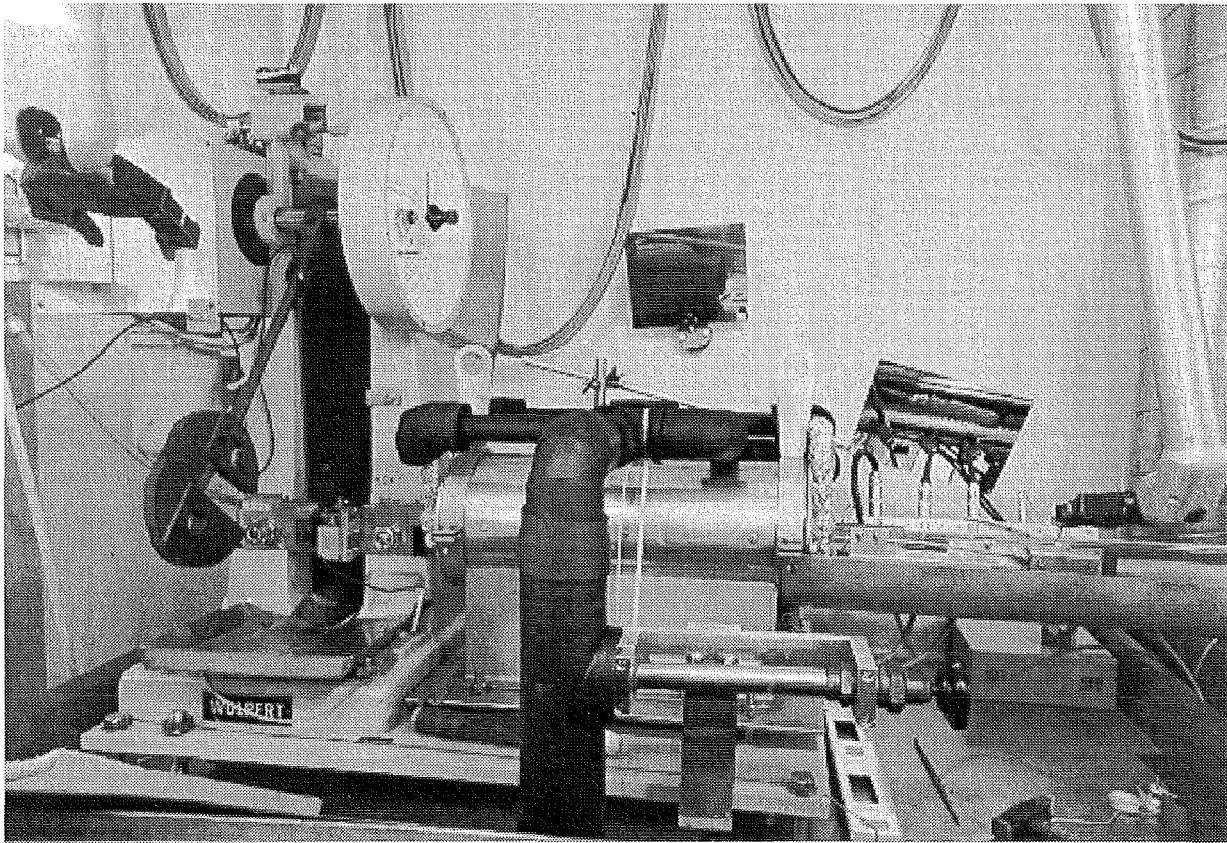
The characterisation of both large ($d = 2 \text{ mm}$) and small ($d = 0,1 - 0,2 \text{ mm}$) beryllium pebbles before and after irradiation have

concentrated on metallographic and mechanical properties, Be/steam chemical reactivity and Tritium and Helium retention/reactivity. It turned out that helium and tritium release behaviour is a complex function of both irradiation temperature and time and that tritium and helium reside in common bubbles in irradiated material and thus indicate a common release pattern. For more details see TTBB-007: „PIE of Be pebbles irradiated in EXOTIC-8“.

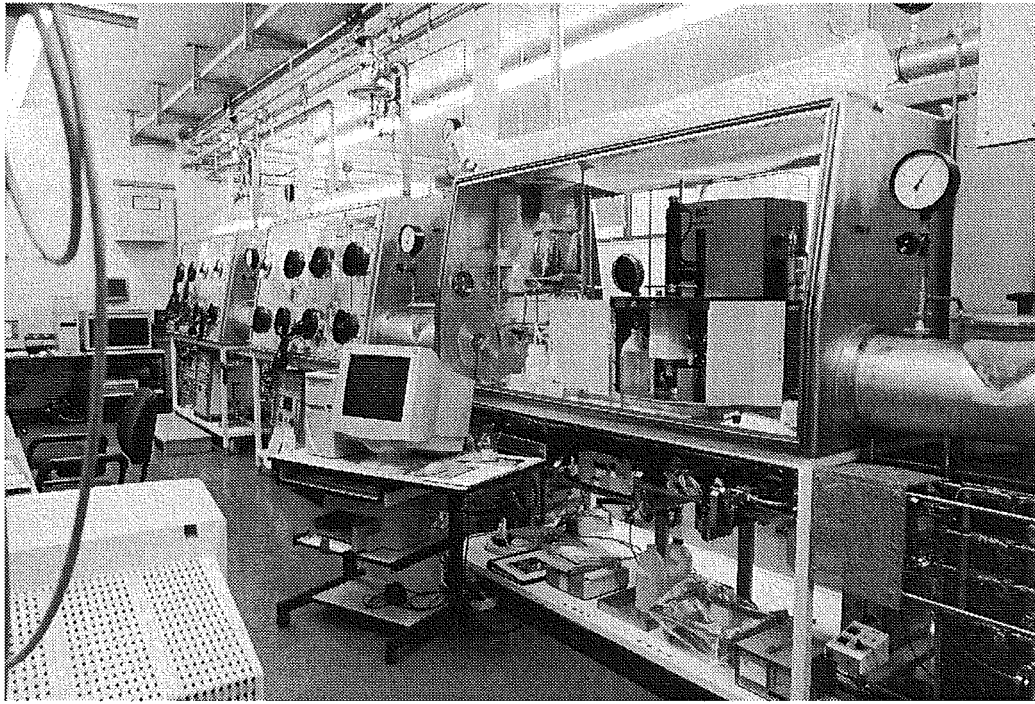
For the investigation of the tritium and helium kinetics as a function of neutron fluence, temperature and damage dose specimens of the plasma facing material candidates graphite, carbon fiber composites and beryllium were irradiated in the High Flux Reactor (HFR) Petten and post irradiation experiments were performed in the reporting period. It turned out that the amounts of tritium found in the samples were significantly higher than expected which needs further clarification and the release kinetics of tritium and helium were again found to be concurrent (see T 438/04: „Investigation of D/T retention in n-irradiated PFC materials“).

Operation and Upgrade of the Tritium Laboratory Karlsruhe (TLK)

The TLK is the only laboratory in Europe which provides the possibility to carry out experiments with tritium for the development and test of technologies in key areas of the fuel cycle. Present activities are focussed on technologies and components for the exhaust gas system for ITER-FEAT and on subjects of tritium balancing, detritiation and waste treatment in the framework of JET activities. Furthermore new analytical methods are developed and existing ones enhanced in order to increase effectiveness, frequency and quality of measurements. Another aspect is the reduction of sample waste.



Fully automatic charpy testing device in a glove box of the hot cell complex



Chemo-analytical laboratory

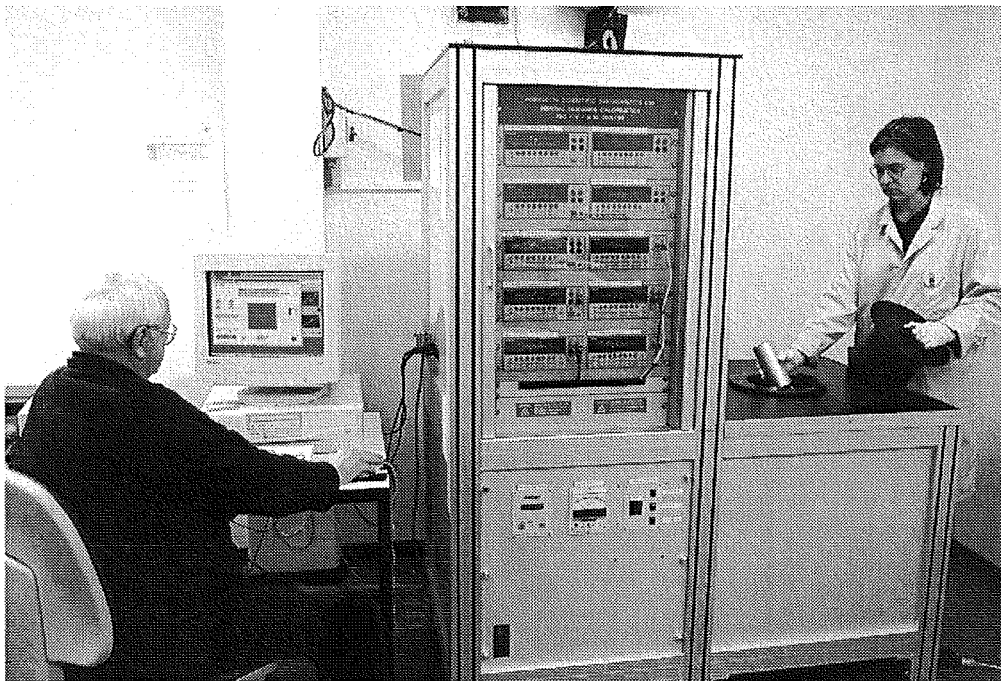
The concept of the Tokamak Exhaust Processing System (TEP) for ITER-FEAT is examined in the semi-technical facility CAPER. The performance of the permeator, which is the first process step of CAPER was tested under operational conditions expected for the ITER front-end permeators. The operation of the main components (since 1994) which are the methane crackers, the water gas shift reactor and the permeators has been successfully continued in the reporting period. For more details see TR 1 „Tokamak exhaust processing“.

Analytical methods such as Laser Raman spectroscopy, gas chromatography, calorimetry and Omegatron mass

spectrometer have been further developed and tested for specific applications.

Significant improvements in Raman detectability have been achieved using the new Laser-Raman analysis system (LARA). Hence Laser-Raman spectroscopy is well suited for real-time quantitative analyses of tritiated gas mixtures (see TR 2 „Development of tritium instrumentation“).

A cryogenic cold trap constitutes the main process step for the removal of tritiated water vapour. A series of tests have demonstrated the ability of the cold trap to reduce very



A new calorimeter for the Tritium Laboratory

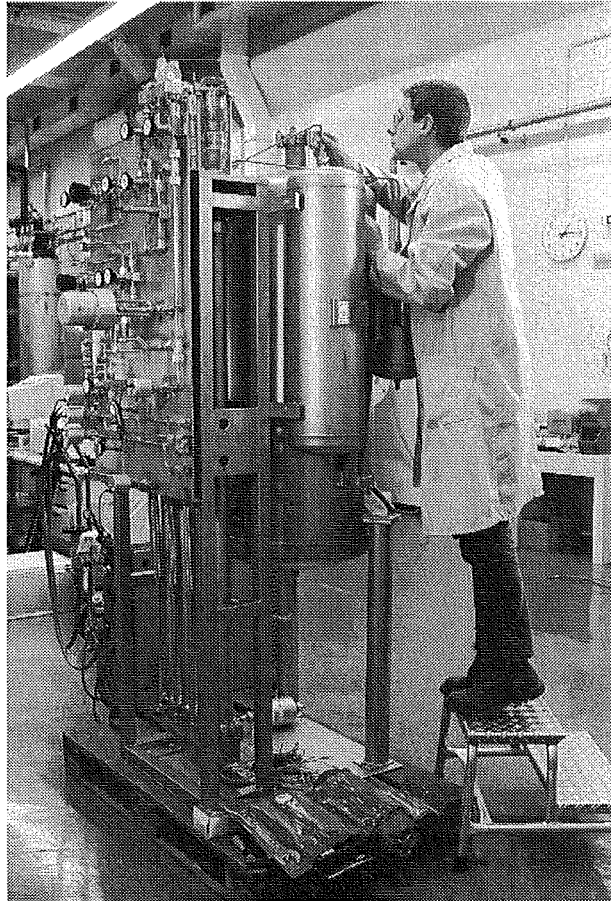
effectively the water vapour content of a helium stream at high flow rates. A further activity comprised the elaboration of a concept for the measurement of the tritium production in the HCPB test blanket module in ITER-FEAT (see TR 6 „Tritium extraction and helium purification“)

In the framework of the task TR 5 “Tritium recovery from liquid and solid wastes” the following activities were carried out:

- Work on the detritiation of molecular sieve (MS) beds with the AMOR facility was going on; so far almost 4 tons of MS's have been successfully regenerated.
- In the course of upgrading of the isotope separation system (ISS) valuable experience has been accumulated on the degree of tritium contamination of various components.
- The development of technology for the detritiation of oils from pumps employed in JET was continued.
- A new research activity was initiated regarding the development of a water detritiation process for JET.

The tritium storage facility was upgraded by four additional uranium beds and the getter material zirconium-cobalt (ZrCo) was tested as additional getter material compared to uranium. The results indicate that under the employed conditions the sorption rate by ZrO is slightly faster than that of uranium. See TEP 3 A „Tritium storage in ZrCo“.

For the design of a tritium compatible Roots pump an experimental rig has been designed and constructed in order to test the ferrofluidic seal under ITER relevant conditions. The tests demonstrated that ferrofluidic seals fulfil the required specifications, see T 456/02 „Development of a tritium compatible Roots pump“.



New separation column for the isotop separation system of the Tritium Laboratory

Physics Integration

Microwave Heating for Wendelstein 7-X

1. Introduction

The task includes the development, construction, test and operation of the complete 10 MW-140 GHz Electron Cyclotron Resonance Heating (ECRH) system for continuous wave (CW) operation on the stellarator W7-X at IPP Greifswald in a collaboration between Forschungszentrum Karlsruhe, IPF Stuttgart and IPP Greifswald/Garching [1]. The stellarator plasma will be created and heated from the neutral filling gas by this ECRH system. With 10 MW heating power the plasma parameter region of long free mean path length, which is relevant for fusion reactors, can be reached. In addition, a stationary non-inductive current can be driven to influence the plasma profile for better plasma confinement. The 10 MW of rf power should be obtained using ten 140 GHz gyrotrons each having 1 MW output power. The millimeter wave power will be transmitted via two multi-beam waveguides (MBWG) with a length of about 50 m from the gyrotrons to the plasma torus.

2. Development of a Prototype Gyrotron

A 1 MW 140 GHz gyrotron with a chemical vapour deposition (CVD) diamond window for continuous wave (CW) operation and a single-stage depressed collector for energy recovery and improvement of efficiency has been designed and constructed in collaboration with the Swiss Association EURATOM-CRPP Lausanne and Thomson Tubes Electroniques, Vélizy. F. [2]. It operates in the $TE_{28,8}$ cavity mode and provides a linearly polarized $TEM_{0,0}$ Gaussian rf beam. The gyrotron consists of a diode MIG gun, an improved beam tunnel, a high-mode purity low-ohmic loss cavity ($<2\text{kW/cm}^2$), an optimised non-linear up-taper, a highly efficient internal quasi-optical mode converter employing an improved launcher together with one quasi-elliptical and two toroidal beam shaping reflectors and a horizontal rf output. The large single-stage depressed collector is at ground potential and is equipped with a beam sweeping magnet.

The superconducting magnet system has been delivered to Karlsruhe from Oxford Instruments in November 1999 with 6 months delay. Due to a transportation damage, the whole system had to be shipped back to England. After repair the magnet system has been delivered to Forschungszentrum Karlsruhe in June 2000 and has been tested successfully.

The first gyrotron tube (maquette) has been installed in our gyrotron test facility (Fig. 1) and put into operation. First rf power measurements at pulse lengths of 1 ms gave 0.65 MW at 40 A and 82 kV in the $TE_{28,8}$ mode at 140.3 GHz. The measured frequency is in very good agreement with the design value of 140.2 GHz.

Table 1: Design parameters of the 140 GHz/1MW, $TE_{28,8}$ gyrotron

Accelerating voltage V_b	80 kV
Beam current I_b	40 A
Cavity magnetic field B_0	5,56 T
Beam radius in the cavity	10,1 mm
Average pitch angle (α)	1,5
Peak cavity wall loading	$<2\text{ kW/cm}^2$
rf power	1 MW, CW
Overall efficiency	45%
Window material	CVD Diamond

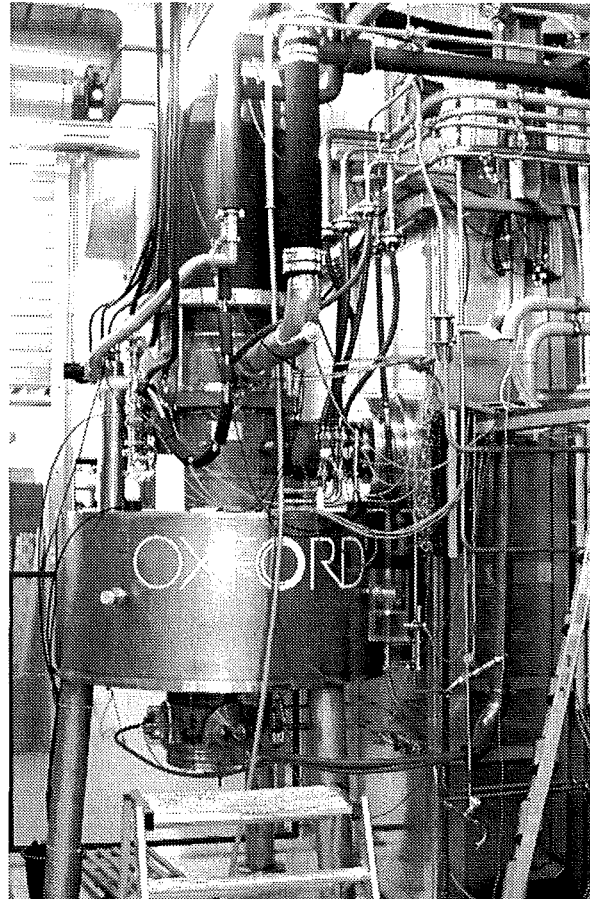


Fig. 1: Photograph of the 140 GHz gyrotron in the teststand

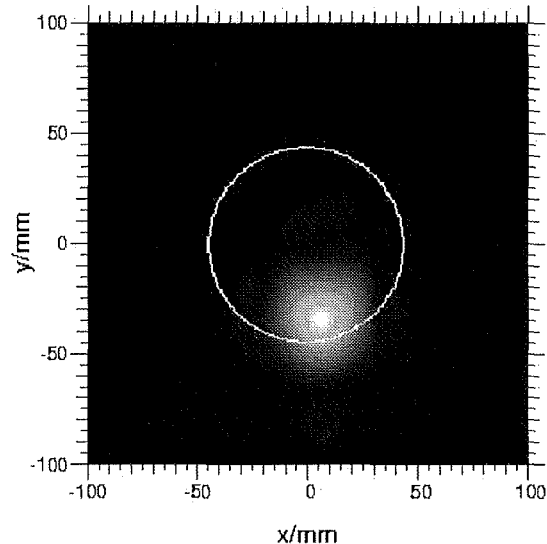


Fig. 2: Calculated rf beam field distribution at the window plane

Despite careful optimisation it was not possible to increase the output power and the efficiency. Measurements of the rf-field distribution by an IR camera showed a strong shift of the rf-beam downwards by 30 mm at the window plane (Fig. 2). The same shift also was observed in our low power measurements with a coldest q.o. mode converter system. The shift leads to a power reflection of more than 20% back into the gyrotron. In former experiments with other gyrotrons it was shown that these reflections cause a deterioration of the quality of the electron beam, which influences the output power considerably. The shift

of the rf beam is caused by a design error of the q.o. mode converter.

In order to avoid the risk of damaging the diamond window due to non-symmetrically heating of the window cuffs, the rf-measurements were limited to short pulse operation up to about 10 ms. For this pulse length, operation with depressed collector has been performed successfully up to depression voltages of 30 kV resulting in an efficiency enhancement by a factor of 1.6. In order to prove the sufficient operation of the collector sweeping, long pulse operation (up to 1 s) has been done at depression voltage (~ 55 kV) without rf generation. The sweeping range of the electron beam along the collector has been shown to be too small, due to distortions of the AC power supply output signal at high amplitudes and high frequencies. The normal conducting AC coil power supply will be changed.

3. Development of Quasi-Optical Transmission Line

As the multi-beam waveguide (MBWG) mainly determines the transmission properties of the complete transmission system, a careful optimisation of the shape of the mirrors as well as their orientation was performed [3,4].

Calculations give very low mode conversion resulting in a high transmission efficiency of the transmission system. For the design of the water-cooled mirrors, thermo-mechanical calculations have been performed for several materials or combinations there of, and for a variety of frame structures on the backside of the mirrors.

To test the transmission properties of such a system a test facility with diagnostic tools has been constructed. This includes a measurement system for ohmic loss of mirrors and a reflectometer to detect possible deformations of its surfaces in case of thermal loads. A mirror mount for the MBWG-mirrors was equipped with position sensors to test stability, reproducibility, and sensitivity against external mechanical and thermal loads. The development of an alignment control system based on reflectometry from shallow gratings in Littrow geometry on the mirrors is continued. A prototype transmission line has been installed at the IPF Stuttgart. First experiments showed a transmission efficiency of 90% compared to the theoretical one of more than 94%.

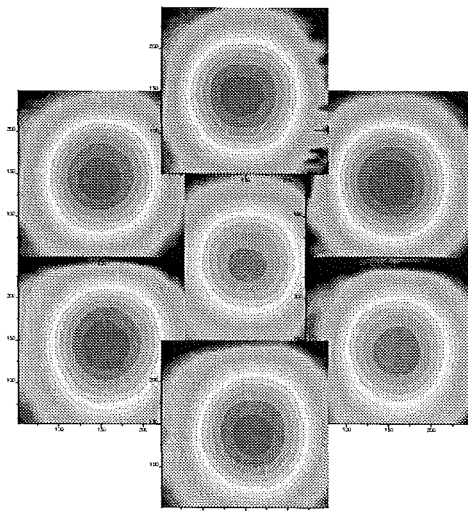


Fig. 3: Imaging properties of the MBWG

The output beam patterns of the 6 beams are shown in Fig. 3. The reason for this difference is seen in the poor input system

with too high non-Gaussian distribution. The input system will be improved.

4. Development of In-Vessel Components

Development has been started to optimise the surface structures for the back reflectors which will be mounted at the inner wall of the vacuum vessel of W7-X to redirect the non-absorbed part of the beam back into the plasma in a controlled way. This is necessary for heating of high-density plasmas in 2nd harmonic O-mode, where the absorption is modest [4].

5. Auxilliary Systems

The power supplies for depressed collector operation have been tested successfully in short pulse operation with the gyrotron. The water cooling circuits for the gyrotron were installed and it was proven that the designed pressures and water flow rates could be achieved. The flow rate for the cavity, however, is reduced strongly due to a too high pressure drop in the cavity-launcher system. Tests are being performed on a duplicate in order to find out the reason for the increased pressure drop. The RF-tight microwave box to house the mirrors, water load and field distribution measurement devices for the rf tests are equipped for short pulse operation and adopted to the maquette tube. Long pulse operation will be possible in the nearest future as soon as the water cooled mirrors to focus the beam into the CW load are installed.

Literature:

[1] V. Erckmann, G. Dammertz, D. Dorst, L. Empacher, W. Förster, G. Gantenbein; T. Geist, W. Kasperek, H.P. Laqua, G.A. Müller, M. Thumm, M. Weissgerber, H. Wobig, IEEE Trans. on Plasma Science, Vol. 27, No. 2, pp. 538-546.

[2] G. Dammertz, S. Alberti, A. Arnold, E. Borie, V. Erckmann, W. Förster, G. Gantenbein, P. Garin, E. Giguet, S. Illy, W. Kasperek, H. Laqua, G. Le Cloared, Y. Le Goff, H. Leonhardt, R. Magne, G. Michel, G. Müller, B. Piosczyk, M. Schmid, M. Thumm, M.Q. Tran, Proc. 25th Int. Conf. on Infrared and Millimeter Waves, Beijing, China, 2000, pp. 15-16.

[3] W. Kasperek, L. Empacher, V. Erckmann, G. Gantenbein. F. Hollmann, H.P. Laqua, P.G. Schüller, M. Weißgerber, H. Zohm, JAERI-memo 12-041 (2000), 630-635.

[4] W. Kasperek, V. Erckmann, H.P. Laqua, E. Borie, G. Dammertz, L. Empacher, W. Förster, G. Gantenbein, S. Illy, G. Michel, G. Müller, B. Piosczyk, M. Thumm, D. Wagner, M. Weißgerber, H. Zohm, Proc. of the Int. Workshop on Strong Microwaves in Plasma, Nizhny Novgorod, Russia (2000), pp. 185-204.

Staff:

- | | |
|---------------------------|-----------------|
| A. Arnold (Uni Karlsruhe) | D. Mellein |
| E. Borie | G. Neffe |
| G. Dammertz | S. Nold |
| A. Götz | B. Piosczyk |
| P. Grundel | M. Schmid |
| S. Illy | W. Spiess |
| H. Kunkel | J. Szczesny |
| M. Kuntze | <u>M. Thumm</u> |
| W. Leonhardt | |

Appendix I: FZK Departments Contributing to the Fusion Programme

FZK Department	FZK Institut/Abteilung	Director	Ext.
Institute for Materials Research	Institut für Material- und Festkörperforschung (IMF)	I. Prof. Dr. K.-H. Zum Gahr	3897
		II. Prof. Dr. D. Munz	4815
		III. Prof. Dr. H. Haußelt	2518
Institute for Pulsed Power and Microwave Technology	Institut für Hochleistungs-Impuls- und Mikrowellentechnik (IHM)	Prof. Dr. M. Thumm	2440
Institute for Nuclear and Energy Technology	Institut für Kern- und Energietechnik (IKET)	Dr. T. Schulenberg	3450
Institute for Reactor Safety	Institut für Reaktorsicherheit (IRS)	Prof. Dr. D. Cacuci	2550
Institute for Technical Physics	Institut für Technische Physik (ITP)	Prof. Dr. P. Komarek	3500
Central Experimental Department	Hauptabteilung Versuchstechnik (HVT)	Dr. K. Schubert	3114
- Hot Cells	- Heiße Zellen (HVT-HZ)	Dr. W. Nägele	3650
- Tritium Laboratory Karlsruhe	- Tritiumlabor Karlsruhe (TLK)	Dr. R.D. Penzhorn	3239
Central Department for Data Processing and Electronics	Hauptabteilung Prozeßdatenverarbeitung und Elektronik (HPE)	Prof. Dr. H. Gemmeke	5635

Contributing:

Institute for Nuclear and Particle Physics, Technical University Dresden	Institut für Kern- und Teilchenphysik der Technischen Universität	Prof. Dr. H. Freiesleben	0351/4635461
Underwater Technology Centre of the Institute of Materials Science University of Hannover	Unterwassertechnikum Hannover des Instituts für Werkstoffkunde der Universität Hannover	Prof. Dr.-Ing. Dr.-Ing. e.h.mult. H. Haferkamp	0511/7624311

Appendix II: Fusion Programme Management Staff

Head of the Research Unit	Dr. J.E. Vetter	ext. 5460 e-mail: joerg.vetter@pkf.fzk.de
Secretariate:	Mrs. I. Sickinger	ext. 5461 e-mail: ingeborg.sickinger@pkf.fzk.de
	Mrs. I. Pleli	ext. 5466 e-mail: ingrid.pleli@pkf.fzk.de
	Mrs. V. Lallemand	ext. 5466 e-mail: vera.lallemand@pkf.fzk.de
Programme Budgets, Administration, Documentation	BW. G. Kast	ext. 5462 e-mail: guenter.kast@pkf.fzk.de
Studies, ITER / NET Contracts, Superconducting Magnets, Gyrotron Development	Dr. J.E. Vetter	ext. 5460 e-mail: joerg.vetter@pkf.fzk.de
Tritium Technology, Structural Materials	DI. S. Gross	ext. 5468 e-mail: Sigurd.Gross@pkf.fzk.de
Blanket Technology, Reactor Studies, Neutron Source	DI. W. Bahm	ext. 5465 e-mail: werner.bahm@pkf.fzk.de

Address:

**Forschungszentrum Karlsruhe GmbH
Nuclear Fusion Programme Management
Post Office Box 3640, D - 76021 Karlsruhe / Germany**

Telephone No:

07247-82- Extensions

Telefax No:

07247-82-5467

world wide web:

<http://www.fzk.de/pkf>

Appendix III: Glossary

BET	Brunauer, Emmet and Teller
BIOMASS	BIOspheric Modelling and ASSEssment
BSMI	Bed-structure Mechanical Interaction
CBM	Carbon Based Materials
CCD	Charge Coupled Device
CDA	Conceptual Design Activity
CDE	Conceptual Design Evaluation
CFC	Carbon Fibre Composite
CICC	Cable in Conduit Conductor
COINLOSS	Conductor Insulation Loss (software module)
COOLSORP	Measurement of Sorption Isotherms at Cryogenic Temperatures
CP	Cooling Plate
CRPP-EPFL	Centre de Recherches en Physique des Plasmas Ecole Polytechnique Fédérale de Lausanne
CS	Central Solenoïd
CT	Cold Trap
CVD	Chemical Vapor Deposition
CW	Continuous Wave
DBTT	Ductile Brittle Transition Temperature
DP	Dew Point
DTL	Drift Tube Linear, accelerator structure
EAF	European Activation File
EASY	European Activation System
EB	Electron Beam
EC(R)H	Electron Cyclotron (Resonance) Heating
ECCD	Electron Cyclotron Current Drive
EDM	Electro Discharge Method
EFF	European Fusion File
EMPA	Electron Microprobe Analysis
EOL	End-of-Life
EVITA	Experimental Vacuum Ingress Test Apparatus
FBI	F = Force, B = Magnetic Field, I = Current
FCGR	Fatigue Crack Growth Rate
FCI	Flow-channel Inserts
FDR	Final Design Report
FE	Finite Element

FEAT	Fusion Energy Advanced Tokamak
FEM	Finite Element Method
FM	Ferritic-martensitic
FNG	Frascati Neutron Generator
FPCC	Fusion Power Coordination Committee
FW	First Wall
HCPB	Helium Cooled Pebble Bed
HCS	Helium Cooling Subsystem
HEBLO	Helium Blanket Test Loop
HECOP	<u>H</u> eat <u>C</u> onduction of <u>P</u> ebble Bed
HETP	High Equivalent to a Theoretical Plate
HFI	High Fluence Irradiation
HFR	High Flux Reactor at Petten
HIP	Hot Isostatic Pressing
HP	Heating Plate
ICS	Intercoil Structure
IEAF	Intermediate Energy Activation File
IFMIF	International Fusion Materials Irradiation Facility
IGA	Inert Gas Atomization
IGUN [®]	Ion GUN, program code
IPF	Institut für Plasmaforschung der Universität Stuttgart
ISRM	Inelastic Strain Rate Modified
ISS	Isotope Separation System
ITER	International Thermonuclear Experimental Reactor
JAERI	Japan Atomic Energy Research Institute
JETT	J Evaluation on Tensile Test
LARA	Laser-Raman Analysis System
LCF	Low Cycle Fatigue
LCT	Large Coil Task
LEBT	Low Energy Beam Transport
LM	Liquid-metal
LOFA	Loss of Flow Accident
LSC	Liquid Scintillation Counting
MAG	Metal Arc Gas (Weld)
MAGS	Magnet Safety (software module)
MCE	Multi-channel Effect
MEBT	Medium Energy Beam Transport

MEKKA	Magneto-hydrodynamic Experiments in Sodium and Potassium Karlsruhe
MHD	Magneto Hydrodynamics
MS	Molecular Sieve
MTS	Material Testing Systems (Trade mark of MTS company)
PD	Point Defect
PF	Poloïdal Field
PFC	Plasma Facing Components
PFM	Plasma Facing Material
PICOLO	Pb-Li Corrosion Loop
PIE	Post-irradiation Examination
QMS	Quadrupole Mass Spectrometer
RA	Reduced Activation
RAFM	Reduced Activation Ferritic Martensitic
REP	Rotating Electrode Process
RF	Radio Frequency
RFQ	Radio Frequency Quadrupol, accelerator structure
R-MHD	Radiation Magneto hydrodynamics
RMS	Root Mean Square
SAD	Secondary Angular Distributions
SAGBO	Stress Accelerated Grain Boundary Oxidation
SDS	Storage and Delivery System
SEM	Scanning Electron Microscope
SULTAN	Superconductor Test Facility, Villigen, Switzerland
TBM	Test Blanket Module
TCF	Thermal Low Cycle Fatigue
TCWS	Tokamak Cooling Water System
TEM	Transmission Electron Microscope
TEP	Tokamak Exhaust Processing
TES	Tritium Extraction
TFMC	Toroïdal Field Model Coil
TIG	Tungsten Inert Gas
TIMO	Test Facility for ITER Model Pump
TITAN	Tieftemperaturadsorption
TLK	Tritium Laboratory Karlsruhe
TMS	Tritium Measurement System
TOSKA	Toroïdalfest Spulentest Karlsruhe
TPB	Tritium Permeation Barrier

TÜV	Technischer Überwachungs Verein
UCT	Uniaxial Compression Test
VHP	Vacuum Hot Pressing
VTA	Vertical Test Assemblies
WCLL	Water Cooled Lithium-lead Blanket
XRD	X-ray Diffraction Analysis
ZrCo	Zirconium-Cobalt